UNIVERSITAT DE BARCELONA

Jets as Probes of Strongly Coupled Quark-Gluon Plasma

Daniel Pablos Alfonso

Jets as Probes of Strongly Coupled Quark-Gluon Plasma

Author: Daniel Pablos Alfonso

Director: Jorge Casalderrey-Solana

Tutor: Domènec Espriu Climent

A thesis submitted to the University of Barcelona for the degree of Doctor of Philosophy

Programa de Doctorat de Física

April 2016

Acknowledgements

I would like to thank my supervisor Jorge for his endless patience and his support during all these graduate years. I am also indebted to Krishna for his support and for hosting me at the CTP. Meeting them has been an enriching experience in many senses, and a great luck indeed.

I am very grateful to my collaborators Guilherme, Doga and Konrad, and all the people with whom I have shared the passion for physics around the world, who have taught me so many things. I would also like to thank the people at the ECM department and the CTP for a fantastic scientific environment. I am grateful to the LNS for giving me access to their computer cluster and specially to Jan Balewski for his tremendous help.

I thank all the good colleagues and friends I have made at home and abroad during my research for making my life more pleasant and interesting.

Thanks to all the friends in Tarragona, Barcelona, Madrid and Berlin for who you are and for being part of my life.

To my wonderful family and wife Daniela I dedicate the effort of this work. Your love and faith in me make me a better person everyday.

Resum

En aquesta tesi estudiem com excitacions d'alta energia es propaguen a través d'un plasma no abelià fortament acoblat. Aquest nou estat de la matèria es produeix a les col·lisions de ions pesats als nostres acceleradors i permet l'estudi d'una etapa de l'evolució del nostre Univers que va tenir lloc durant els primers microsegons després del Big Bang. En aquestes condicions extremes de temperatura i densitat, la matèria ordinària de la qual estem fets es comporta com un fluid perfecte, de fet el més perfecte conegut per la humanitat a dia d'avui. La teoria de les interaccions fortes és posada a prova a una escala d'energia que tot i ser prou alta per fondre els hadrons, no arriba al punt en què la constant d'acoblament és prou feble com per permetre una descripció pertorbativa. Al plasma, el contingut en camps partonics, els quarks i els gluons, deixen de ser els graus de llibertat rellevants i una descripciò microscòpica en termes de quasi-partícules no és possible. Una eina molt útil per posar a prova l'autèntic comportament d'aquest fluid fortament acoblat és l'anàlisi de les modificacions dels jets com a resultat de la seva interacció amb el plasma.

En una primera part introductòria hem donat els conceptes necessaris per a visualitzar com es desenvolupen les col·lisions d'ions pesats tal i com som capaços d'entendre-les avui dia. Hem introduit les tècniques més habituals per a descriure la propagació de partons dins d'un medi deconfinat tant pel règim d'acoblament feble com pel d'acoblament fort, i les hem fetes servir per obtenir el ràtio de pèrduda d'energia que descriuen la degradació en l'energia d'aquestes sondes en el seu pas a través del plasma. A acoblament feble, el principal mecanisme responsable de la pèrduda d'energia és l'emissió estimulada de gluons, i interessants fenòmens d'interferència ocorren que condueixen a una dependendència en la distància recorreguda que va com L^2. Aquests fenòmens són coneguts com efectes de coherència i el seu estudi esdevé més ric considerant l'emissió de múltiples gluons, tal com fem a la Part III. La descripció a acoblament fort fa servir holografia per mapejar una excitació vestida movent-se a través d'un plasma fortament acoblat a una corda que es propaga en un espai amb dimensions extra que conté un forat negre. Com que la teoria no abeliana en què es realitza el càlcul no es QCD, sinó que és $\mathcal{N} = 4$ SYM, prenem

aquests resultats com una intuïció amb què descriure la propagació d'un partó energètic en un model de jet quenching per col·lisions d'ions pesats. El diferent nombre de graus de llibertat entre les dues teories s'espera que dugui a diferències en la distància d'aturada, la qual es correspon amb el temps que triga l'extrem de la corda en creuar l'horitzó del forat negre.

Tot i que assumim que els intercanvis amb el medi són prou suaus com per incloure efectes no pertorbatius, tal com descriu la dualitat gauge/gravetat, els partons energètics que es produeixen a la col·lisió generalment tenen virtualitats altes, les quals relaxen a través de particions successives. Aquestes últimes ocorren a escales de longitut que no són resolubles pel medi, i per tant haurien de procedir com en el buit. Aquesta observació ens motiva a adoptar una descripció híbrida per a la interacció entre el jet i el QGP, fent servir cada descripció a l'escala on es suposa que es vàlida. Aquesta descripció fenomenològica ha demostrat ser molt exitosa en la descripció de les dades de dijets i fotó-jet per diferents centralitats. A més a més, a través de la combinació de les funcions de fragmentació del jet principal i del jet secundari d'un dijet, hem trobat un observable que és molt sensible al mecanisme de pèrduda d'energia concret, el qual és força interessant tenint en compte la dependència moderada que tenen altres observables. En vistes a les dades que arribaran en algun punt d'aquest any del run 2 del LHC, hem calculat prediccions per l'energia al centre de masses de 5.02 ATeV amb especials expectatives en les mesures de fotó-jet, per les quals l'augment en l'estadística s'estima que serà al voltant d'un factor 10. Aquesta millorada precisió ens ajudarà a discernir entre els diferents models de pèrduda d'energia donada l'apreciable separació que les seves prediccions presenten en observables com en el desequilibri en energia dels parells fotó-jet.

A la següent part del treball extenem el nostre model híbrid amb la inclusió de dos efectes, l'eixamplament i la resposta del medi, amb especial motivació en la millora de l'habilitat de les nostres simulacions per descriure els desafiants observables intra-jet, com per exemple les funcions de fragmentació i les formes de jet. El primer efecte, l'eixamplament, es deu al moviment Brownià que les sondes experimenten en un bany termal, i com el seu nom indica tendeix a eixamplar la distribució de les partícules dins

del jet. Aquest mecanisme és un candidat capaç de reproduir el comportament observat en la modificació de la densitat d'energia transversa dels jets en el medi, que consisteix en una reducció a r mitjanes i un increment a r altes. Tot i així, resulta que l'observable que quantifica aquestes modificacions, les formes de jet, són bastant insensibles a la inclusió d'aquest efecte degut a l'efectivitat del fort quenching, el qual suprimeix els fragments més suaus tot deixant una estructura prima que esdevé lleugerament inclinada. No obstant, mitjançant la restricció del rang de p_T de les partícules que formen part de l'anàlisi, hem estat capaços de produir un nou observable que mostra una alta dependència en la força concreta del mecanisme d'eixamplament. Mesures d'aquest tipus d'observables podrien fer-se servir per obtenir una extracció directa de la magnitut d'aquest efecte dins del medi.

El segon efecte involucra la conservació general de l'energia i el moment. L'energia ràpidament termalitzada depositada pels partons energètics modifica el plasma, induint fluctuacions en la temperatura i la velocitat de les cel·les de l'entorn. Aquesta pertorbació es propaga llargues distàncies prenent la forma d'un solc que eventualment decau en hadrons suaus, les orientacions dels quals guarden una correlació amb la direcció del jet i per tant produeixen un efecte net fins i tot després de la substracció del rerefons. Nosaltres estimem l'impacte d'aquest efecte assumint que la pertorbació és petita, el qual duu a simplificacions importants en la seva implementació. Les conseqüències observables es fan més patents en les mesures d'intra-jet tals com les formes de jet i les funcions de fragmentació, on es veu clarament que la inclusió d'aquesta física concorda amb la tendència experimental observada, i que esdevé simplement essencial quan s'estableixen comparacions amb anàlisis globals en què es tenen en compte totes les partícules de l'esdeveniment i les seves correlacions.

El plantejament híbrid ja ens ha atorgat un esquema calculacional sistemàticament millorable, dins del qual podem testejar les prediccions d'acoblament fort a través de la confrontació amb mesures experimentals d'observables de jets. Això demostra que aquest enfocament ara es pot fer servir per explorar i subsegüentment testejar nous observables com els que hem proposat, els quals ens poden donar indicacions sobre la rellevància de determinats fenòmens. Aspectes de la física no tinguda en compte fins ara que podrien ser

implementats al nostre esquema, inclouen correccions de N_c finit, λ finit, i correccions no nul·les en N_f/N_c per l'expressió de la pèrduda d'energia, o com aquesta raó canvia en una teoria fortament acoblada que no és conforme. També es podria considerar la reducció de l'espai de fases en la fragmentació d'un partó a la cascada de PYTHIA com a resultat de la pèrduda d'energia, o la possibilitat que interaccions suaus múltiples indueixin particions addicionals a la cascada. Una millora especialment interessant involucra els efectes de coherència, els quals estan relacionats amb el poder de resolució finit del medi, un problema que s'encara a l'última part de la tesis.

La part final del treball consisteix en el càlcul de l'emissió estimulada de dos gluons en el context de QCD pertorbativa. Estudiant la resposta completa en diferents límits arribem a la conclusió que des del punt de vista del plasma la propagació del jet és percebuda com una col·lecció d'emissors efectius depenenent del poder de resolució, el qual per un plasma prim és de l'ordre de l'invers de la massa d'apantallament de Debye μ_D. Tal com hem dit abans, al model de jet quenching presentat a aquesta tesis encara li manca aquesta física, i la seva inclusió s'espera que tingui conseqüències importants pels observables més diferencials, una tasca que s'emprendrà en un treball futur.

Aquests són temps molt emocionants per a la física de les interaccions nuclears fortes. La naturalesa fortament acoblada del QGP fa l'estudi d'aquest sistema extremadament interessant, així com el d'altres sistemes fortament acoblats com els superconductors d'alta temperatura o els àtoms freds. Hem vist com les preguntes més fonamentals sobre la naturalesa de la fase de la matèria comú a altes temperatures poden ser adreçades amb l'estudi del jet quenching i de les seves conseqüències observables. Aquesta tesis representa un esforç en la confrontació de les seductores idees d'holografia amb els experiments. La possibilitat que una teoria familiar alhora que innegablement desafiant com QCD pot ser descrita en termes de cordes que es propaguen en dimensions adicionals no és només convenient, sinó que absolutament fascinant. Tenint els mitjans per confrontar noves idees quantitativament, tal i com hem fet al llarg d'aquest treball, nous obervables i noves dades són essencials si finalment volem entendre les propietats del líquid fortament acoblat que la Natura ens ha servit.

Contents

Part I

Introduction

Chapter 1

Hot QCD

1.1 QCD

Even though the discovery of Quantum Chromodynamics (QCD) as the theory responsible of the nuclear strong interactions was made more than half a century ago, major conceptual and computational problems have not yet been solved. QCD is hard. Its coupling strength runs with the energy in such a way that for common low energies (long distances) the interaction is non-perturbative, yielding a series expansion hopeless. On the other hand, at very high energies (short distances) the coupling tends to zero and then the theory is tractable. This is the phenomenon of asymptotic freedom, and it arises as a consequence of the fact that gluons, the strong force carriers, have colour charge and can therefore interact with themselves. This important feature of non-abelian theories is in stark contrast with abelian ones, such as Quantum Electrodynamics (QED), where photons are neutral and one does not encounter the sort of rich and challenging emergent phenomena characteristic of QCD.

The theory of QCD contains quarks and gluons as the basic degrees of freedom in terms of which the fundamental Lagrangian is expressed. However, one cannot detect these particles (in contrast to photons and leptons), but can only access to the great variety of bound states that quarks produce, the so called hadrons, among which our beloved neutrons and protons sit. Most of the hadrons mass comes from the energy of the gluons interchanged among the quarks, and very little from the quark current mass itself.

The inability to directly detect partons (i.e. quarks and gluons) represents the well known confinement problem. The real existence of these partons beyond a convenient mathematical formulation to describe hadron phenomenology had to be proven through different experiments such as Deep Inelastic Scattering (DIS), where the point-like electron-quark interaction could be described by use of the Bjorken scaling variable, or others such as the electron-positron collisions with three or more jet (collimated sprays of hadrons) events, which represented the indirect discovery of the gluon.

Jets are some of the emergent phenomena in QCD, which arise as a combination of virtuality relaxing successive splittings, described in terms of partons, and a posterior fragmentation from these partons to hadrons when the virtuality reaches the confinement scale $\Lambda_{\mathrm{QCD}} \sim 200$ MeV. Generically, all particles produced in inelastic collisions start being off-shell, which means that even massless particles can radiate. QCD and QED are to this respect quite similar, since both theories develop particle showers, although QCD ones are more stuffed since gluons can radiate and also the strong coupling constant α_s, which plays a crucial role in emission probabilities, is at collider relevant energies 10 times larger than the electromagnetic one α_{EM}.

The major difference between the two theories lies precisely in the fact that QCD is confined. The formation of hadrons out of partons follows as an unavoidable step in the system evolution once it has reached the confinement scale. The nature of this process is non-perturbative and there are no known analytical techniques to describe it; the best we have so far are phenomenological models such as the Lund string model, which regards the interaction among coloured objects to be mediated by strings, dynamical objects representing the energy contained in the QCD vacuum. Due to the finite tension of the strings, their energy increases as they get stretched up to a certain point in which it is more efficient to generate a quark-antiquark pair, and the string breaks into two. This string is therefore confining.

Because of the way the mass of the hadrons depends on their spin, following the linear

Regge trajectories which come out naturally from a string-like picture, it was originally thought before the establishment of QCD that string theory was in fact the theory of strong interactions. With the appearance of holography this idea has been reinterpreted in a very appealing way: in non-abelian theories with a gravity dual, quarks can be understood as strings which propagate in a space with an extra dimension. Due to the curvature this higher dimensional space has, the new coordinate is a measure of the energy scale at which the theory is being probed. Applications of this correspondence are most useful at the limit of strong coupling, where these strings become classical and computations notably simplify. The discovery that nuclear matter under extreme temperature conditions behaves as a strongly coupled fluid, challenging traditional perturbative techniques, has opened a rich window of phenomenological applications for holography.

In this introductory part of the thesis we will review basic features of the phase transition that QCD experiences in heavy ion collisions, as well as the study both at weak and strong coupling of the passage of energetic jets through the created plasma, which are very useful probes that can help us characterize the properties of this new state of matter.

1.2 An Estimate of the Transition Temperature

Nuclear matter together with the electrons constitute the totality of the matter we experience in our everyday life. Under standard conditions of temperature and density we have get familiarized with the different phases substances can have. Intuitively, the choice of a specific phase can be understood by the condition that the free energy of a system, $A = U - TS$, should be minimized. For instance, by increasing the temperature T at a fixed pressure of solid water, we will reach a point beyond which the very ordered atomic disposition that minimizes the internal energy U will be abandoned, for the greater the temperature the greater the weight of the measure of disorder, entropy S, will have in the free energy formula. The temperature at which this happens is the melting temperature of ice at a given pressure.

This mundane transition doesn't involve the consideration of the internal structure of the hydrogen or oxygen nuclei, such degrees of freedom are effectively frozen and the most convenient description lies at the atomic level. But, what would happen if one increased the temperature beyond thousands of times the one at the center of the Sun? Is there a regime where the quarks and gluons lying confined in the nucleons would find it worth it to adopt other configurations? And what about a cold, but extremely dense system such as a neutron star; do we expect different configurations there too?

An early attempt to address the possibility of a high temperature phase transition lead to the MIT bag model [1]. Despite its simplicity, it predicts a transition temperature remarkably close to the one extracted from more advanced techniques, using only common thermodynamic relations which involve the counting of hadronic and partonic degrees of freedom, and the inclusion of a "vacuum energy" in order to account for confinement. We will briefly summarize its main features next.

This phenomenological model crudely incorporates the effects of asymptotic freedom and confinement by representing hadrons as bubbles of (perturbative) vacuum, or "bags", in a confining medium. Inside the bag, quarks and gluons appear as free particles, while outside they do not due to the presence of a constant vacuum energy density B, the bag constant, that keeps them confined. In this way. the hadron mass M is given by

$$M = \frac{4\pi}{3} R^3 B \,. \tag{1.1}$$

In order to derive the condition for a deconfinement phase transition between a hadron gas phase and a quark-gluon plasma phase we basically need to compare their pressures, which read

$$P_{hg} = \nu_b^{hg} \frac{\pi^2 T^4}{90} \,, \qquad P_{qgp} = (\nu_b + \frac{7}{4}\nu_f) \frac{\pi^2 T^4}{90} - B \tag{1.2}$$

where ν_b and ν_f are the bosonic and fermionic degrees of freedom in the quark-gluon plasma phase respectively, and ν_b^{hg} are the bosonic degrees of freedom in the hadron gas phase. We have considered that the hadron gas phase is dominated by the ground state

at zero chemical potential, meaning we mainly have pions, which are bosons, and then $\nu_b^{hg} = 3$ for this phase. For the quark-gluon plasma phase one needs to add a term BV to the free energy representing the vacuum energy in the confining medium, or in other words the energy cost of having quarks and gluons free. The gluonic number of degrees of freedom is $\nu_b = 2(N^2 - 1)$, while the fermionic ones are $\nu_f = 2NN_f$, with N_f being the number of flavours. Inserting the physical quantities $N = 3$ and $N_f = 2$, corresponding to up and down quarks, and equating the pressures gives

$$T_c = \left(\frac{45B}{17\pi^2}\right)^{1/4} \simeq 144\,\mathrm{MeV} \tag{1.3}$$

with a bag constant $B^{1/4} \simeq 200$ MeV from (1.1) by using for instance the proton parameters $R \simeq 1$ fm and $M \simeq 1$ GeV. It is a first-order transition despite the name "critical temperature" used.

This temperature value is confirmed by lattice QCD calculations, which represent the most reliable and precise computations of non-perturbative effects and shall be discussed next. The bag model is however not reliable because of its simplicity for regions of the parameter space such as $T = 0$, $\mu \neq 0$, where the transition is only possible for a narrow range of values of the bag constant, making it difficult to understand physically.

1.3 Lattice QCD at $T \neq 0$

The correct way to study the thermodynamics of QCD is by analysing the quantum partition function $\mathcal{Z}$ within the path integral formalism. With this form, the connection between quantum mechanics and statistical mechanics is almost trivial, since one only needs to perform a Wick rotation, consisting in the change of variables $t \to i\tau$ to imaginary time, and restrict the time integration in the action to be $[0, \beta]$ with $\beta \equiv 1/T$, where T is the

temperature of the system. Thus we can write the partition function as

$$\mathcal{Z} = \int \mathcal{D}\bar{\Psi}(\mathbf{x},\tau)\mathcal{D}\Psi(\mathbf{x},\tau)\mathcal{A}^a_\mu(\mathbf{x},\tau)e^{-\int_0^\beta d\tau \int d^3x \mathcal{L}_E(\bar{\Psi},\Psi,A^a_\mu)}\,, \tag{1.4}$$

where $\bar{\Psi}$ and Ψ are the anti-quark and quark fields respectively and A^a_μ is the gluon field. Here, the τ coordinate is not really a time; systems in global thermal equilibrium are time independent.

The partition function $\mathcal{Z}$ corresponds to the trace of the matrix of density of states, trρ, or in other words to the "thermal bubbles", in opisition to the case at $T = 0$ which represents the vacuum-to-vacuum transition amplitude. Then, to calculate expectation values of operators we just define

$$< \mathcal{O} >= \frac{\int \mathcal{D}\bar{\Psi}(\mathbf{x},\tau)\mathcal{D}\Psi(\mathbf{x},\tau)\mathcal{A}^a_\mu(\mathbf{x},\tau)\,\mathcal{O}[\bar{\Psi},\Psi,A]\,e^{-\int_0^\beta d\tau \int d^3x \mathcal{L}_E(\bar{\Psi},\Psi,A^a_\mu)}}{\int \mathcal{D}\bar{\Psi}(\mathbf{x},\tau)\mathcal{D}\Psi(\mathbf{x},\tau)\mathcal{A}^a_\mu(\mathbf{x},\tau)e^{-\int_0^\beta d\tau \int d^3x \mathcal{L}_E(\bar{\Psi},\Psi,A^a_\mu)}}\,. \tag{1.5}$$

The name Lattice QCD corresponds to the numerical evaluation of this quantity, for a certain operator $\mathcal{O}$, by discretizing spacetime into $N_s^3\,N_\tau$ cells. The integrals are done via Monte Carlo algorithms by use of the Metropolis method for importance sampling. This method works well at zero chemical potential, but presents problems at $\mu \neq 0$. The reason is that the chemical potential would enter the euclidean Lagrangian with a factor i that leads to oscillations of the integrand, making the convergence much worse.

An important operator is now of our particular interest to understand QCD phase transitions, namely the Polyakov loop operator, defined as

$$L = \frac{1}{3}\mathrm{tr}\left(\mathcal{P}\,\mathrm{e}^{\mathrm{ig}\int_0^\beta \mathrm{d}\tau\,\mathrm{A}_4(\mathbf{x},\tau)}\right)\,. \tag{1.6}$$

Given that L is gauge independent, we can choose a gauge for the gluon field in which its τ dependence vanishes, so that

$$e^{ig\int_0^\beta d\tau\, A_4(\mathbf{x},\tau)} = e^{ig\beta A^a_4(\mathbf{x})\frac{\lambda^a}{2}} = e^{-\beta H_{int}} \tag{1.7}$$

This accepts the interpretation of the interaction energy of an infinitely heavy quark, sitting

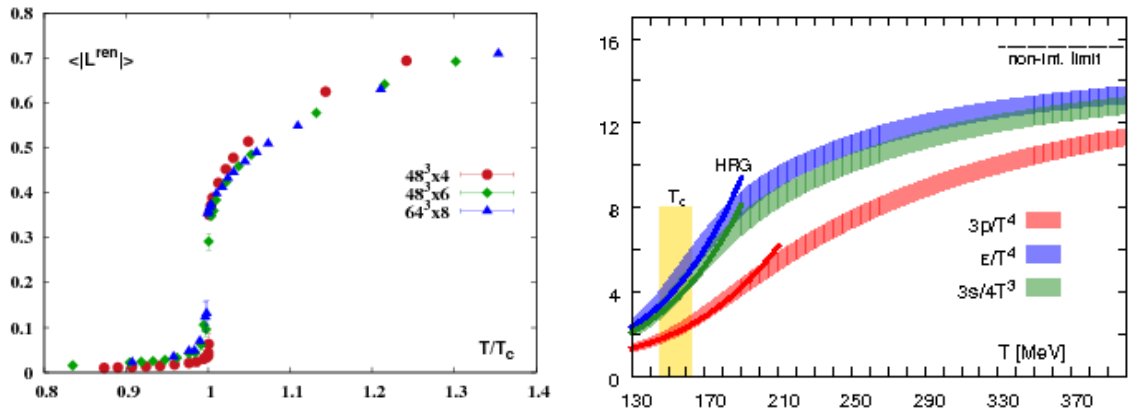

Figure 1-1: Left: The (renormalized) Polyakov loop expectation value $\langle L \rangle$ as a function of T/T_c, as calculated in [**?**] for different lattice spacings. Right: Energy density (blue band) in units of T^4 as a function of T (plot taken from [3]). Reaching T_c already requires energy densities of the order of $\epsilon \sim 1\,\mathrm{GeV/fm}^3$, and going to higher temperatures is even more expensive due to the T^4 scaling. Pressure and entropy density are also shown, with the results from Hadron Resononace Gas (HRG) matching lattice data up to moderate temperatures $T \sim 180$ MeV.

at position $\mathbf{x}$ with color current density $J^a_\mu(\mathbf{y}) = ig\frac{\lambda^a}{2}\delta(\mathbf{y}-\mathbf{x})(1,0,0,0)$, with the gluon field $A^a_\mu(\mathbf{y})$ such that

$$H_{int} = -L_{int} = \sum_{\mu=0}^{4} \int d^3y J^{\mu,a}(\mathbf{y}) A^a_\mu(\mathbf{y}) = ig\frac{\lambda^a}{2} A^a_4(\mathbf{x}) \tag{1.8}$$

This means that a vanishing $\langle L \rangle$ indicates infinite energy for a free quark: this is confinement. We can see from the left panel in Fig. 1-1 how this is the case for low temperatures and how $\langle L \rangle$ rapidly increases with a maximum in the susceptibility at the critical coupling β_{cr}, which can be mapped to a critical temperature around $T_c \sim 150$ MeV.

The liberation of quarks and gluons in the deconfined phase produces a strong raise in the energy density around T_c, as can be seen in the right panel of Fig. 1-1. A massless gas of quarks and gluons has an energy density that is proportional to T^4, where the proportionality constant reflects the number of massless degrees of freedom. These can be accounted for in an analogous way as we did in 1.2, and correspond to the Stefan-Boltzmann (SB) non-interacting limit. While the lattice calculation lies around a 20% below the SB limit above T_c, it rapidly decreases below this temperature due to hadronization: the massive hadrons

are exponentially suppressed, reducing the equivalent massless degrees of freedom. The fact that the lattice calculation lies so close to the SB limit in the deconfined phase could naively lead to think that the QGP behaves almost as a free gas of quarks and gluons; this turns out to be a poor indicator of the actual nature of the plasma degrees of freedom as we will see in Section 3.1; indeed, in the limit of infinite strong coupling one obtains thermodynamical quantities which are 75% of the non-interacting limit. Even though asymptotic freedom of QCD suggests that non-perturbative effects should disappear at large energy scales and that hot strong-interaction matter approaches ideal gas behavior asymptotically, the temperatures which are covered by current heavy ion collisions still correspond to a strongly coupled regime where quasiparticles are absent, as induced from the fact that the system produced behaves as an almost ideal fluid.

We have seen how the QCD Lagrangian gives indications from first principle calculations of the existence of a high temperature phase. This phase was, according to the standard cosmological model, present in the first microseconds after the Big Bang. The Universe expansion and its cooling down lead us through other lower temperature phases, all of which still remain obscure to us due to the opacity of the dense Universe until the decoupling of photons when the CMB was emitted. It would therefore be of unique interest to be able to study systems created in our laboratory which can explore the deconfined phase of nuclear matter, by generating Little Bangs which resemble these first instants of our known Universe: this possibility is nowadays materialized by the study of Heavy Ion Collisons (HIC).

In Fig. 1.3 we can see a sketch of what is known today about the phase diagram of QCD in the temperature, chemical potential (net baryon density) (T, μ_B) plane. Cold nuclear matter lies at $T = 0$ and $\mu_B \sim 0.96$ GeV. By going to increasingly higher temperatures, more hadrons are excited and we have a hadron-resonance gas. Thanks to lattice QCD calculations, we know that a phase transition occurs along the temperature axis from the hadron gas to the quark-gluon plasma, which instead of being a sharp phase transition it behaves as a rapid cross-over. The nature of the transition at non zero chemical potential along the critical line is first order. At low temperatures and very large densities, only

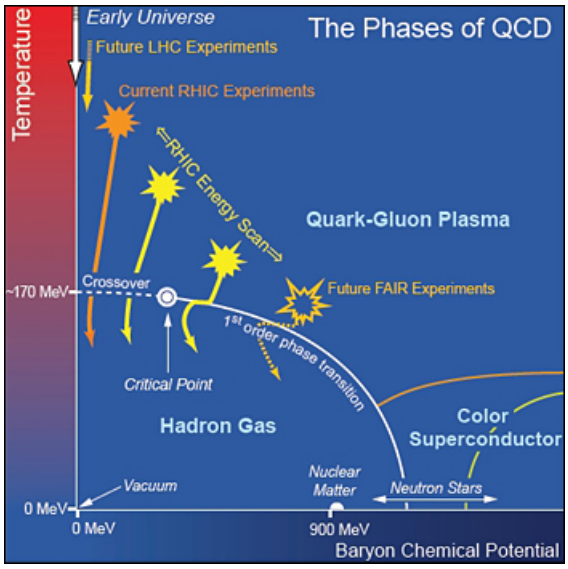

Figure 1-2: The QCD phase diagram as we currently understand it (figure from https://www.ntnu.edu/physics/theoretical/thermqcd)

reachable at the core of neutron stars, the color superconducting phase dominates [4]. In the figure we can also see drawn some trajectories that heavy ion collisions allow us to explore. The higher the center of mass energy of the nuclei, the more transparent they are and therefore the less amount of incoming baryons get stopped at the center of the collision, so that there is almost no baryon anti-baryon asymmetry and μ_B gets closer to zero. For the LHC, the entropy per nucleon ratio is high enough that one can effectively consider it as baryon free.

1.4 Heavy Ion Collisions

In this Section we will review the most important features of the production and evolution of the system generated in a heavy ion collision. In the last Section we have stated that at collider accessible temperatures the system is strongly coupled; we will see next which are its most important signatures in experiments. Given that above the transition temperature the evolution is well described by hydrodynamics, we will comment on this surprising collective behaviour and explain the role that transport coefficients play in it.

1.4.1 Geometry and Flow

In our accelerators we have been colliding nucleus against each other for nearly two decades. Due to their great speed, close to speed of the light, they are Lorentz contracted along the longitudinal direction and look to us in the laboratory frame as pancake shaped. Given that the nucleus have a radius of several femtometers (along which the energy density varies), the impact parameter at which the collision takes place (see left panel of Fig.1-3) greatly determines the particle output. The higher the overlap, the higher the number of participants N_{part} in the collision and therefore we expect to produce a greater amount of energy than for the more peripheral collisions where most of the energy ends up flying down the beam pipe. The impact parameter b is then correlated with multiplicity (total number of particles produced in the collision), being used nowadays the terminology of centrality classes in order to classify them. For instance, the 10% highest multiplicity events correspond to the 10% of events with the smallest b. Given that the probability of selecting a certain b goes like db^2, and assuming that the probability of colliding (so that the nucleus don't fly away without interacting) is approximately 1, we can deduce the range of values for b from the total cross section σ_{TOT}, such that for the 10% most central events we have $0.1 = \frac{\pi b_{10}^2}{\sigma_{\mathrm{TOT}}}$.

For a given b, the in general almond shape overlapping region can be said to have a certain eccentricity, a quantity that takes into account the average positions in the transverse plane of every pair of nucleons within σ_{inel}^{NN} (the cross section for inelastic nucleon-nucleon collisions at a given $\sqrt{s}$). Its definition is

$$\epsilon_n e^{in\Phi_n} = \frac{< r^n e^{in\phi} >}{< r^n >}\,, \tag{1.9}$$

with ϵ_n being the magnitude and Φ_n the direction. The positions of the nucleons in the (r, ϕ) plane have to be obtained from a model describing the nuclear energy density, being our choice the popular Glauber model as pictured in the right panel of Fig.1-3 (other models relying on the physics of saturation ([5]) have gained a lot of relevance in the last years, for which the eccentricities can be quite different from the ones obtained with the Glauber model. Such models are not studied in this work, see e.g. [6]). The different values of n

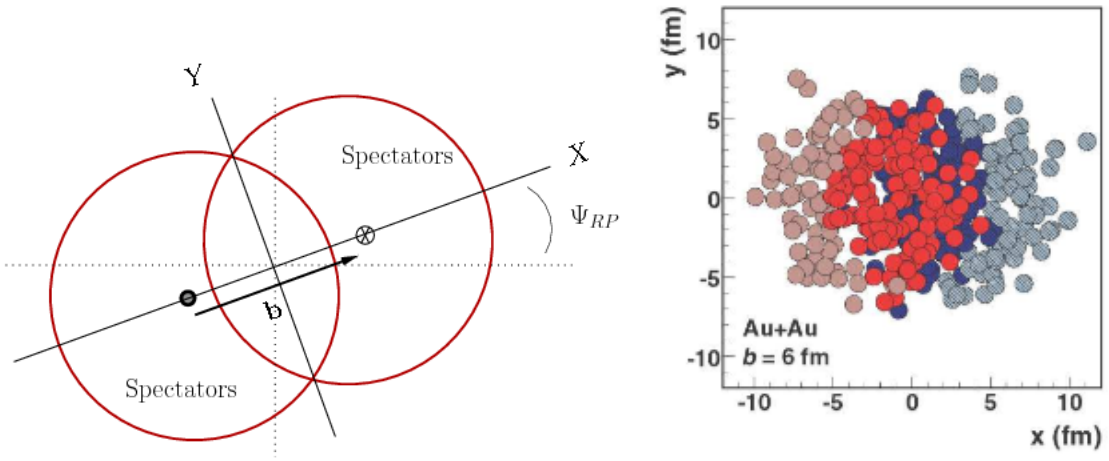

Figure 1-3: Left: A schematic picture of the transverse plane in a heavy ion collision, taken from [7]. Both the magnitude and direction of the impact parameter b can be determined on an event by event basis. Ψ_{RP} is called the reaction plane angle, a parameter mostly irrelevant for event averaged quantities. Right: A Glauber Monte-Carlo event (Au+Au) with impact parameter $b = 6$ fm. The darker discs correspond to the participating nucleons. Figure taken from [8].

label the different possible kind of eccentricities, e.g. $n = 2$ is elliptic, $n = 3$ is triangular... and so on. Given the almond shape of the collision, one expects the elliptic eccentricity to be the dominating one, in which case we get

$$\epsilon_n e^{i2\Phi_2} = \frac{< r^2 e^{i2\phi} >}{< r^2 >} = \frac{< y^2 - x^2 >}{< y^2 + x^2 >} \,. \tag{1.10}$$

Eccentricities fluctuate from event to event, so we can use the event averaged squared eccentricity $< \epsilon_n^2 >$.

How important are normal statistical fluctuations compared to geometric fluctuations associated to the N_{part}? This is an important question if we want to relate the final particle distribution to the initial geometry of the collision. Given that the number of charged particles per rapidity bin measured in a PbPb collision at the LHC at $\sqrt{s_{NN}} = 2.76$ TeV is $dN_{ch}/d\eta \sim 1600$, and having $< N_{part} > \sim 400$ (twice the number of nucleons per Pb nucleus), we have the following number of particles per collision per rapidity bin

$$\frac{1}{(N_{part}/2)} \frac{3}{2} < \frac{dN_{ch}}{d\eta} > \sim \frac{3}{2} \frac{1600}{200} = 12 \,, \tag{1.11}$$

which is a rather large number. This means that within each rapidity bin, normal statistical fluctuations $1/\sqrt{N}$ are smaller by $1/\sqrt{12}$ than the corresponding fluctuations due to the number of participants (geometry). In addition, by using the full rapidity range, the number of particles per collision increases by ~ 10. With this estimate we have convinced ourselves that the long range correlations that might be present in the collision are completely dominated by the geometry (and its fluctuations). How can we quantify these correlations?

We can define the correlation function $C(\Delta\phi)$, that measures the probability to find two particles who are separated by an angle $\Delta\phi = \phi_1 - \phi_2$, as

$$C(\phi_1 - \phi_2) \equiv \frac{< \frac{dN}{d\phi_1}\frac{dN}{d\phi_2} >}{< \frac{dN}{d\phi_1} >< \frac{dN}{d\phi_2} >} = 1 + 2\sum_{n=1}^{\infty} < v_n^2 > \cos(\mathrm{n}(\phi_1 - \phi_2)) + \mathcal{O}(\frac{1}{\mathrm{N}}) \,, \quad (1.12)$$

where the term $\mathcal{O}(1/N)$ refers to the order of the rest of correlations which are not geometric, such as jets, momentum and charge conservation, thermal fluctuations, resonances... which are typically short range. The coefficients v_n come from the Fourier series expansion, and correspond to the quantities that are fitted to data.

The measured $C(\Delta\phi)$ for nucleus-nucleus collisions, which corresponds to a projection in ϕ of the 2D two-particle correlation function shown in the left panel of Fig.1-4, can then be used to extract the flow coefficients v_n. The relatively large value for the coefficient v_2 signals the importance of the elliptic shape of the overlapping region. There is a clear interpretation based on collective fluid motion: the anisotropic pressure gradients have induced momentum anisotropies, leading to an excess of particles in the directions where the gradients are greater. This picture would not apply if the system behaved as a free gas of quarks and gluons, where the low interacting partons would fly in all directions and readily isotropize, washing away the initial geometric profile information. Collective motion would instead naturally generate *flow* as a response to eccentricities, such that $v_2 \propto \epsilon_2$, $v_3 \propto \epsilon_3$... and so on (see the right panel of Fig.1-4 for a determination of v_2).

As it turns out, hydrodynamic simulations have done an excellent job at describing

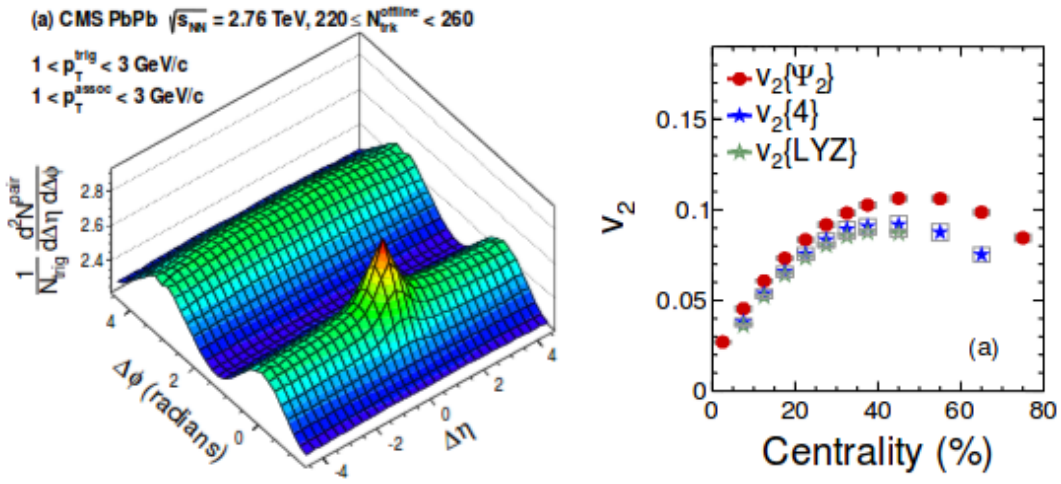

Figure 1-4: Left: The 2D two-particle correlation functions for 2.76 TeV PbPb collisions for pairs of charged particles with $1 < p_T^{trig} < 3$ GeV and $1 < p_T^{assoc} < 3$ GeV within the $220 < N_{\text{off.tr.}} < 260$ multiplicity bin (figure from [9]). The near side ridge which signals the presence of long-range rapidity correlations is clearly visible. The sharp peak is due to jet correlations. Right: Extraction of the v_2 coefficient from the function $C(\Delta\phi)$, which is the projection in ϕ of the 2D two-particle correlation (figure from [10]).

many features of heavy ion collisions (some of which we will comment later on). Generally, a system is effectively described by hydrodynamics when its typical length scales are larger than any correlation length in the underlying theory. Therefore, at the scales when the hydrodynamic description is valid, each point in space is assigned a macroscopic fluid cell, characterised by its energy density ϵ, its pressure P and its velocity u^μ. For a fluid without conserved charges (as is the case of our interest, a system with very small μ_B), the fluid properties are completely characterised by the stress tensor $T^{\mu\nu}$. Hydrodynamics can then be viewed as a gradient expansion which in the infinite wavelength limit contains only the ideal part $T^{\mu\nu}_{\text{ideal}} = (\epsilon + P)u^\mu u^\nu + P\, g^{\mu\nu}$, where the convention for the metric is here mostly plus. Considering the first order corrections to the gradient expansion introduces new length scales related to viscosities, which measure the system response to perturbations or deformations and can be encapsulated in the transverse stress tensor $\Pi^{\mu\nu} = -\eta(\epsilon)\sigma^{\mu\nu} - \xi(\epsilon)\Delta^{\mu\nu}\nabla \cdot u$, where η and ξ are the shear and bulk viscosities, $\nabla^\mu = \Delta^{\mu\nu}d_\nu$ with d_μ the covariant derivative, $\Delta^{\mu\nu} = g_{\mu\nu} + u_\mu u_\nu$ is the projector into the space components of the fluid rest frame, and $\sigma^{\mu\nu}$ is a symmetric traceless tensor in terms of derivatives of the velocity field.

By performing fits to data one can extract the parameters and initial conditions that provide an accurate description of the fireball evolution in terms of hydrodynamics. Moreover, by using the pieces of physics that we already know from lattice QCD, such as the equation of state $P(\epsilon)$ or the smallness of the bulk viscosity ξ (as it is for the case of nearly conformal theories where the $(\epsilon - 3P)/(\epsilon + P)$ ratio is small), one can better constraint the values of the rest of the parameters, such as the shear viscosity η.

However, it is rather surprising (at first glance at least) to be able to apply hydrodynamics to a system such as nuclear collisions. Is it reasonable at all? Under which circumstances? We will briefly address these questions next.

1.4.2 On the Validity of Hydrodynamics

Our goal in this section is to obtain a parametric estimate on the conditions a system must satisfy in order to be within the regime of hydrodynamics, end for which we will need to gain some intuition on the shear viscosity η.

The strength of η determines the effectiveness in momentum diffusion, or in other words how momentum is exchanged between regions of space with momentum anisotropies. As a toy example, imagine two streams of fluid moving in opposite directions which are put in contact at $y = 0$. Because of Brownian motion, there will be a random walk of momenta starting at the contact region which will propagate and eventually lead to a equilibrium situation in region Δy after a time Δt. The momentum transferred to the upper layer is

$$\begin{aligned} \Delta P^x &= \int_{y>0} dy\, \Delta T^{0x} = \int_0^{\Delta y} dy\, (\epsilon + P) \Delta u^x = \\ &= -\int_0^{\Delta y} dy\, (\epsilon + P) \frac{\partial u^x}{\partial y}\, y = -(\epsilon + P) \frac{(\Delta y)^2}{2}\, \frac{\partial u^x}{\partial y}\,, \end{aligned} \tag{1.13}$$

where we have used that $T^{0x} \simeq (\epsilon + P) u^x$. By defining the momentum diffusion coefficient D_η as $(\Delta y)^2 = 2 D_\eta\, \Delta t$, and comparing the previously obtained expression to the relation

defining the shear viscosity η, i.e. $\Delta P^x/\Delta t = -\eta\,\partial u^x/\partial y$, we conclude that

$$D_\eta \equiv \frac{\eta}{\epsilon + P}\,. \tag{1.14}$$

To proceed we will need some parametric estimates regarding the kinematics of the process. The spatial extent to which the momentum has spread, Δy, is proportional to the amount you move each step, the mean free path l_{mfp}, times the number of steps $\Delta t/\tau_{coll}$, where τ_{coll} is the time between collisions, which in turn can be expressed as l_{mfp}/v_{th}, with v_{th} the typical speed (generally the speed of sounds c_s). With these ingredients, we get

$$(\Delta y)^2 \sim (\frac{\Delta t}{\tau_{coll}})\, l_{mfp}^2 \sim v_{th}^2\, \tau_{coll}\, \Delta t\,. \tag{1.15}$$

By the definition of D_η, this last relation allows us to say that $D_\eta \sim v_{th}^2\,\tau_{coll}$, which in turn implies that

$$\eta \sim \frac{(\epsilon + P)}{n\sigma} v_{th}\,, \tag{1.16}$$

where we used that $\tau_{coll} \simeq (n\,\sigma\,v_{th})^{-1}$. Now, by adopting a quasi-particle picture for the medium constituents, we can consider the energy density ϵ to be the typical one, meaning $\epsilon = nE \sim n\,v_{th}\,p$, so that $(\epsilon + P) \sim n\,v_{th}\,p_{typ}$ and then the shear viscosity becomes

$$\eta \sim \frac{p_{typ}}{\sigma}\, v_{th}^2\,. \tag{1.17}$$

This expression does not depend on the density, and is inversely proportional to the cross section σ. This relation makes manifest the notion that strongly coupled systems have lower viscosities than weakly coupled ones, a fact which at first can seem counter intuitive. The way to think about it is by realizing that it is easier for momentum to be transported away (more viscosity) the less it interacts with nearby regions (lower cross section).

It is worth to stop to discuss when the quasi-particle picture that we have used to derive Eq. 1.17 is valid. By adopting this description we have implicitly assumed that the system is at a very high temperature T such that the mean free path (the typical spacing)

is parametrically much larger than the De Broglie wavelength associated to the particle, $\lambda_{\text{De Brog.}} \sim 1/T$. Given that the density $n \propto T^3$ and the cross section $\sigma \propto \alpha_s^2(T)/\mu_D^2$, with μ_D the Debye screening mass scaling like $\mu_D^2 \sim \alpha_s T^2$, it all ends up depending on the running of the QCD coupling constant α_s; only if $\alpha_s \ll 1$, meaning very high T, can we regard the medium constituents as quasi-particles. Given that at collider relevant temperatures $\alpha_s \sim 0.3$, the fireball description in terms of quasi-particles does not seem not be the most natural one.

For now, we just focus on the essential condition for hydrodynamics to be appliable: the system size L has to be much larger than any other microscopic scale, so that a coarse-graining can be justified. In our case, this condition translates into $L \gg l_{mfp}$, or equivalently $\tau_{coll} \ll \tau_0$, where τ_0 is the expansion rate of the system as derived from a longitudinally expanding boost-invariant fluid

$$\frac{1}{V}\frac{dV}{dt} = \partial_\mu u^\mu = \frac{1}{\tau_0}\,. \tag{1.18}$$

Using the previously derived relations (and also that $(\epsilon + P) = s\,T$) we secure the basic condition for the regime of applicability of hydrodynamics as

$$\frac{\eta}{s}\,\frac{1}{c_s^2}\,\frac{1}{T\tau_0} \ll 1\,. \tag{1.19}$$

We can better quantify the relation by taking some educated values for $T \simeq 300$ MeV, $\tau_0 \simeq 1$ fm and $c_s^2 = 1/3$. In this way

$$0.6\,\left(\frac{\frac{\eta}{s}}{0.3}\right)\,\left(\frac{1\,\text{fm/c}}{\tau_0}\right)\,\left(\frac{300\,\text{MeV}}{T}\right) \ll 1\,. \tag{1.20}$$

This simple estimate shows some important features. The lower the shear viscosity over entropy density ratio η/s, the more we can rely on hydrodynamics to describe the system. Strongly coupled systems have large cross sections, and as inferred from (1.17) they possess small shear viscosities. We will say more about viscosity in strongly coupled plasmas in section 3.1. On the other hand, we can also get to the regime of validity by going to very

high temperatures, or fast expansion rates. We have in this way seen how this parametric estimate gives support to the application of hydrodynamics in a system such as heavy ion collisions, subject to the circumstances just described.

1.4.3 The Stages of Heavy Ion Collisions

As it seems, we have good reasons to believe that the deconfined phase predicted by lattice QCD for nuclear matter above the critical temperature behaves as a droplet of liquid undergoing *collective motion*, an extremely interesting feature that confronts the quasiparticle picture and challenges our most basic understanding of quantum field theories. In the following we will sketch our current understanding of the different stages the heavy ion system experiences, from the two nuclei to the thousands of hadrons flying to our detectors.

At the very beginning of the collision, pressure gradients are so large that the system cannot be described hydrodynamically, since as mentioned above the latter is an effective theory relying on an expansion of gradients. In this way, if the system is to behave as a fluid eventually, there has to be a mechanism of isotropization and thermalization of the collision debris initially sitting at mid-rapidity. There have been two main roads taken to describe these physics, namely weakly coupled QCD and strongly coupled $\mathcal{N} = 4$ Super Yang Mills, a supersymmetric relative of QCD. We briefly review the general understading in the weakly coupled regime first and then we continue with the strongly coupled one.

We have learned from the study of parton distribution functions (PDFs) that gluons completely dominate the interior of nucleons at small energy fraction x. Saturation models, which started with the McLerran-Venugopalan model, state that by going to very low x the density of gluons eventually saturates, meaning that gluon recombination becomes as likely as gluon splitting given their large occupation number, of the order of $1/\alpha_s$ at the dominant momentum scale Q_s, the saturation scale. This macroscopic number of gluons liberated at mid-rapidity through the collision behaves coherently initially, and can then be described in terms of classical fields, converting the problem into solving classical Yang-

Mills equations in the presence of very strong color sources, a system commonly known as Color Glass Condensate (CGC).

This state evolves reducing the occupancies due to longitudinal expansion down to a point where the effective description has to be changed to effective kinetic theory by the use of the Boltzmann equation, which involves elastic and inelastic scatterings among the partons in the system. The radiative break up that this stage induces refills the occupation numbers while isotropizing and bringing the system closer to thermal equilibrium, eventually describing the same physics as hydrodynamics itself and therefore completing the evolution picture. Such a proof of principle calculation has been done recently in [11].

From the strongly coupled regime, and by the use of holography (which is introduced in Section 3.2) it is also possible to extract important phenomenological insights on the hydrodynamization of a far from equilibrium system by numerically solving the full non-linear Einstein equations for the collision of shock waves in the gravity theory; in the gauge theory dual, these shock waves correspond to lumps of energy propagating at the speed of light. The formation of the non-Abelian plasma in the gauge theory corresponds to the formation of a black hole in the gravity dual which will relax to equilibrium. By comparing the pressure from the holographic calculation with the one that would correspond to the system if it was describable in terms of $T_{\mu\nu}$ one can measure the hydrodynamization time, which has found to be remarkably fast, of the order of $1/T$ [12, 13], which means that the hydrodynamic description of a non-Abelian plasma follows naturally in the strongly coupled regime. Moreover, by assigning different energy density profiles to the shock waves, one can explore different center of mass energy collisions, being able to describe the regimes in which the after collision debris behaves, whether it has been stopped at mid-rapidity or flows transparently, as described in [14], which is in clear consonance with what is observed from RHIC energies to LHC ones.

More recently the heavy ion community has been wondered by the fact that p-Pb and p-p collisions of high multiplicity do show some collective motion behaviour, in the sense that

large $\langle v_n^2 \rangle$ of the order of Pb-Pb ones are found. The possibility of thermalizing such a small system is not expected at all, unless we use the insights from holography. From the strong coupling perspective, any system capable of collapsing into a black hole in the dual theory will behave hydrodynamically (the question is to what energy would that correspond in real life collisions, this is QCD). Recent results [15] have confirmed these intuitions, increasing the perception that holography has much to say about the physics of deconfinement.

The against the vacuum exploding fireball evolution in spacetime can be very well described by event by event numerical hydrodynamic simulations which require a few number of input parameters to initialize, namely the thermalization time τ_0, the initial energy density profile and the transport coefficients (such as shear viscosity η and bulk viscosity χ), and also requires the knowledge of the equation of state, which can be obtained from lattice calculations.

These transport parameters are different depending on the underlying microscopic dynamics assumed to calculate them. A way to test which picture better suits the QGP properties is to use experimental data to constrain the values of such parameters doing a multiple parameter fit. The large values found for the flow coefficients $\langle v_n^2 \rangle$ impose important bounds on the interplay between the thermalization time (the time at which the system starts behaving collectively) and viscosity (which regulates the amount of momentum dissipated into heat). The higher the value of τ_0, the longer the system will have expanded isotropically, smearing out the initial eccentricity and therefore reducing the amount of flow. Viscosity also reduces the strength of flow by producing entropy at expenses of momentum. These fits to data translate into important constraints on the transport coefficients, such as the value for the shear viscosity over entropy density ratio η/s. Recent analysis that even include the possibility of pre-equilibrium flow (see [16] for more details), therefore allowing for thermalization time to be larger, give a best fit of $\eta/s \simeq 0.135 \simeq 1.7\,\frac{1}{4\pi}$, which is remarkably close to universal strongly coupled lower bound found in [17].

Due to the expansion of this thermalized system, driven by the thermal pressure, the

fireball cools and its energy density decreases. When the energy density reaches $\epsilon \sim 1\,\text{GeV/fm}^3$, the partons convert into hadrons. These hadrons keep rescattering with each other for some time, maintaining the expansion flow until the system becomes so dilute that the average distance between the hadrons surpasses the range of strong nuclear force. At this moment, the scattering stops and the hadrons decouple, this is the so called freeze out. By the time this total decoupling happens, the chemical abundances have already been fixed at the chemical freeze out, which takes place before the kinetic freeze out. The chemical freeze out signals the moment when inelastic collisions cease, while the kinetic freeze out corresponds to the point when also elastic collisions cease (elastic collisions include also the production of short-lived resonances that decay back into the original hadrons). The latter processes don't change the chemical composition, but contribute to keep the momenta of the system thermalized due to the large resonant cross sections. After the decoupling, hadrons fly to our detectors and the event reconstruction begins.

While the above corresponds to the evolution of the bulk of particles generated in a heavy ion collision, there are others with higher p_T (transverse momentum) which are also produced in the collision (although at lower rates). These rarer hard excitations have so much energy that don't get to thermalize, but rather pass through the system becoming very useful probes with which to test the properties of the short-lived plasma they explore. These highly energetic particles undergo collinear emissions, developing parton showers which end up building a collimated spray of particles that is commonly known as *jet*. This thesis will describe how these jets interact with the QGP both from a weakly coupled and strongly coupled perspective, developing a realistic model with which to perform simulations that are to be compared to data in order to gain information on the microscopic nature of the plasma.

Chapter 2

Jet Quenching

QCD jets are essential objects in modern particle physics. Many of the searches for new physics at the LHC involve the detailed analysis of the production and properties of these energetic spays of particles that arise from the colour neutralisation of energetic partons produced in hadronic collisions. Jets also play a central role in the analysis of hot and dense matter formed in the debris of high energy Pb-Pb collisions (for a recent review of LHC heavy-ion results see [18]). Since long, these objects have been identified as the most powerful tomographic tools with which to diagnose the properties of the formed matter [19]. The tremendous combined capabilities of the LHC (and its associated detectors) have converted this potential into reality; the copious production of jet samples at LHC energies enables detailed studies of jet properties in a heavy ion environment [20, 21, 22, 23, 24, 25, 26, 27, 28, 29, 30, 31, 32, 33, 34, 35].

Early LHC results on jet physics in Pb-Pb collisions at $\sqrt{s_{\rm NN}} = 2.76$ TeV have shown a strong suppression in the jet production rate as compared to proton-proton collisions at the same energies [32, 33, 34]. This reduction of the jet rate can be understood as a result of the energy loss experienced by jets on their way out of the collision zone. This phenomenon, known as jet quenching, was identified previously at RHIC by the observation of a strong suppression in the production of high energy hadrons in heavy ion collisions [36, 37]. While the latter suppression is mostly sensitive to the energy loss by the hardest jet fragments, the variety of the observed jet modifications in a heavy-ion environment demands addressing the jets as sources of several partons propagating simultaneously through

the QCD medium.

At high energies, parton energy loss is controlled by the stimulated radiation of medium-induced gluons as a result of the scattering with the medium constituents. Many of the properties of the modification of jets may be inferred from the single-gluon emission rate, first computed by BDMPS-Z [38, 39, 40]. In a finite length medium, an opacity expansion of the multiple scattering series resummed in BDMPS-Z was introduced in [41, 42, 43], in which the expansion parameter may be viewed as the ratio of the medium length to the mean free path.[1] These computations are at the heart of the different formalisms later developed to address the dynamics of energetic partons in plasma [44, 45, 46, 47, 48, 49, 50, 51, 52, 53]. Generalising this picture in order to treat the interactions of QCD showers with the medium, one usually relies on working models that iterate the single-gluon emission rate without considering possible multi-parton correlations. For different Monte-Carlo implementations, see [54, 55, 56, 57, 58]. Nevertheless, in vacuum jet physics it has been long understood that interference effects between the shower constituents, known as coherent branching or angular ordering, are essential to completely describe intra-jet properties in high-energy colliders [59]. In Part III of this thesis we address this last subject by studying the coherent in-medium emission of two gluons in $N = 1$ opacity (or in other words, in a dilute system where all the medium can be replaced by a single medium exchange/scattering centre). As a preliminary, and to gain intuition on the physics of radiative energy loss, in this introductory Part I we also compute the one gluon emission rate at $N = 1$ opacity in Section 2.3.

The coming Sections of this Chapter are devoted to provide a brief conceptual introduction to the theoretical techniques playing a key role in the description of jet quenching from a perturbative point of view, by assuming that the relevant energy scale at which α_s is evaluated corresponds to asymptotically high temperatures, far beyond the reach of current accelerators. For realistic values of the temperature, this picture starts losing validity, the quasi-particle description breaks down and one has to resort to strong coupling computations, which are reviewed in Section 3.3. Nevertheless, the techniques and concepts

[1] This ratio is usually referred to as the medium opacity.

extracted from these perturbative calculations are basic for a full understanding of the jet quenching phenomena in all its regimes, since some of the features arising at weak coupling might have a counterpart in strong coupling whose presence is a priori less evident.

2.1 Hard Processes

Hard processes are those involving large momentum transfers, which given the running of α_s with the energy, they are computable perturbatively and are under good theoretical control. The complete evolution from the two colliding protons to the jets flying to our detectors is however still far from being completely understood: parton distribution functions and fragmentation functions from partons to hadrons are in general non-perturbative quantities which need to be fitted to data (but whose evolution follows the famous DGLAP evolution equations). Luckily, one can separate the computation of these different pieces thanks to the factorization theorems in QCD [60], which can be expressed as

$$\sigma^{AB\to h} = f_A(x_1, Q^2) \otimes f_B(x_2, Q^2) \otimes \sigma(x_1, x_2, Q^2) \otimes D_{i\to h}(z, Q^2) \tag{2.1}$$

meaning that the cross section to produce a hadron h out of two colliding hadrons A and B corresponds to the convolution of the two PDFs with the hard cross section $\sigma(x_1, x_2, Q^2)$ and with the probability to find a hadron h with momentum fraction z out of a parton i.

Regarding the medium induced modification of final hadrons distribution, one may wonder which are the parts in this process that are being affected by the presence of the QGP. It is well known that nuclear parton distribution functions (nPDFs) are different from standard PDFs due to the effects of shadowing and anti-shadowing, constructive or destructive interference effects among the hadrons within the nuclei [61]. These effects play a minor role for high p_T processes, and as such will be neglected throughout this work. The hard cross section, at high enough energy, can also be considered to be unaffected with respect to p-p collisions, since by the uncertainty principle the time scale during which the hard process occurs is $\Delta t \sim 1/\sqrt{Q^2}$, which is generally much shorter than the time it

takes for the medium to form. These assumptions have been put to test by studying colorless probes (which don't interact with the medium), such as prompt photon production processes, where it has been seen how the distribution is (at high p_T) unchanged from the N_{coll} scaled extrapolation of the vacuum case [23]. Also studies of jet quenching in $Pb-p$ systems (where no QGP is formed, or at least its size is neglectable compared to the Pb-Pb case), where no energy loss was observed [123], have confirmed the assumption that medium modification is a final state effect, an interplay between the parton shower and the plasma constituents.

2.2 Parton Propagation within the QGP

In this section we will review important aspects on the propagation of a fast projectile through a color bath, which gets color rotated and gets broadened as well (if we go beyond the eikonal approximation). We will introduce the gauge invariant Wilson lines and also perform medium averages in order to see how the jet transport parameter $\hat{q}$ emerges and which is its physical interpretation.

Due to the high momentum of the incoming parton, which is well above the typical momentum transferred from the medium, we make the assumption that the momenta of the projectile is not altered by the interactions with the plasma. The latter can be then considered as a background field, rendering the problem as a semiclassical one where there is no medium response, no recoil.

By taking the medium to be a collection of scattering centres, we can compute the contribution to the S matrix of the interaction with one of them as

$$S_1(p',p) = \int d^4x\, e^{i(p'-p)x} \bar{u}(p') ig A^a_\mu(x) T^a \gamma^\mu\, u(p)\,, \tag{2.2}$$

where $A^a_\mu(x)$ is the field produced by the scattering centre. One finds it convenient to use light-cone coordinates, defined as $x_\pm \equiv\ 1/\sqrt{2}(x_0 \pm x_3)$, with a scalar product as $xp =$

$p_+x_- + p_-x_+ - \mathbf{p}_\perp\mathbf{x}_\perp$. Due to the huge Lorentz contraction, all the medium dependence in the x_- coordinate can be neglected as if the whole process happened at a sheet of constant x_-. By using the eikonal approximation, meaning $p' \simeq p$, one gets

$$S_1(p',p) \simeq 2\pi\delta(p'_+ - p_+)2p_+ \int d\mathbf{x}_\perp e^{-i\mathbf{x}_\perp(\mathbf{p}'_\perp - \mathbf{p}_\perp)} \left[ig \int dx_+ A_-(x_+,\mathbf{x}_\perp)\right] , \qquad (2.3)$$

where we used $\frac{1}{2}\sum_\lambda \bar{u}^\lambda(p)\gamma^\mu u^\lambda(p) = 2p^\mu$ and $p^\mu A^a_\mu \simeq p_+ A^a_-$. Now, the contribution of two scatterings reads

$$\begin{aligned} S_2(p',p) = \int \frac{d^4p_1}{(2\pi)^4} d^4x_1 d^4x_2\, e^{i(p_1-p)x_1} e^{i(p'-p_1)x_2} \bar{u}(p') ig A^{a_1}_{\mu_1}(x_1) T^{a_1} \gamma^{\mu_1} \times \\ \times\, i\frac{\not{p}_1}{p_1^2 + i\epsilon} ig A^{a_2}_{\mu_2}(x_2) T^{a_2} \gamma^{\mu_2} u(p)\,. \end{aligned} \qquad (2.4)$$

By use of the Dirac equation we can simplify previous expression in the eikonal limit as

$$S_2(p',p) = -ig^2(2p_+)^2 \int \frac{d^4p_1}{(2\pi)^4} d^4x_1 d^4x_2\, \frac{e^{i(p_1-p)x_1 + i(p'-p_1)x_2}}{p_1^2 + i\epsilon} A_-(x_1) A_-(x_2)\,. \qquad (2.5)$$

Since the medium is x_- independent, the only non-trivial integral on the internal momentum p_1 is the one in p_{1-}, which reads

$$\int dp_{1-} \frac{e^{i(x_{1+}-x_{2+})p_{1-}}}{2p_{1+}p_{1-} + i\epsilon} = -\Theta(x_{2+} - x_{1+}) \frac{2\pi i}{2p_{1+}}\,, \qquad (2.6)$$

where consistently with the eikonal approximation we have neglected the transverse momentum so that $p_1^2 \simeq 2p_{1+}p_{1-}$. In this way, the amplitude for two scatterings reads

$$S_2(p',p) = 2\pi\delta(p'_+ - p_+)2p_+ \int d\mathbf{x}_\perp e^{-i\mathbf{x}_\perp(\mathbf{p}'_\perp - \mathbf{p}_\perp)} \frac{1}{2}\mathcal{P}\left[ig \int dx_+ A_-(x_+,\mathbf{x}_\perp)\right]^2 , \qquad (2.7)$$

where $\mathcal{P}$ means path ordering of the fields $A_\mu(x)$. The generalisation to n scattering centres is straightforward, giving

$$S_n(p',p) = 2\pi\delta(p'_+ - p_+)2p_+ \int d\mathbf{x}_\perp e^{-i\mathbf{x}_\perp(\mathbf{p}'_\perp - \mathbf{p}_\perp)} \frac{1}{n!}\mathcal{P}\left[ig \int dx_+ A_-(x_+,\mathbf{x}_\perp)\right]^n . \qquad (2.8)$$

The sum over all possible number of scatterings is then

$$S(p',p)=\sum_{n=0}^{\infty}S_n(p',p)\simeq 2\pi\delta(p'_+-p_+)2p_+\int d\mathbf{x}_\perp e^{-i\mathbf{x}_\perp(\mathbf{p}'_\perp-\mathbf{p}_\perp)}W(\mathbf{x}_\perp)\,, \tag{2.9}$$

where the object $W(\mathbf{x}_\perp)$ is called a Wilson line and is defined as

$$W(\mathbf{x})\equiv\mathcal{P}\text{exp}\left[ig\int dx_+A_-(x_+,\mathbf{x})\right]\,. \tag{2.10}$$

This was derived for an incoming quark; the calculation for an incoming gluon follows analogously with some replacements such as introducing indices in the adjoint color representation for the external fields. The corresponding adjoint Wilson line is then labelled as $W^A(x)$. Here, the only effect of the medium is a color rotation of the projectile as encoded in the Wilson line. We can go a bit further by relaxing the eikonal approximation such that $p_\perp^2\sim 2p_+p_-$, so that the integral in p_- now gives

$$\int dp_-\frac{e^{i(x_{i+}-x_{(i+1)+})p_-}}{2p_+p_--p_\perp^2+i\epsilon}=-\Theta(x_{(i+1)+}-x_{i+})e^{i\frac{p_\perp^2}{2p_+}(x_{i+}-x_{(i+1)+})}\frac{2\pi i}{2p_+}\,, \tag{2.11}$$

making in turn the integral over p_T to give

$$\begin{aligned}&\int\frac{d^2p_{i\perp}}{(2\pi)^2}e^{i\frac{p_\perp^2}{2p_+}(x_{i+}-x_{(i+1)+})}e^{-i\mathbf{p}_{i\perp}(\mathbf{x}_{i+}-\mathbf{x}_{(i+1)+})}=\\&=\frac{p_+}{2\pi i(x_{i+}-x_{(i+1)+})}\text{exp}\{-i\frac{p_+}{2}\frac{(\mathbf{x}_{i\perp}-\mathbf{x}_{(i+1)\perp})^2}{x_{i+}-x_{(i+1)+}}\}\,.\end{aligned} \tag{2.12}$$

This last expression precisely corresponds to the Feynman propagator of a free particle $G_0(\mathbf{x}_{(i+1)\perp}-\mathbf{x}_{i\perp};x_{(i+1)+}-x_{i+})$, and can therefore be written in terms of a path integral

$$G_0(\mathbf{x}_{(i+1)\perp}-\mathbf{x}_{i\perp};x_{(i+1)+}-x_{i+})=\int\mathcal{D}\mathbf{x}_\perp(x_+)\text{exp}\{i\frac{p_+}{2}\int dx_+\left[\frac{d\mathbf{x}_\perp}{dx_+}\right]^2\}\,. \tag{2.13}$$

With these ingredients, we can finally reorganise the scattering amplitude as

$$S(p',p) \simeq 2\pi\delta(p'_+ - p_+)2p_+ \int d\mathbf{x}_\perp e^{-i\mathbf{x}_\perp(\mathbf{p}'_\perp - \mathbf{p}_\perp)} \times \\ \times \int \mathcal{D}\mathbf{r} \exp\{i\frac{p_+}{2}\int dx_+ \left[\frac{d\mathbf{r}}{dx_+}\right]^2\} W(\mathbf{r})\,. \tag{2.14}$$

In general, to calculate physical quantities what one needs is to average among medium field configurations such that the overall color is neutralised. Here we show as an example the average of two Wilson lines in the fundamental representation

$$\frac{1}{N}\mathrm{Tr}\left\langle W^\dagger(\mathbf{x}_\perp)W(\mathbf{y}_\perp)\right\rangle = \\ = \frac{1}{N}\mathrm{Tr}\left\langle \mathcal{P}\exp\left[ig\int dx_+ A_-(x_+,\mathbf{x}_\perp)\right]\mathcal{P}\exp\left[-ig\int dx_+ A_-(x_+,\mathbf{y}_\perp)\right]\right\rangle\,. \tag{2.15}$$

By expanding the exponentials, we find that the leading contribution is of order g^2. We transform to Fourier space and obtain

$$\frac{1}{N}\mathrm{Tr}\left\langle W^\dagger(\mathbf{x}_\perp)W(\mathbf{y}_\perp)\right\rangle_{1\,\text{scatt}} \simeq 1 - C_F\int\frac{d^2\mathbf{q}}{(2\pi)^2}|a(\mathbf{q})|^2(1-e^{i(\mathbf{y}_\perp-\mathbf{x}_\perp)\mathbf{q}}) = 1-\frac{1}{2}\sigma(\mathbf{y}_\perp-\mathbf{x}_\perp)\,, \tag{2.16}$$

where the $a(\mathbf{q})$ are the Fourier modes of the background field and we have defined $\sigma(\Delta\mathbf{x}_\perp)$ as the so called dipole cross section. Implicit in this calculation is included the possibility of having a single scattering centre interacting twice with either the quark or the anti-quark: these are the so called contact terms and correspond to unitarity corrections. It is useful to include a scatterer density in (2.16) as $n(x^+) = \sum_{i=0}^N \delta(x_+ - x_{i+})$. In this sense, what we have obtained now is the first term in the *opacity* expansion. Given that the sum of higher orders exponentiates, we can resum the average quantity as

$$\frac{1}{N}\mathrm{Tr}\left\langle W^\dagger(\mathbf{x}_\perp)W(\mathbf{y}_\perp)\right\rangle \simeq \exp\left[-\frac{C_F}{2}\int dx_+ n(x_+)\sigma(\mathbf{y}_\perp-\mathbf{x}_\perp)\right] \tag{2.17}$$

When the density of scatterers is large, one cannot keep only the lowest order opacity terms and it is convenient to take the the dipole cross section at leading logarithmic accuracy [], getting only the small distance component as $\sigma(\mathbf{r}) \simeq C\mathbf{r}^2$. Neglecting the logarithm

is tantamount to neglect rare high momentum transfers on the basis of the *multiple soft scattering* approximation. It states that given the large number of scatterings, the most probable momentum transfer will be the typical one, and one can neglect the possibility of the rarer and harder ones, whose contribution is encapsulated into the logarithm. The factor C is used to define the transport coefficient $\hat{q}(x_+) \equiv 2\sqrt{2}n(x_+)C$, which encapsulates all the medium properties and dynamics. Then one can write

$$\frac{1}{N}\text{Tr}\left\langle W^\dagger(\mathbf{x}_\perp)W(\mathbf{y}_\perp)\right\rangle \simeq \exp\left[-\frac{C_F}{4\sqrt{2}}\int dx_+\hat{q}(x_+)(\mathbf{y}_\perp-\mathbf{x}_\perp)^2\right] . \tag{2.18}$$

We can better understand the role of the $\hat{q}$ parameter by considering the distribution of particles with a given momentum after going through the medium, which can be obtained from the S matrix as

$$\mathcal{M}(\mathbf{p}'_\perp) \equiv \frac{d^2\mathcal{N}}{d\mathbf{p}_\perp^{'2}} \propto \int dp'_+\delta(p'^2-m^2)\frac{1}{N}\left\langle |S(p',p)|^2\right\rangle . \tag{2.19}$$

Given that the average squared transverse momentum broadening (times normalization) is computed as $\mathcal{N}\ \langle \mathbf{p}_\perp^2\rangle = \int d^2\mathbf{p}'_\perp\ \mathbf{p}_\perp^{'2}\,\mathcal{M}(\mathbf{p}'_\perp)$, we can use (2.14) to write

$$\begin{aligned}\mathcal{N}\left\langle \mathbf{p}_\perp^2\right\rangle \propto \int d^2\mathbf{p}'_\perp \int d\mathbf{x}_\perp d\mathbf{x}'_\perp \mathbf{p}_\perp^{'2} e^{-i\mathbf{p}'_\perp(\mathbf{x}_\perp-\mathbf{x}'_\perp)}\int \mathcal{D}\mathbf{r}\mathcal{D}\mathbf{r}'\times \\ \times\exp\left\{i\frac{p_+}{2}\int dx_+\left(\left\{\frac{d\mathbf{r}}{dx_+}\right\}^2-\left\{\frac{d\mathbf{r}'}{dx_+}\right\}^2\right)\right\}\frac{1}{N}\text{Tr}\left\langle W^\dagger(\mathbf{r}')W(\mathbf{r})\right\rangle .\end{aligned} \tag{2.20}$$

By replacing $\mathbf{p}'_\perp$ by the operator $i\nabla_{\Delta\mathbf{x}_\perp}$ acting on $\exp(i\mathbf{p}'_\perp\Delta\mathbf{x}_\perp)$, integrating by parts twice and then performing the integration on $\mathbf{p}'_\perp$, we are allowed to write

$$\begin{aligned}\mathcal{N}\left\langle \mathbf{p}_\perp^2\right\rangle \propto \lim_{\Delta\mathbf{x}_\perp\to 0} -\nabla^2_{\Delta\mathbf{x}_\perp}\int \mathcal{D}\mathbf{r}\mathcal{D}\mathbf{r}'\exp\left\{i\frac{p_+}{2}\int dx_+\left(\left\{\frac{d\mathbf{r}}{dx_+}\right\}^2-\left\{\frac{d\mathbf{r}'}{dx_+}\right\}^2\right)\right\}\times \\ \times\ \frac{1}{N}\text{Tr}\left\langle W^\dagger(\mathbf{r}')W(\mathbf{r})\right\rangle .\end{aligned} \tag{2.21}$$

In order to simplify this expression, we consider the high energy limit where $p_+ \gg \mu$, being μ the typical momentum transfer from the medium, and then it suffices to project the

path integral to the path minimizing the action, this is the classical one where $d\mathbf{r}/dx_+ = 0$. By similar manipulations on the normalization $\mathcal{N}$ we can write

$$\left\langle \mathbf{p}_\perp^2 \right\rangle = -\frac{1}{\mathrm{Tr}\left\langle W^\dagger(\mathbf{x}_\perp)W(\mathbf{x}_\perp)\right\rangle}\nabla^2_{\Delta\mathbf{x}_\perp}\,\mathrm{Tr}\left\langle W^\dagger(\bar{\mathbf{x}}_\perp - \frac{\Delta\mathbf{x}_\perp}{2})W(\bar{\mathbf{x}}_\perp + \frac{\Delta\mathbf{x}_\perp}{2})\right\rangle\,, \quad (2.22)$$

where we used that $\bar{\mathbf{x}}_\perp = (\mathbf{x}_\perp + \mathbf{x}'_\perp)/2$. For the situations in which the multiple soft scattering approximation is valid, we conclude

$$\left\langle \mathbf{p}_\perp^2 \right\rangle = \frac{1}{\sqrt{2}}\int dx_+ \hat{q}(x_+)\,, \quad (2.23)$$

making clear the interpretation of $\hat{q}$ as the momentum broadening per unit length.

We conclude this section by noting that the Wilson lines introduced here will also be important for the determination of quark properties at strong coupling, as will be reviewed in Section 3.3. The formalism here developed has had important applications in jet quenching studies at weak coupling, being the most interesting to us the medium induced radiation of a parton travelling the QGP. We will not take next the general approach but rather focus in the leading opacity contribution, which already captures the most important physics of the process, namely the interference phenomena and the path length dependence of radiative energy loss; this is why we find appropriate to provide the detailed calculation of stimulated one gluon emission that follows in the next Section. In Part III of the thesis we will extend the computation within this formalism to the case of two gluon emission, which follows the same logic and is obtained with the same effective Feynman rules as the one gluon emission case.

2.3 Single Gluon Emission at $N = 1$ Opacity

We compute the inclusive rate off a hard quark that emits a single soft gluon while it interacts with a single coloured scattering. In the absence of scattering centres, those gluons originate from the relaxation of virtuality of the microscopic process that generates the energetic quark. The presence of one scattering centre leads to a modification of the vacuum

spectrum by changing the transverse momentum of one of the gluons emitted at the production vertex. Moreover, the additional momentum transferred to the jet supplemented by the scattering centre leads to an additional source of radiation of gluons with transverse momentum of the order of the momentum transfer. This process is the stimulated emission of gluons in the medium. We explicitly study the effect of interferences among these different physics processes in the final emission rate. We will work in light-cone coordinates $X = (x^+, x^-, \boldsymbol{x})$, where $x^\pm \equiv (x^0 \pm x^3)/2$ and $\boldsymbol{x} = (x_1, x_2)$ denotes a transverse vector, $x \equiv |\boldsymbol{x}|$. For future reference,

2.3.1 Medium model

As the partons produced in a jet shower plough through a QCD medium, they exchange energy and momentum with its constituents. Since these interactions are mediated by the exchange of gluons, an effective way to encode those interactions is by analysing the propagation of energetic partons in a fluctuating colour gauge field, A, sourced by the quarks and gluons in the medium. For high-energy probes, the light-cone gauge $A^+ = 0$, with the plus-momentum component the largest momentum of the parton, is particularly convenient. In this gauge, typical fluctuating fields in the background will have all other components of comparable order. Since in the eikonal limit the coupling of a parton of momentum P^μ to the medium gauge field is proportional to $P \cdot A$, the contribution of the perpendicular field components A^i to the probe-medium interactions is suppressed with respect to the contribution of the A^- component.

The high-energy approximation also leads to simplifications in the momentum exchange with the medium. Assuming that the p^+ component of the probe is much larger than the momentum exchanged in the medium, q, the effect of the q^+ exchanged momentum is always suppressed with respect to the transverse momentum exchanges, $\boldsymbol{q}$, since by energy momentum conservation in the vertex the former is always added to the large parton momentum. This is equivalent to neglecting drag ($q^+ \approx 0$) for high-energy probes. With these assumptions, we can model the medium by a gauge field with only one non-vanishing

component, which takes the form

$$A^-(Q) \equiv t^a A^{a,-}(Q) = 2\pi\delta(q^+) \int \mathrm{d}x^+ e^{iq^-x^+} \mathcal{A}(x^+;\boldsymbol{q})\,, \tag{2.24}$$

where the medium field is real, $\mathcal{A}^*(x^+;\boldsymbol{q}) = \mathcal{A}(x^+;-\boldsymbol{q})$.

The medium dynamics leads to the randomisation of the field. From the point of view of the probe, we may characterise the medium by cumulants of the fluctuating field configurations. Odd cumulants vanish as a consequence of colour neutrality of the medium. Even n-point medium correlators exhibit correlation lengths of order the inverse medium exchange. This allows us to approximate the medium average of the background gauge field to

$$\langle \mathcal{A}^a(x^+;\boldsymbol{q}) \mathcal{A}^{*\,b}(x'^+;\boldsymbol{q}')\rangle = \delta^{ab} m_D^2 n(x^+)\,\delta(x^+ - x'^+)\,(2\pi)^2\delta(\boldsymbol{q}-\boldsymbol{q}')\mathcal{V}(\boldsymbol{q})\,, \tag{2.25}$$

where $n(x^+)$ is the density of scattering centres in the x^+ direction. In the simplest of cases, a static medium with fixed density and length L, $n(x^+) \equiv 1/L\,\Theta(x^+)\Theta(L-x^+)$. As a consequence of Lorentz contraction, the correlation length along the x^- direction can be neglected and we may consider exchanges as instantaneous in x^-. Furthermore, $\mathcal{V}(\boldsymbol{q})$ is the scattering potential, usually assumed to be screened at the scale of the Debye mass μ_D. However, in our discussion the exact form of this potential does not matter as long as it is *isotropic* in the transverse plane.

The locality in x^+ of the correlator Eq.2.25 also implies that higher-order cumulants vanish in this high-energy approximation, such that higher-order medium correlators are simply products of the two point functions Eq.2.25. The $N = 1$ opacity approximation consists in describing all medium effects by the two point function Eq.2.25. This is a good approximation when the medium is dilute, $\alpha_s n_0 L \ll 1$. If the medium is dense, a resummation of an arbitrary number of medium exchanges is required. Nevertheless, in this work we will employ the $N = 1$ opacity approximation as a tool to explore the dynamics of energetic jet showers in QCD medium, but we will make no assumptions on whether this approximation correctly captures the properties of the quark-gluon plasma formed in heavy-ion collisions.

Figure 2-1: The two diagrams that correspond to a coming from infinity quark emitting a gluon induced by a single collision with the medium.

The following diagramatic computation is performed by the use of a set of effective Feynman rules which are derived in Appendix B, which are very well suited to the hierarchy of scales we are considering. This formalism can also be applied to the two gluon emission problem as long as one of the gluons is very soft compared to the other one, which is the situation we will consider in the original work of Part III of the thesis, and where the use of these effective rules becomes most powerful.

2.3.2 Radiation from a Quark Coming from Infinity

To start we will consider the gluon stimulated radiation off a coming from infinity on-shell quark. Despite it is not the situation we are ultimately interested in, it leads to the so called Gunion-Bertsch spectrum which we will often refer to in Part III. It also useful to clearly see the essential differences between stimulated radiation in abelian and non-abelian gauge theories.

The medium induced of an on-shell gluon off an on-shell quark coming from infinity has three contributions, being the QED-like two of them the ones in Fig.2-1. Using the standard Feynman rules we can write the amplitude for collision after emission as

$$M_{1.1} = \int_q \bar{u}^t(p_f)(ig\gamma^\mu t^a A_\mu(q))S(p_i - k)(ig\gamma^\nu t^b \epsilon^*_{\nu,\lambda}(k))u^s(p_i)\,, \tag{2.26}$$

where the fermionic propagator is $S(k) = \sum_s u^s(k)\bar{u}(k)^s D(k)$, with $D(k) = i/(k^2 + i\epsilon)$. By using the effective Feynman rules derived in Appendix B, we can express this amplitude as

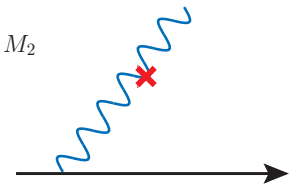

Figure 2-2: In this diagram, M_2, it is the emitted gluon who receives a kick from the medium.

$$M_{1.1} \cong \int_q U_Q^a(p^+,\mathbf{q}) D(p-k) V_G^{b,i}(p^+,k^+,\mathbf{k}) \cong 2ig^2(t^a t^b) \int_q \mathcal{A}(\mathbf{q}) \frac{\mathbf{k}^i}{\mathbf{k}^2}(2p^+)\,, \quad (2.27)$$

where it is understood that the index i is contra contracted with the gluon transverse polarization vector $\epsilon^*_{\nu,\lambda}(k)$. The terms $U_Q^a(p^+,\mathbf{q})$ and $V_G^{b,i}(p^+,k^+,\mathbf{k})$ are the vertices for the quark interacting with the background field and the quark emitting a soft gluon respectively (see Appendix B for the expressions). Similarly for the contribution coming from collision before emission

$$M_{1.2} = \int_q \bar{u}^t(p_f)(ig\gamma^\nu t^b \epsilon^*_{\nu,\lambda}(k)) S(p_f+k)(ig\gamma^\mu t^a A_\mu(q)) u^s(p_i)\,, \quad (2.28)$$

which in terms of the effective Feynman rules reads

$$M_{1.2} \cong \int_q V_G^{b,i}(p^+,k^+,\mathbf{k}) D(p+k) U_Q^a(p^+,\mathbf{q}) \cong -2ig^2(t^b t^a) \int_q \mathcal{A}(\mathbf{q}) \frac{\mathbf{k}^i}{\mathbf{k}^2}(2p^+)\,. \quad (2.29)$$

Given that gluons have color charge there is yet another diagram to consider as depicted in Fig. 2-2, where the emitted gluon interacts with the medium

$$\begin{aligned} M_2 = \quad & \int_q \bar{u}^t(p_f)(ig\gamma^\mu t^c) G_{\mu\nu}(k+q) i V_{cba}^{\nu\alpha\beta}(k+q,-k,-q) \epsilon^*_{\alpha,\lambda}(k)) A_\beta(q) u^s(p_i) \\ & \cong \int_q V_G^{c,i}(p^+,k^+,\mathbf{k}+\mathbf{q}) D(k+q) u_G^{bac}(k^+,q) \mathcal{A}(\mathbf{q}) \\ & \cong -2ig^2[t^a,t^b] \int_q \mathcal{A}(\mathbf{q}) \frac{(\mathbf{k}+\mathbf{q})^i}{(\mathbf{k}+\mathbf{q})^2}(2p^+)\,, \end{aligned} \quad (2.30)$$

where the term $u_G^{bac}(k^+,q)$ is the vertex for gluon interaction with the background field and $G_{\mu\nu}(k)$ is the gluon propagator (again, see Appendix B for details). The sum of the three

diagrams is

$$M \equiv M_{1.1} + M_{1.2} + M_2 \cong -2ig^2[t^a, t^b] \int_q \mathcal{A}(\mathbf{q})\mathbf{L}(k,q)(2p^+) \tag{2.31}$$

where we have defined the so called Lipatov vertex as

$$\mathbf{L}(k,q) = \frac{(\mathbf{k}+\mathbf{q})^i}{(\mathbf{k}+\mathbf{q})^2} - \frac{\mathbf{k}^i}{\mathbf{k}^2}\,. \tag{2.32}$$

It is worth noting that the amplitude is proportional to the commutator of the color matrices, which means that in abelian theories such as QED, in the high energy limit photon emission is suppressed. In non-abelian theories instead, the quark can change its charge in several ways; it gets "repainted". The emission rate is proportional to the squared amplitude and gives the Gunion-Bertsch spectrum

$$w\frac{dI}{dw} \propto \left\langle \mathbf{L}^2 \right\rangle\,, \tag{2.33}$$

so that one can appreciate the interference between the QED-like radiation and the genuine non-abelian contribution.

However, in Nature there aren't on-shell quarks. When a hard scattering produces a quark it is an off-shell quark, with a certain virtuality, which can therefore emit even in vacuum without the need of medium stimulation. The most convenient way to treat objects which have a finite production time x_H^+ is by the use of the propagators in the mixed representation as described in Appendix B. With the intuition gained gained in this Section on the physics of stimulated soft and collinear emissions, we move now to the computation of the actually relevant amplitudes corresponding to the stimulated emission of gluons for a quark that was created within the medium.

2.3.3 Radiation from a Quark Created in the Medium

By the use of the mixed representation and the effective Feynman rules in Appendix B we can correctly take into account the finite time production of the hard probe and in this way we can resolve the interplay between the emission and collision times, which as we will

Figure 2-3: These new diagrams do now see the quark, in the sense that they know not only what is going on but also *when*.

see at the end of the computation lead to important interference phenomena. The updated version of the QED-like diagrams is shown in Fig. 2-3 and their amplitudes read

$$\begin{aligned} M_{1.1} \cong \quad & \int_q \int_0^{x_c^+} dx_E^+ \, U_Q^a(p^+, \mathbf{q}) Q(x_c^+ - x_E^+) V_G^{b,i}(p^+, k^+, \mathbf{k}) e^{ik^- x_E^+ - \epsilon x_E^+} Q(x_E^+) \\ & \cong 2ig^2(t^a t^b) \int_q \mathcal{A}(\mathbf{q}) \frac{\mathbf{k}^i}{\mathbf{k}^2} (-1 + e^{i\frac{x_c^+}{\tau_0}}) \,, \end{aligned} \tag{2.34}$$

where the production time has been set to $x_H^+ = 0$ and we have defined the formation time $\tau_0 \equiv 2w/k_\perp^2$, whose physical interpretation will be clear later on. Here $Q(x^+) \equiv 1/2p^+$ is the quark propagator in the mixed representation where the time ordering has been taken into account and no phase is present since $p^- \sim 0$. For collision before emission the amplitude is now

$$\begin{aligned} M_{1.2} \cong \quad & \int_q \int_{x_c^+}^{\infty} dx_E^+ \, e^{ik^- x_E^+ - \epsilon x_E^+} V_G^{b,i}(p^+, k^+, \mathbf{k}) Q(x_E^+ - x_c^+) U_Q^a(p^+, \mathbf{q}) Q(x_c^+) \\ & \cong -2ig^2(t^b t^a) \int_q \mathcal{A}(\mathbf{q}) \frac{\mathbf{k}^i}{\mathbf{k}^2} e^{i\frac{x_c^+}{\tau_0}} \,. \end{aligned} \tag{2.35}$$

Analogously for the emitted gluon scattering as shown in Fig. 2-4 gives

$$\begin{aligned} M_2 \cong \quad & \int_q \int_0^{x_c^+} dx_E^+ \, e^{ik^- x_E^+ - \epsilon x_E^+} V_G^{c,i}(p^+, k^+, \mathbf{k} + \mathbf{q}) G(x_c^+ - x_E^+, k + q) u_G^{bac}(k^+, q) \mathcal{A}(\mathbf{q}) Q(x_E^+) \\ & \cong -2ig^2[t^a, t^b] \int_q \mathcal{A}(\mathbf{q}) \frac{(\mathbf{k} + \mathbf{q})^i}{(\mathbf{k} + \mathbf{q})^2} e^{-ix_c^+(1/\tau_1 - 1/\tau_0)} (-1 + e^{i\frac{x_c^+}{\tau_1}}) \,, \end{aligned} \tag{2.36}$$

where we have defined a new formation time $\tau_1 \equiv 2w/(\mathbf{k}_\perp + \mathbf{q}_\perp)^2$. One could indeed check that by setting the production time of the energetic quark to be $t_H \to -\infty$, and by considering the $-i\epsilon$ prescription implicit in our propagators, we would obtain the results of

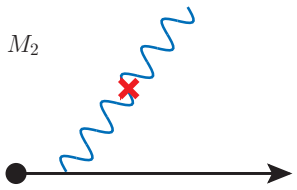

Figure 2-4: The equivalent new version of the old M_2

Section 2.3.2 times an overall phase, as it must be. Given that now the hard quark can emit even in vacuum, there are still a set of contributions that we must take care of, which are computed in the next Section.

2.3.4 Vacuum Medium Interference

For a quark created in the medium, at order g^4 we don't only get the contributions from the real diagrams of Section 2.3.3 squared, but also must consider the interference between vacuum emission (order g) and double medium scattering plus emission (order g^3), whose interference is also order g^4. The latter are the so called unitarity corrections, and for simplicity we will calculate them in the contact limit, where one identifies the two scatterings as coming from the same scattering centre. This approximation makes sense when one considers extremely dilute systems where we necessarily assume that the color correlation length of the medium is small compared to the mean free path of the gluon, λ_g, so that the scatterer does not get randomized before it collides again.

The vacuum emission (Fig. 2-5) is obtained easily as

$$\begin{aligned} M_0 \cong & \int_q \int_0^\infty dx_E^+ \, e^{ik^- x_E^+ - \epsilon x_E^+} V_G^{b,i}(p^+, k^+, \mathbf{k}) Q(x_E^+) \\ & \cong -2g\, t^b \, \frac{\mathbf{k}^i}{\mathbf{k}^2} \, . \end{aligned} \tag{2.37}$$

The following diagrams with two scatterings can already be medium averaged and given that we are working on the contact limit the two scatterings are indentified as the same, implying $\mathbf{q}_1 = -\mathbf{q}_2$ and reducing the number of diagrams considerably, a situation in which the computations greatly simplify. The two first diagrams we consider can be seen

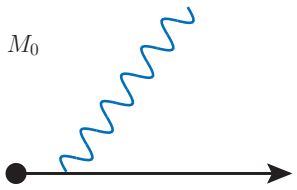

Figure 2-5: Radiation in vacuum is allowed if the emitting particle is off-shell, as it's shown in this diagram M_0

as the convolution of the $M_{1.1}$ and $M_{1.2}$ ones with an extra scattering for the quark, and read as

$$\begin{aligned}\langle M_{2M:1.1}\rangle \cong \quad & n(x_c^+)\mu_D^2(2\pi)^2\int_q \mathcal{V}(\boldsymbol{q})\int_0^{x_c^+} dx_E^+\, u_Q^a(p^+)\frac{Q(0)}{2}u_Q^a(p^+)Q(x_c^+-x_E^+)\\ & \times V_G^{b,i}(p^+,k^+,\mathbf{k})e^{ik^-x_E^+-\epsilon x_E^+}Q(x_E^+)\\ & \cong -g^3C_F\,t^b\,n(x_c^+)\mu_D^2(2\pi)^2\int_q \mathcal{V}(\boldsymbol{q})\,\frac{\mathbf{k}^i}{\mathbf{k}^2}(-1+e^{i\frac{x_c^+}{\tau_0}})\,, \end{aligned} \tag{2.38}$$

$$\begin{aligned}\langle M_{2M:1.2}\rangle \cong \quad & n(x_c^+)\mu_D^2(2\pi)^2\int_q \mathcal{V}(\boldsymbol{q})\int_{x_c^+}^{\infty} dx_E^+\, e^{ik^-x_E^+-\epsilon x_E^+}V_G^{b,i}(p^+,k^+,\mathbf{k})Q(x_E^+-x_c^+)\\ & \times u_Q^a(p^+)\frac{Q(0)}{2}u_Q^a(p^+)Q(x_c^+)\\ & \cong g^3C_F\,t^b\,n(x_c^+)\mu_D^2(2\pi)^2\int_q \mathcal{V}(\boldsymbol{q})\frac{\mathbf{k}^i}{\mathbf{k}^2}e^{i\frac{x_c^+}{\tau_0}}\,, \end{aligned} \tag{2.39}$$

where the factor $1/2$ multiplying $Q(0)$ comes from $\Theta(0)$. The next diagram is called the dipole contribution as it depicts collisions with both the quark and the emitted gluon, as shown in the left of Fig. 2-7, and it corresponds to either of the two since in the contact limit they are indistinguishable. The amplitude reads

$$\begin{aligned}\langle M_{2M:Dip}\rangle \cong \quad & n(x_c^+)\mu_D^2(2\pi)^2\int_q \mathcal{V}(\boldsymbol{q})\int_0^{x_c^+} dx_E^+\, e^{ik^-x_E^+-\epsilon x_E^+}u_Q^a(p^+)Q(x_c^+-x_E^+)\\ & \times V_G^{c,i}(p^+,k^+,\mathbf{k}+\mathbf{q})G(x_c^+-x_E^+,k+q)u_G^{bac}(k^+)Q(x_E^+)\\ & \cong g^3C_A\,t^b\,n(x_c^+)\mu_D^2(2\pi)^2\int_q \mathcal{V}(\boldsymbol{q})\frac{(\mathbf{k}+\mathbf{q})^i}{(\mathbf{k}+\mathbf{q})^2}e^{-ix_c^+(1/\tau_1-1/\tau_0)}(-1+e^{i\frac{x_c^+}{\tau_1}})\,. \end{aligned} \tag{2.40}$$

Finally, the diagram with two scatterings on the emitted gluon, as shown in the right of Fig.

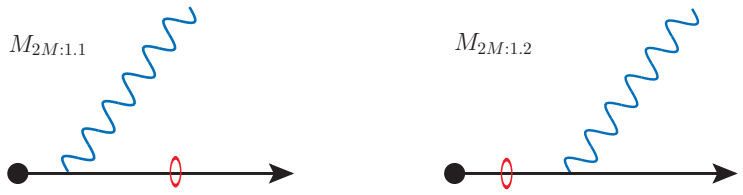

Figure 2-6: The two first M_{2M} diagrams, where the double scattering in the contact limit is represented by the red circle.

2-7, gives a very simple result thanks to the contact limit and reads

$$\begin{aligned}\langle M_{2M:2}\rangle \cong \quad & n(x_c^+)\mu_D^2(2\pi)^2\int_q \mathcal{V}(\boldsymbol{q})\int_0^{x_c^+} dx_E^+\, e^{ik^- x_E^+ - \epsilon x_E^+} V_G^{c,i}(p^+,k^+,\boldsymbol{k}) \\ & \times G(x_c^+ - x_E^+,k)u_G^{dac}(k^+)\frac{G(0,k+q)}{2}u_G^{bad}(k^+)Q(x_E^+) \\ & \cong -g^3 C_A\, t^b\, n(x_c^+)\mu_D^2(2\pi)^2\int_q \mathcal{V}(\boldsymbol{q})\frac{\mathbf{k}^i}{\mathbf{k}^2}(-1+e^{i\frac{x_c^+}{\tau_0}})\,. \end{aligned} \tag{2.41}$$

Now that we have computed all necessary diagrams we can move on to the computation of the stimulated one gluon emission rate performed in the next Section.

2.3.5 Radiative Energy Loss

By summing the real and virtual contributions and averaging over colors we get

$$\begin{aligned}\frac{1}{N_c}\mathrm{tr}(\langle|\mathcal{M}_{(1)}|^2\rangle + 2\,\mathrm{Re}\,\langle\mathcal{M}_{(2)}\mathcal{M}_{(0)}^*\rangle) \quad &= \quad 4g^4 C_F N_c n(x_c^+)\mu_D^2(2\pi)^2 \\ &\times \quad \int_q \mathcal{V}(\boldsymbol{q})\,\mathbf{L}\cdot\mathbf{A}(1-\cos(x_c^+/\tau_1))\,, \end{aligned} \tag{2.42}$$

where $\mathbf{A}$ is defined through $\mathbf{L} = \mathbf{A} - \mathbf{B}$ with $\mathbf{B} = \mathbf{k}^i/\mathbf{k}^2$. The radiation cross section is proportional to the probability of the process (squared amplitude) times the phase space of the final gluon $dG = dk_\parallel d^2\mathbf{k}/2w(2\pi)^3$ (where we have factored out the hard quark production cross section and its phase space). We can also manipulate this expression to put it in terms of the medium length L and the mean free path λ_q by using $\lambda_q = 1/\rho\,\sigma_{el}$, with ρ the volumetric density of scattering centres. Given that the factor μ_D^2 is a measure of the transverse density of scatterers (since the total charge neutralizes beyond a distance $1/\mu_D$ due

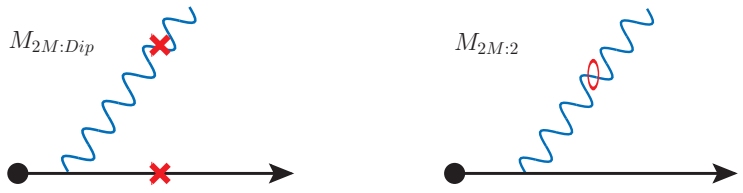

Figure 2-7: The so called dipole diagram $M_{2M:Dip}$ (left) and the double scattering with the emitted gluon $M_{2M:2}$ (right).

to screening) we can write $\mu_D^2 = L/\lambda_q \sigma_{el}$, allowing us to set our expression in terms of the elastic scattering cross section, where the latter is defined as $\sigma_{el} = g^2 C_F \, (2\pi)^2/2 \int_q \mathcal{V}(\boldsymbol{q})$. In this way the gluon emission rate reads

$$w\frac{dI}{dw\, d^2\mathbf{k}_\perp} = \frac{2\alpha_s C_F}{\pi^2}\frac{L}{\lambda_g} n(x_c^+) \int_q \widehat{\mathcal{V}}(\boldsymbol{q})\, \mathbf{L}\cdot\mathbf{A}(1-\cos(x_c^+/\tau_1))\,, \tag{2.43}$$

where we have used $dk_\parallel \simeq dw$, $\alpha_s \equiv g^2/4\pi$, $\lambda_g = \lambda_q C_F/C_A$ and the potential is normalized. This is the general expression for a defined position (in the direction of the jet) of the scattering centre. We now want to study for every possible position, with $x_c^+ \equiv z$ and assuming the specific density function $n(z) = 1/L\,\Theta(z)\Theta(L-z)$, so we may perform the integral over z

$$\frac{1}{L}\int_0^L dz(1-\cos(z/\tau_1)) = \frac{1}{L}(L - \frac{\sin(L/\tau_1)}{1/\tau_1}) = 1 - \frac{\sin(L/\tau_1)}{L/\tau_1}\,, \tag{2.44}$$

where τ_1 is the in-medium *formation time* of the gluon, τ_f, and plays a crucial role in stimulated emission physics. With this last step, we can rewrite our final expression for the energy loss rate as

$$w\frac{dI}{dwd^2\mathbf{k}_\perp} = \frac{2\alpha_s C_F}{\pi^2}\frac{L}{\lambda_g}\int_q \widehat{\mathcal{V}}(\boldsymbol{q})\, \mathbf{L}\cdot\mathbf{A}\left(1-\frac{\sin(L/\tau_f)}{L/\tau_f}\right) \tag{2.45}$$

Thus when the formation time of the gluon is considerably larger than the time of collision, this rate vanishes, the radiation gets frustrated. This effect is also called the Landau-Pomeranchuk-Migdal (LPM) effect, in which the medium scatters with our qg system too early to see the gluon decohered from the quark, fact which tends to suppress radiation. This behaviour arised due to the assumption that the jet was produced in the medium, short

before it emitted or collided.

One can understand the physics of formation time by asking which is the time at which a gluon gets decohered from its emitter. For that to happen, the gluon has to be able to *resolve* its separation from the quark, i.e. $\lambda_\perp \sim r$, where $\lambda_\perp$ is the gluon transverse wavelength and r the system separation. Parametrically, after a time t the transverse distance between the emitter and the collinear gluon is $r_\perp \sim \theta\, t$, where $\theta \sim k_\perp/w$ is the emission angle. By the uncertainty principle, $\lambda_\perp \sim 1/k_\perp$ and then $\tau_f \sim w/k_\perp^2$, with τ_f being the time at the moment of resolution.

Incoherent Limit and Path Length Dependence

The rate we have calculated corresponds only to the medium induced radiation, but the total energy loss also depends on the vacuum radiation. We try to figure out this implications in the following limit: sending $w \to 0$ (this means $\tau_f \ll \tau_{coll}$) makes the time dependent part of the rate vanish and we are left with the simpler form

$$w\frac{dI_{med}}{dw d^2\mathbf{k}_\perp} = \frac{2\alpha_s C_F}{\pi^2}\frac{L}{\lambda_g}\int_q \widehat{\mathcal{V}}(\boldsymbol{q})\,\mathbf{L}\cdot\mathbf{A} \tag{2.46}$$

We can write $\mathbf{L}\cdot\mathbf{A}$ as

$$\mathbf{L}\cdot\mathbf{A} = \frac{1}{2}(\mathbf{L}^2 + \mathbf{A}^2 - \mathbf{B}^2) \tag{2.47}$$

Now, we know that

$$w\frac{dI_{vac}}{dw} = \frac{\alpha_s C_F}{\pi^2}\langle\mathbf{B}^2\rangle \tag{2.48}$$

so that we can express the *total* energy loss rate as

$$w\frac{dI_{tot}}{dw} = w\frac{dI_{vac}}{dw} + w\frac{dI_{med}}{dw} \tag{2.49}$$

The medium part contains a $\frac{L}{\lambda_g}$ factor that the vacuum part does not, getting

$$w\frac{dI_{tot}}{dw} = \frac{\alpha_s C_F}{\pi^2}\langle\mathbf{B}^2\rangle(1-\frac{L}{\lambda_g}) + \frac{\alpha_s C_F}{\pi^2}\frac{L}{\lambda_g}(\langle\mathbf{L}^2\rangle + \langle\mathbf{A}^2\rangle) \tag{2.50}$$

When we consider that the gluon has had plenty of time to form, we get such an *incoherent* sum of different processes involving radiation. We see that the term proportional to $\langle \mathbf{B}^2 \rangle$, which corresponds to radiation in vacuum, gets a reduced probability due to the fact that considering the medium implies that there's a certain probability for the quark to scatter (which is proportional to $\frac{L}{\lambda_g}$)

The term $\langle \mathbf{L}^2 \rangle$ corresponds to the result of section 2, this is the stimulated radiation of a coming from infinity quark, but gets corrected in (2.50) by the contribution of a gluon emitted (by an off-shell quark) long before the scattering centre interacts with him ($\langle \mathbf{A}^2 \rangle$). When this gluon receives a kick from the plasma, it does being a final state gluon (in contrast to what we commented in the end of section 2.3.2).

We can learn more things from expression (2.45) regarding the parametric dependence on the path length travelled by the quark projectile (a full analysis of the integral can be found in [63]). The integral in $k_\perp$ is dominated by $k_\perp \sim q_\perp$, and the typical momentum transferred from the plasma for a standard screened potential is $q_\perp \sim \mu_D$. We can then see that the gluon emission rate goes like

$$w\frac{dI}{dw} \sim \frac{1}{\lambda}\left(L - \sin\left(\frac{L\mu_D^2}{2w}\right)\frac{2w}{\mu_D^2}\right) . \tag{2.51}$$

By defining w_c as the energy that makes the argument of the oscillatory function of order one, $w_c \sim \mu_D^2 L$ (which means that $\tau_f \sim L$), we see that the integral over w has two separate regimes: $w \gg w_c$ and $w \ll w_c$. When $w \ll w_c$, the second term goes to zero, so that the emission spectrum does not depend on w. When $w \gg w_c$, the argument can be expanded. In this way we get

$$w\frac{dI}{dw} \sim \begin{cases} \frac{1}{\lambda}\frac{L^3\mu_D^4}{w^2} & \text{for } w \gg w_c \\ \frac{L}{\lambda} & \text{for } w \ll w_c \end{cases} \tag{2.52}$$

This means that for small frequencies, the lost energy from the quark scales like

$$\Delta E|_{w \ll w_c} \sim \int_0^{w_c} w\frac{dI}{dw} \sim \frac{1}{\lambda} L w_c \,, \tag{2.53}$$

while for high frequencies it is

$$\Delta E|_{w\gg w_c} \sim \int_{w_c}^{\infty} w\frac{dI}{dw} \sim \frac{1}{\lambda}\frac{L^3\mu_D^4}{w_c} \sim \frac{1}{\lambda}Lw_c\,, \tag{2.54}$$

where one can see how the LPM interference effects suppress emissions at large w and only the lower cut-off w_c contributes. Noting that both regimes have the same parametric dependence, we conclude that

$$\Delta E \sim \frac{1}{\lambda}Lw_c \sim L^2\,\hat{q}\,, \tag{2.55}$$

which corresponds to the well known L^2 dependence of radiative energy loss (we have used that $\hat{q} \sim \mu_D^2/\lambda$). This behaviour arised due to the consideration of the LPM interference effects; otherwise the dependence would have been only L. We will use this parametric dependence for our benchmark studies of jet quenching as described in Section 4.2.3.

Chapter 3

Strongly Coupled Energy Loss

In this Chapter we will briefly review the ideas behind calculations at asymptotically strong coupling, far beyond the reach of perturbative techniques, for certain theories which possess a holographic dual: a map between a non-gravitating gauge theory in d dimensions and a gravity theory of strings in $d+1$ dimensions. The reason why this is relevant for heavy ions is that, as we have stressed a number of times in Chapter 1, the fireball produced in the collisions behaves as a strongly coupled fluid where the quasi-particle picture does not apply. The techniques introduced in this Chapter suppose nowadays one of the few tools with which to study such strongly coupled systems, specially in out of equilibrium situations where lattice calculations are still in its infancy. Holography is for this and other reasons a very lively topic nowadays, which has led to impressive insights on the physics and phenomenology of heavy ion collisions.

3.1 Holographic Quark-Gluon Plasma

Gauge/gravity duality is a useful tool to study non-Abelian plasmas. Although no gravitational dual to QCD is known, gauge/gravity duality has provided much insight into the dynamics of many theories that share many qualitative properties with QCD. The most widely studied example is $\mathcal{N}=4$ SYM. Even though at $T \neq 0$ the two theories are nothing alike, the deconfined plasma phases of QCD and SYM have more in common. We will briefly comment some of these features next:

+ $\mathcal{N} = 4$ doesn't confine at any scale. Due to is specific field content, its beta function is exactly zero, a really remarkable property that makes this theory invariant under conformal transformations. While QCD confines into hadrons at $T = 0$, it becomes deconfined above T_c.

+ Even though $\mathcal{N} = 4$ is a supersymmetric theory, this supersymmetry is broken at $T \neq 0$. In a thermodynamic context, this can be seen by noting that fermions have antiperiodic boundary conditions along the Euclidean time circle while bosons are periodic. This makes supersymmetry a less relevant feature for the characterization of plasma properties at finite temperature.

- The degrees of freedom between the two theories for $N_c = 3$ is quite different. $\mathcal{N} = 4$ has a richer field content, and one needs to figure out how to map the physical quantities from one theory to the other taking this into account. There are, however, quantities which are independent of the details of the theory and only require that it possesses a gravity dual (as it is the case of η/s bound).

- Most of the calculations using the duality are done in the $\lambda \to \infty$ and $N_c \to \infty$ limits. Even though we are interested in large couplings, one should expect $1/\lambda$ corrections, as well as $1/N_c$ corrections, which have to be calculated to check the robustness of the infinite limit.

- Even though the difference between fermions and bosons is not important, the difference between fundamental and adjoint representations degrees of freedom is, specially for thermodynamics; QCD has $N_f = 3$ d.o.f. (at collider relevant temperatures) in the fundamental representation, and most calculations are done assuming $N_f \ll N_c$.

Even though the plasma phases of the two theories are certainly different, we will attempt to gain insight on the QCD physics by the study of a simpler version, $\mathcal{N} = 4$ SYM, which nevertheless still captures the main physics aspects we are interested in. This supersymmetric theory might not look simple from the field theory point of view, but the large amount of symmetry it enjoys translates into the simplest dual gravitational description that we know

of. This is the feature that makes the study of holography in terms of $\mathcal{N} = 4$ SYM so convenient and rewarding. In the coming text we present some of the remarkable lessons that can be extracted from the use of gauge/gravity duality.

A rather striking result obtained from holography is the fact that thermodynamic quantites don't seem to depend much on the precise value of the coupling constant [64]

$$\frac{s_{\lambda=\infty}}{s_{\lambda=0}} = \frac{P_{\lambda=\infty}}{P_{\lambda=0}} = \frac{\epsilon_{\lambda=\infty}}{\epsilon_{\lambda=0}} = \frac{3}{4} \tag{3.1}$$

We understand now why the closeness of the energy density between lattice QCD calculations and the Stefan-Boltzmann limit shown in Section 1.3 is no proof for a weakly coupled plasma: an infinitely coupled one is also only about a 25% away.

This is in stark contrast with the behaviour of transport coefficients, which do show a very different behaviour between weakly and strongly coupled regimes, since for instance the shear viscosity η is inversely proportional to the cross section as derived in section 1.4.2. For the specific case of $\mathcal{N} = 4$ one finds [65, 66]

$$\frac{\eta_{\lambda\to 0}}{s_{\lambda\to 0}} = \frac{A}{\lambda^2 \log\left(B/\sqrt{\lambda}\right)} \qquad \frac{\eta_{\lambda=\infty}}{s_{\lambda=\infty}} = \frac{1}{4\pi}\,, \tag{3.2}$$

with $A = 6.174$ and $B = 2.36$, and other values for different theories. The first thing we confirm is that weakly coupled theories cannot achieve low values of the dimensionless η/s ratio, making it hard for them to describe almost ideal fluids such as the one created in our accelerators. Secondly, and perhaps most importantly, it is worth noting that while the weak coupling regime depends on the details of the specific microscopic theory, the strong coupling regime does not. This behaviour could be due to the different description of the plasma degrees of freedom, since at weak coupling one works in terms of quasi-particles while at strong coupling these are absent. Even though this reasoning has not been proved yet, these are clear hints that the strong coupling limit shows a remarkable universality among theories which have a gravity dual. The discovery that the value of η/s found for the QCD plasma in our accelerators is very close to this lower bound works in favour of

this argument (if one assumes that QCD actually has a dual gravitational description).

There are many features of heavy ion physics which can be understood by the use of holography, such as the fireball thermalization and its hydrodynamic evolution (as commented in Section 1.4.3), meson melting... and many others which we will not cover here since they are not in direct relation to the subject of this thesis (for a review see [67]). Given the importance of the gauge/gravity duality, not only in heavy ion physics but also in general theoretical physics, we will introduce the basic concepts behind its elucidation to provide the reader with an intuition on the physics of holography.

3.2 Gauge/Gravity Duality

The renowned holographic conjecture [68], found within the context of string theory, states that certain large N gauge theories at strong coupling (hard to solve) are dual to classical gravity in higher dimensions (doable). The paradigmatic and most studied example corresponds to the $\mathcal{N} = 4$ Super Yang-Mills gauge theory in $3 + 1$ dimensions (at large N), which is dual to classical gravity in AdS_5 (Anti de Sitter space) in $4 + 1$ dimensions. What is truly remarkable about this duality is that, in some sense, gravity is regarded as an emergent phenomenon induced by quantum correlations, representing one of the few insights that we have nowadays on quantum gravity.

Historically, in the quest to find a theory of everything that unifies the known quantum field theories and gravity in a consistent way, it is natural to ask whether massless spin-2 particles can arise as bound states of lower spin particles (such as photons, leptons, quarks, gluons...) from a field theory perspective. However, Weinberg-Witten no-go theorem [69] states that a theory that allows a Lorentz-covariant, conserved current $T^{\mu\nu}$, cannot contain massless particles of spin > 1 [1]. This would a priori forbid the possibility of emergent gravity for all renormalizable QFTs, but the theorem is formulated in a fixed number of

[1] This theorem does not forbid the graviton from General Relativity, since in this theory there is no conserved Lorentz-covariant $T^{\mu\nu}$

space-time dimensions. In the holographic duality, gravity does not live in the same number of dimensions as the original theory. This sort of loophole in the theorem is precisely what makes the duality possible. An early realization of the holographic features of gravity came from the physics of black holes and the necessity to treat them as thermodynamic objects possessing an associated entropy, which is proportional to its *area*.

3.2.1 On Black Holes and the Holographic Principle

Consider an isolated system of mass E and entropy S in an asymptotically flat space-time. Let A be the area of a sphere that encloses the system and M_A the mass of a black hole (BH) with horizon area A. Indeed, one must have $E \leq M_A$. If we now add $M_A - E$ amount of energy to the system (keeping A fixed), we form a black hole and $S_{BH} \geq S_0 + S'$, being S' the entropy of the added energy. This means that $S_0 \leq S_{BH} = \frac{A}{4\pi G_N}$, implying that the maximal entropy inside a region bounded by an area A is given by

$$S_{max} = \frac{A}{4\pi G_N}\,, \tag{3.3}$$

which is proportional to the area, and not the volume. Recall now the definition of entropy in quantum statistical physics, given by $S = -\mathrm{Tr}\,\rho \log\rho$, with ρ being the density operator of the system. If the system is a N-dimensional Hilbert space whose density is $\rho = \frac{1}{N}\mathbb{I}$, then the entropy is maximum and equals to $S_{max} = \log N$. We can then conclude that the "effective" dimension of the Hilbert space for a system inside a region of area A is bounded by

$$\log N \leq \frac{A}{4\pi G_N} = \frac{A}{4\, l_p^2}\,, \tag{3.4}$$

where the Planck length is defined as $l_p = \sqrt{\frac{\hbar G_N}{c^3}}$. Even though this bound can be violated for non-gravitating systems, whose number of degrees of freedom is proportional to the volume rather than the area (such as a lattice of spins with lattice spacing a, where $S_{max} = \frac{V}{a^3}\log 2$), we have seen how considerations from quantum gravity have led to a huge reduction of the number of degrees of freedom. This can be summarized as the *Holographic principle*: in quantum gravity, a region of boundary area A can be fully described

by no more than $\frac{A}{4\pi G_N} = \frac{A}{4\,l_p^2}$ d.o.f., i.e. one d.o.f per Planck area.

This important principle lies at the core of the AdS/CFT duality, which corresponds to one of the possible realizations it might adopt. Even though the duality was found by studying the dynamics of D-branes, relatively recent objects in string theory, it was well known before that that there exists some special relation between the large N limit of gauge theories and string theory (which contains spin-2 massless excitations that describe the graviton). Such connection is regarded as one of the key conceptual points of holography and will be briefly discussed next.

3.2.2 Large N Gauge Theories

When 't Hooft considered large N gauge theories [70], a remarkable surprise arised, and it is that the $1/N$ expansion can be related to features of string theory. They key point is that in non-abelian theories, the fields are matrices. For each order in g^2, different topologies will lead to different powers of N: planar diagrams, those which can be drawn on a plane without crossing lines, are enhanced in N with respect to non-planar ones. These planar diagrams are said to correspond to genus $h = 0$, the sphere topology[2]. For any non-planar diagram, there exists an integer h such that the diagram can be straightened out on a genus-h surface, but not on a surface with a smaller genus. Moreover, one can see that the power of N coming from contracting propagators is given by the number of faces on such a genus-h surface .

By considering the limit in which $N \to \infty$ and $g^2 \to 0$, it is convenient to define the 't Hooft coupling $\lambda \equiv g^2 N$, where the combination is kept finite. With this arrangement, each diagram power counting can be expressed as $\mathcal{A} \sim \lambda^{L-1} N^{\chi}$, where L is the number of loops and χ is the Euler number, defined as $\chi \equiv F + V - E$ (number of faces plus number of vertices minus number of propagators). In this way, each diagram can indeed be seen as a partition of the surface into polygons. The Euler number also corresponds precisely to the combination $\chi = 2 - 2h$, so that the sum of all connected diagrams can be expressed

[2]Any orientable two dimensional surface is classified topologically by an integer h, called genus. The genus is equal to the number of holes a surface has.

as

$$\log Z = \sum_{h=0}^{\infty} N^{2-2h} f_h(\lambda) = N^2 f_0(\lambda) + f_1(\lambda) + \frac{1}{N^2} f_2(\lambda) + ... \tag{3.5}$$

where one clearly sees that at large N the leading order is given by planar diagrams (h=0). In summary, in the 't Hooft limit the $1/N$ expansion corresponds to an expansion in terms of topology of Feynman diagrams. The observables dominating at leading order of such a large-N gauge theory corresponds to the so called glueballs, single trace operators $\mathcal{O}_i(x_i)$ whose fluctuations are suppressed as in a classical theory. In general, the parametric dependence of the correlation functions of n glueballs is

$$\langle \mathcal{O}_1(x_1)...\mathcal{O}_n(x_n) \rangle_C = \sum_{h=0}^{\infty} N^{2-n-2h} F_n^h(...) = N^{2-n} + N^{-n} + N^{-n-2} + ... \tag{3.6}$$

In this way, it is natural to assign a value for the glueball coupling constant $\tilde{g} \sim \frac{1}{N}$ as if it corresponded to a basic vertex of a tree level scattering amplitude.

From the string theory side, there is a remarkable fact and it is that summing over topologies automatically includes the interactions of the strings, fully specifying them in fact. In this sum, one needs to include a kind of "chemical potential" for topology that gives a weight to the different terms as $e^{-\lambda \chi}$, which appears naturally in a rigorous string theory derivation. An $h = 0$ genus surface would correspond to the worldsheet of a string nucleating from vacuum and later disappearing, a genus $h = 1$ describes a string that splits and rejoins before disappearing, and so on. By defining the string coupling as $g_s \equiv e^{\lambda}$, and considering n strings scattering (so that $\chi = 2 - 2h - n$ now), one gets

$$A_n = \sum_{h=0}^{\infty} g_s^{n-2+2h} F_n^{(h)} = g_s^{n-2} + g_s^n + g_s^{n+2} + ... \tag{3.7}$$

which shares an identical mathematical structure with the large N expansion. In this sense we can identify the external string states with coupling $g_s = e^{\lambda}$ with the glueballs of coupling $1/N$, and the sum over string worldsheets of genus h with the sum over Feynman diagrams of genus h. It is then natural to state that each Feynman diagram of genus h can be considered as a partition of a genus h surface, a triangulation, with string theory as the

continuum limit that would correspond to the denser triangulations that dominate at strong coupling. However, the identification between the states of the two theories (single trace operators with string states) is difficult.

An explicit realization of this correspondence had to wait first for the discovery of D-branes [71], and then some years more until the seminal work of Maldacena [68]. The two equivalent interpretations that D-branes dynamics can have within string theory are the basis from which all the elements of the duality are derived in the different limits, and for this reason we will give a brief introduction to D-branes and a summary of the main steps that lead to the stablishment of the famous conjecture.

3.2.3 D-branes as Boundary Conditions

Open strings can have either Dirichlet ($\delta X^\mu = 0$) or Neumann ($\partial_\sigma X^\mu = 0$) boundary conditions. At first sight, Dirichlet condition seems to break Lorentz and translational symmetry, unless one can image a space-time defect sitting at some location where open strings can end. Such an object is called a D-brane. For instance, if one has Neumann conditions in all directions, the open strings can end everywhere, so the brane is space-filling.

If we consider N Dp-branes (branes of dimension p) sitting at the same location, we can assign a value to each open string depending on the brane it ends on, as $|\Psi, IJ\rangle$ with $I, J = 1, 2, ...N$, so that each open string excitation becomes a NxN matrix (such as the vector field $(A_\alpha)^I_J$ or the scalar field $(\Phi^a)^I_J$)[3]. In this way, when strings interact joining their ends, it corresponds to matrix products in the I, J indices. Moreover, string interactions have a symmetry realized by assigning a phase factor $e^{i\theta_I}$ to states whose $\sigma = 0$ end is at brane I, and the factor $e^{-i\theta_I}$ to states whose $\sigma = \pi$ end is at brane I. Then, $(\Phi^a)^I_I$ is invariant, and $(\Phi^a)^I_J$ is the complex conjugate of $(\Phi^a)^J_I$. For coincidental branes, since they are indistinguishable from each other, we can reshuffle indices; there is in fact a $U(N)$

[3]For the simple case of the bosonic string, by deriving the massless spectrum of the open string one gets a vector field A_α and $D - p - 1$ scalar fields Φ^a, corresponding to the Poincaré representations of $(1, p) \otimes SO(D - p - 1)$. The massless scalar fields can be seen as the Goldstone bosones for breaking translational symmetries in D-Minkowski.

symmetry

$$|\Psi, IJ\rangle \to U_{IK}U_{JL}|\Psi, KL\rangle\,, \qquad \text{or} \qquad \Psi \to U\,\Psi\,U^\dagger\,, \tag{3.8}$$

where U are unitary matrices. We then conclude that each open string excitation transforms under the adjoint representation of this $U(N)$. On the string worldsheet, this corresponds to a global symmetry, but in space-time, i.e. in the worldvolume of D-branes, this $U(N)$ must be a gauge symmetry - in particular, $(A_\alpha)^I_J$ must be the corresponding gauge bosons. By general arguments of Lorentz covariance and unitarity, the low energy action has to correspond to Yang-Mills theory (fact that can be checked by explicit scattering computations).

D-branes in the bosonic string always have an open string tachyon, which make them unstable. By adding superstrings, D-branes of certain dimensions are free of tachyons and become stable. In general, such D-branes carry a conserved and their worldvolume theory is supersymmetric. In addition to A_α and Φ^a, there are also massless fermions, so that the low energy theory corresponds to Super-Yang-Mills theory.

The bosonic part of the massless closed superstring spectrum contain a set of fields a part of which correspond to differential forms, the so called Ramond-Ramond (RR) fields. These are generalizations of the Maxwell field A_μ, a 1-form whose source is a point particle. Then a p-dimensional object naturally couples to a p+1 form. In electromagnetism, an object coupling to the Hodge dual field $\tilde{A}$ (meaning ${}^*F = \tilde{F} = d\tilde{A}$, so that $F^{01} = \tilde{F}^{23}$ and $F^{23} = \tilde{F}^{01}$) is said to be magnetically charged. One can also dualize a n-form such that $d\tilde{C}^{(D-n-2)} =^* dC^{(n)}$ couples to a $(D-n-3)$-dimensional object; in terms of C^n, this is a magnetic object. A remarkable situation takes place for Type IIB superstring theory, where there is a form, the RR field $C^{(4)}$, whose electric and magnetic part both couple to a D3-brane, satisfying the self-dual condition $F^{(5)} =^* F^{(5)}$. This condition can be seen as a realization of the Montonen-Olive duality that relates electric and magnetic charges in supersymmetric theories with 4 supercharges in 3+1 dimensions. Due to the precise field content and symmetries present one then concludes that on these stable D3-branes lives the $\mathcal{N} = 4$ SYM theory in 4 dimensions.

Up to here, we have treated D-branes as Dirichlet boundary conditions. One can instead

study the geometry that D-branes themselves source as gravitating objects, an analysis that we briefly review in the coming text.

3.2.4 D-branes as Space-time Geometries

From another point of view, let's consider a D3-brane in IIB supergravity (SUGRA), which corresponds to the low energy effective theory of IIB superstring. Its regime of validity is when $g_s \ll 1$, so that the quantum corrections are small, and when the energy satisfies $E^2 < 1/\alpha'$ in order to get massive modes decoupled. One also needs the curvature to be much smaller than $1/\alpha'$ in order to be able to neglect string finite size corrections. Its Lagrangian can then be expressed as $\mathcal{L} = \frac{1}{16\pi G_N} R + ...$ provided that one does the identification $16\pi G_N = (2\pi)^7 g_s^2 \alpha'^4$. Given that the D3-brane is charged under $C^{(4)}$, by Gauss law the electric (q_3) and magnetic (g_3) charges are

$$q_3 = \int_{S^5} {}^*F^{(5)} \qquad g_3 = \int_{S^5} F^{(5)} \,, \tag{3.9}$$

which by the self-dual property are equal $q_3 = g_3$. The Dirac quantization condition implies $q_3 = g_3 = \sqrt{2\pi N}$, allowing one to write the D3-brane tension as $T_3 = q_3/\sqrt{16\pi G_N} = N/(2\pi)^3 g_s \alpha'^2$.

Given that the presence of the brane reduces the symmetry to Poincaré $(1,3) \otimes SO(6)$, we try the following ansatz for the metric

$$ds^2 = f(r)\left(-dt^2 + dx_1^2 + dx_2^2 + dx_3^2\right) + h(r)\left(dr^2 + r^2 d\Omega_5^2\right) \,, \tag{3.10}$$

being the D3-brane sitting at $r = 0$. By solving Einstein's equations, one finds $f(r) = H^{-1/2}(r)$ and $h(r) = H^{1/2}(r)$, with $H(r) = 1 + R^4/r^4$ and $R^4 = \frac{4}{\pi^2} G_N T_3 N = 4\pi g_s N \alpha'^2$. For the limit in which $r \to \infty$, $H = 1$ and the metric reduces to Mink$_{10}$. For intermediate situations where $r \gg R$, one gets long range corrections from the Coulomb potential in $\mathbb{R}^6$. For the interesting case where $r \to 0$, $H \simeq \frac{R^4}{r^4}$ and the spacetime acquires an horizon,

with a geodesically long "throat" at $r \simeq 0$. The metric becomes

$$ds^2 = \frac{r^2}{R^2}\left(-dt^2 + d\mathbf{x}^2\right) + \frac{R^2}{r^2}dr^2 + R^2 d\Omega_5^2 \,. \tag{3.11}$$

From this expression we notice that the S^5 has constant radius R, and that the point at $r = 0$ indeed sits at infinite proper distance away. This metric corresponds then to $AdS_5 \otimes S^5$, where the AdS_5 metric is

$$ds^2_{AdS_5} = \frac{r^2}{R^2}\left(-dt^2 + d\mathbf{x}^2\right) + \frac{R^2}{r^2}dr^2 \,. \tag{3.12}$$

With these two approaches we have obtained two different descriptions for D3-branes:

A D-branes in flat Minkowski$_{10}$ where open strings live

B Space-time metric $AdS_5 \otimes S^5 \, + \, F_5$ flux on S^5 with only closed strings.

In principle, both descriptions can be valid for all $\alpha^{'}$ and g_s. In **A**, we have an open string sector that corresponds to $\mathcal{N} = 4$ SYM with $U(N)$ gauge group, and a closed string sector which contains excitations such as the graviton and the dilaton. However, the couplings between massless closed and open strings, or between closed strings themselves, go like $G_N \propto g_s^2 \alpha'^4$, and in the low energy limit $E \to 0$, the dimensionless combination $G_N E^8 \to 0$ (since gravity is infrared free). In this way, in the low energy limit **A** corresponds to a theory with $\mathcal{N} = 4$ SYM plus free gravitons.

Regarding **B**, since we are dealing with a curved space-time, one has to be careful with which energy to consider. In **A**, the energy is defined w.r.t. t, i.e. the time at $r = \infty$. At fixed r, the local proper time is $d\tau = H^{-1/4}dt$, and the corresponding energy is $E_\tau = H^{1/4}E$. For $r \ll R$, then $H \simeq \frac{R^4}{r^4}$ and the condition $E^2\alpha' \to 0$ translates to

$$E_\tau^2 \frac{r^2}{\sqrt{4\pi g_s N}} \to 0 \,, \tag{3.13}$$

meaning that for *any* E_τ we can achieve the low energy limit by going close enough to $r \to 0$. We can then state the equivalence between these two descriptions in the low

energy limit as

$$\mathcal{N}=4\,\text{SYM with}\,U(N) \qquad \longleftrightarrow \qquad \text{IIB string theory in}\,AdS_5\times S^5\,, \tag{3.14}$$

a statement which supposes a specific realization of the holographic principle and lies at the origin of the physical revolution of our times.

The main important result for us consists in the observation that in the limit of large N_c and large λ, the gravitational dual to $\mathcal{N}=4$ SYM in $4d$ is described by classical supergravity on the ten dimensional $AdS_5\times S^5$ geometry. Moreover, studying the theory at finite temperature corresponds to adding a black hole to this geometry with a non zero Hawking temperature, a metric that will call AdS-BH.

Aspects on AdS geometry, the matching of symmetries, the state/operator correspondence and in general all the duality toolbox will not be discussed here and we refer the reader to the reviews [72, 67].

3.3 Energy Loss at Strong Coupling

From the gauge/gravity duality context, the most important result for the goal of this thesis concerns the study of jet energy loss within a strongly coupled gauge theory, a problem that has been studied extensively. (See Refs. [75, 76, 77, 78, 79, 80, 81, 82, 83, 84, 85, 86, 87] for entries into the literature for the propagation of light degrees of freedom.) These studies can be divided into two general classes: those in which a hard process in a strongly coupled gauge theory is studied via the gauge/gravity correspondence, for example via analyzing the decay of a virtual external $U(1)$ field into strongly coupled matter within the plasma [79, 80, 81, 83, 84]; and those in which single energetic excitations are described as a string moving in the dual gravitational spacetime whose endpoint is attached to a space-filling D7-brane and can therefore fall into the horizon [75, 78, 87]. The former has the advantage that the set-up is fully determined within the strongly coupled theory, while in

the latter the initial conditions that characterize the hard creation of these excitations need to be specified. The latter has the advantage that the string describes an isolated excitation whose energy can be tracked, emerging from the initial configuration. These two approaches lead to qualitatively similar results for certain observables, such as the parametric dependence of the maximal stopping distance of energetic partons, but differ quantitatively. While both computations are valid within the context of strongly coupled gauge theories, it is unclear which is a better proxy for QCD hard processes in strongly coupled medium. Since the string-based computations provide the energy loss rate explicitly [87], we will adopt this second approach to extract the energy loss physics that we need to construct our jet quenching model in Part II of the thesis.

Given the absence of jets in $N = 4$ SYM at strong coupling as we know them from QCD [76], the usual path that people have take, as stated above, consists in constructing states which have highly energetic and localized configurations that propagate arbitrarily far through plasma before thermalizing. A convenient choice is to consider a dressed quark configuration in terms of the conserved current J^{μ}_{baryon} which is present when coupling $\mathcal{N} = 4$ SYM to a fundamental representation $\mathcal{N} = 2$ hypermultiplet. On the gravity side of the duality, the addition of this hypermultiplet is accomplished by adding a $D7$ brane to the $10d$ geometry [88] on which one of the ends of an open string ends. According to Maldacena, infinitely heavy, static strings are Wilson lines [74] evaluated along the trajectory that the endpoint of the string follows. This is in consonance with our derivation of the quark propagator in terms of the Wilson line in Section 2.2, so that an identification between open strings and quarks is quite natural. By allowing the endpoint of the string to move, one is effectively relaxing the eikonal approximation within the AdS/CFT framework.

The $D7$ brane fills a volume of the AdS-BH geometry that extends from the boundary at $u = 0$ down to a maximal radiate coordinate u_m, wrapping an S^3 of the S^5. In general, by separating a brane from the rest by a distance d, we are effectively inducing a mass term for the open strings stretching from this brane to the others as $M^2 = (d/2\pi\alpha')^2 + ...$ This

means that the gauge symmetry is broken as $U(N) \to U(N-1) \otimes U(1)$, which can be seen as a realization of the Higgs mechanism. For our case, this implies that the bare mass M of the hypermultiplet is proportional to $1/u_m$ [73], meaning that for massless quarks the $D7$ brane fills all of the $5d$ AdS-BH geometry. The open strings which end on the $D7$ brane representing the dressed $q\bar{q}$ pair can then fall unimpeded toward the event horizon down to the radial coordinate u_m where the $D7$ brane ends, and if the quarks are light enough, or massless, they can fall into the horizon.

Therefore, the open string configurations we consider here may be regarded as the dual description of dressed quarks. Given our heavy ion collisions phenomenological interests, we consider that weak coupling physics in asymptotically free QCD is responsible for creating a high energy excitation whose propagation through the plasma is modelled by studying the dynamics of the same kind of excitation in a strongly coupled $\mathcal{N} = 4$ plasma. We also focus on jets that have vanishingly small size at the moment of creation, which in the dual gravitational description requires considering strings that are produced arbitrarily close to the AdS boundary. Since we are also interested in the in-medium propagation of highly energetic partons with a neglectable mass, we will drive our efforts into the computation of the light quark energy loss, which involves a more complicated computation than in the heavy quark case given the absence of stationary regimes.

While the energy loss rate for a heavy quark depends only on the quark's velocity, λ and the temperature [73], this is not the case for light quarks. The initial conditions for a classical string involve two free functions: the initial string profile and its time derivative. The instantaneous energy loss rate of a light quark depends strongly on the choice of these initial functions. This is reflected in the dual field theory as the fact that a complete specification of an initial state containing an energy quark must also include the characterization of the gauge field configuration. However, the maximum distance a quark of energy E can travel before thermalizing, Δx_{max}, is rather insensitive to the precise initial conditions. We will also focus on energetic excitations whose stopping distance is large enough that the specific initial details on the string profile become irrelevant, since all this information is

washed away during a transient time of order $1/T$ due to the ultrarelativistic propagation of the string, whose duration is arbitrarily small when compared to the total distance that the endpoint travels through AdS-BH.

Next we will review the setup that leads to the strongly coupled energy loss rate whose form we use as an insight from non-perturbative jet/plasma interplay. This is not original work of this thesis but is rather a result we use for the construction of our model in Part II. Given its importance for us we reproduce the basic steps of the computation here, where the full analysis can be found in [87].

In the limit of large λ, where the string action and the energy both scale like $\sqrt{\lambda}$, quantum fluctuations in the string worldsheet are suppressed and the dynamics of strings can be described by the classical equations of motion coming from from the Nambu-Goto action.

$$S_{NG} = -T_0 \int d\tau d\sigma \sqrt{-g}\,, \tag{3.15}$$

with $T_0 \equiv \frac{\sqrt{\lambda}}{2\pi}$ the string tension, λ the 't Hooft coupling, σ and τ are the world-sheet coordinates, $g \equiv \det g_{ab}$ with $g_{ab} = \partial_a X \cdot \partial_b X$ the string world-sheet metric and $X^M = \{t(\tau,\sigma), x(\tau,\sigma), 0, 0, u(\tau,\sigma)\}$ are the embedding functions. The target space G_{MN} metric is Schwarzschild Anti de-Sitter

$$ds^2 = \frac{1}{u^2}\left[-f(x,u)\,dt^2 + d\mathbf{x}^2 + \frac{du^2}{f(x,u)}\right], \tag{3.16}$$

where $f(x,u) = h(u)$ for $0 < x < L$ with $h(u) = 1 - \frac{u^4}{u_h^4}$ and $f(x,u) = 1$ otherwise. The temperature of the plasma is related to the black hole horizon position through $u_h = 1/\pi T$, being the boundary located at $u = 0$. This configuration is the strongly coupled analogous of the QGP brick studied in perturbation theory; it is a non-physical situation where a fireball rests without exploding against vacuum, which will nevertheless allow us to perform analytical calculations from which we expect to extract the most important features of the problem we want to study.

One can express the equations of motion in terms of the canonical world-sheet momenta

$$\pi^0_M = -T_0 \frac{G_{MN}}{\sqrt{-g}} \left[(\dot{X} \cdot X') X'^N - (X')^2 \dot{X}^N \right] \tag{3.17}$$

$$\pi^\sigma_M = -T_0 \frac{G_{MN}}{\sqrt{-g}} \left[(\dot{X} \cdot X') \dot{X}^N - (\dot{X})^2 X'^N \right] , \tag{3.18}$$

where $\dot{} \equiv \partial_\tau$ and $' \equiv \partial_\sigma$, so that

$$\partial_\tau \pi^0_0 + \partial_\sigma \pi^\sigma_0 = 0 \, . \tag{3.19}$$

We model the creation of a pair of quarks as a string that originates at $X^M_{\text{create}} = \{0, x_0, 0, 0, u_0\}$ that subsequently expands, with its endpoints propagating at the speed of light c and in a direction transverse to the string (due to open string boundary conditions). The physics of our problem leads us to consider strings that initially move in the x direction asymptotically close to c and fall only slowly in the holographic direction, corresponding to strings with $E_{\text{string}} \to \infty$ possessing a small inclination, i.e. a small opening angle in analogy with QCD jets with small $\theta \sim \frac{m}{E} = \frac{\sqrt{E^2 - \mathbf{p}^2}}{E}$. This limit $E_{\text{string}} \to \infty$ makes the string effectively tensionless, with all the pieces of the string travelling at the speed of light. The null string satisfies $g(X_{\text{null}}) = 0$, so that one has divergent energy density. To extract meaningful quantities one thus needs to expand around the null configuration

$$X^M = X^M_{\text{null}} + \epsilon \delta X^M_{(1)} + \epsilon^2 \delta X^M_{(2)} + ... \tag{3.20}$$

where ϵ is a book-keeping parameter that will eventually be sent to $\epsilon = 1$. We also need to fix the gauge by selecting the worldsheet coordinates as $\tau = t$ and σ via the conditions $\partial_\tau X_{\text{null}} \cdot \partial_\sigma X_{\text{null}}$ and $\delta X^M_{(n)} = \{0, \delta x_{(n)}, 0, 0, 0\}$. We need then to solve the string equations (3.19) perturbatively in ϵ, end for which we construct first the null string solutions. Each null geodesic can be labelled by σ and parametrized by time t. The congruence of geodesics build up a null string, which can be written as $X^M_{\text{null}} = \{t, x_{geo}(t, \sigma), 0, 0, u_{geo}(t, \sigma)\}$ and

imply that the null geodesic equations for x_{geo} and u_{geo} are

$$\frac{\partial}{\partial t}\left(\frac{1}{f}\frac{\partial x_{geo}}{\partial t}\right)+\frac{1}{2f}\left(1+\frac{1}{f^2}\left(\frac{\partial u_{geo}}{\partial_t}\right)^2\right)\frac{\partial f}{\partial x}=0 \tag{3.21}$$

$$-f+\left(\frac{\partial x_{geo}}{\partial t}\right)^2+\frac{1}{f}\left(\frac{\partial u_{geo}}{\partial t}\right)^2=0\,. \tag{3.22}$$

Since the function f is piecewise constant in x, we can integrate these last equations once and obtain

$$\frac{\partial x_{geo}}{\partial t}=\frac{f}{\xi} \tag{3.23}$$

$$\frac{\partial u_{geo}}{\partial t}=\frac{f\sqrt{\xi^2-f}}{\xi}\,, \tag{3.24}$$

which means that each geodesic satisfies the null trajectory

$$\frac{\partial u_{geo}}{\partial x_{geo}}=\sqrt{\xi^2-f}\,, \tag{3.25}$$

where $\xi(\sigma)$ is a constant of integration that is piecewise time independent in each interval. In the region $x<0$ where $f=1$ one readily obtains

$$x_{geo}=t\,\mathrm{cos}\sigma+x_0,\; u_{geo}=t\,\mathrm{sin}\sigma+u_0\,. \tag{3.26}$$

Here we can identify σ as the angle of the geodesic trajectory in the half-plane $(x,u>0)$, being $\sigma_*\equiv\mathrm{min}(\sigma)$ the one labelling the endpoint geodesic.

In the region $0<x<L$ the geodesic equation is solved by

$$x_{geo}=\frac{u_h^2}{u_{in}}{}_2F_1(\tfrac{1}{4},\tfrac{1}{2};\tfrac{5}{4};\tfrac{u_h^4}{\zeta u_{in}^4})-\frac{u_h^2}{u_{geo}}{}_2F_1(\tfrac{1}{4},\tfrac{1}{2};\tfrac{5}{4};\tfrac{u_h^4}{\zeta u_{geo}^4})\,, \tag{3.27}$$

where $\zeta\equiv 1/(1-\xi_0^2)$, with ξ_0 being the integration constant in the range $0<x<L$ as derived from the geodesic equations. Here, ${}_2F_1$ is the Gauss hypergeometric function. In the region $x>L$, we again have $f=1$ and the solution asymptotically corresponds to the expanding semicircular arc of region $x<0$ with a large endpoint angle $\bar{\sigma}_*>\sigma_*$ (more

details on this feature and its physical implications in [89]. In this sense, the end of the slab is seen from $x \gg L$ as a point-source emitter for null geodesics in the (x, u) plane just as $x = X_0$ and $u = u_0$ was.

We can now look into the first order perturbations $\delta x_{(1)}$ which, up to $\sqrt{\epsilon}$ corrections, give for the worldsheet energy densitiy and flux

$$\pi_0^0 = -\frac{T_0\,\xi\,\partial_\sigma u_{geo}}{u_{geo}^2}\sqrt{\frac{-\xi}{2\epsilon\,\partial_t \delta x_{(1)}}}, \qquad \pi_0^\sigma = 0\,. \tag{3.28}$$

This result implies that according to (3.19) the equation of motion for $\delta x_{(1)}$ is just $\partial_t \pi_0^0 = 0$, meaning that π_0^0 is time independent and energy is transported along geodesics with $\sigma =$ const.. In order to know the energy density as a function of σ, we use that in $x < 0$ region $\delta x_{(1)}$ has to satisfy

$$\partial_t^2 \delta x_{(1)} + \frac{2(t\,\text{sin}\sigma - u_0)}{t\,\text{sin}\sigma + u_0}\partial_t \delta x_{(1)} = 0\,, \tag{3.29}$$

whose solution reads

$$\delta x_{(1)} = \phi(\sigma) + \frac{\text{sin}\sigma(3t\,\text{sin}\sigma(t\,\text{sin}\sigma + u_0) + u_0^2)}{3(t\,\text{sin}\sigma + u_0^3)}\,\Psi(\sigma)\,, \tag{3.30}$$

where $\Phi(\sigma)$ and $\Psi(\sigma)$ are arbitrary smooth functions, with the constrain that $\Psi(\sigma_*) = 0$ due to the requirement that the endpoint moves at the speed of light. One then gets

$$\pi_0^0 = -T_0\,\text{csc}^2\sigma\sqrt{\frac{\text{csc}2\sigma\,\text{sin}\sigma}{\epsilon\,\Psi(\sigma)}} + \mathcal{O}(\sqrt{\epsilon})\,. \tag{3.31}$$

We introduce next the maximal stopping distance x_{stop}, the distance at which the endpoint of the string and hence the whole of it falls below the horizon, something that would eventually happen for $L \to \infty$. In the dual gauge theory, this is the distance a jet can penetrate in the plasma before completely thermalizing. This distance corresponds to

$$x_{stop} = -u_h\,{}_2F_1(\tfrac{1}{4}, \tfrac{1}{2}; \tfrac{5}{4}; \tfrac{1}{\zeta(\sigma_*)}) + \frac{u_h^2}{u_{in}(\sigma_*)}\,{}_2F_1(\tfrac{1}{4}, \tfrac{1}{2}; \tfrac{5}{4}; \tfrac{u_h^4}{\zeta(\sigma_*)u_{in}(\sigma_*)^4})\,. \tag{3.32}$$

From now on we will focus on the limit $x_{stop} \gg u_h$, which requires that $\sigma_* \ll 1$. For the case of our interest, a jet that traverses the plasma without losing all its energy, we need to

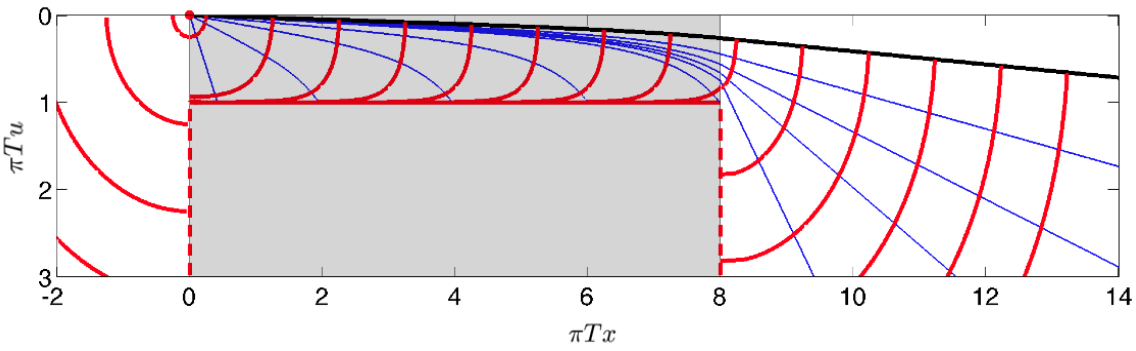

Figure 3-1: This picture shows different snapshots of the evolution of the string profile (red curves) in the (x, u) plane as time goes by. The string is created very close to the boundary ($u = 0$) and then expands. Some of the geodesics (blue lines) whose congruence build up the string fall into the black hole horizon before the string exits the slab, which translates into energy loss. The distance at which even the endpoint (black trajectory) is absorbed by the black hole is called the stopping distance x_{stop} and depends on the energy E of the string and the temperature T of the black hole.

know which are the geodesics that fall in the horizon at a certain distance x, a function we define as $\sigma_h(x)$. This corresponds to the solution of

$$x = -u_h \, {}_2F_1(\tfrac{1}{4}, \tfrac{1}{2}; \tfrac{5}{4}; \tfrac{1}{\zeta(\sigma)}) + \frac{u_h^2}{u_{in}(\sigma)} {}_2F_1(\tfrac{1}{4}, \tfrac{1}{2}; \tfrac{5}{4}; \tfrac{u_h^4}{\zeta(\sigma) u_{in}(\sigma)^4}) \,, \tag{3.33}$$

so that $\sigma_h(x_{stop}) = \sigma_*$. We can then compute the outgoing and ingoing energy of the string as the contribution of all the geodesics above the horizon at the exit and entrance of the string in the slab of plasma respectively as

$$E_{out} = -\int_{\sigma_*}^{\sigma_h(L)} d\sigma \, \pi_0^0, \qquad E_{in} = -\int_{\sigma_*}^{\sigma_h(0)} d\sigma \, \pi_0^0 \,. \tag{3.34}$$

By assuming $u_0 \to 0$ (strings created near the boundary) and $\sigma_* \ll 1$ (initial momentum in the x direction) we see from (3.31) that $\pi_0^0(\sigma)$ becomes very concentrated near $\sigma = \sigma_*$. If we expand $\Psi(\sigma) = \Psi'(\sigma_*)(\sigma - \sigma_*) + \mathcal{O}((\sigma - \sigma_*)^2)$, we get the leading order expression for the energy density

$$\pi_0^0 = \frac{-T_0}{\sigma^2 \sqrt{2\epsilon \, \Psi'(\sigma_*)(\sigma - \sigma_*)}} \,. \tag{3.35}$$

With these ingredients we can then obtain the fractional energy lost by the high energy

parton as it propagates through the slab as

$$\frac{E_{out}}{E_{in}} = \frac{\hat{\sigma}_h(0)\left(\sqrt{\hat{\sigma}_h(L)-1}+\hat{\sigma}_h(L)\cos^{-1}\sqrt{\frac{1}{\hat{\sigma}_h(L)}}\right)}{\hat{\sigma}_h(L)\left(\sqrt{\hat{\sigma}_h(0)-1}+\hat{\sigma}_h(0)\cos^{-1}\sqrt{\frac{1}{\hat{\sigma}_h(0)}}\right)}\,, \tag{3.36}$$

where $\hat{\sigma}_h(x) \equiv \sigma_h(x)/\sigma_*$. In the phenomenologically interesting situation where the energetic pair of quarks is created just next to the slab of plasma (meaning fixed x_0, with $u_0 = 0$ and $\sigma_* \to 0$) one finds that the stopping distance is

$$x_{stop} = \frac{u_h \Gamma(\frac{1}{4})^2}{4\sqrt{\pi\sigma_*}} + (x_0 - u_h) + \mathcal{O}(\sqrt{\sigma_*})\,, \tag{3.37}$$

which means that for small enough σ_* one can approximate $\sigma_* = \mathcal{O}(u_h^2/x_{stop}^2)$. Given that the energy of the string is greatest near the endpoint, to leading order in σ_* (3.34) gives for the initial energy

$$E_{in} = \frac{\pi T_0}{2\sigma_*^{3/2}\sqrt{2\epsilon\,\Psi'(\sigma_*)}}\,, \tag{3.38}$$

yielding a relation between the initial energy and the stopping distance as

$$x_{stop} = \frac{\pi^{4/3}\mathcal{C}}{\pi T}\left(\frac{E_{in}}{\sqrt{\lambda}\pi T}\right)\,, \tag{3.39}$$

where we used $T_0 = \frac{\sqrt{\lambda}}{2\pi}$, $u_h = 1/\pi T$ and the constant $\mathcal{C}$, which for optimally prepared jets (the ones with the highest survival rates) is approximately $\mathcal{C} \simeq 0.526$, was analytically calculated in [85]. Now, by considering a slab of plasma with $L < x_{stop}$ and taking into account all mentioned assumptions, (3.37) implies $\hat{\sigma}_h(L) = \left(\frac{x_{stop}}{L}\right)^2$, which we can insert in (3.36) in order to differentiate with respect to L and obtain

$$\frac{1}{E_{in}}\frac{dE_{out}}{dL} = -\frac{4L^2}{\pi x_{stop}^2\sqrt{x_{stop}^2 - L^2}}\,. \tag{3.40}$$

This equation exhibits a path length dependence that is reminiscent of a Bragg-like peak, in which most of the energy is lost suddenly in a final burst. One can understand this behaviour from the fact that most of the energy is concentrated at the endpoint, the segment

of the string that is the last to thermalize. The energy loss rate in (3.40) is a good approximation to the situation depicted in Fig. 3-1, and can be used to deduce the lost energy by a quark traversing a supersymmetric strongly coupled plasma. Taking insights from these results one can model the energy loss rate of partons in a QCD plasma instead, taking into account the expected differences, due for instance to the different number of degrees of freedom between the two theories.

The motion of the string through AdS-BH, and specially the deposition of energy into the black hole, produce metric perturbations δg_{MN} whose near boundary behaviour encodes the stress tensor of the quark $T_{\mu\nu}$. This information can be used to track where the lost energy from the quark went to, as done first in [90] for the heavy quark. In Chapter 7 in Part II we incorporate this ideas by a simple computation of the medium response to the jet passage assuming small perturbations in order to account for overall energy momentum conservation. This is a very important piece of physics that brings together our understanding of jet energy loss and its effects on the rest of the system.

Part II

The Hybrid Model for Jet Quenching

Chapter 4

A Hybrid Strong/Weak Coupling Approach to Jet Quenching

One of the most striking results obtained from heavy ion collisions at the Large Hadron Collider (LHC) is the strong suppression of high energy jets observed in Pb-Pb collisions with a center of mass energy of 2.76 TeV per nucleon-nucleon collision [20, 21]. This suppression, commonly referred to as jet quenching, is due to the energy loss suffered by the components of the jets on their way out of the hot QCD medium formed in a high energy heavy ion collision. The phenomenon of jet quenching was discovered prior to the LHC measurements, without reconstructing individual jets, primarily via the strong reduction in the number of intermediate-p_T hadrons in heavy ion collisions at RHIC relative to proton-proton collisions [91, 92]. Jet quenching has come to be seen as one of the most powerful experimentally accessible tools with which to analyze the properties of deconfined QCD matter. The large magnitude of the effects of energy loss observed in heavy ion collisions at the LHC, together with the ability to study the effects of energy loss on many properties of individually reconstructed jets, increases the potential of these probes to provide accurate medium diagnostics, provided the mechanism by which they interact with the medium can be understood with sufficient precision.

One of the reasons why high energy jets are superior to other probes is that their production occurs at very high energy scales, $Q \gg \Lambda_{QCD}$, which guarantees that their production spectrum is under good theoretical control, since it can be determined via perturbative

QCD. Similarly, many of the properties of jets in vacuum are also controlled by physics at high energy scales and are therefore well understood theoretically. Therefore, observed deviations of those properties in a heavy ion environment must be due to the interaction of the different jet components with the hot hadronic medium that the nascent jet traverses on its way out of the collision zone. In general, the interaction with the medium constituents will lead to the degradation of the jet energy, but the precise mechanism or mechanisms by which this occurs depend on the nature of the medium.

Although the production of a hard parton that will become a jet, and the fragmentation of that parton as it propagates, are controlled by weakly coupled physics at high momentum scales, the physics of the medium produced in experimentally realizable heavy ion collisions is not weakly coupled. At sufficiently high temperatures the quark-gluon plasma must be a weakly coupled plasma of quark and gluon quasiparticles. However, in the temperature range explored by current colliders, namely $T \sim 150 - 600$ MeV, we know from the comparison of more and more precisely measured experimental observables to more and more sophisticated calculations of relativistic viscous hydrodynamics that the quark-gluon plasma produced in heavy ion collisions is a droplet of strongly coupled liquid that expands and flows collectively, hydrodynamically (For a review, see Ref. [93]). This fact makes the quark-gluon plasma a very interesting form of matter that has attracted the interest of scientists in other fields in which other forms of strongly coupled matter arise. However, this fact also complicates the theoretical understanding of the properties and dynamics of the medium rather significantly. For this reason, in recent years there has been a growing interest in strongly coupled techniques that can shed light on the dynamics of the liquid plasmas that arise as the hot deconfined phases of other non-Abelian gauge theories which have holographically dual descriptions as gravitational theories in $4+1$-dimensional spacetimes containing a black hole horizon. The simplest example to which this gauge/gravity duality has been applied is the plasma that arises at nonzero temperature in strongly coupled $\mathcal{N} = 4$ supersymmetric Yang Mills (SYM) theory in the limit of a large number of colors N_c. Holographic analyses performed in this and other gauge theories have led to many qualitative insights into the properties of the QCD plasma, its dynamics in heavy ion collisions, and the dynamics of probe particles propagating through the strongly coupled

plasma. (See Ref. [67] for a review).

The way in which a high energy excitation interacts with a deconfined non-Abelian plasma is well understood in two extreme, and unrealizable, limits. At weak coupling, by which we mean at unrealizably high temperatures at which the coupling constant at the medium scale is small, perturbative analyses show reliably that the dominant mechanism of in-medium energy loss is the radiative process of stimulated gluon emission caused by the scattering of the high energy parton off particles in the medium [38, 40, 43, 41, 44, 45]. The rate of emission of these radiated gluons forms the basis of most current analysis of jet modification in the environment produced in heavy ion collisions. (See Refs. [52, 50, 94, 95] for reviews.) In addition, many of these studies also include a second energy loss process, that is in principle subleading for very high energy partons, namely the elastic transfer of energy to medium constituents, referred to as collisional energy loss [47]. The second unrealizable limit is the limit in which the coupling constant is assumed to be large at all relevant energy scales. In this case, gauge/gravity duality has made it possible to use holographic calculations to analyze the way in which varied energetic probes have their energy degraded, and are otherwise modified, as they propagate through strongly coupled plasma [73, 96, 97, 98, 78, 75, 79, 80, 99, 100]. (For a review, see Ref. [67].) These computations provide detailed dynamical information on the energy loss processes in this limit. The intuition that comes from these calculations is phrased in terms of the dual gravitational description, rather than in terms of gauge theory degrees of freedom. While these two extremes each provide invaluable guidance to understanding energy loss processes in a heavy ion environment, because the medium is strongly coupled while much of the physics of jets is governed by weakly coupled high momentum physics, at least as they are currently constituted neither approach can capture all important aspects of the dynamics.

The main difficulty in understanding jet dynamics in a strongly coupled QCD medium resides in the interplay between physics at very different energy scales. After their production via a (very) hard scattering, jets relax their large initial virtuality down toward the hadronic scale via an evolution process of branching into a shower of partons. In vacuum, this fragmentation process is governed by the Dokshitzer-Gribov-Lipatov-Altarelli-Parisi

(DGLAP) equation. This perturbative process is crucial to understanding most jet properties. In the medium, this evolution occurs while at the same time partons in the developing shower suffer many soft exchanges of momenta of order the medium temperature T, which alter the fragmentation pattern. Since the momenta transferred in these interactions are not large, this physics is not weakly coupled just as the physics of the medium itself is not weakly coupled. This means that a part of the dynamics of jets propagating through the medium produced in a heavy ion collision is out of the regime of validity of perturbative QCD. Thus, jets are multi-scale probes sensitive to both strongly and weakly coupled physics. In the long run, their description in controlled calculations will require either a strongly coupled approach to far-from-equilibrium dynamical processes in QCD or calculations done via gauge/string duality that incorporate asymptotic freedom at short distance scales or both. As, at present, neither seems on the horizon we must limit our goals. A successful phenomenological model that describes the modifications of jets in the medium, today, must be a hybrid model in which one can simultaneously treat the weakly coupled physics of jet production and hard jet evolution and the strongly coupled dynamics of the medium and the soft exchanges between the jet and the medium. In this work, we will put forward a phenomenological approach which combines different physics mechanisms at different scales. While there have been other attempts to combine results obtained from weak and strong coupling [101, 102, 103, 104], our approach is distinct since it focusses on using different calculational frameworks at the different energy scales.

This Part of the thesis is organized as follows: we describe how we set up our hybrid approach in Section 4.1. The interaction of partons with a strongly coupled medium is reviewed in Section 4.2. In Section 4.3 we discuss how to implement these ideas in a simple Monte Carlo simulation of jets in heavy ion collisions, using a hydrodynamic description of the spacetime dynamics of the medium. We use this implementation of our hybrid approach to determine several jet observables, which we confront with data on jet $R_{\rm AA}$, the dijet asymmetry and jet fragmentation function ratios in Chapter 5. In Chapter 6 we further test our model against boson-jet observables, such as photon-jet and Z^0-jet, and present predictions for the center of mass energy of run 2 at LHC. We also introduce a

new observable, the ratio of inclusive over associated jet fragmentation functions, which shows a strong dependence on the precise energy loss mechanism. In Chapter 7 we extend our hybrid model with the inclusion of broadening and medium back-reaction. We then compare against intra-jet structure observables and other more recent observables in which the long-range correlations between a dijet system and the rest of the event can be studied.

4.1 Motivation

As we have stressed in the preceding Introduction, no single theoretical framework is currently available within which controlled calculations of all important aspects of jet quenching in heavy ion collisions can reliably be carried out. This is so since we must simultaneously describe the perturbative dynamics at short distances and the strongly coupled physics at the medium scale. We will therefore resort to phenomenological modeling of the main physical processes occurring during the propagation of high energy partons through strongly coupled plasma. To simplify our analysis, we will focus on high energy, high virtuality jets, since a large separation between the hard and medium scales allows us to better separate the treatment of these two regimes. In this Section, we will spell out and motivate the main assumptions behind our model.

Our first assumption is that the exchange of momentum with the medium, which in the absence of coherence effects among several plasma constituents is of the order of the temperature T, is smaller than the virtuality of any of the jet partons at any stage of the evolution. For sufficiently high energy jets, this assumption is certainly valid at the early stages of the evolution process, but it becomes more questionable at the late stages, when the evolution approaches the hadronization scale. Fortunately, these late stages also happen at later times, when almost all the partons in the shower are outside of the medium [105]. Since these small momentum exchanges cannot lead to a significant variation of a parton's virtuality, we will assume that the splitting kernel at each point in the evolution is as in the vacuum. This motivates our second assumption: because each splitting that occurs as the original parton fragments happens at smaller distance scales than the medium can resolve, we assume that the splitting probabilities are as in vacuum. Keeping the splitting kernel

unmodified implies, in particular, that, in a probabilistic approach, the emission probability at each step in the Markovian chain remains independent of the medium dynamics.

It will be important to return to the second assumption above in future work for at least two reasons. First, we will be assuming that the splitting probability is unmodified even as the partons lose some of their energy and will thus be neglecting the fact that even in vacuum the splitting kernel depends on parton energy (through Sudakov logs, which is to say via the phase space for splitting). Second, we will be neglecting the possibility of additional splitting induced by multiple soft exchanges with the strongly coupled plasma, which accumulate into a hard momentum transfer. As such an effect is known to be important in a weakly coupled plasma with point-like constituents, it will, in the future, be interesting to investigate how to incorporate it within the hybrid model we are setting up in the present work. However, assuming the physics at the medium scale to be strongly coupled, as we shall do throughout, renders any such weakly coupled large momentum transfer processes, and their modification, subleading in their consequences.

We now wish to apply a prescription for how much energy each parton in the shower loses as it propagates through the medium. That means that we need to know the temperature of the medium in which a particular parton in the shower finds itself, which in turn means that we need to know where each parton in the shower is in space and time. The DGLAP evolution equations that describe the fragmentation of the parent parton and the evolution of the resulting shower are derived in perturbative QCD in momentum space. They contain little information about how the process of showering, and the attendant relaxation in the virtuality of the individual partons in the shower, develops in space and time. This space-time information is unimportant in vacuum physics, since the partonic components of the jet do not interact with anything; all they do is fragment and in describing the jet in the final state it is completely unimportant where and when each splitting happened. However, in a heavy ion environment before the shower emerges from the medium every parton in the shower interacts with the medium, and the medium itself changes as a function of space and time. We therefore need to know where and when each splitting occurs. Based on the analysis of soft gluon emission, most jet Monte Carlo studies assign a time to each rung of the evolution equation related to the formation time of the emitted

gluon $\tau_f = 2\omega/k_\perp^2$. However, the detailed implementation varies from one Monte Carlo implementation to another, which gives a sense of the theoretical uncertainty concerning the space-time evolution that is common to all in-medium event generators. In this work, we will use the prescription of Ref. [105] and assign a life-time to each rung of the decay chain (*i.e.* to each parton in the shower) determined from their virtuality Q and energy E as

$$\tau = 2\frac{E}{Q^2}\,, \tag{4.1}$$

with the factor of two chosen such that in the soft limit it coincides with the standard expression for the formation time. We will also assume that the strong virtuality ordering in the QCD shower translates into time ordering, with the hardest splittings occurring first. This implies that the later stages of the evolution, for which the virtuality is closer to the hadronization scale, occur at later times.

In between any of the virtuality relaxing splittings, the partons in the jet propagate through the strongly coupled plasma. The momenta exchanged between these partons and the medium is of order the medium temperature, and therefore, for plasma temperatures not far above the deconfining transition, these momentum exchanges are not weakly coupled processes. This is where strongly coupled dynamics plays a role. From the point of view of the jet shower, the medium takes energy away from each of the propagating partons and rapidly turns that energy into heating of, and collective motion of, the medium itself – which is to say extra soft particles in the final state, moving in random directions (as a first approximation). This directly yields a reduction in the overall energy of the jet. This is in stark contrast with the perturbative mechanism of radiative energy loss, where energy is lost through medium induced radiation of gluons with momenta that are well above the medium scale and that are typically almost collinear with the initial hard parton when they are produced. This radiative loss of energy by the hard parton translates into a loss of energy for the jet in the final state only if the radiated gluons are either (atypically) produced at large angles relative to the direction of the hard parton or if the radiated gluons are deflected by their further interactions with the medium [106, 107].

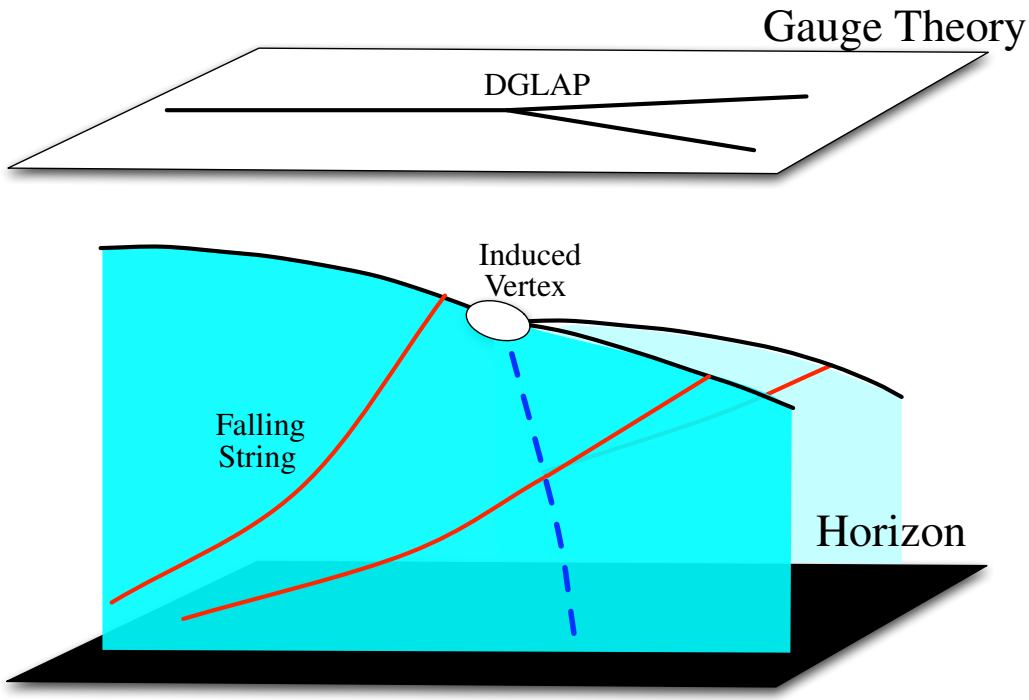

Figure 4-1: Sketch of two views of the interaction of a high energy jet with the strongly coupled plasma. In the gauge theory, represented by the white plane at the top of the figure, an energetic virtual parton propagates through the medium, loses energy, and splits via (vacuum) DGLAP evolution. There is no (easy) way to describe the strong soft interactions between the partons and the medium in this representation. In the dual gravitational view, represented below, the soft interactions are represented by a string trailing behind each parton, transporting energy from the parton "down" to the horizon which is represented by the black plane at the bottom of the figure. The parton itself, represented by the endpoints of the string which is to say by the black lines, is also pulled "downward" toward the horizon. In this representation, there is no (easy) way to describe the splitting of one string into two, which is to say the hard splitting process in the gauge theory. In the picture we represent the splitting vertex at which one string becomes two by a white oval below which a hypothetical string-splitting curve shown as a blue dashed line trails. At present there is no known calculation underlying these aspects of the figure.

In a nutshell, we shall assume that no hard radiative processes occur between the DGLAP vertices and that the dynamics of these partons in the plasma is analogous to that of energetic objects propagating through the strongly coupled plasma in a gauge theory with a dual gravitational description. While the theories that possess a gravity dual do not yet include QCD, we will utilize the powerful ideas of the duality to gain qualitative understanding of the relevant strongly coupled dynamics, an approach that has proved useful in many contexts. (See Ref. [67] for a review.) However, keeping in mind that these calculations are not done in QCD itself, we will use the explicit results obtained via holographic calculations only as indicative, specifically by keeping all of their parametric dependences while introducing one free dimensionless parameter that we shall fit to data. We shall describe how we do this in concrete terms over the course of Sections 4.2 and 5.

One important aspect of how we set up our hybrid model is minimalism. We will keep, as much as possible, only well-understood weakly coupled and strongly coupled physics and introduce as few as possible (in fact only one for the first exploratory analysis) phenomenological parameters that govern how we put the two together and that need to be fixed by fitting to data.

The underlying picture that we are putting forward in this work is sketched in Fig. 4-1. In the gauge theory, any of the partons of the jet which propagate in plasma may suffer a hard splitting, governed by the DGLAP equations. In addition to these hard splittings, these partons possess associated soft fields that interact strongly with the medium. These have a natural interpretation in a dual gravitational representation: they are strings trailing behind the quark, which is represented by the end point of the string. As noted in Ref. [78] the string end point itself does not live on the boundary of the spacetime, but "falls" downward, away from the boundary and toward the horizon, as the system evolves. In the gravitational representation, the trailing strings carry energy from the quarks "down" toward the horizon. This represents the process by which each quark loses energy, energy which subsequently thermalizes, making a little more or a little hotter plasma. Reading the figure from left to right, one string enters from the left, with its shape controlled by well-understood gravitational dynamics that describes how the single quark represented by its endpoint loses energy. Next, a perturbative hard splitting, described in the gauge theory by

DGLAP, occurs. It is not presently known whether, and if so how, this splitting process can be described in the gravitational representation. The gravitational description must be supplemented by some induced vertex and an associated line along which string world sheets merge, but the form of this vertex and string merging line are not known. Nevertheless, the gauge theory representation demands that after this splitting process, we have two string end points below each of which a string trails. In fact, if one of the daughter partons is a gluon, a double string must be formed, trailing below the corresponding endpoint. So, somehow, the single incident string worldsheet splits into the several world sheets that describe the decay products of the DGLAP splitting. Again, we describe this process in the gauge theory because it is not known how to describe it gravitationally.

Since splitting processes happen at short distances, the induced vertex must occur first as close as possible to the boundary, *i.e.* where the string end point splits, and only later propagate toward the horizon as represented in Fig. 4-1 by the blue dashed line. This can also be interpreted as a delay in the ability of softer modes to resolve the splitting of color charges. Nevertheless, since the geodesic distance in AdS from the horizon to the boundary is finite, of order $1/(\pi T)$, after this short time the string world-sheet is fully split and each of the objects propagate independently through the strongly coupled plasma.[1] After the transient behavior associated with the splitting, the energy loss of each of the daughter partons in the strongly coupled plasma is described by the dynamics of their own trailing string — until each of the daughters itself splits at a new hard vertex, and the process iterates. We are far from providing a firm theoretical footing for the hybrid physical picture we have described. Each half of the hybrid is built upon solid ground, but different solid ground. In this work, we will explore the phenomenological consequences of these ideas in a simplified model implementation which we hope captures the main features of some future complete computation.

[1] Here, we are describing a delay of order $1/(\pi T)$ in the response of the energy loss process to a sudden change in the nature of the object losing energy, namely the splitting process. In Ref. [108] a similar delay time, also of order $1/(\pi T)$, arises (and is analyzed quantitatively) in the case where the object losing energy (a heavy quark being dragged at constant velocity) is unchanged but the temperature of the strongly coupled medium changes suddenly.

4.2 In-medium Energy Loss of Energetic Particles

The principal ingredient that remains to be specified in the description of our hybrid model is the rate of energy loss of energetic particles in the medium. In our model we shall apply such a prescription to each of the partons in a shower, while those partons find themselves in a medium with local temperature T, with T varying as a function of space and time. In this Section, we specify the different prescriptions for energy loss that we have investigated by giving them for the case of a single energetic parton propagating through a medium with constant temperature T. Our principal goal is of course to investigate the validity of the hybrid strong/weak coupling approach to jet quenching that we have described, in which the shower develops according to a weakly coupled prescription and each parton in it loses energy according to a strongly coupled prescription. However, to provide benchmarks for our computations we shall also try employing weakly coupled prescriptions for how each parton in the shower loses energy in our formalism and compare results obtained in this way to the results we obtain in our hybrid strong/weak coupling model. In the two subsections below we specify the details of the strongly coupled and weakly coupled expressions for parton energy loss that we shall employ.

4.2.1 Parton energy loss at strong coupling from falling semiclassical strings

In Section 3.3, we have discussed the physics and sketched the derivation of the holographic energy loss rate that we adopt for the description of the strongly coupled dynamics of the jet/plasma interplay. Here we briefly review those results in order to put them into the context of our interest: a realistic modelling of jet quenching physics at actual heavy ion accelerators.

In Refs. [78, 87], a pair of high energy 'quark jets' in the fundamental representation of the gauge group are produced moving in opposite directions. In Ref. [87] the setup is such that one of the 'quark jets' is incident upon a 'slab' of strongly coupled plasma with temperature T, that is finite in extent with thickness x. The dual gravitational description of

the 'quark jet' is provided via a string whose endpoint falls downward into the bulk, as in the left portion of the sketch in Fig. 4-1. After propagating for a distance x through the plasma the string, which is to say the quark, emerges into vacuum. The energy E of the 'quark jet' that emerges from the slab of plasma, as well as its other properties, can be compared to the initial energy $E_{\rm in}$ of the parton incident upon the slab and to the properties of the 'jet' that would have been obtained had their been no slab of plasma present [87]. For our purposes, we are interested in how the energy of the 'quark jet' depends on x, which is to say the rate of energy loss dE/dx, whose precise form was derived in Section 3.3. If the high energy 'quark' is produced next to the slab, meaning that it enters it immediately without first propagating in vacuum, and if the thickness of the slab is large enough that initial transients can be neglected, meaning $x \gg 1/(\pi T)$, the rate of energy loss is independent of many details of the string configuration and takes the form [87]

$$\frac{1}{E_{\rm in}}\frac{dE}{dx} = -\frac{4}{\pi}\frac{x^2}{x_{\rm stop}^2}\frac{1}{\sqrt{x_{\rm stop}^2 - x^2}} \tag{4.2}$$

where $E_{\rm in}$ is the initial energy of the 'quark', as it is produced and as it is incident upon the slab of plasma and where $x_{\rm stop}$ is the stopping distance of the 'quark'. Since $E \to 0$ as $x \to x_{\rm stop}$, the expression (4.2) is only valid for $1/(\pi T) \ll x < x_{\rm stop}$. The parametric dependence of $x_{\rm stop}$ on $E_{\rm in}$ and T was obtained previously in Refs. [75, 78]. For a string whose initial state is prepared in such a way as to yield the maximal stopping distance for a 'quark' produced with a given $E_{\rm in}$ propagating through the strongly coupled $\mathcal{N} = 4$ SYM plasma with temperature T, it is given by

$$x_{\rm stop} = \frac{1}{2\,\kappa_{\rm sc}}\,\frac{E_{\rm in}^{1/3}}{T^{4/3}}\,, \tag{4.3}$$

where we have introduced a dimensionless constant $\kappa_{\rm sc}$, the subscript signifying "Strong Coupling", that in the calculation of Ref. [78] is given by $\kappa_{\rm sc} = 1.05\,\lambda^{1/6}$, with λ the ´t Hooft coupling. In the case of a slab of plasma in which T, and therefore $x_{\rm stop}$ is constant, the energy loss rate (4.2) can easily be integrated to obtain $E(x)$ [87]. We shall be describing the energy loss of partons in a shower that are propagating through a medium

whose temperature is changing as a function of space and time as in a heavy ion collision; in this context what we need from Ref. [87] is dE/dx, namely (4.2).

The energy loss rate Eq. (4.2) has two characteristic features that distinguish it parametrically from analogous perturbative expressions that describe the energy loss of a single hard parton propagating through (a slab of) weakly coupled plasma with temperature T, expressions that we shall provide in the following subsection. First, while x is not yet comparable to $x_{\rm stop}$ the rate of energy loss dE/dx is independent of $E_{\rm in}$ and grows rapidly with x, with a characteristic x^2 dependence. Later, though, once x has become comparable to $x_{\rm stop}$ we see that dE/dx depends in a nontrivial (*i.e.* non-power-law) way on both $E_{\rm in}$ and x and grows rapidly, diverging as $x \to x_{\rm stop}$ and $E \to 0$. We note that in spite of the simple relation between $E_{\rm in}$ and the stopping distance $x_{\rm stop}$, the parametric dependence of the energy loss rate on the path length x is intricate, deviating from a simple power of the length very substantially at late times.

The energy lost by the energetic parton propagating through the strongly coupled plasma is quickly converted into hydrodynamic excitations with wave vectors $q \sim \pi T$ and smaller. This happens over a very short time $1/\Gamma_1$, with $\Gamma_1 = 2\pi T \sim T/0.16$ the width of the lowest non-hydrodynamical quasinormal mode of the strongly coupled plasma, determined in the dual gravitational theory in Ref. [109]. The hydrodynamic excitations are, in turn, dissipated as heat after a damping time $3Ts/(4q^2\eta)$ (for sound waves) or $Ts/(q^2\eta)$ (for diffusive modes) [110]. If we take the shear viscosity to entropy density ratio to be $\eta/s \sim 2/(4\pi)$, hydrodynamic modes with $q \sim \pi T$ dissipate over a time $\sim (0.5-0.6)/T$. Longer wavelength modes live longer. This means that most of the 'lost' energy rapidly becomes part of the plasma, thermalizing and resulting in a little more, or a little hotter, plasma. From an experimental point of view, the lost energy becomes extra, soft, hadrons with momenta $\sim \pi T$. These extra hadrons will be uniformly distributed in angle, on average, if the passage of the jet does not induce any substantial collective motion of the plasma, an assumption we will make for now.

Because we shall focus on reconstructed jet data, which is to say measurements of the components of the jet that emerge from the plasma, we shall make no attempt to track the lost energy in our hybrid model. Of course, since the 'lost' energy ends up as soft hadrons

going in *all* directions, some of it *will* end up in the jet cone. We will make no attempt to add soft hadrons corresponding to some of the lost energy to the jets in our model. The reason that we make no such addition to our jets is that when experimentalists reconstruct jets from data, they use some background subtraction procedure designed to remove soft hadrons that are uncorrelated with the jet direction, for example subtracting an $\eta \leftrightarrow -\eta$ reflection of the event from the real event. This means that if the 'lost' energy ends up perfectly uniformly distributed in angle, it will be subtracted during the jet reconstruction procedure. If this assumption is correct, the 'lost' energy does not appear in the jets as reconstructed by the experimentalists. We therefore make no attempt to add it to the jets we obtain from our model. We leave to Section 7 the investigation of fluctuations and collective flow that can in fact result in the 'lost' energy that is deposited in the jet cone not being fully removed during the background subtraction, meaning that some of it ends up being counted as a part of the jet. The uncertainty associated with these considerations means that when we compute jet fragmentation functions in Section 5.3, they may not be reliable for components of the jet with momenta of order 1-2 GeV.

Although the energy loss rate dE/dx in (4.2) was derived within the string-based computation of Refs. [78, 87], the parametric dependence of the stopping distance for excitations with the maximum possible stopping distance for a given energy $E_{\rm in}$ given by the expression (4.3) is common to both ways of describing high energy excitations in the plasma discussed above, which makes it seem a robust expectation from strong coupling computations within the gravitational description of large-N_c $\mathcal{N} = 4$ SYM theory. In contrast, the explicit value of the dimensionless constant $\kappa_{\rm sc}$, and even its dependence on the ´t Hooft coupling, are not robust in the same sense. There is every reason to expect that the numerical value of $\kappa_{\rm sc}$ will be smaller in the strongly coupled QCD plasma than in the strongly coupled $\mathcal{N} = 4$ SYM plasma. And, even in the latter theory, the calculations of Refs. [79, 80] indicate a value $\kappa_{\rm sc}$ that is $\mathcal{O}(1)$, *i.e.* finite in the $\lambda \to \infty$ limit, rather than $\mathcal{O}(\lambda^{1/6})$ as in the string-based calculation of Ref. [78]. We shall return to this point in Section 7.3 when we discuss the implications of the value of $\kappa_{\rm sc}$ that we shall obtain via comparison to data in Section 5.

Both Eqs. (4.2) and (4.3) were derived for energetic particles in the fundamental repre-

sentation of the gauge group, proxies for energetic quarks propagating through the strongly coupled plasma. However, it is impossible to model hard processes in high energy hadronic collisions without also having the means with which to include energetic particles in the adjoint representation, *i.e.* energetic gluons. In our context, regardless of the identity of the initial parton produced in a hard scattering, the shower of partons that results and whose energy loss we shall be following necessarily includes both gluons and quarks. Studies of high energy particles in the adjoint representation, modeled by double strings propagating through the plasma, were initiated in Ref. [75] and have shown that these excitations also have $x_{\rm stop} \propto E_{\rm in}^{1/3}/T^{4/3}$. Within the string-based picture, because the string configuration representing an energetic gluon possesses two strings trailing behind the 'endpoint' (actually, in this case, the point where the string folds back upon itself) it is natural to expect that the stopping distance for a gluon is identical to that for a quark with half the energy of the gluon [78]. We will further interpret this factor 2 as the large N_c limit of the ratio of the Casimirs of the adjoint and the fundamental representations of the color gauge group. Given these considerations, we will assume that an energetic gluon has the same energy loss rate Eq. (4.2) but with the prefactor in the stopping distance (4.3) given by

$$\kappa_{\rm sc}{}^{G} = \kappa_{\rm sc}\left(\frac{C_A}{C_F}\right)^{1/3} \tag{4.4}$$

with $C_A/C_F = 9/4$ the ratio of Casimirs, meaning that $x_{\rm stop}$ for gluons is shorter than that for quarks with the same energy, but only by a factor of $(9/4)^{1/3}$.

Because of the small $1/3$ power, the difference between the rate of energy loss of quarks and gluons is smaller in the strongly coupled plasma than would be the case in a weakly coupled plasma. We will elaborate on the potential consequences of this observation in Section 5.5.

4.2.2 Comparison with other approaches

The realization that the physics at the medium scale is not weakly coupled has motivated several previous phenomenological attempts to implement strongly coupled computations of the in-medium interaction of high energy particles in the modeling of hard processes

in heavy ion collisions. Before we continue, it is important to compare and contrast our implementation to those in previous work.

Some early explorations were based on the straightforward use of energy loss rates based upon results derived for a single heavy or light quark traversing the strongly coupled plasma of a gauge theory with a holographic description [111, 112, 102, 113, 103, 86, 104]. These computations are all aimed at describing the suppression of the production of a single high-$p_{\rm T}$ hadron, *i.e.* the leading hadron in a jet. None of these early explorations included the calculation of jet observables; we shall analyze three complementary classes of jet observables in Section 5. These early explorations also do not include the perturbative QCD evolution of the hard virtual parton. And, as they describe single partons, they cannot address the question of how the propagation through the strongly coupled plasma does or does not modify the jet fragmentation function, a question that we shall find plays a significant role in differentiating between energy loss mechanisms. Furthermore, in some cases [112, 102, 104] the rate of energy loss of a hard parton is assumed to be a power law in the parton energy and the propagation distance, whereas we now know from Ref. [87] that this is true only for partons which do not travel a significant fraction of their stopping distance, as for those and only those partons $dE/dx \propto E_{\rm in}^0 x^2$. The complete dependence of dE/dx in (4.2) on x and $E_{\rm in}$ is very different from a power law. In other cases [103], the energy loss rate employed was based on approximations to the numerical analysis of Ref. [82], which do not coincide in any limit with the expression derived in Ref. [87]. The energy loss expressions obtained more recently in Ref. [86] are complementary, in that they are derived in the dual gravitational theory using semiclassical strings that do not satisfy standard open string boundary conditions, meaning that it remains to be determined how they can be used in the description of light quark energy loss.

Among the work that comes before ours, the study that is in many respects most similar to ours is that described in Ref. [101], although like in the previous work above this study focusses on hadronic observables rather than computing jet observables as we do. Unlike in the previous work above, this study involves a Monte Carlo implementation of a shower in which partons produced at high virtualities evolve down to a hadronic scale. However, the implementation of the strongly coupled dynamics used in Ref. [101] is very different

than our own, as it is based on an early interpretation of strongly coupled energy loss in partonic-like terms advocated in Refs. [114, 76]. In this approach, the energy loss of a hard parton in strongly coupled plasma is interpreted in the language of radiative energy loss, except with a momentum transfer from the plasma which grows linearly with propagation distance. (In the standard weakly coupled perturbative analysis of radiative energy loss, it is the square of the momentum transfer which grows linearly with propagation distance.) Based upon this earlier work, the authors of Ref. [101] assumed an energy loss mechanism in which weakly coupled high momentum gluons are radiated (as at weak coupling) but in which the momentum transverse to the jet direction that is transferred to the radiated gluons accumulates linearly with propagation distance (unlike at weak coupling). So, although we follow Ref. [101] in the sense that we are developing a hybrid model that melds together features of energy loss in a strongly coupled gauge theory with a Monte Carlo (in our case PYTHIA) implementation of perturbative splitting in a parton shower, our implementation of the strongly coupled physics is completely different than that in Ref. [101], since we (i) treat all strongly coupled processes as occurring at soft, nonperturbative, scales; (ii) use the energy loss rate derived from a complete strong coupling computation that was not yet available at the time of the study in Ref. [101]; and (iii) incorporate a feature that is by now understood to be characteristic of energy loss in a strongly coupled plasma, namely that the 'lost' energy becomes extra heat or extra plasma, which is to say soft particles whose directions are (for now) uncorrelated with the jet direction.

4.2.3 Perturbative benchmarks: radiative and collisional energy loss in a weakly coupled plasma

To gauge the sensitivity of the classes of jet measurements that we will use to constrain our hybrid approach, we wish to compare its results to those in which we replace the strongly coupled result (4.2) for the energy loss rate of a parton in the shower with a perturbatively inspired expression for dE/dx. We shall in fact use two different variants as benchmarks.

In the high parton energy limit, upon assuming weak coupling between the energetic parton and the medium the dominant mechanism of energy loss is the radiation of nearly

collinear gluons from the energetic parton that is induced by interactions between the parton and the medium. If the medium is sufficiently large that many gluons are radiated from the propagating parton, the energy loss rate for a parton in representation R is given, to leading logarithmic accuracy, by [40]

$$\frac{dE}{dx} = -\alpha_s \frac{C_R}{2} \hat{q}\, x \ , \tag{4.5}$$

with α_s and C_R being the strong coupling constant and the Casimir of the parton, and where the jet quenching parameter $\hat{q}$ is the transverse momentum squared picked up by the parton per distance travelled. While the expression (4.5) describes energy loss in the limit in which many gluons are radiated, in most phenomenological applications of radiative energy loss it is assumed that a finite number of hard gluons are emitted from the the energetic partons and Eq. (4.5) describes the average over many partons with a fixed energy. We have seen in Section 2.3 how to understand this expression from the one gluon emission rate, which already captures the interference phenomena (LPM effect) which are responsible for the x^2 parametric dependence.

By dimensional analysis, the jet quenching parameter $\hat{q} \propto T^3$. For a very weakly coupled plasma at exceedingly high temperatures, temperatures such that leading order, leading logarithm, perturbative computations are trustworthy, the jet quenching parameter is given by [115]

$$\hat{q} = C_A \alpha_s m_D^2 T \log B_{\rm rad} \ , \tag{4.6}$$

where $m_D^2 = g^2 T^2 (2N_c + N_f)/6$ is the square of the Debye screening length of weakly coupled quark-gluon plasma with N_c colors and N_f flavors, and $B_{\rm rad}$ is a jet-energy-dependent regulator that cuts off large momentum transfers to the plasma. A regulator is necessary because in a weakly coupled plasma $\hat{q}$ diverges logarithmically with the jet energy E. The precise value of $B_{\rm rad}$ is not currently known, although some authors estimate it to be $B_{\rm rad} \approx 1 + 6ET/m_D^2$. (See Ref. [115] for an extensive discussion of estimates of the value of $B_{\rm rad}$ and hence $\hat{q}$ in different approximations.) We shall ignore all logarithms, lumping them into a prefactor that we shall denote by $\kappa_{\rm rad}$, with the subscript referring to

'Radiative', and write

$$\frac{dE}{dx} = -\kappa_{\rm rad} \frac{C_R}{C_F} T^3 \, x \; , \tag{4.7}$$

with $C_R/C_F = 1$ for an energetic quark and $C_R/C_F = 9/4$ for an energetic gluon. Although below we shall treat $\kappa_{\rm rad}$ as a parameter to be fit to data, before we go on we should estimate its value in a weakly coupled plasma using the leading logarithmic order perturbative calculation, which we denote by ${\kappa_{\rm rad}}^{\rm pert}$. Combining Eqs. (4.5) and (4.6), we obtain

$${\kappa_{\rm rad}}^{\rm pert} = 2\pi C_F C_A \left(\frac{2N_c + N_f}{6} \right) \alpha_s^3 \log B_{\rm rad} \, . \tag{4.8}$$

For later reference, we may evaluate this expression for typical values of the strong coupling constant $\alpha_s = 0.2 - 0.3$, as utilized in fits to the data in Ref. [115], obtaining

$${\kappa_{\rm rad}}^{\rm pert} \sim (0.3 - 1.0) \log B_{\rm rad} \sim (2 - 6) \, , \tag{4.9}$$

where in the second equality we have used the expression for $B_{\rm rad}$ given above for jets with energy $E = 100$ GeV in a plasma with temperature $T = 300$ MeV. Note that this logarithm is large, which suggests that, even for the high energy jets at the LHC, leading logarithmic expressions such as Eqs. (4.5) and (4.6) are inapplicable and a resummation, as advocated in Refs. [116, 117, 118], may be needed.

The expression (4.7) captures the leading x and T dependence of radiative energy loss at weak coupling. We shall treat $\kappa_{\rm rad}$ as a free parameter, fitting it to one piece of experimental data and then asking how a model in which we use the expression (4.7) to describe the energy loss of the partons in a shower fares in comparison to other data.

One reason why it makes sense to treat $\kappa_{\rm rad}$ as a parameter to be fit to data is that not all of the energy radiated from the initial parton corresponds to jet energy loss. At emission, the radiated gluons are nearly collinear with the energetic parton, meaning that if the gluons are energetic enough they remain part of the jet. This corresponds to medium modification of the branching probability within the shower, without significant energy loss from the jet cone. However, the subsequent rescattering and further splitting of the radiated gluons

can serve to rapidly soften the gluons, and decorrelate their directions with that of the energetic parton. This decorrelation between the directions of the radiated gluons and the jet direction is expected to be most efficient for the softer radiated gluons and less efficient for the harder radiated gluons [106]. What this means is that the $\kappa_{\rm rad}$ that we need should be smaller than that obtained in the perturbative calculations, smaller by a factor that is at present hard to estimate.

Note that we do not propose our simplified approach as a competitor to more sophisticated Monte Carlo methods for analyzing the effects of radiative energy loss on jets being developed by others [54, 55, 57, 56, 119, 120]. It is in fact clearly inferior, since we do not track the radiated gluons, treating them as 'lost'. This approach makes sense in our hybrid model, where the lost energy rapidly becomes soft thermal radiation. It does not make sense quantitatively here. Our goal is solely to have a benchmark against which to compare our hybrid model.

Finally, and with the aim of exploring the sensitivity of different observables to the path-length dependence of the jet energy loss, we will study a somewhat more extreme model for energy loss at weak coupling in which we assume that dE/dx is given by a collisional rate. Collisional energy loss is subdominant to radiative energy loss at weak coupling in the high parton energy limit, and for this reason it is neglected in many studies. However, it has been pointed out [47] that, while subdominant, these processes play an important role, especially for heavy quarks moving through the plasma. Here, we shall not advocate any underlying dynamical picture on the basis of which to justify including collisional processes. What we shall do, simply, is to introduce a third model in which, like in our hybrid model, parton branching within the shower proceeds as in vacuum and in which the energy loss of each parton in the shower is given by the collisional energy loss rate in a weakly coupled plasma, whose parametric dependence takes the form [47]

$$\frac{dE}{dx} = -\kappa_{\rm coll}\frac{C_R}{C_F}T^2 \ , \tag{4.10}$$

where we treat $\kappa_{\rm coll}$ (this time the subscript signifies "Collisional") as a fit parameter to be constrained by one piece of experimental data. This expression captures the leading

temperature, energy and path length dependence of the perturbative collisional rate. For an ultra-relativistic parton in a weakly coupled plasma, $\kappa_{\rm coll}$ is given to leading logarithmic order in perturbation theory by [47]

$$\kappa_{\rm coll}{}^{\rm pert} = C_F \pi \alpha_s^2 \left(\frac{2N_c + N_f}{6} \right) \log B_{\rm coll} \,. \tag{4.11}$$

where, as before, $B_{\rm coll}$ regulates the effect of large momentum transfer scatterings in the medium and is understood to be proportional to the parton energy. The precise expression for $B_{\rm coll}$ depends on the criteria used in the regularization; see Ref. [47] for a compilation of expressions from the literature. As in the case of radiative energy loss, we can substitute $\alpha_s = 0.2 - 0.3$ into (4.11) and estimate the value of $\kappa_{\rm coll}$ if we assume that these values of α_s are small enough for a leading logarithmic calculation to be relevant, obtaining

$$\kappa_{\rm coll}{}^{\rm pert} \sim (0.25 - 0.6) \log B_{\rm coll} \sim 1.6 - 3.3 \,, \tag{4.12}$$

where in the second equality, we have used $B_{\rm coll} = 6ET/m_D^2$. As in the case of radiative energy loss, the logarithmic factor is large which means that it is doubtful that these values of α_s are small enough for these leading logarithmic expressions to be reliable.

We have chosen the ratio of Casimirs appearing in both Eqs. (4.7) and (4.10) such that the parameter $\kappa_{\rm rad}$ (or $\kappa_{\rm coll}$) that we shall obtain by fitting our expressions for the radiative (or collisional) energy loss to data is that for the energy loss of a quark moving through a weakly coupled plasma, while a gluon gets an additional factor C_A/C_F.

4.2.4 The Effects of Flow on the Rate of Energy Loss

In the previous Section, we have specified the rate of energy loss for an energetic parton traversing static plasma with some constant temperature T. In order to use these expressions in the description of how an energetic parton loses energy as it traverses the expanding, flowing, cooling, plasma created in a heavy ion collision, we will exploit the fact that the expansion, flow and cooling of this fluid are described well by nearly inviscid hydrodynamics. This implies that the dynamic medium can be described as a collection of fluid

cells that are each close to thermal equilibrium, locally. As is standard in fluid mechanics, local thermal equilibrium should be understood from a coarse-grained point of view: at every fluid cell there is a macroscopic system of size much larger than any microscopic scale, such as the inverse temperature of the cell. From this coarse-grained perspective, the temperature and the velocity of the fluid cell change from point to point, and from time to time.

We assume that the temperature T appearing in the formulae for dE/dx varies in space and time, and at each point in spacetime passed by the energetic parton is given by the temperature of the fluid at that point in spacetime. The basic assumption behind this adiabatic prescription is that the length scale on which an infinitesimal energy loss occurs is small compared to the length scale over which T changes.

It is clear from their derivations that Eq. (4.2) (or Eq. (4.7) and (4.10)) describe the rate of energy loss of an energetic parton moving through this fluid *in the local fluid rest frame.* If this is not the collision center-of-mass frame, dE/dx in that frame must be obtained via a Lorentz transformation. Incorporating the effects of fluid flow on the rate of energy loss has significant effects on our results at large rapidity, since it is at large rapidity that the boost between the local fluid rest frame and the collision center-of-mass frame becomes large.

Let us denote the rate of energy loss in the local fluid rest frame by

$$\frac{dE_F}{dx_F} = \mathcal{F}_F(x_F, E_{\rm in}^F)\,, \tag{4.13}$$

where the function $\mathcal{F}_F(x_F, E_{\rm in}^F)$ is given by the right-hand side of Eq. (4.2) (or Eq. (4.7) and (4.10)) and where we have highlighted in the notation that dE_F/dx_F depends upon the distance x_F that the parton has travelled in the local fluid rest frame and, in the case of Eq. (4.2), upon the initial energy $E_{\rm in}^F$ that the parton had when it was produced at a splitting point in the shower, again as evaluated in the local fluid rest frame. In making this statement, we have assumed that the effects of the spatial and temporal gradients in the fluid on dE_F/dx_F can be neglected.[2] We now Lorentz transform the rate of energy loss

[2]The effects of spatial and temporal gradients in the fluid on the rate of energy loss of an infinitely heavy quark moving through strongly coupled plasma have been computed, to lowest order in fluid gradients [**?**, **?**,

(4.13) back to the collision center-of-mass frame, obtaining a result that we shall denote by

$$\frac{dE}{dx} = \mathcal{F}(t, E_{\rm in})\,, \tag{4.14}$$

where t is the time in the collision center-of-mass frame since the parton was produced and $E_{\rm in}$ is the energy that the parton had, in that frame, when it was produced. We can change from x to t at will because throughout our treatment we are assuming that the energetic partons in the shower move at (very close to) the speed of light. The functions $\mathcal{F}_F$ and $\mathcal{F}$ are related explicitly by a Lorentz transformation that we present next.

In the local fluid rest frame, the change in the four-momentum of a parton which propagates for an infinitesimal time dt_F is given by

$$dP_F^\mu \;=\; \mathcal{F}_F\left(x_F, E_{\rm in}^F\right)\frac{P_F^\mu}{E_F}dt_F\,, \tag{4.15}$$

where and P_F^μ and E_F are the four momentum and energy of the parton in the local fluid rest frame and $\mathcal{F}_F\left(x, E_{\rm in}^F\right)$ is the functional form of the rate of energy loss in that frame, in the notation that we introduced in Eq. (4.13), and is given by the right-hand side of Eq. (4.2) in our hybrid model or by the right-hand side of one of the expressions Eq. (4.7) or (4.10) in our control models. In writing the expression (4.15) we have used our assumption that the exchanges of momentum and energy between the parton and the medium do not change the direction of the parton significantly.

The Lorentz structure of the expression (4.15) simplifies the boost back to the collision center-of-mass frame. First of all, it is easy to show that

$$\frac{dt_F}{E_F} = \frac{dt}{E}\,, \tag{4.16}$$

where t and E are the time and energy in the collision center-of-mass frame. Second, after a Lorentz transformation, $P_F^\mu \to P^\mu$ and $dP_F^\mu \to dP^\mu$, with P^μ and dP^μ the four-momentum

?]. They can be significant early in a collision, before hydrodynamization. Once the fluid is hydrodynamic, these effects are small. We expect that the same is true for the effects of fluid gradients on the rate of energy loss of a massless parton moving through the plasma, but we defer checking this by explicit calculation to future work.

and the infinitesimal four-momentum loss in the collision center-of-mass frame. Therefore

$$\frac{dP^\mu}{dt} = \mathcal{F}_F\left(x_F, E^F_{\rm in}\right)\frac{P^\mu}{E}\,, \tag{4.17}$$

where the arguments of $\mathcal{F}_F$ are still expressed in terms of quantities in the local fluid rest frame.

We next express the initial parton $E^F_{\rm in}$ in the local fluid rest frame as a function of quantities in the collision center-of-mass frame via the Lorentz transformation

$$E^F_{\rm in} = E_{\rm in}\,\gamma_F\left(1 - \mathbf{w}\mathbf{v}\right)\,, \tag{4.18}$$

where $\mathbf{w} = \mathbf{P}/E$ is the velocity of the parton in the collision center-of-mass frame and $\mathbf{v}$ is the local velocity of the fluid in the same frame, which is to say it is the velocity vector for the boost between the two relevant frames. γ_F is the gamma factor of the local fluid velocity $\mathbf{v}$.

The relation between x_F and x, the distances travelled in the two frames, requires further discussion. In the derivation of the rate of energy loss by one of the partons in the shower, x_F is the distance that that parton has travelled through the fluid. However, as partons propagate through the hot plasma created in an heavy ion collision, the temperature and velocity of the fluid at their location in space and time changes. We will assume that x_F is the accumulated distance of the parton summed in such a way that each infinitesimal contribution dx_F is evaluated in the local fluid rest frame. This means that (if the rate of energy loss depends on x_F, as in Eq. (4.2) and Eq. (4.7), the energy lost by a parton traversing some dx_F depends on the total x_F accumulated by that parton over its previous passage through the flowing plasma. With this prescription, which neglects gradient effects, we have

$$d\mathbf{x}_F = \mathbf{w}dt + \gamma_F\left(\mathbf{w}_L - \mathbf{v}\right)dt\,, \tag{4.19}$$

where $\mathbf{w}_{T,L}$ are the transverse and longitudinal components of the parton velocity in the collision center-of-mass frame. After some algebra, the increment in the accumulated dis-

tance is given by

$$\left(\frac{dx_F}{dt}\right)^2 = \mathbf{w}^2 + \gamma_F^2\left(\mathbf{v}^2 - 2\mathbf{vw} + (\mathbf{vw})^2\right) . \tag{4.20}$$

Summing over the previous history of the parton, we obtain

$$x_F(t) = \int_{t_0}^{t} dt \sqrt{\left[\mathbf{w}^2 + \gamma_F^2\left(\mathbf{v}^2 - 2\mathbf{vw} + (\mathbf{vw})^2\right)\right]} , \tag{4.21}$$

where t_0 is the creation time of the parton. We have used (4.17), (4.18) and (4.21) in (4.22), (4.23) and (4.24). The result takes on the surprisingly simple form

$$\mathcal{F}(x, E_{\rm in}) = \mathcal{F}_F(x_F, E^F_{\rm in}(E))) \tag{4.22}$$

where $E^F_{\rm in}$ and x_F are the initial energy and the path length in the local fluid rest frame. These are related to quantities defined in the collision center-of-mass frame by

$$E^F_{\rm in} = E_{\rm in}\,\gamma_F\left(1 - \mathbf{wv}\right) , \tag{4.23}$$

$$x_F(t) = \int_{t_0}^{t} dt \sqrt{\left[\mathbf{w}^2 + \gamma_F^2\left(\mathbf{v}^2 - 2\mathbf{vw} + (\mathbf{vw})^2\right)\right]} , \tag{4.24}$$

where $\mathbf{w} \equiv \mathbf{p}/E$ is the parton velocity, $\mathbf{v}$ and γ_F are the fluid velocity and Lorentz factor, t_0 the time the parton was produced and t is the observation time, all in the collision center-of-mass frame.

The result (4.22) implies that if the rate of energy loss does not depend explicitly on the energy of the parton or the distance that the parton has travelled through the medium, as in the case of the collisional rate in Eq. (4.10), the fluid velocity will have no effect on dE/dx. In the case of the radiative energy loss rate in Eq. (4.7), or for the strongly coupled rate of energy loss Eq. (4.2) that we employ in our hybrid model, one expects that including the effects of fluid flow on the energy degradation of jets will be particularly important for jets at large rapidity.

As a simple but illustrative example, let us consider the energy lost by an energetic parton propagating through a fluid that is experiencing Bjorken flow, namely boost-invariant

longitudinal expansion with no transverse flow. If the parton has a large rapidity, the fluid that it is propagating through has a large longitudinal velocity meaning that there is a substantial boost between the local fluid rest frame and the collision center-of-mass frame. Assuming that both the parton and the boost invariant fluid are produced at the same time, the longitudinal velocity of the parton coincides with the fluid velocity at its location. If the parton travels a distance L in the collision center-of-mass frame during a time t, then according to Eq. (4.24) the distance that the parton travels through the fluid in the local fluid rest frame is

$$x_F(t) = \int_0^t |\mathbf{w}_T|\, dt = \frac{L}{\cosh y}\,, \tag{4.25}$$

where $\mathbf{w}_T$ and y are the transverse velocity of the parton its rapidity respectively. For particles with significant rapidity y, say $y > 1$, we see that the distance they travel in the local fluid rest frame is substantially less than the distance they travel in the collision center-of-mass frame. If the rate of energy loss is given by the expression in Eq. (4.7) inspired by radiative energy loss, this is the principal effect of flow on the energy loss suffered by an energetic parton. If the rate of energy loss is given by the strongly coupled form Eq. (4.2), as in our hybrid model, this effect is important but it is also important to note that $E_{\rm in}$ is also different in different frames. Using (4.23),

$$E_{\rm in}^F = \frac{E_{\rm in}}{\cosh y} \tag{4.26}$$

in this simple Bjorken flow. The effect of this diminution in $E_{\rm in}^F$ on the rate of energy loss Eq. (4.2) is complex. On the one hand, reducing $E_{\rm in}^F$ reduces the rate of energy loss. On the other hand, it reduces $x_{\rm stop}$ which increases the rate of energy loss. The net effect, which is specially important for the jet quenching species dependence given the different quark and gluon jets abundances at different rapidities, is not clear *a priori*. We retake this discussion, in posession of the full Monte Carlo simulation results, in Section 5.5.

4.3 Monte Carlo Implementation

The implementation of the hybrid model that we have described requires several steps, beginning with the generation of jets and the modification of their evolution due to energy loss, but also including the hydrodynamic calculation of the space and time dependence of the bulk medium created in the heavy ion collision. The procedures used for the calculations reported in this work are presented in this Section.

We generate hard processes using PYTHIA 8.183 [121]. Since at the LHC center of mass energy and in the range of momentum relevant for our analysis ($p_{\rm T} \sim \mathcal{O}(100{\rm GeV})$), the modification of the nuclear parton distribution functions with respect to the proton ones is very small [122, 123], we simulated high energy jet production in proton-proton collisions at $\sqrt{s} = 2.76$ TeV. Since these events are later embedded into a hydrodynamic model for the bulk matter produced in the nucleus-nucleus collisions, we do not include the underlying event in the PYTHIA treatment of the proton-proton collision in our calculation. We use the PYTHIA $p_{\rm T}$-ordered shower to evolve the hard process from the initial virtuality down to a typical hadronic scale of $Q_0 = 1$ GeV, at which we stop the evolution. At this scale, vacuum event generators switch to phenomenological models of hadronization, like the Lund string model which is incorporated into PYTHIA. For a number of reasons, the nonperturbative hadronization process is expected to be altered in a heavy ion collision relative to that in vacuum. For example, most of the soft hadrons in a heavy ion collision will be formed via the coalescence of quarks and gluons from the expanding and cooling plasma rather than directly from partons produced initially and their fragments [**?**, **?**]. Furthermore, even if we only look at hadrons that are formed via fragmentation, hadronization in this setting is still modified by the presence of the medium via changes in how color flows [124, 125, 126, 127, 128, 129]. In order to avoid complicating the interpretation of our results with currently unconstrained hadronization dynamics, throughout this analysis we will work at the partonic level and focus on observables that are less sensitive to the hadronization process. For example, in jet observables these corrections are, at least in vacuum, smaller than 10% [130].

On an event by event basis, the events generated by PYTHIA each initiate a decay chain

which will be the starting point for our implementation of medium effects. As we have argued in Section 4.1, in our hybrid model we shall neglect the possibility that the presence of the medium may result in modification of the splitting probabilities, or modification to the locations in space and time where splitting occurs obtained via Eq. (4.1). We are neglecting the fact that the reduction in the available energy due to the loss of energy of a parton in the shower leads to a reduction in the phase space available when that parton subsequently splits. In this exploratory study we will neglect such phase space effects and assume that the overall structure of the decay chain remains the same even after we make the partons in the shower lose energy.

We place the point of origin of each of the dijet processes generated by PYTHIA in the plane transverse to the collision axis at a location selected with a probability proportional to the number of binary collisions at that location in the transverse plane as dictated by the ensemble-averaged MC-Glauber initial conditions [8], where for simplicity we are neglecting all effects of event-by-event fluctuations. The showers generated by the dijets proceed in space and time according to Eq. (4.1), propagating outward along their (randomly selected) direction of motion. Since the dijet production process is hard, dijets are produced very early ($\tau \sim 1/Q$), prior to the proper time at which the plasma produced in the collision hydrodynamizes, $\tau_{\rm hydro}$. We will assume that during the short proper time before $\tau_{\rm hydro}$, the jets propagate unperturbed.[3] After $\tau_{\rm hydro}$, the jets encounter the hydrodynamically expanding plasma and the different fragments of the jet suffer energy loss, according to (4.2) in our hybrid strong/weak coupling model or according to (4.7) or (4.10) in our models of weakly coupled radiative or collisional energy loss. To determine the local properties of the plasma at the position of the fragments, we embed the jet shower into a set of hydrodynamic simulations of Pb-Pb collisions at $\sqrt{s} = 2.76$ ATeV and 5.02 ATeV provided to us by Shen and Heinz, based upon the codes developed by them and their collaborators in Refs. [131] and

[3]This is an assumption that could be improved upon in future, once the analysis of the early pre-equilibrium energy loss of heavy quarks in Ref. [108] is extended to light quarks. That analysis indicates that energy loss sets in only after a delay time of order $1/(\pi T)$ after the moment during the collision when the energy density is at its maximum, T being the temperature at the time of hydrodynamization. In addition, the analysis of the collision of sheets of energy density in Ref. [14] indicates that if the sheets are thin enough there is a prior delay of order $1/(\pi T)$ between the collision time and the time when the energy density peaks. The results of Refs. [108, 14] together indicate that there will surely be some energy loss before $\tau_{\rm hydro}$ but that it is not expected to be large.

[132]. These 2+1-dimensional simulations, with boost-invariant longitudinal expansion, incorporate an equation of state from Ref. [133] (referred to there as the s95p-v1-PCE150 equation of state) that incorporates results from lattice QCD calculations and from a hadron resonance gas at low temperatures. With this equation of state, it is possible for us to set the T_c below which we stop parton energy loss within a range $145\,\mathrm{MeV} < T_c < 170\,\mathrm{MeV}$ that reflects results for the range of crossover temperatures from current lattice calculations, see for example Refs. [134, 3]. We shall employ this variation in our choice of T_c as a device with which to estimate the systematic uncertainty in the results that we obtain from the computations that we shall perform using our hybrid model. Because we are not concerned with the evolution below T_c, we evolved the initial conditions using viscous hydrodynamics alone, with no cascade afterburner. For simplicity, the hydrodynamic calculations employ a temperature-independent $\eta/s = 1/(4\pi)$. Since in the simulations of Ref. [131, 132] the hydrodynamic fields are initialized at $\tau_{\mathrm{hydro}} = 0.6$ fm, we will take this as our hydrodynamization time. From these simulations we determine the temperature of the plasma at each point in space and time, and hence the spacetime-dependent temperature that each parton in the fragmenting shower encounters on its way through and eventually out of the expanding, cooling, droplet of plasma. We use this spacetime-dependent temperature to integrate the different expressions for the energy loss rate dE/dx discussed in Section 4.2 over the path of each parton in the shower during its lifetime, *i.e.* from the time when it is produced in a splitting process to the time when it itself splits.

The procedure described above assigns an energy loss to each of the virtual partons in the shower. However, it does not determine how the lost energy is distributed among the several particles that are produced when each virtual parton splits, or decays. Consistent with the assumption that the medium does not change the splitting probabilities in the shower, since these splitting probabilities depend on the energies of the daughter partons only through the fraction of the parent parton energy that each daughter obtains as a result of the splitting we choose to distribute the energy lost by the parent parton as a reduction in the initial energy of each of the daughters according to this fraction. As they themselves propagate through the medium subsequently, these decay partons loose additional energy until they split again. Therefore, the total energy lost by a particular final parton that es-

capes from the medium depends on the detailed history of splitting and propagation that led to that parton.

Since the goal of this work is to study the effect on high energy jets of energy loss in strongly coupled plasmas, we will not describe the degradation of the jet energy in the hadron gas produced after the plasma cools through the QCD phase transition at $T \sim T_c$. We focus only on the energy loss as the jet propagates through the strongly coupled plasma with $T > T_c$. To ensure that we do not apply the strong coupling results to the late time resonance gas, we will stop the computation of energy loss when the temperature of the system falls below T_c, which we identify with the crossover temperature of the QCD transition that separates the plasma from the hadron gas. Since the QCD transition is a cross-over, T_c is not sharply defined and its precise value depends on the procedure used to determine it.

Finally, in addressing RHIC data we will employ an identical procedure except that we start with hard dijets produced (by PYTHIA) in collisions with $\sqrt{s} = 200$ GeV per nucleon and we replace the hydrodynamic profile for LHC collisions with that for RHIC collisions, also obtained from Ref. [131, 132].

In the next Section, we describe how we reconstruct the jets in our hybrid model and compare them, in various ways using various measured observables, to jets reconstructed from heavy ion collision data.

Chapter 5

Comparison with Single-Jet and Dijet Data for $\sqrt{s} = 2.76$ ATeV and Predictions for Observables at $\sqrt{s} = 5.02$ ATeV

We have described the implementation of our hybrid model in full detail in the two previous Sections. All that remains is to choose the one dimensionless free parameter $\kappa_{\rm sc}$, defined in Eq. 4.3, that we have introduced into our description of the energy loss of an individual parton in the PYTHIA shower as it propagates through the strongly coupled plasma and the model will then be fully specified. As explained in Section 4.2, we are assuming that the strongly coupled dynamics fixes the parametric dependence of the energy loss rate dE/dx, given in Eq. (4.2), and the stopping distance $x_{\rm stop}$, given in Eq. (4.3), but not the overall normalization of $x_{\rm stop}$. Therefore, our model possesses one free parameter, which we need to fit to data. Once this has been done, we will be able to study different jet observables and extract the effect of the medium on each of them.

5.1 Jet Reconstruction and Jet $R_{\rm AA}$ at $\sqrt{s} = 2.76$ ATeV

The first observable that we shall compute is $R_{\rm AA}$ for jets, as a function of p_T, the transverse momentum of the jet, and as a function of the centrality of the heavy ion collision.[1] The jet $R_{\rm AA}$ is the ratio of the number of reconstructed jets with a given p_T that we find in heavy ion collisions in a given centrality bin to the number of jets with that same p_T in $N_{\rm binary}$ proton-proton collisions with the same p_T, where $N_{\rm binary}$ is the number of proton-proton collisions that occur in a heavy ion collision of the given centrality, according to a Glauber model. Because the production cross-section for jets is a rapidly falling function of p_T, if the jets in a heavy ion collision have lost energy due to the passage of the partons in the jet through the strongly coupled medium this results in $R_{\rm AA} < 1$. To determine the prediction of our model for the jet $R_{\rm AA}$, we need to reconstruct jets both in heavy ion collisions within our model (as described in previous sections, including the effects of energy loss) and in proton-proton collisions as described by PYTHIA with the underlying event switched off, as explained in Section 4.3. To obtain the principal results of this work, we generated 300,000 PYTHIA events with p_T greater than a cut that we set to 50 GeV for collisions with centralities in each of four ranges (0-10%, 10-30%, 30-50% and 50-70%). We varied the p_T cut to make sure that the jet spectrum in the (higher) range of p_T where we performed our analyses was insensitive to the value of the cut. We

[1]The "centrality" of a collision between heavy ions refers to its impact parameter. Nearly head-on collisions, with the smallest impact parameters, are referred to as central collisions; peripheral collisions, with large impact parameter, are noncentral. The impact parameter is not directly measured, but it is nevertheless possible to bin heavy ion collision data as a function of impact parameter, for example using the fact that the total number of hadrons produced in a heavy ion collision is anticorrelated with the impact parameter of the collision. Central collisions have the highest multiplicity; peripheral collisions the lowest. Experimentalists therefore bin their events by multiplicity, using that as a proxy for the impact parameter. The terminology used refers, for example, to the "0-10% centrality bin" and the "10-20% centrality bin", meaning the 10% of events with the highest multiplicities (and lowest impact parameters) and the next 10% of events with the next highest multiplicities (and next lowest impact parameters). The correlation between event multiplicity and impact parameter is described well by the Glauber model of multiple scattering [135, 8], which relates the event multiplicity to the number of nucleons that participate in the collision ($N_{\rm part}$) which in turn can be related via a geometrical calculation to the impact parameter of the collision. In our calculations, we take the tabulation of the range of impact parameters that corresponds to a given centrality bin defined via the multiplicity distribution for Pb-Pb collisions at the LHC from Ref. [136]. When we distribute the points of origin of our PYTHIA jets in the transverse plane, we do so with a probability distribution for the impact parameter b dictated by the number of collisions at each b within the range corresponding to a given centrality bin. In order to then apply our energy loss prescription to the partons in the PYTHIA shower, we embed the PYTHIA jet in the hydrodynamic solution from Ref. [131, 132] corresponding to the mean value of the impact parameter in the interval associated with the given centrality bin.

used the PYTHIA events without modification to describe jets in proton-proton collisions. As described in Sections 4.2 and 4.3, to describe quenched jets in heavy ion collisions we embed the PYTHIA events in a hydrodynamic description of the matter produced in a heavy ion collision and apply our prescription for energy loss to each parton in the PYTHIA shower. We then analyze the output of our model calculations of quenched jets in heavy ion collisions and of proton-proton jets using FastJet [137], with which we reconstruct jets using the anti-k_t algorithm [138]. Defining a jet, via any reconstruction algorithm, requires the specification of a resolution parameter, R. This parameter can be understood as the opening angle (in radians) of the jets we reconstruct, although the precise meaning of R is different for different reconstruction algorithms. We shall set the reconstruction parameter in the anti-k_t algorithm to $R = 0.3$ for Pb-Pb collisions at LHC energies and to $R = 0.2$ for Au-Au collisions at RHIC energies because we shall compare the predictions of our model to jet measurements from LHC and RHIC data that employ these values of R. As we have discussed in Section 4.3, the output of our model is partons not hadrons, and we are reconstructing jets from those partons. For this reason, we will focus on jet observables that are relatively insensitive to details of the hadronization process.

In order to fit the value of the one free parameter $\kappa_{\rm sc}$ in our parametrization (4.2) and (4.3) for the rate of energy loss dE/dx of each of the partons in the PYTHIA shower, we calculate $R_{\rm AA}$ for jets with $100 \leq p_T \leq 110$ GeV in the range of pseudorapidities $-2 \leq \eta \leq 2$ in the 0-10% most central Pb-Pb collisions at LHC energies, with collision energy $\sqrt{s} = 2.76$ TeV per nucleon pair. This quantity has been measured by the CMS collaboration, and in the data it lies between 0.42 and 0.51. (For this and for all experimental data quoted in our work, we have added the statistical and systematic errors in quadrature.) We find that we can reproduce this measured result with our model as long as we choose $\kappa_{\rm sc}$ between 0.32 and 0.41. In determining this range of allowed values of the parameter $\kappa_{\rm sc}$ we have included the theoretical uncertainty in the critical temperature T_c, discussed in Section 4.3, as well as the uncertainty that enters via the uncertainty in the experimentally measured quantity. The latter dominates the uncertainty in the extracted value of $\kappa_{\rm sc}$. Henceforth, in all our plots we will show a band of results obtained from our model corresponding to varying $\kappa_{\rm sc}$ between 0.32 and 0.41, a range that incorporates both experimental and

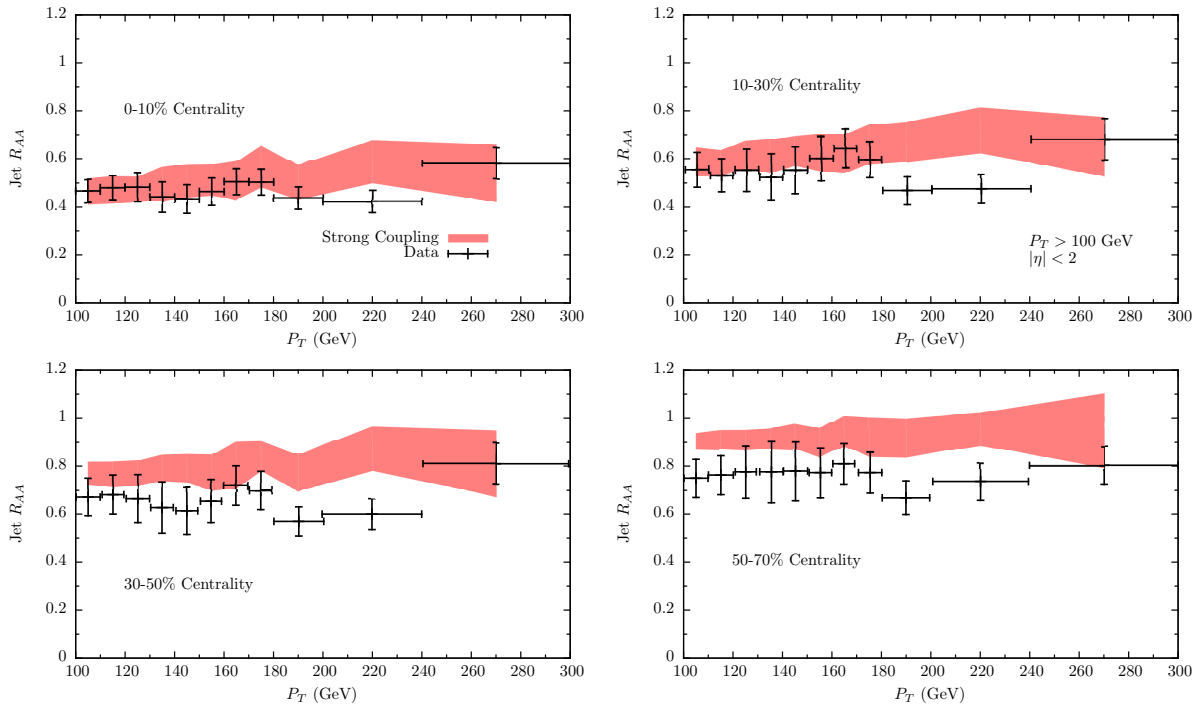

Figure 5-1: Jet $R_{\rm AA}$ as a function of $p_{\rm T}$ for different centralities in our hybrid model for jet quenching in strongly coupled plasma compared to preliminary CMS data from Ref. [139]. The results of our calculations in our hybrid strongly coupled model, shown by the colored bands, are completely specified once we have fixed the one free parameter in the model so that the model agrees with the left-most data point in the top-left panel, namely the jets with $100\ {\rm GeV} < p_{\rm T} < 110\ {\rm GeV}$ in the most central collisions. Once this point has been fitted, the $p_{\rm T}$ dependence and centrality dependence of $R_{\rm AA}$ are outputs of the model.

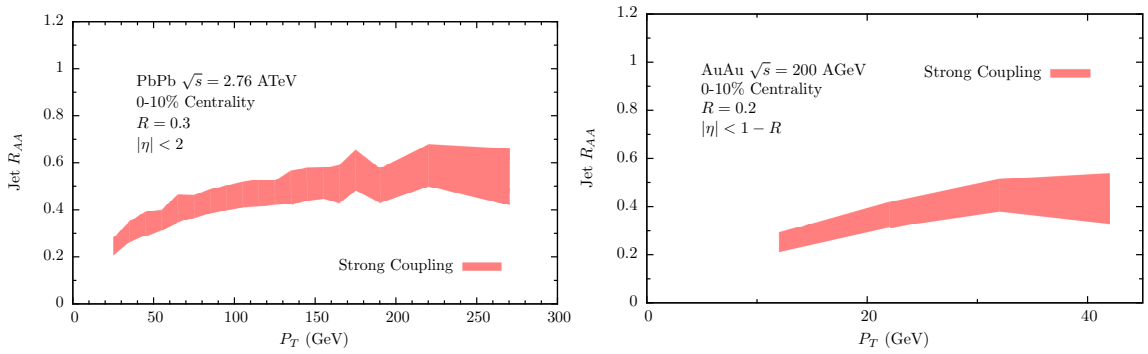

Figure 5-2: Predictions of our hybrid strongly coupled model for jet $R_{\rm AA}$ as a function of $p_{\rm T}$ for central Pb-Pb collisions at the LHC with $\sqrt{s} = 2.76$ TeV per nucleon (left) and Au-Au collisions at RHIC with $\sqrt{s} = 200$ GeV per nucleon (right). In both cases, we only show our results for collisions in the 0-10% centrality bin.

theoretical uncertainty.

With $\kappa_{\rm sc}$ now fixed, the first results that we obtain from our model are the dependence of the jet $R_{\rm AA}$ on p_T and on the centrality of the collision, for Pb-Pb collisions at $\sqrt{s} = 2.76$ TeV. We show our results in Fig. 5-1. We see that our hybrid model predicts a jet $R_{\rm AA}$ that is only weakly p_T-dependent, in agreement with the preliminary CMS data from Ref. [139]. The evolution of the jet $R_{\rm AA}$ with increasing centrality is consistent with the data until we get to the most peripheral bin, for which our model predicts less quenching than is seen in the data. This discrepancy may be due in part to the fact that we are not including the energy loss in the hadronic phase in our computation, since peripheral collisions will spend less time in the plasma phase making the time spent in the hadronic phase proportionally more relevant.

In Fig. 5-2 we further explore the $p_{\rm T}$ and $\sqrt{s}$ dependence of the jet $R_{\rm AA}$ within our hybrid approach. In the left panel, we extend our computation of jet suppression down to 15 GeV for the most central LHC collisions, using a sample of PYTHIA jets generated with $p_{\rm T}$ greater than a 10 GeV cut. Because the jet production cross-section falls rapidly with $p_{\rm T}$, in order to have sufficient statistics over this wide range in $p_{\rm T}$ we generated several independent samples of jets, each with $p_{\rm T}$ greater than a higher value of the cut than in the sample before, employing cuts of 10, 35 and 50 GeV. We then merged each sample with the previous one away from these cuts. In this way we were able to obtain a sample of jets with reasonable statistics for $p_{\rm T}$ ranging all the way from 15 GeV to 270 GeV. Even over

this extended range of $p_{\rm T}$, the jet suppression factor $R_{\rm AA}$ varies relatively little with transverse momentum. This is in qualitative agreement with $R_{\rm CP}$ measurements by ATLAS [25] and charged jet $R_{\rm CP}$ measurements by ALICE [28], which both report suppression measurements down to this range of $p_{\rm T}$ with a similarly weak dependence on $p_{\rm T}$. Nevertheless, at present we refrain from a quantitative comparison with these data, for two reasons. $R_{\rm CP}$ is the ratio of the number of jets with a given $p_{\rm T}$ in central collisions to an expectation based upon data in peripheral collisions, rather than an expectation based upon data in proton-proton collisions as in $R_{\rm AA}$. Given the disagreement that we see between our model and the data in the peripheral bin at the higher values of $p_{\rm T}$ displayed in Fig. 5-1, we cannot make a direct comparison between our results at lower values of $p_{\rm T}$ in Fig. 5-2 and measurements of $R_{\rm CP}$. And, since we are working at the partonic level, we are at present hesitant to compare our results to measurements of jets defined via charged hadrons only, rather than calorimetrically. In the right panel of Fig. 5-2, we repeat our analysis for the lower jet energies available in RHIC collisions with a center of mass energy of $\sqrt{s} = 200$ GeV per nucleon, extending our analysis down to 12 GeV using a sample of PYTHIA jets generated with $p_{\rm T}$ greater than a 5 GeV cut. We chose the jet reconstruction parameter $R = 0.2$, as in Ref. [140]. Our results are in good agreement with the preliminary experimental measurements reported by the STAR collaboration in Ref. [140], at present still with significant systematic uncertainties. However, we have again refrained from making a direct comparison since, as before, it is not easy to compare our partonic jet results with the charged jet measurements reported in Ref. [140]. Also, in making these measurements the STAR collaboration requires the presence of a semi-hard ($p_{\rm T} = 5 - 7$ GeV) charged hadron within the jet, a criterion that is hard for us to reproduce from our partonic computation.

The predictions of our model for both the momentum dependence and the centrality dependence of jet suppression are in encouraging agreement with experimental data. To avoid over-interpreting this agreement, it is important to assess the sensitivity of the jet $R_{\rm AA}$ observable to the underlying dynamics of the energy loss. To gauge this sensitivity, we have repeated the analysis for the two other models of the energy loss rate dE/dx described in Section 4.2. In Fig. 5-3 we show the jet suppression factor $R_{\rm AA}$ in two centrality bins for the strongly coupled (red), radiative (grey) and collisional (blue) energy loss models.

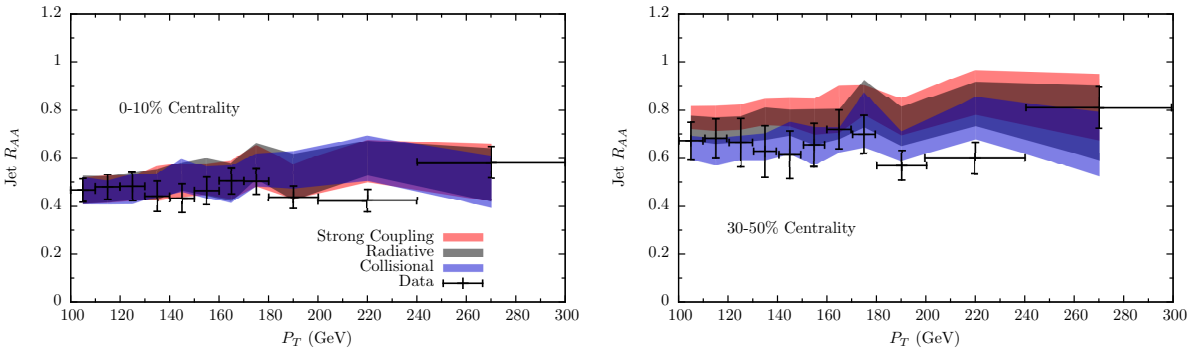

Figure 5-3: Jet $R_{\rm AA}$ as a function of $p_{\rm T}$ for LHC collisions in two different centrality bins for the three energy loss models from Section 4.2, as compared to preliminary CMS data [139]. Each of the three models for the rate of energy loss dE/dx includes one free parameter, and in each case we have fitted the value of this parameter to obtain agreement between the model and the data for $100\ {\rm GeV} < p_{\rm T} < 110\ {\rm GeV}$ in the most central $(0-10\%)$ collisions.

In all three models, as in Fig. 5-1 we have fitted the one free parameter in our description of dE/dx to the left-most data point in the left panel, finding $0.97 < \kappa_{\rm rad} < 1.8$ for the parameter $\kappa_{\rm rad}$ defined in the expression (4.7) for dE/dx in our model for weakly coupled radiative energy loss and $1.8 < \kappa_{\rm coll} < 3.0$ for the parameter $\kappa_{\rm coll}$ defined in the expression (4.10) for dE/dx in our model for weakly coupled collisional energy loss. Remarkably, despite the fact that the energy dependence and the path-length dependence of the three different expressions (4.2), (4.7) and (4.10) are very different for the three quite different energy loss mechanisms that we are modelling, the $p_{\rm T}$ dependence and the centrality dependence of the jet $R_{\rm AA}$ are quite similar in all three models.

5.2 Dijet Asymmetry at $\sqrt{s} = 2.76$ ATeV

After constraining and then confronting the three models with data on the jet suppression $R_{\rm AA}$, we turn now to a different jet observable, the dijet imbalance A_J [20, 21]. Following the data analysis procedure used in the analysis of the experimental data reported in Ref. [22], in our Monte Carlo simulation we select events containing dijet pairs reconstructed with the anti-k_t algorithm with jet reconstruction parameter $R = 0.3$ in the pseudorapidity range $|\eta| < 2$ such that the leading jet has $p_{\rm T1} > 120$ GeV and the subleading jet has $p_{\rm T2} > 30$ GeV. The asymmetry variable is then defined as $A_{\rm J} \equiv (p_{\rm T1} - p_{\rm T2})/(p_{\rm T1} + p_{\rm T2})$.

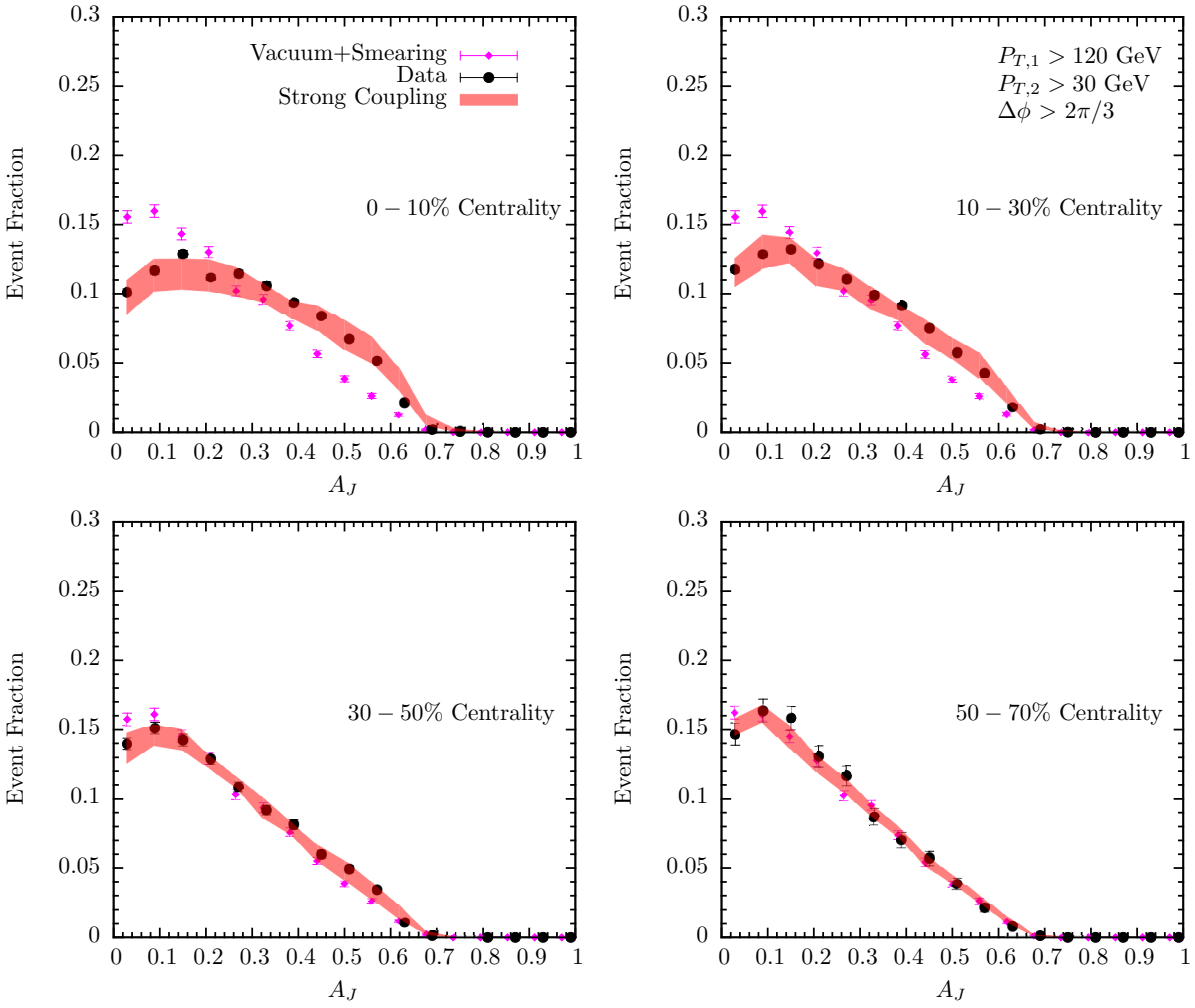

Figure 5-4: Red bands show the probability distributions for the dijet imbalance A_J in LHC collisions with four different ranges of centrality predicted by our strongly coupled hybrid model. The jet momenta are smeared, according to the prescription given in Ref. [141] in order to mimic background subtraction effects. Experimental data points are taken from Ref. [22]. As a comparison, we show the distributions of the dijet imbalance A_J in the proton-proton collisions that we have obtained from PYTHIA, including the (centrality dependent) momentum smearing needed in order to make a fair comparison to the heavy ion results.

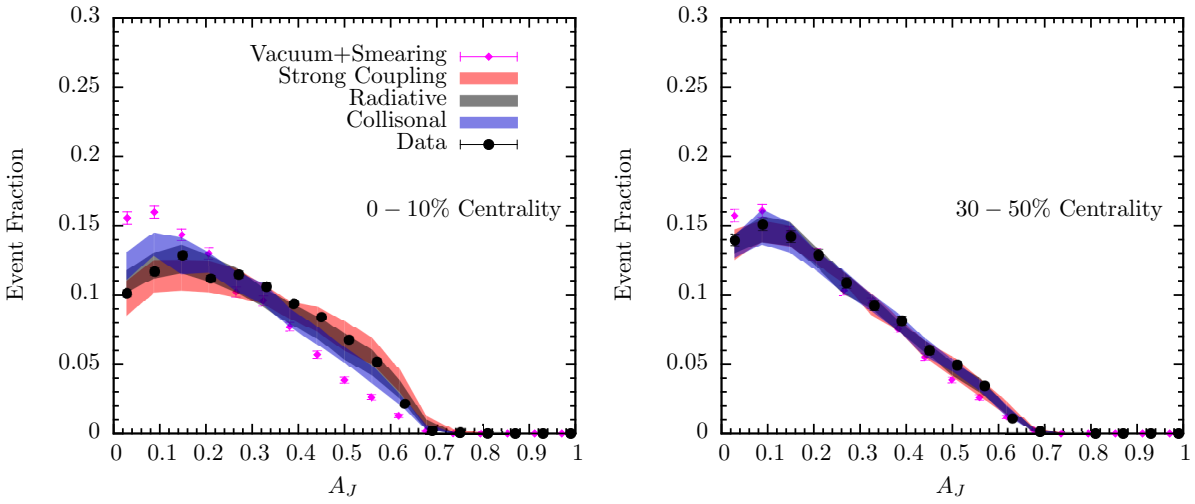

Figure 5-5: Probability distribution for the smeared dijet imbalance A_J for three different models of the rate of energy loss dE/dx in LHC heavy ion collisions in two different ranges of centrality.

Since the data presented by both ATLAS [20] and CMS [21, 22] for this observable are not fully unfolded from resolution effects, a direct comparison of the result of our computations with data is not possible. However, the CMS collaboration has demonstrated that a simple centrality and momentum dependent smearing procedure can reproduce the systematics of such effects, at least for γ-jet observables, and has provided an explicit parameterization for such smearing in that type of measurement [141]. Since the corresponding parameterization for dijet measurements is not yet available, we will use the procedure advocated in Ref. [141] also for dijets. The result of these computations is a prediction from our strongly coupled hybrid model for the probability distribution for A_J for heavy ion collisions at the LHC with four different centrality bins shown in Fig. 5-4. The centrality dependence of the smearing function is illustrated by the violet points which show the results of applying the (centrality dependent) smearing to proton-proton events from PYTHIA. The energy loss experienced by both jets in the dijet pair tends to increase A_J in heavy ion collisions, more so in more central collisions. We see this in Fig. 5-4 as the widening of the asymmetry distribution in more central collisions, both in the predictions of our model and in the data. We see from the figure that there is good agreement between the predictions of our model and measurements made using LHC data.

As before, before over-interpreting the good agreement between the strongly coupled

hybrid model prediction for the dijet asymmetry distribution and the data, in Fig. 5-5 we show the (smeared) results for the dijet asymmetry distribution in events with two different ranges of centrality if we use the strongly coupled (red), radiative (grey) and collisional (blue) models for the rate of energy loss dE/dx. As in the case of the jet suppression $R_{\rm AA}$, our results for the A_J distribution is only weakly dependent on our choice of the underlying model. Even though the three different models have quite different path-length dependence for dE/dx, all three models lead to similar dijet asymmetries. Although it is a small effect, we do notice here that the strongly coupled model yields a slightly larger dijet imbalance in the most central collisions and that this means it is in somewhat better agreement with the data than the other two models. Nevertheless, the larger message of Fig. 5-5 is the approximate agreement between the predictions of three models with energy loss rates that feature very different path-length dependence, indicating that the these types of jet observables have only limited sensitivity to the shape of the underlying medium, as observed previously in Ref. [**?**].

5.3 Fragmentation Functions Ratio at $\sqrt{s} = 2.76$ ATeV

We have seen that inclusive jet observables like the jet suppression factor $R_{\rm AA}$ and the dijet asymmetry A_J are not particularly sensitive to the differences between the three energy loss models that we are investigating. This motivates us to investigate more differential observables such as jet fragmentation functions. From our model, we can compute partonic fragmentation functions, which are probability distributions for the fraction of the total jet momentum that is carried by an individual parton in the final state jet. In Fig. 5-6, we show the ratio of the partonic fragmentation function for the quenched jets in our hybrid strongly coupled model with dE/dx as in (4.2), as well as for the analogous weakly coupled radiative and collisional energy loss models with dE/dx as in (4.7) and (4.10), to the fragmentation function for a PYTHIA jet in vacuum with the reconstructed jet energy in the same interval as for the quenched jets. This ratio is analogous to the fragmentation function ratio measured in Pb-Pb collisions at the LHC by both ATLAS and CMS [24, 143, 142], but of course they measure the fraction of the total jet momentum that

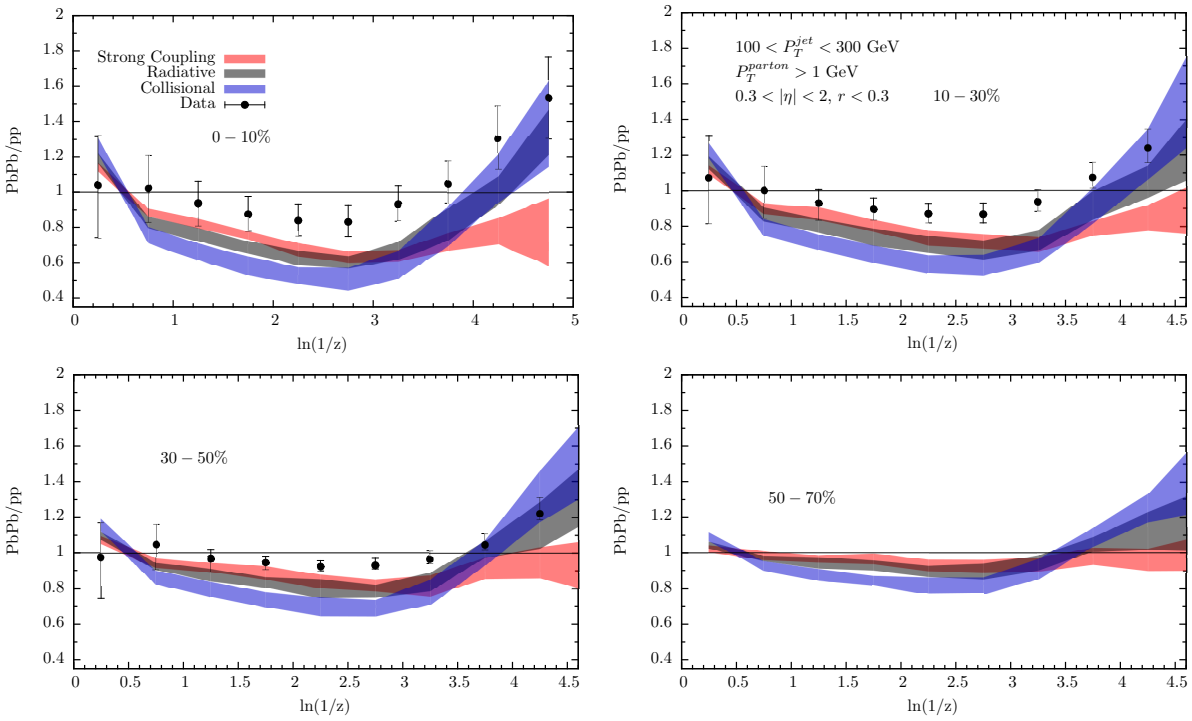

Figure 5-6: Ratio of the partonic level fragmentation function for our quenched jets to that for proton-proton jets in the same reconstructed jet p_T interval $100 < p_T < 300$ GeV, for jets with $0.3 < |\eta| < 2$ and for different centrality bins. The data points are the analogous experimentally measured fragmentation function ratio from Ref. [143], for hadrons rather than partons.

is carried by individual hadrons whereas our calculation is performed at the parton level. As in the experimental analysis in Ref. [24, 143], we determine the jet axis and momentum using the anti-k_t algorithm with $R = 0.3$ and we then search for all the partons in a cone with radius $r \equiv \sqrt{(\Delta\phi)^2 + (\Delta\eta)^2} < 0.3$ centered on the jet axis and use the projection of the parton momentum onto the jet axis to define $z = p_{\parallel}^{\text{parton}}/p^{\text{jet}}$. Since we have stopped the DGLAP evolution in PYTHIA for each parton that reaches a minimum virtuality $Q_0 = 1$ GeV, we stop our computation of the fragmentation function ratio in Fig. 5-6 at $\ln(1/z) = \ln(100) = 4.6$. This also reduces our sensitivity to the effects of hadronization on the fragmentation function, which we are leaving out of our partonic calculation. For z values smaller than our cut, the effects of hadronization become more important, since the dynamics of hadronization can soften particles below 1 GeV.

The overall message from Fig. 5-6 is that the fragmentation function of a quenched jet is very similar to that of a vacuum jet with the same energy as the quenched jet. This was first pointed out in Ref. [24] and remains the case in the data from Ref. [143] that we have shown in the Figure, and it is also the case for our hybrid strongly coupled model. The collisional model that we have set up as a foil in this work does not share this feature. The fragmentation function ratio predicted by the collisional model lies below the data over several decades of $1/z$, meaning that this model can be ruled out by the comparison of its fragmentation function to the data. The fragmentation function ratio predicted by our hybrid strongly coupled model does best, comparing reasonably well with the data in Fig. 5-6. The weakly coupled radiative model fares in between, predicting a fragmentation function ratio that is in some tension with the data, particularly in mid-centrality collisions. It should be noted that since in the case of radiative energy loss the 'lost' energy is expected to include some moderate-p_{T} particles that initially stay within the jet cone, the assumption that we are making in our implementation of this model that all of the 'lost' energy becomes soft particles moving in directions that are uncorrelated with the jet direction may be suspect here. If so, our calculation of the fragmentation function in our implementation of radiative energy loss is incomplete.

Note that in comparing our model calculations of the fragmentation function ratio to data in Fig. 5-6 we are ignoring the softest part of the fragmentation function ratio shown

in the Figure. We do so for two reasons. First, although we have ended our partonic calculation at $Q_0 = 1$ GeV and cut the figure of at $z = 1/100$ precisely to reduce this problem, comparison of our partonic fragmentation functions to the data on hadronic fragmentation functions may not be appropriate at the smallest z's we have plotted, given that hadronization tends to soften softer partons. Second, the low $p_{\rm T}$ particles that populate the smallest z region that we have plotted in Fig. 5-6 have momenta that are small enough that many of them could certainly come from the thermal distribution of particles formed as the quark-gluon plasma cools and hadronizes. The background subtraction procedure used in the analyses of experimental data will subtract such particles, on average, if they are uncorrelated with the jet direction. This subtraction may not be perfect, however, either because of fluctuations in the bulk droplet of plasma or because some of the energy lost by the jet, which we are assuming ends up as a little hotter or a little extra plasma, may also manifest itself in collective motion of the plasma, meaning that although the 'lost' energy becomes soft particles these soft particles might not be completely uncorrelated with the jet direction. For both these reasons, the subtraction of whatever fraction of the 'lost' energy ends up in the jet cone may not be complete. We have checked that adding only one soft particle per jet can result in a substantial upturn in the fragmentation function ratio at $\ln(1/z) \gtrsim 4$, and for this reason we will not compare to the data in this regime. In Section 7 of this part of the thesis we will estimate the effect of the medium response to the jet passage by a complete Monte Carlo simulation, which takes into account that the thermalized energy is still correlated with the direction of the jet and it can have implications for this sort of observables.

We have observed that the collisional model leads to a much stronger depletion of the quenched fragmentation functions relative to what is measured in data, over several decades of z. This is a direct consequence of the lack of path-length dependence in dE/dx in this model, meaning that our conclusion that this model is disfavored seems robust. The radiative model seems to be marginally in agreement with the data. Remarkably, the weaker modification of the in-medium fragmentation function within the strongly coupled hybrid model achieves the best qualitative agreement with the fragmentation function ratio in the experimental data. A more quantitative, and more definitive, statement along these

lines would require including hadronization in our strongly coupled hybrid model, would require investigating where the energy 'lost' by the jet ends up rather than just assuming that it becomes soft particles uncorrelated with the jet direction, and would require including the soft particles corresponding to the plasma itself in our model and subtracting them during jet reconstruction as in the analyses of experimental data. We leave some of these investigations for Section 7 of this thesis.

5.4 Predictions for Single-Jet and Dijet Observables at $\sqrt{s} = 5.02$ ATeV

In this Section we provide predictions for Pb-Pb collisions at $\sqrt{s} = 5.02$ ATeV for the single jet and dijet observables that we presented in detail in previous Sections. This is the center of mass energy per nucleon in the Heavy Ion Run II of LHC, which will deliver much of the data we want to confront our hybrid model with somewhere late this year 2016.

We study 10^6 dijet events in p-p collisions at $\sqrt{s} = 5.02$ TeV generated by PYTHIA 8.183 [121] without any underlying event. For each of the centrality bins we consider, we embed these hard scattering processes into the hydrodynamic simulations along the lines of those in Ref. [131], but now these are simulations of heavy ion collisions with $\sqrt{s} = 5.02$ ATeV. We then follow the procedure for determining the energy loss outlined in Section 4.3. As in our previous computations, we smear our predictions to simulate resolution effects. However, we use the smearing functions determined at $\sqrt{s} = 2.76$ ATeV, since they are yet unknown at $\sqrt{s} = 5.02$ ATeV.

Fig. 5-7 shows the hybrid strong/weak coupling model predictions for the suppression factor R_{AA}^{jet} of jets in heavy ion collisions with $\sqrt{s} = 5.02$ ATeV reconstructed with the anti-k_T algorithm with $R = 0.3$. We do not fit even a single parameter here, or anywhere in this Section. The model is fully constrained by the data on collisions with $\sqrt{s} = 2.76$ ATeV, with its one parameter having been fixed as described in Section 5.1. The width of the displayed bands is a combination of our theoretical uncertainties (estimated by varying the temperature T_c below which we stop quenching, see Section 4.3) together with the experi-

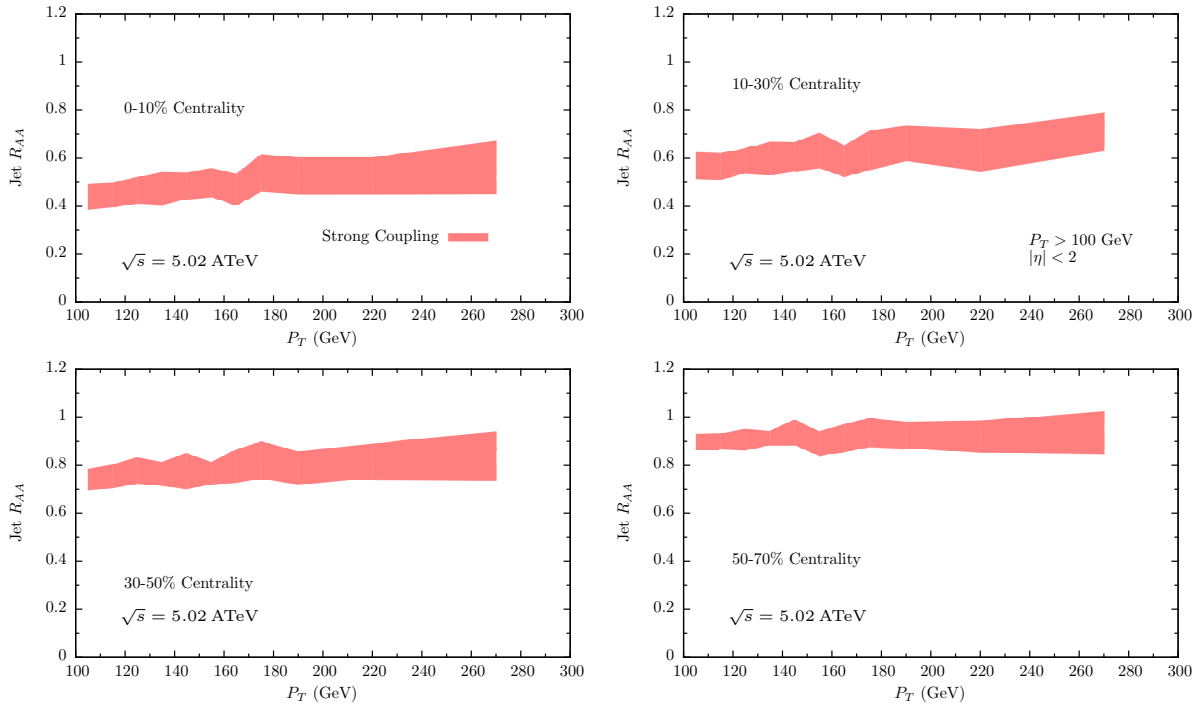

Figure 5-7: Hybrid model prediction for Jet $R_{\rm AA}$ as a function of $p_{\rm T}$ for different centralities at $\sqrt{s} = 5.02$ ATeV. The single model parameter has been fitted to $\sqrt{s} = 2.76$ ATeV data previously and no additional parameters have been introduced.

mental uncertainties in the data that we use to fix the one parameter in each model. Both the centrality dependence and the transverse momentum dependence of $R_{AA}^{\rm jet}$ in collisions with $\sqrt{s} = 5.02$ ATeV are very similar to what we have seen previously at $\sqrt{s} = 2.76$ ATeV, with a slight increase in the suppression of $R_{AA}^{\rm jet}$ at the higher collision energy. Similar conclusions can be drawn from the strong coupling predictions for the dijet imbalance in collisions with $\sqrt{s} = 5.02$ ATeV, displayed in Fig. 5-8. The centrality dependence and the momentum dependence of this observable are very similar at the two collision energies as well.

The sensitivity of these predictions to the form we assume for the rate of energy loss is examined in Fig. 5-9. As at the lower collision energy, this set of predictions shows little discriminating power to our choice among the three models for the rate of energy loss that we have investigated. The strongly coupled form (4.2) for dE/dx leads to a slightly large suppression and a slightly bigger dijet imbalance than the two control models (4.7) and (4.10), bottom-left panel of Fig. 5-9, but the effect is small compared to current

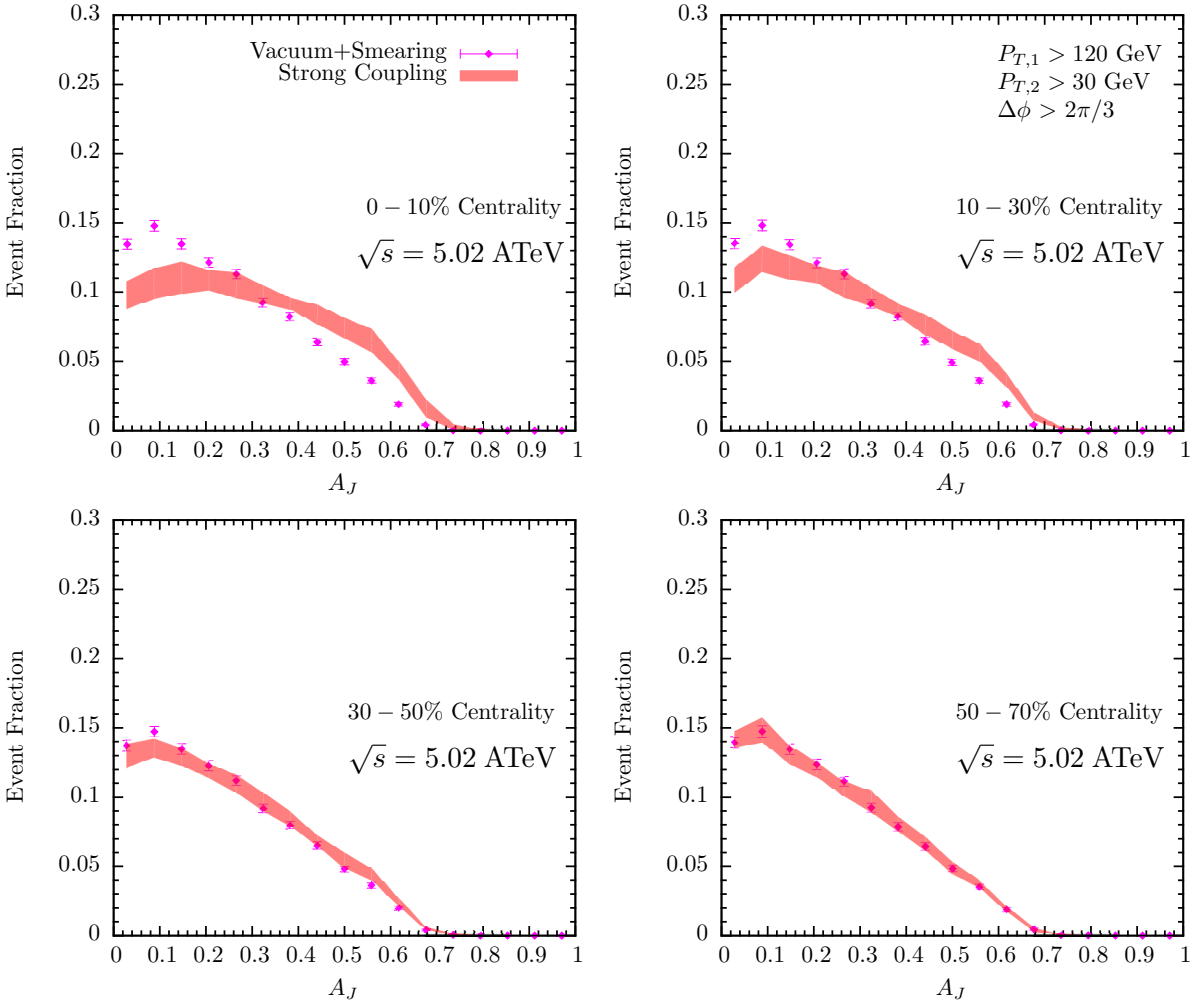

Figure 5-8: Hybrid model predictions for the dijet imbalance A_J in Pb-Pb collisions at $\sqrt{s}$=5.02 ATeV with different centralities. Both the theoretical calculations and the proton-proton reference are smeared according to the prescription in Ref. [141].

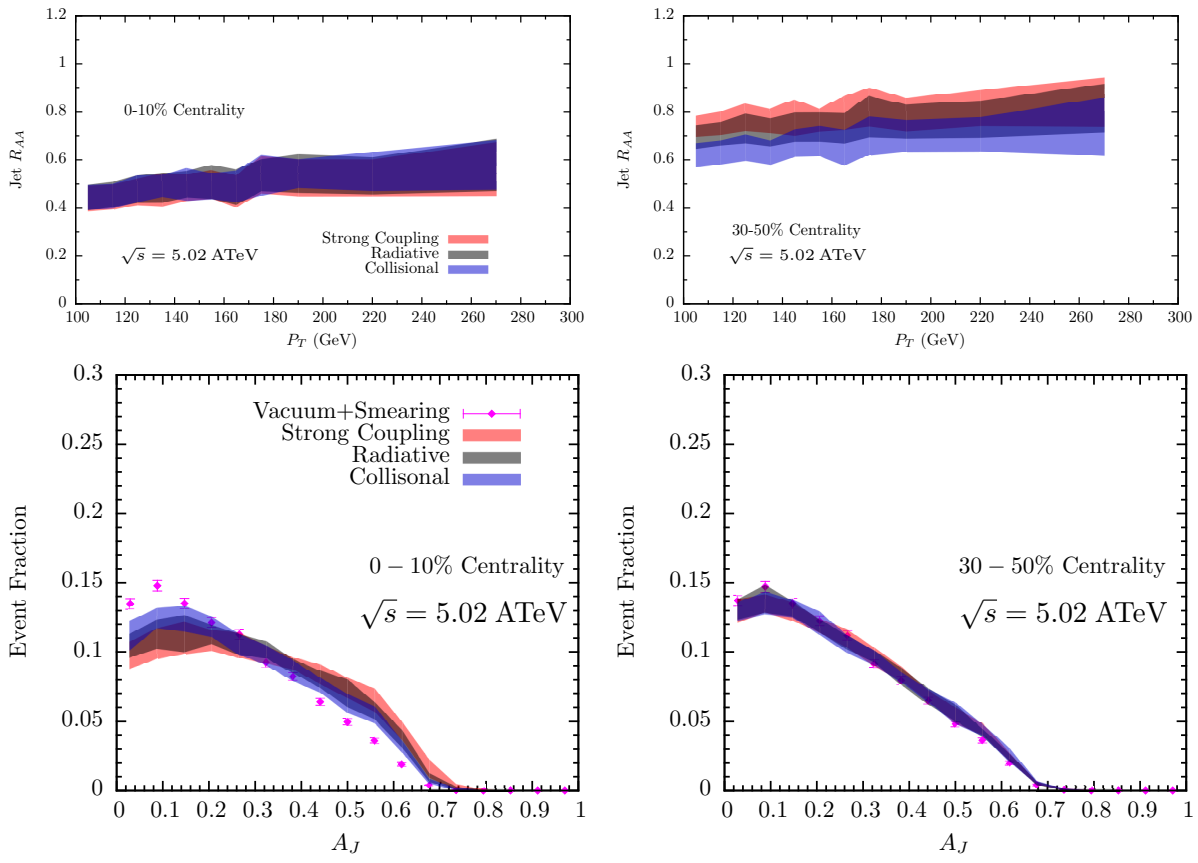

Figure 5-9: Model dependence of dijet observables for Pb-Pb collisions with $\sqrt{s} = 5.02$ ATeV. Upper panel: Jet R_{AA} as a function of p_{T} for LHC collisions in two different centrality bins for the three energy loss models from Section 4.2.1 and Section 4.2.3. Lower panel: Dijet imbalance distribution in two different centrality bins for the three energy loss models.

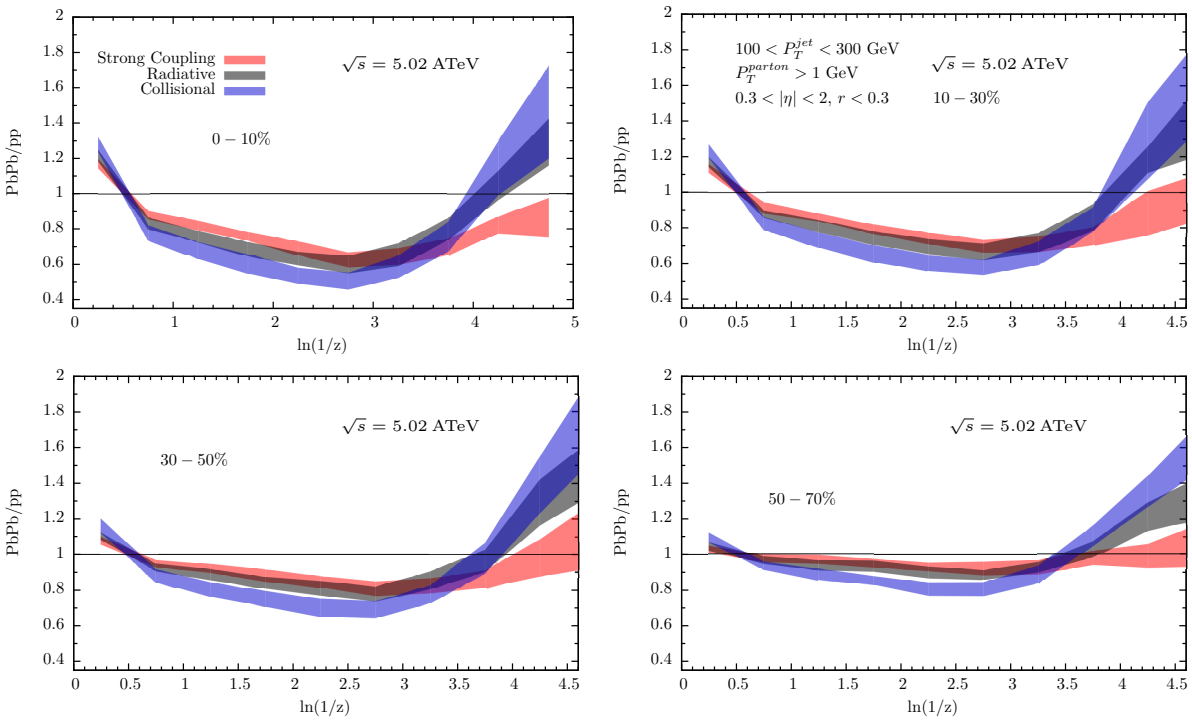

Figure 5-10: Partonic fragmentation functions for jets of $100 < p_{\mathrm{T}}^{\mathrm{jet}} < 300$ GeV in heavy ion collisions with $\sqrt{s} = 5.02$ ATeV for three different models for the rate of energy loss and for four different centralities. Jets are reconstructed with the anti-k_T algorithm with $R = 0.3$. The jet fragments consist of final state partons within a cone of angle $r = 0.3$ around the jet axes determined by the reconstruction algorithm. These partons are classified with respect to the longitudinal variable $z = p^{\parallel}/p^{\mathrm{jet}}$ with $p^{\parallel}$ the momentum of the fragments along the jet axis.

uncertainties. Some separation among models is observed with increasing centrality, top right panel of Fig. 5-9, although the largest centralities are more and more sensitive to the energy lost by energetic partons during the hadronic phase of the collision, which we are neglecting.

Finally, in Figure 5-10 we compare the predictions for partonic fragmentation functions obtained from the three models for the rate of energy loss. These are, again, similar to one another. The modest separation between the model predictions at intermediate values of z observed at $\sqrt{s} = 2.76$ ATeV is also observed at $\sqrt{s} = 5.02$ ATeV. However, the model predictions separate most in the region of $\log z > 3.5$ where they cannot be relied upon. In this softest region of the fragmentation function, there is an additional contribution that is not included in the model: the backreaction of the medium to the jet passing through it will

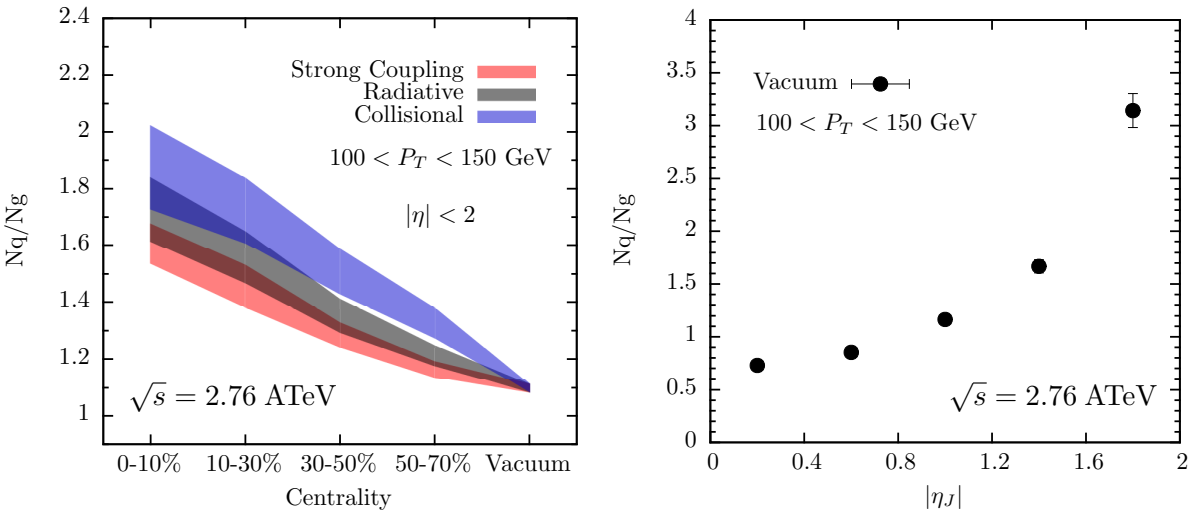

Figure 5-11: Left panel: Ratio of quark-initiated jets to gluon-initiated jets with $|\eta| < 2$ as a function of centrality for different models. Right panel: Ratio of quark-initiated jets to gluon-initiated jets as a function of jet pseudorapidity for p-p collisions in vacuum, according to PYTHIA.

result in additional soft particles in the jet cone.

5.5 Species Dependence of Jet Suppression

In order to investigate the potential species dependence that different quenching mechanisms may present, specially motivated by the relative weight that the energy loss formulas atribute to the color charge dependence, we show in the right panel of Fig. 5-11 the ratio of the number of quark-initiated jets to the number of gluon-initiated jets (N_q/N_g) with jet momenta in the range $100 < p_{\mathrm{T}} < 150$ GeV and $|\eta| < 2$ as a function of centrality for the three models we have studied. We have defined the species of the jet-initiator from our PYTHIA "data" (in a way that is impossible to do in experimental data) as the identity of the parton that initiated the DGLAP shower to which the hardest particle in the jet belongs. Despite the manifest differences between the relative suppression of quarks compared to gluons among the different models, or the different way in which they affect the substructure of the jet (as studied in Section 5.3), there is not much of a strong separation among the three bands. As expected, though, it is the strongly coupled energy loss the one where the differences between quark initiated jets and gluon initiated jets are less pronounced.

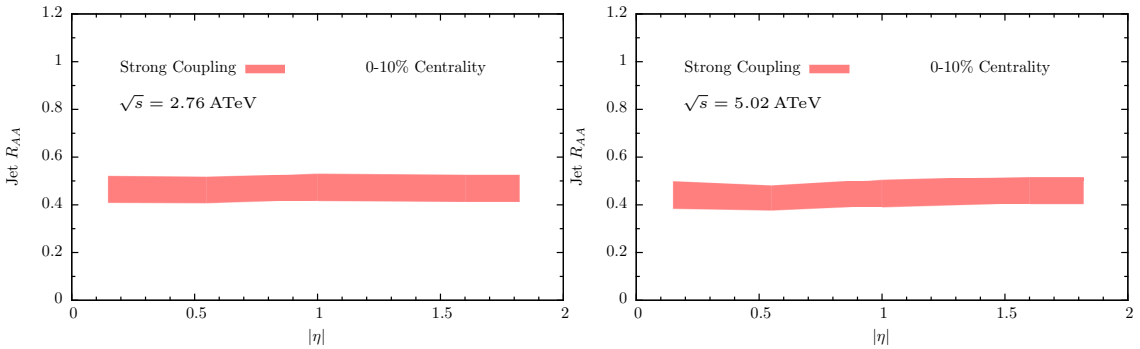

Figure 5-12: Pseudorapidity dependence of jet R_{AA} in our hybrid model for $\sqrt{s} = 2.76$ ATeV (left) and $\sqrt{s} = 5.02$ ATeV (right).

If we did not include flow effects, for those models in which the energy loss rate contains physical quantities which need to be boosted to the local fluid rest frame (for radiative energy loss (4.7) and more importantly for the strongly coupled rate (4.2)) jets at large rapidity would suffer way more quenching than the ones at mid rapidity. Given the great difference in the relative abundance of quark initiated jets with respect to gluon initiated jets as a function of rapidity, as depicted in the right panel of Fig. 5-11 for the vacuum case, the incorrect omission of flow effects would lead to a strong separation of the models when calculating N_q/N_g. This fact stresses the need of performing realistic Monte Carlo simulations in order to effectively assess the true importance of a certain effect when everything else is also taken into account.

We close this section by noting that despite the substantial rapidity dependence of the species-dependence of jet production, and of jet quenching, the resulting net jet $R_{\rm AA}$ is remarkably independent of rapidity in our hybrid model, as shown in Fig. 5-12. This was noted previously in Ref. [144], and we find the same behavior in our control models in which we choose the dependence of dE/dx according to either one of the expressions (4.7) or (4.10). Although given the strong species-dependence manifest in the right panel of Fig. 5-11 the flatness of the rapidity dependence seen in Fig. 5-12 appears coincidental, it is in agreement with experimental results from the ATLAS collaboration [32]. Our understanding of this flatness comes from the fact that the $R_{\rm AA}$ of quark or gluon initiated jets

is not different enough to make the difference in species abundance seen in the left panel of Fig. 5-11 translate into a decrease of quenching. A model which showed such a raise in $R_{\rm AA}$ would be treating quark and gluon jets too differently and its predictions would be in tension with experiments.

5.6 Significance of the Extracted Parameters

We have seen in Section 5 that our hybrid approach, with perturbative QCD (via PYTHIA) describing the parton splitting that occurs within a jet while at the same time each parton in the jet loses energy according to the expression (4.2) for dE/dx for a light quark traveling through strongly coupled plasma, derived via a holographic calculation in Ref. [87], is very successful in describing the available jet data at the LHC. After fixing the one free parameter in the model, defined in (4.3), using the measured value of the suppression factor $R_{\rm AA}$ for jets in one $p_{\rm T}$-bin in the most central Pb-Pb collisions at the LHC, we obtain a completely satisfactory description of the dependence of the jet $R_{\rm AA}$ on both $p_{\rm T}$ and centrality as well as of the dijet asymmetry A_J, including its centrality dependence. In addition, we make predictions for the jet $R_{\rm AA}$ at RHIC. We also find that the (small) deviations between the fragmentation functions of quenched jets measured in heavy ion collisions at the LHC and those of vacuum jets with the same energy as the quenched jets compare well with the corresponding fragmentation function ratios described by our hybrid model.

The above successes are important, but they should not be over-interpreted. The current uncertainties in the measurements of jet $R_{\rm AA}$ translate into a significant dispersion in our theoretical computations, reflected in the width of all the colored bands in our plots in Section 5. And, partly as a consequence of these uncertainties and partly as a consequence of the insensitivity of inclusive jet observables to the mechanism by which energy is lost, we have found that present measurements of the jet suppression factor $R_{\rm AA}$ and the dijet asymmetry A_J are described almost as well if we use the models for dE/dx motivated by weakly coupled radiative or collisional energy loss that we have described in Section 4.2. The comparisons between the partonic fragmentation function ratios that we can compute in our models and the fragmentation functions measured at the LHC that we have made in

	Strong Coupling	Radiative	Collisional
Parameter	$0.32 < \kappa_{\rm sc} < 0.41$	$0.97 < \kappa_{\rm rad} < 1.8$	$1.8 < \kappa_{\rm coll} < 3.0$

Table 5.1: Values of the fit parameters needed in the specification of dE/dx in our three different energy loss models, in each case as extracted by comparing model predictions for $R_{\rm AA}$ for jets with 100 GeV$< p_{\rm T} <$110 GeV in central Pb-Pb collisions at the LHC to experimental data.

Section 5.3 do favor the hybrid strongly coupled approach over the model with collisional energy loss and, to some degree, over the model with radiative energy loss. However, this is a comparison between a partonic calculation and a hadronic measurement, so perhaps we should not take the fact that the data favors the strongly coupled energy loss rate as definitive.

The success (or partial success in the collisional case) of all these energy loss mechanisms, which arise from very different pictures of the underlying dynamics, crucially depends on the freedom to choose the overall strength of energy loss by fitting one model parameter to data. It therefore becomes important to confront the parameters extracted from data to expectations from theoretical calculations.

The three models for dE/dx that we have tested in this work each include one free parameter that we have fitted to experimental measurements of $R_{\rm AA}$ for jets with 100 GeV$<$ $p_{\rm T} <$110 GeV in central Pb-Pb collisions at the LHC. We have collected the values of these parameters obtained via fitting to this data in Table 5.1. See Eqs. (4.3), (4.7) and (4.10) for the definitions of the parameters.

The values of $\kappa_{\rm rad}$ and $\kappa_{\rm coll}$ in the weakly coupled radiative and collisional models for dE/dx obtained via our fit to data should be compared to expectations based upon perturbative calculations given in Eqs. (4.8) and (4.9) and in Eqs. (4.11) and (4.12). We see that our fit to data corresponds to a value of the strong coupling constant α_s that is smaller (larger) than the range $0.2 < \alpha_s < 0.3$ that we used in making the estimate (4.9) for $\kappa_{\rm rad}$ (the estimate (4.12) for $\kappa_{\rm coll}$.) In the case of radiative energy loss, as we discussed in Section 4.2 it may be that we are underestimating $\kappa_{\rm rad}$ because we are neglecting the fact that much of the 'lost' energy is initially radiated in the form of gluons moving in the same direction as the jet, meaning that some of this radiated energy may remain correlated with

the jet direction. If this is so, by neglecting this we would be overestimating the energy loss at a given $\kappa_{\rm rad}$ and hence our fit would be underestimating $\kappa_{\rm rad}$.

As we have discussed in Section 4.2 and as is manifest in Eqs. (4.8) and (4.11), because of rare radiative or collisional processes in which a large momentum is transferred the perturbative evaluation of $\kappa_{\rm rad}$ or $\kappa_{\rm coll}$ leads to logarithms of ratios of scales, $B_{\rm rad}$ and $B_{\rm coll}$, which may depend on the kinematics of the colliding objects and whose evaluation is beyond the accuracy of current theoretical calculations. Since the precise expressions for both $B_{\rm rad}$ and $B_{\rm coll}$ are unknown, it is best to think of our fits to data as constraining the product of the appropriate power of α_s times the appropriate large logarithm, as in the middle expressions in Eqs. (4.9) and (4.12). Our fits yield relatively large values for this product, both in the case of radiative energy loss and in the case of collisional energy loss. If the logarithmic corrections were small, as would be required for the simple perturbative expansion to be accurate, our analysis would yield such large values of α_s that perturbation theory would clearly be invalid. Or, if small values of α_s are chosen, as in the last expressions in Eqs. (4.9) and (4.12), then the logarithms become large which again invalidates the simple perturbative expansion, in this case pointing towards the need for a resummation as discussed in Refs. [116, 117, 118]. Note also that despite our simplified approach to energy loss, our results are compatible with those of more sophisticated approaches, such as those described in Ref. [115], when the large logarithms are evaluated as prescribed in those works. The bottom line for the two weakly coupled models that we have introduced as benchmarks is that within our model context they can describe LHC data on jet $R_{\rm AA}$ and the dijet asymmetry A_J if we choose values of the single parameter in each model that correspond to values of α_s that are large enough to make the reliability of a perturbative calculation questionable. At the same time, as we saw in Section 5.3 the collisional model cannot reproduce LHC data on the fragmentation function ratio and the radiative model is in some tension with this data, at best in marginal agreement with it.

We now turn to the strongly coupled model. The comparison of the value of $\kappa_{\rm sc}$ that we have obtained via fitting our results to jet observables measured in heavy ion collisions at the LHC to the value obtained in theoretical calculations performed holographically, *i.e.* via gauge/gravity duality, is of necessity uncertain. The holographic calculations that we

have employed were done in large-N_c, strongly coupled $\mathcal{N} = 4$ SYM theory, not in QCD. There are by now large classes of theories with known gravitational duals, but the gravitational dual of QCD itself (if one exists) is not known. Present holographic calculations are therefore best used to gain qualitative insights, like for example the form of dE/dx in (4.2) and the parametric dependence of $x_{\rm stop}$ in (4.3). But there is no one right answer for how to compare a numerical value of $\kappa_{\rm sc}$ extracted via comparison to experimental measurements — of course in QCD — to a numerical value of $\kappa_{\rm sc}$ computed in $\mathcal{N} = 4$ SYM theory. That said, it is a generic expectation that the stopping distance $x_{\rm stop}$ will be longer, meaning that $\kappa_{\rm sc}$ will be smaller, in strongly coupled QCD plasma than in strongly coupled $\mathcal{N} = 4$ SYM plasma with the same temperature because QCD has fewer degrees of freedom than $\mathcal{N} = 4$ SYM theory by a factor ≈ 0.4. There are various prescriptions in the literature for how this reduction in the energy density of the plasma at a given temperature may affect holographic calculations of various quantities, but this has not been investigated for the stopping distance of a light quark. And, of course, the QCD plasma differs from that in $\mathcal{N} = 4$ SYM theory in other ways also.

The comparison of the value of $\kappa_{\rm sc}$ that we have extracted via comparison with data to theoretical expectations originating in holographic calculations is further complicated by the fact that, as we have discussed in Section 4.2, theorists have developed several different ways of modeling jets in $\mathcal{N} = 4$ SYM theory, given that jets are not actually produced in hard processes in this theory. Different values of $\kappa_{\rm sc}$ are obtained in $\mathcal{N} = 4$ SYM theory depending on whether a jet is modeled as a single string moving through the plasma, in which case ${\kappa_{\rm sc}}^{\mathcal{N}=4} = 1.05\lambda^{1/6}$ [78], or via analyzing the decay of a virtual external $U(1)$ field into $\mathcal{N} = 4$ SYM matter with initial virtuality q and initial position in the holographic direction D/q with D an unknown factor that is of order unity, in which case ${\kappa_{\rm sc}}^{\mathcal{N}=4} = 1.24D^{1/3}$ [79]. Although these two estimates of $\kappa_{\rm sc}$ differ parametrically, the first being of order $\lambda^{1/6}$ while the second is of order unity, their numerical values are similar. If we set $N_c = 3$, the 't Hooft coupling is $\lambda \equiv g^2 N_c = 12\pi\alpha_s$ meaning that if we choose $0.2 < \alpha_s < 0.3$ this corresponds to $7.5 < \lambda < 11.3$ or $1.4 < \lambda^{1/6} < 1.5$. So, combining the two estimates, we learn that if we apply an $\mathcal{N} = 4$ SYM theory calculation done with $N_c \to \infty$ and $\lambda \to \infty$ to $\mathcal{N} = 4$ SYM theory with $N_c = 3$ and $7.5 < \lambda < 11.3$

we conclude that $1.2 \lesssim {\kappa_{\rm sc}}^{\mathcal{N}=4} \lesssim 1.6$, with the lower end of the range uncertain by a factor that is of order unity. From this we conclude that the value of $\kappa_{\rm sc}$ that we have extracted by comparing our results to experimental data on $R_{\rm AA}$ for jets in the QCD plasma produced in LHC collisions is smaller than that in $\mathcal{N} = 4$ SYM theory by a factor of about 1/3 to 1/4, meaning that $x_{\rm stop}$ is longer in the QCD plasma produced in a heavy ion collision than in the $\mathcal{N} = 4$ SYM plasma by a factor of about 3 to 4.

We conclude that the hybrid strongly coupled approach to jet quenching that we have developed is in good agreement with all the various measured jet observables to which we have compared it in Section 5 when we take all the parametric dependence of dE/dx and $x_{\rm stop}$ from the expressions (4.2) and (4.3) derived for the $\mathcal{N} = 4$ SYM plasma, and set the numerical value of $x_{\rm stop}$ in the QCD plasma longer than that in the $\mathcal{N} = 4$ SYM plasma as expected, longer by a factor of 3 to 4.

Chapter 6

Boson-Jet Correlations, Including Predictions for $\sqrt{s} = 5.02$ ATeV Collisions and for Z-jet Correlations

The extensive exploration in Chapter 5 has demonstrated that the hybrid model that we have developed describes currently available inclusive jet and dijet data from LHC heavy ion collisions rather successfully. This gives us considerable confidence in the model framework. However, this class of observables proves not to be very sensitive to whether we choose dE/dx as in (4.2) (or (4.7) and (4.10)). The distinctions between the strongly coupled form for dE/dx and our two control models provided by these observables are not sufficient to differentiate between these different hypotheses for the microscopic dynamics of energy loss, at least with present uncertainties. The strongly coupled form for dE/dx does provide a better description of the dijet imbalance, but its predictions are not sufficiently distinct from those of the control models. We must, therefore, consider further observables.

In deciding how to go further, we face a choice. We could start adding more physics to the model, which would allow us to confront new classes of observables. For example, if we were to add in the transverse momentum kicks that the medium delivers to the shower partons passing through it, and the recoil that the shower partons delivers to the medium, we could engage with jet shape observables. This is an attractive prospect, but we defer it to Chapter 7. Before adding to the model, and in particular before adding a second free

parameter, it is our responsibility to first ask whether there are further observables that our present model, with its single parameter already fixed as described in the previous Section, could reasonably be expected to describe. This is our goal in this Chapter. For most of the remainder of this Chapter, we turn to observables involving jets back-to-back with either an energetic and isolated photon or a Z-boson. We will keep the parameter $\kappa_{\rm sc}$ in our hybrid model fixed exactly as in the previous Section, and confront our model with existing data on three different observables describing γ-jet correlations in Pb-Pb collisions at $\sqrt{s} = 2.76$ ATeV. As before, our model describes the data well, although it is fair to note in advance that the statistical error bars on these measurements are substantial because to this point the data sets of γ-jet events have not been large. Nevertheless, the confrontation of the hybrid model with these three new sets of data provides a strong independent validation of our hybrid model, which has no further adjustable parameters.

Our central purpose now is to use our hybrid model to provide predictions for the measurements that the data sets with higher statistics by about an order of magnitude that are anticipated late this year will make possible. To this end, we provide predictions for three γ-jet observables and three Z-jet observables in Pb-Pb collisions at $\sqrt{s} = 5.02$ ATeV. In making these predictions, we will keep the parameter $\kappa_{\rm sc}$ in the hybrid model and the parameters $\kappa_{\rm rad}$ and $\kappa_{\rm coll}$ in the control models set to the same values that we obtained in the previous Chapter by fitting to one data point at $\sqrt{s} = 2.76$ ATeV. The principal change in going from $\sqrt{s} = 2.76$ ATeV to $\sqrt{s} = 5.02$ ATeV is a (modest) increase in the temperature of the plasma. The principal effects of this increase arise from the explicit temperature dependence in (4.2) or (4.7) and (4.10), and so are included in our analysis. We are leaving out any small decrease in the values of the κ's that may arise if the plasma becomes slightly less strongly coupled, anticipating that this effect will likely be too small to be resolved given other uncertainties, both theoretical and experimental.

Although the observables that we study in this Section are similar in some respects to those that describe dijet events, since neither γ's nor Z-bosons interact strongly with the plasma, when one triggers on an energetic γ or Z-boson the jets produced in the same hard scattering have points of origin that are distributed through the collision volume differently than is the case for dijet pairs, where selection bias favors points of origin closer to the

surface where at least one of the jets will suffer less energy loss. This means that the jets produced in association with a γ or a Z-boson sample a different path-length distribution than the jets in dijet pairs. A second difference between boson-jet events and dijet events is that both γ's and Z-bosons are much more likely to be produced in association with a quark jet than with a gluon jet. The third difference is that since the γ or Z-boson suffers no energy loss, as they do not interact with the medium, their energy and direction are good proxies for the initial energy and initial direction of the hard parton (usually, the quark) going in the opposite direction. This is quite different than in the case of dijet events, where generically both jets should be expected to have lost some energy. Of course, the hard parton opposite a γ or Z-boson may split into more than one jet; in the analysis of γ-jet and Z-jet correlations, it cannot be assumed that the boson is back-to-back with only one jet in the final state.

6.1 Generation and Selection of Monte Carlo Events

For our study of photon-jet correlations we analyzed 10^5 hard scattering processes, in PYTHIA 8.183 [121] p-p collisions at $\sqrt{s} = 2.76$ TeV and another 10^5 such events in PYTHIA p-p collisions at $\sqrt{s} = 5.02$ TeV. We require at least one photon with a transverse momentum above a desired cut, typically choosing ${p_{\rm T}}^{\gamma} > {p_{\rm T}}^{\rm cut} = 60$ GeV, and with a pseudorapidity in the range $|\eta_\gamma| < 1.44$. We set the ${p_{\rm T}}^{\rm min}$ parameter in PYTHIA (basically, the minimum momentum transfer in the hard processes that PYTHIA is sampling) safely lower than ${p_{\rm T}}^{\rm cut}$, for example choosing ${p_{\rm T}}^{\rm min} = 40$ GeV if we are recording events that include a photon with ${p_{\rm T}}^{\gamma} > 60$ GeV, since PYTHIA does not reliably reproduce the photon spectrum all the way down to its ${p_{\rm T}}^{\rm min}$.[1] The Monte Carlo implementation of these hard scatterings and their embedding into the heavy ion environment is completely analogous to the one performed in the study of the observables of previous Chapter; we refer the reader to Section 4.3 for the details.

Next, we analyze the 10^5 events in order to "measure" each observable that is of in-

[1] For one of our observables, we wanted to include photons with ${p_{\rm T}}^{\gamma} > {p_{\rm T}}^{\rm cut} = 40$ GeV in our analysis. For this observable, we ran 10^5 events with ${p_{\rm T}}^{\rm min} = 20$ GeV.

terest to us. In doing so, we only analyze the (modified) parton showers coming from the hard scattering. We do not include any of the particles that would be created as the hydrodynamic fluid freezes out. This means that we do not have any background particles and we therefore do not perform any background subtraction in our calculation of observables. When we compare to data, we of course compare to measurements made after the experimentalists have done their background subtraction. For this reason, for those observables which have not been fully unfolded in the experimental analysis we include the smearing procedure described in previous Chapter.

Although we of course know (from PYTHIA) exactly which photons in our events are the photons coming from the originating hard process (prompt photons) and which photons are instead produced in the parton shower (fragmentation photons), we do not use this information in our computation of observables. Instead, we perform an isolation analysis of all high energy photons in our Monte Carlo data, patterned upon what experimentalists must do. This procedure allows us to study a sample of photons which is closer to that in experimental analyses, since in experiments prompt and fragmentation photons can only be distinguished via isolation cuts, with finite efficiencies. As it turns out, quenched jets associated with prompt photons constitute about 80% of our final "data" sets, with about 20% coming from fragmentation of jets in events without a prompt photon.

For readers who would like a little more detail, our procedure is as follows. We select events containing at least one photon with ${p_{\rm T}}^{\gamma} > {p_{\rm T}}^{\rm cut}$ and $|\eta_\gamma| < 1.44$. After quenching the parton showers in these events as described above, following the analysis of Refs. [23, 145] we consider a photon to be isolated if the sum of the energy of all the particles within a cone around this photon of radius $\Delta r \equiv \sqrt{\Delta\phi^2 + \Delta\theta^2} = 0.4$ is below 5 GeV. Contrary to what is done in the analysis of experimental data, we perform this isolation cut at the partonic level, instead of at the hadronic level. In the unlikely situation that two or more isolated photons are found in a single event, we treat the one with the highest transverse momentum as the leading photon. Next, we construct a sample of photon-jet pairs from our sample of isolated photons. We reconstruct jets using the anti-k_T algorithm [137, 138], typically choosing $R = 0.3$, and keep those events in which we find an associated jet at an angular distance $\Delta\phi > 7\pi/8$ from the isolated photon. This angular cut suppresses the

contribution of events in which the isolated photon is a fragmentation photon and events with more than one associated jet to our final photon-jet sample.

We generate a sample of Z-jet events via an analogous procedure. We select 10^5 PYTHIA events in which a hard scattering process produces a Z-boson with ${p_{\rm T}}^Z > {p_{\rm T}}^{\rm cut}$, again typically choosing ${p_{\rm T}}^{\rm cut} = 60$ GeV. We need not worry about fragmentation Z-bosons: the large mass of the Z makes it very unlikely that they are produced in the parton showers. We therefore need not apply any isolation procedure: any Z is a prompt Z. For the sake of simplicity, we use the same $p_{\rm T}$ and η cuts applied to photon events. We reconstruct jets using the anti-k_T algorithm as before, again typically choosing $R = 0.3$, and obtain our Z-jet sample by requiring an associated jet at an angular distance $\Delta\phi > 7\pi/8$ from the Z. In experimental measurements, Z-bosons are reconstructed through their di-muon decay. Since high energy muons are not modified at all by their passage through the plasma, and since the properties of the associated jets are the same no matter how the Z-boson decays, to increase the size of our sample we simply do not allow our Z-bosons to decay, keeping all of them in our sample.

6.2 Photon-Jet Observables: Comparison with Experimental Results at $\sqrt{s} = 2.76$ ATeV and Predictions for $\sqrt{s} = 5.02$ ATeV

We use the Monte Carlo samples of photon-jet events, prepared and quenched as described above, to construct different observables which can be confronted with experimental data. In this section, we describe these observables, we show the results obtained from our model for collisions at $\sqrt{s} = 2.76$ ATeV and compare them to data, and we provide the predictions that we obtain from our model for collisions at $\sqrt{s} = 5.02$ ATeV.

We first construct the photon-jet imbalance. This is analogous to the dijet imbalance, except that here we have a photon instead of a leading jet. In the case of dijets we define the associated jet as the jet in the pair that has less transverse momentum, meaning that the ratio of the transverse momentum of the associated jet to that of the leading jet is less than one by

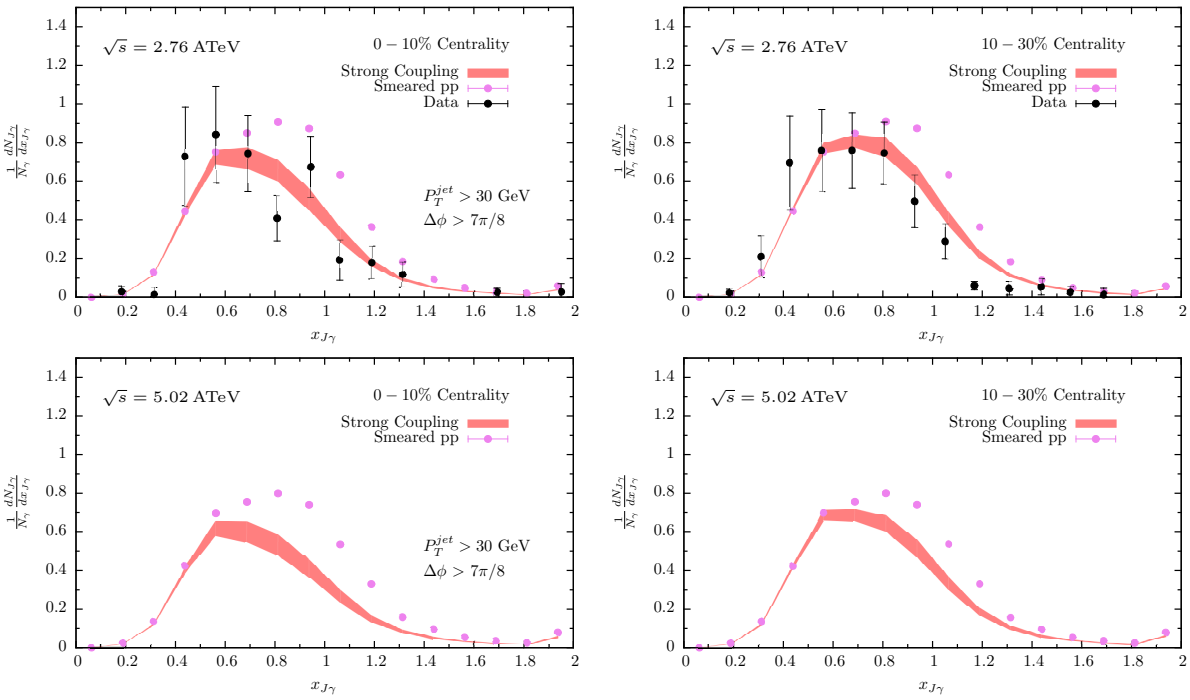

Figure 6-1: Distribution of the transverse momentum imbalance of photon-jet pairs, $x_{J\gamma} \equiv {p_{\rm T}}^{\rm jet}/{p_{\rm T}}^{\gamma}$, for Pb-Pb collisions. The left and right panels show the 0-10% and 10-30% most central events, respectively. The upper panels show our results for collisions with $\sqrt{s} = 2.76$ ATeV, as well as data from Ref. [145]. The lower panels show our predictions for heavy ion collisions with $\sqrt{s} = 5.02$ ATeV, anticipated for late this year.

definition. This is not so in the case of the photon-jet imbalance, since the associated jet can have more or less transverse momentum than the photon. Defining $x_{J\gamma} \equiv {p_{\rm T}}^{\rm jet}/{p_{\rm T}}^{\gamma}$, this observable can be less than or greater than one. For example, in p-p collisions in vacuum, an associated jet can have more transverse momentum than the photon if there is a second jet in the event, in the same hemisphere as the photon. In a heavy ion collision, the energy loss experienced by the partons propagating through the medium pushes $x_{J\gamma}$ downwards. However, if the passing jet sweeps particles from the plasma into the jet cone this can in principle push $x_{J\gamma}$ upwards, but this effect is expected to be small at large energies. Our hybrid model neglects this possibility, meaning that in every event in our sample $x_{J\gamma}$ is less than (or equal to) what it would have been in the absence of the medium.

In Fig. 6-1, we show the distribution of the imbalance in the transverse momentum of the associated jet relative to that of the photon, $x_{J\gamma}$, for events with two different centralities and for events with two different collision energies. Following the conventions established

in the experimental analyses in Refs. [23, 145], these distributions are normalized to the total number of photons, rather than to the total number of photon-jet pairs; integrating each of the curves in Fig. 6-1 therefore yields a number below one. Also as in the experimental analysis, we only consider photons with transverse momentum ${p_{\rm T}}^{\gamma} > 60$ GeV. The associated jet is reconstructed with the anti-k_T algorithm with $R = 0.3$; we only count events in which the associated jet has a transverse momentum ${p_{\rm T}}^{\rm jet} > 30$ GeV. The widths of the colored bands that illustrate our results in this Figure — and in many Figures that follow — incorporate both the uncertainty that comes from varying T_c between 145 and 170 MeV and the uncertainty that comes from varying our model parameter $\kappa_{\rm sc}$ over its allowed range $0.32 < \kappa_{\rm sc} < 0.41$, determined in Section 5.1. That is, we obtain four curves by repeating our calculation of the observable in question, here $x_{J\gamma}$, with T_c and $\kappa_{\rm sc}$ each set to its lowest and its highest value, and plot the band that extends from whichever one of the four curves is lowest to whichever curve is highest at each point in the Figure.

As a reference, in Fig. 6-1 we display the $x_{J\gamma}$ distribution in p-p collisions at the same nucleon-nucleon energy as predicted by PYTHIA, *i.e.* with no medium-induced parton energy loss. In order to mimic the effects of jet-energy resolution on the transverse momentum of the associated jet obtained in the analysis of the Pb-Pb data after the subtraction of the background, in our p-p results we have smeared the momenta of the associated jets obtained from our Monte Carlo calculation with a centrality-dependent Gaussian broadening. The parameters of this smearing, reported in Ref. [141], were tuned to reproduce the measured distributions after embedding PYTHIA-generated photon-jet samples into real lead-lead events. For this reason, the smeared proton-proton distribution is not identical in the left and right panels of Fig. 6-1, which display our results for Pb-Pb collisions with two different centralities. For the present, these smeared p-p results are the correct reference to which both the experimental results as measured by the CMS collaboration [22] and our results for quenched jets in Pb-Pb collisions should be compared. (See Ref. [146] for fully unfolded experimental results to come.) Given that in our Pb-Pb simulations there is no background, and consequently no background subtraction effects, in obtaining the results represented by the colored bands in Fig. 6-1 we have applied the same smearing procedure to our simulated quenched jets. The smearing parameters are at present known only for

$\sqrt{s} = 2.76$ ATeV, not for $\sqrt{s} = 5.02$ ATeV. For the present, we have decided to employ the same smearing parameters at the higher collision energy. Our predictions therefore assume that the effects of background subtraction on these observables are similar at these two collision energies.

The differences between the (smeared) proton-proton Monte-Carlo data and the results of our in-medium calculations displayed in Fig. 6-1 are due to energy loss. The sample of isolated photons we have used to construct these distributions is dominated by prompt photons, which do not lose momentum when traversing the plasma.[2] The partons in the showers that become the associated jets, however, interact strongly with the medium and lose energy according to (4.2) as they propagate through it. In some cases, this pushes the transverse energy of the associated jet below 30 GeV, meaning that the event does not get counted as a photon-jet in our Pb-Pb analysis although it was counted in our p-p analysis. This is why the integrals of the curves illustrating our Pb-Pb results in Fig. 6-1 are smaller than the integrals of our p-p results. More on this below. In other cases, when the transverse energy of the associated jet remains above 30 GeV, the effect of the energy loss is to reduce $x_{J\gamma}$, displacing the photon-jet imbalance distribution toward smaller values of $x_{J\gamma}$.

Keeping in mind that we fixed the single parameter in our hybrid model by comparing it to the single-jet suppression R_{AA}, see Section 5.1, it is remarkable how well the photon-jet imbalance distribution that we obtain from our model agrees with CMS measurements in $\sqrt{s} = 2.76$ ATeV collisions in both centrality bins in Fig. 6-1. The fact that only one side of photon-jet pair loses energy makes the interpretation of this observable cleaner than in the case of the dijet imbalance. Of course, at present the large statistical uncertainties in the photon-jet measurements is a limitation on their use to differentiate between different model assumptions for the rate of energy loss dE/dx, which is to say a limitation on their use as diagnostics of the mechanism of energy loss. We illustrate this point Section 6.4, where we present the results that we obtain by repeating our photon-jet and Z-jet calculations using the control models for dE/dx in (4.7) or (4.10). We find that these control models make predictions that *are* distinct from those of our hybrid strong/weak coupling

[2]The small fraction of fragmentation photons which fulfill the isolation requirement do suffer energy loss via the quenching of the partons from which they originate. This effect is small for this observable, but it can have consequences for more differential observables, as we will discuss below

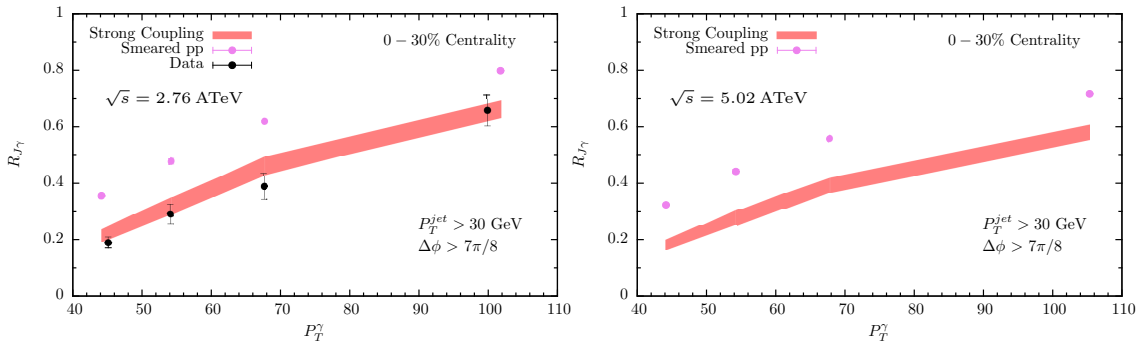

Figure 6-2: Fraction of events with an isolated photon in which we find a photon-jet pair, which is to say in which we find an associated jet with $p_{\rm T}^{\rm jet} > 30$ GeV at an azimuthal angle more than $7\pi/8$ away from that of the isolated photon. We plot this fraction as a function of the photon transverse momentum, in collisions with $\sqrt{s} = 2.76$ ATeV (left) and $\sqrt{s} = 5.02$ ATeV (right). The colored band shows the results from our hybrid model, with its strongly coupled form for the rate of energy loss. For comparison, the violet dots show the smeared p-p calculations (see text for details). Our results for $\sqrt{s} = 2.76$ ATeV are compared to CMS data [145].

model, with dE/dx given by (4.2), but the distinctions are too small to be resolved by the present data, with their statistical uncertainties.

Given these considerations, perhaps the most important results that we can use our model to provide are our predictions for the upcoming runs of the LHC, at $\sqrt{s} = 5.02$ ATeV, where the photon-jet data sets are expected to be larger by about an order of magnitude and the statistical uncertainties are expected to be substantially smaller than at present. For this reason, in the lower panels of Fig. 6-1 we show the predictions of our hybrid model, with its strongly coupled form for the rate of energy loss, for the photon-jet imbalance distribution in Pb-Pb collisions at $\sqrt{s} = 5.02$ ATeV. We have applied the same kinematical cuts used in current measurements (and our calculations) at $\sqrt{s} = 2.76$ ATeV. The imbalance distribution shows little dependence on the collision energy.

To further test the success of our hybrid approach, we now turn to exploring other photon-jet observables. In Fig. 6-2 we show the fraction of isolated photons that come with an associated jet, as reconstructed with the anti-k_T algorithm with $R = 0.3$, that has $p_{\rm T}^{\rm jet}$> 30 GeV and $\Delta\phi > 7\pi/8$. We plot this quantity, which we denote by $R_{J\gamma}$, as a function of the transverse momentum of the isolated photon for heavy ion collisions with $\sqrt{s} = 2.76$ ATeV (left) and $\sqrt{s} = 5.02$ ATeV (right). In the plots in Fig. 6-2, the

smeared proton-proton PYTHIA simulations are represented by the violet dots, the results of our hybrid strong/weak coupling model are represented by the colored band, and the experimental results from Ref. [145] for $\sqrt{s} = 2.76$ ATeV are the black data points.[3] The broad $x_{J\gamma}$ distribution seen in Fig. 6-1 implies that this ratio must be an increasing function of ${p_{\rm T}}^{\gamma}$ for both collision energies, since the 30 GeV cut on the associated jet energy is more and more easily satisfied as the momentum of the photon is made larger and larger. Quenching reduces $R_{J\gamma}$ since it pushes the energy of some of the associated jets below 30 GeV. As for the photon-jet imbalance distribution, we find good agreement between the $R_{J\gamma}$ obtained from our hybrid model and that measured in present experiments with $\sqrt{s} = 2.76$ ATeV, in this case for all values of the photon momenta.[4] Our predictions for heavy ion collisions with $\sqrt{s} = 5.02$ ATeV are shown in the right panel of Fig. 6-2. As before, this observable shows little sensitivity to the collision energy, at least within these kinematical cuts.

We have also analyzed the spectrum of jets produced in association with an isolated photon. In Fig. 6-3, we show the ratio of the spectrum of associated jets in Pb-Pb collisions to that in proton-proton collisions, I_{AA}, for two different ranges of photon transverse momenta, 60 GeV$<{p_{\rm T}}^{\gamma}<$80 GeV and ${p_{\rm T}}^{\gamma} > 80$ GeV. The observable I_{AA}, and in particular its suppression below 1, can be thought of as the photon-jet analogue of the single-jet suppression R_{AA}, but instead of being constructed for inclusive jets as R_{AA} is, I_{AA} is constructed using only the associated jets back-to-back with an isolated photon. This implies that the distribution of the jet energies as well as the fragmentation pattern and hence the jet masses, of the p-p jets and of the Pb-Pb jets that enter into the calculations of I_{AA} and R_{AA} are different. Furthermore, the distribution of the point in the transverse plane at which the hard scattering event that produces a jet selected in an I_{AA} analysis is quite different from that for the jets selected in an R_{AA} analysis. It is therefore striking that even though we fitted the single parameter in our hybrid model to a single measured value of R_{AA}, when we compare the results for the photon-jet I_{AA} obtained from the model with data at

[3]Note that the ratio of the integral of the photon-jet imbalance in Pb-Pb collisions to that in p-p collisions, see Fig. 6-1, is the ratio of $R_{J\gamma}$ for all photons with ${p_{\rm T}}^{\gamma} > 60$ GeV in Pb-Pb collisions to that in p-p collisions. The fact that the colored band lies below the violet dots in Fig. 6-2 was therefore foreshadowed in Fig. 6-1.

[4]Note that in order to extend our calculations of $R_{J\gamma}$ down to 40 GeV$<{p_{\rm T}}^{\gamma}<$50 GeV we used a sample of Monte Carlo events with the PYTHIA parameter ${p_{\rm T}}^{\rm min}$ set to 20 GeV.

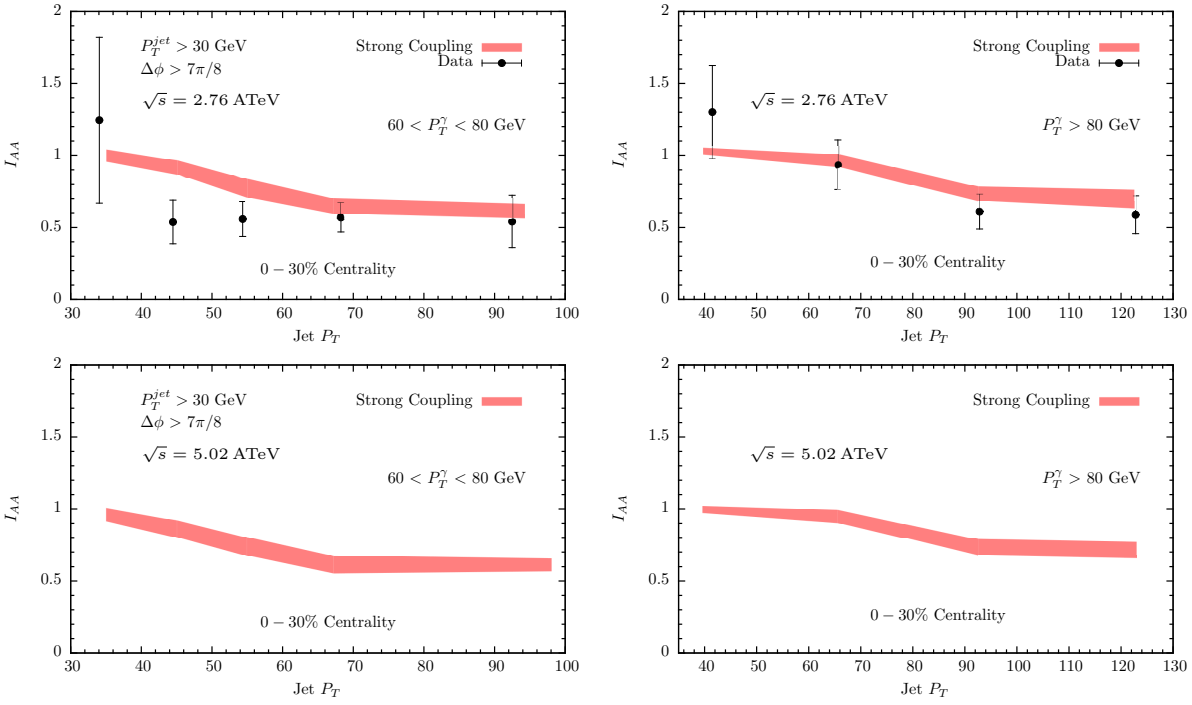

Figure 6-3: Ratio of the transverse momentum spectra of jets associated with an isolated photon in Pb-Pb collisions to that in p-p collisions, as a function of the jet transverse momentum, for two different ranges of the photon transverse momentum and for $\sqrt{s} = 2.76$ ATeV (upper panels) and $\sqrt{s} = 5.02$ ATeV (lower panels). The hybrid model with its strongly coupled form for the rate of energy loss describes the available CMS data at $\sqrt{s} = 2.76$ ATeV well.

$\sqrt{s} = 2.76$ ATeV, displayed in the upper panels of In Fig. 6-3, we see such good agreement, for both ranges of the photon energy and over the whole range of jet $p_{\rm T}$. In the lower panels of Fig. 6-3, we show the predictions from our hybrid model with its strongly coupled rate of energy loss for heavy ion collisions with $\sqrt{s} = 5.02$ ATeV. As for the previous photon-jet observables, the spectrum of the associated jets hardly changes between these two collision energies.

The agreement between the predictions of our hybrid strong/weak coupling model, with its PYTHIA branching and its strongly coupled form for the rate of energy loss, for all of these photon-jet observables and the data available today is very encouraging. Having fixed the single parameter in our model using a single measurement of R_{AA} for inclusive jets, without introducing any new parameters we have obtained a good description of the experimental data for a total of 5 different observables, one involving inclusive jets, one involving dijets, and three involving photon-jets, all with their centrality and energy dependence. These observables sample different in-medium path length distributions of the quenched jets, different shapes of the original jet spectrum, different fragmentation patterns and jet mass distributions, and different quark vs. gluon compositions of the observed jets. Despite all these differences, our model is able to describe the systematics observed in all the data correctly. To avoid over-reaching in drawing conclusions, however, it is important to explore the predictions of the different control models described in Section 4.2.3 for these observables. The results of this analysis can be found in Section 6.4. There are distinctions between the predictions of the control models and our hybrid model, but these distinctions are small compared to the statistical uncertainties in present data. It is therefore not possible at present to use the agreement between our hybrid model and photon-jet data to argue that the data favors a strongly coupled form for the rate of energy loss. We therefore await the higher statistics data expected later this year in collisions with $\sqrt{s} = 5.02$ ATeV, and have provided the predictions of our hybrid model for all three photon-jet observables for collisions at this higher energy. We have also provided such predictions for Z-jet observables below, in Section 6.3. In addition, it is important to investigate the predictions of our hybrid model for intra-jet observables like fragmentation functions, as we shall do in Section 6.5. These are all paths toward using jet data in the service of understanding the dynamics of

the interaction between energetic partons and strongly coupled plasma. In particular, once the statistical precision of the experimental data increases we look forward to identifying deviations between the predictions of our hybrid model and various experimental data as this will allow us to begin to see, quantify, and understand the effects of the physical effects that we are leaving out in our present simple, one-parameter, hybrid model.

6.3 Z-Jet Observables: Predictions for $\sqrt{s} = 5.02$ ATeV

In this section, we turn to the Z^0-jet observables that are complementary to the photon-jet observables of the previous Section. The large Z-mass ensures that Z-bosons seen in a heavy ion collision were almost without exception produced promptly, in hard processes dominated by short-distance physics: it is extremely unlikely for a Z-boson to be produced during the fragmentation of a parton in a jet, unless the jet energy is much higher than is relevant to us. The Z-boson production mechanism is therefore under good theoretical control.[5] Furthermore, because of their large width and short lifetime, Z-bosons decay during the very early stage of a heavy ion collision, even prior to plasma formation. The Z-bosons that are identified in heavy ion collisions are those that decayed leptonically, in particular via $Z^0 \to \mu^+\mu^-$. This means that their decay products do not interact strongly with the pre-equilibrium partonic matter or with the strongly coupled plasma, once it forms. Z-bosons are in this respect similar to prompt photons, making Z-jet events similar in their utility to photon-jet events. The Z-jet events come with the added advantage almost all Z's are prompt Z's. As consequence, the experimental identification of Z-bosons via their $\mu^+\mu^-$ decays do not require isolation cuts, which leads to an arguably cleaner determination of the associated jet energy. The only disadvantage of Z-jet events is that Z's are less numerous than photons.

We construct the same class of observables for Z-jet events that we constructed for photon-jet events in the previous Section. Because of the low statistics of Z-boson production in $\sqrt{s} = 2.76$ ATeV collisions, no constraining measurements exist at present for

[5]Note, of course, that modifications of the nuclear parton distribution function in the relevant intermediate x-region can alter the production rate of Z-bosons, by modifying the composition of the initial flux of partons.

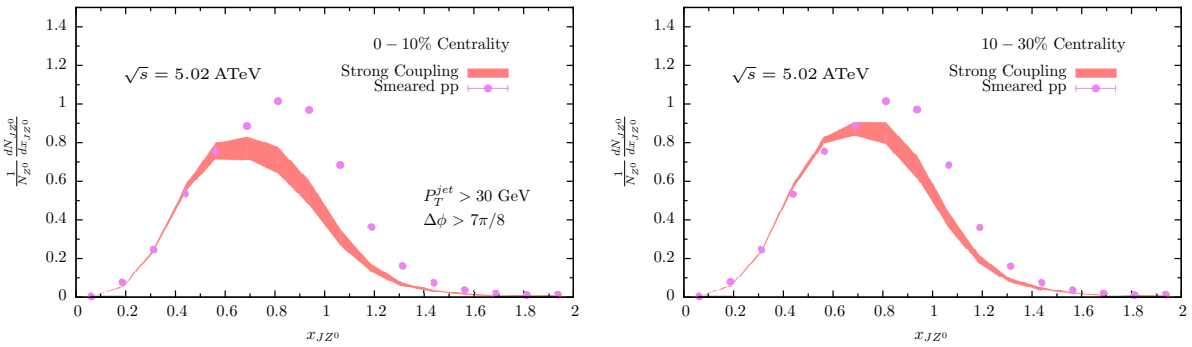

Figure 6-4: Distribution of the transverse momentum imbalance of Z-jet pairs, $x_{JZ} \equiv {p_{\rm T}}^{\rm jet}/{p_{\rm T}}^{\rm Z}$, for Pb-Pb collisions with $\sqrt{s} = 5.02$ ATeV. The left and right panels show the 0-10% and 10-30% most central events, respectively. Here and below, the colored bands show the results from our hybrid model, with its strongly coupled form for the rate of energy loss and the violet dots show the smeared p-p calculations for comparison.

the Z-jet observables that we shall construct.[6] We therefore present predictions for these observables in the $\sqrt{s} = 5.02$ ATeV heavy ion collisions coming soon in LHC heavy ion Run 2. We have chosen the same kinematical cuts for the Z-jet observables that we (and the CMS collaboration) have used in photon-jet observables, to facilitate comparison between our results for the two cases. Of course, once the experimentalists decide on the cuts that they will use for their Z-jet analyses of the data-to-come, we can re-run our analyses with their cuts.

In Fig. 6-4, we show the distribution of the Z-jet imbalance observable $x_{JZ} \equiv {p_{\rm T}}^{\rm jet}/{p_{\rm T}}^{\rm Z}$, in heavy ion collisions with two different ranges of centrality with $\sqrt{s} = 5.02$ ATeV. In both cases the colored band shows the predictions of our hybrid model, with its strongly coupled form (4.2) for the rate of energy loss, for Pb-Pb collisions and the violet dots show the distribution of x_{JZ} for p-p collisions as predicted by PYTHIA. As we did in our analysis of photon-jet observables, we have smeared the momenta of the associated jets in both our Pb-Pb and p-p calculations. For the present, before better guidance becomes available once experimentalists have begun the analysis of LHC Run 2 data, we have used the same smearing functions here as we (and the CMS collaboration) used for the photon-jet observables that we discussed in the previous Section. We obtained the x_{JZ} distributions in Fig. 6-4 from a sample of events in which we required a Z-boson with ${p_{\rm T}}^{Z} > 60$ GeV

[6] For preliminary low-statistics measurements of Z-jet correlations at $\sqrt{s} = 2.76$ ATeV, see Ref. [**?**].

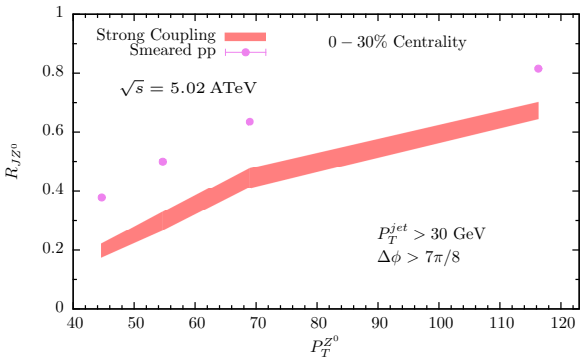

Figure 6-5: Fraction of events with a Z-boson in which we find a Z-jet pair, which is to say in which we find an associated jet with $p_{\rm T}^{\rm jet} > 30$ GeV at an azimuthal angle more than $7\pi/8$ away from that of the Z-boson, in collisions with $\sqrt{s} = 5.02$ ATeV.

and an associated jet reconstructed using the anti-k_T algorithm with $R = 0.3$ that has $p_{\rm T}^{\rm jet} > 30$ GeV and is separated in azimuthal angle from the Z-boson by $\Delta\phi > 7\pi/8$. We required that both the Z and the associated jet have $|\eta| < 1.6$. As in the case of the $x_{J\gamma}$ distribution in photon-jet events, the x_{JZ} distribution is broad in p-p collisions, indicating the importance of events with a Z and two jets, in particular those arising from initial state radiation. This means that at present Z-bosons are not substantially better as taggers of the associated jet energy than photons are, which motivates the future development of methods to suppress events with more than one jet in the final state. Because the transverse momentum of the Z-boson and its $\mu^+\mu^-$ decay products do not change in the medium, the difference between the Pb-Pb distribution and the p-p distribution in our calculation is entirely due to the energy lost by the partons in the associated jet in the Pb-Pb collisions due to their passage through the strongly coupled plasma. As for photon-jet events, we see a reduction in the integral of x_{JZ}, analyzed further below, and a displacement of the distribution toward smaller x_{JZ}. The magnitude of this displacement is comparable to the corresponding shift in the $x_{J\gamma}$ distribution in photon-jet events, see Fig. 6-1. As in that case, there are clear but small distinctions between the results we obtain with our hybrid model, shown in Fig. 6-4, and those we obtain when we use our control models for the rate of energy loss (4.7) and (4.10) instead. We present these in Section 6.4.

In Fig. 6-5, we compute the fraction of Z-bosons in our sample that come with an associated jet, as reconstructed with the anti-k_T algorithm with $R = 0.3$, that has $p_{\rm T}^{\rm jet} > 30$ GeV

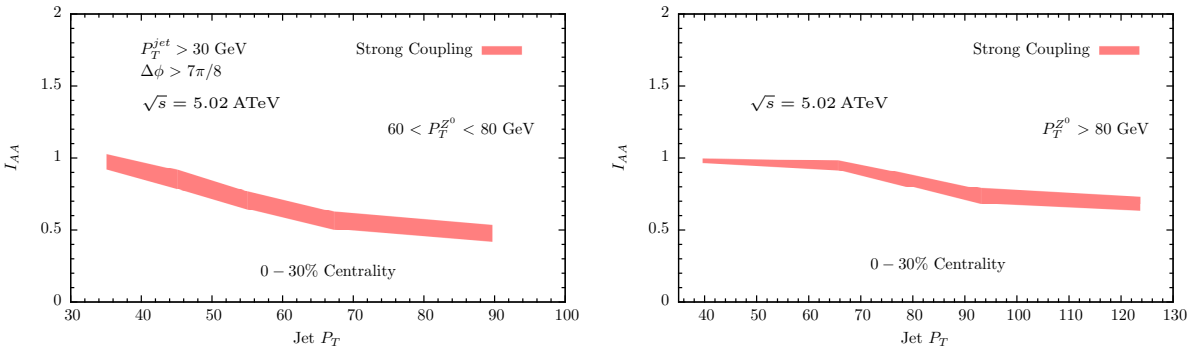

Figure 6-6: Ratio of the transverse momentum spectra of jets associated with a Z-boson in Pb-Pb collisions with $\sqrt{s} = 5.02$ ATeV to that in p-p collisions as a function of the jet transverse momentum, for two different ranges of the Z-boson transverse momentum.

and $\Delta\phi > 7\pi/8$. We plot this quantity, which we denote by R_{JZ}, as a function of the transverse momentum of the Z-boson. We show the results obtained from our smeared proton-proton PYTHIA simulations as the violet dots and the predictions for Pb-Pb collisions from our hybrid strong/weak coupling model as the colored band. As in the photon-jet case, as the partons in the associated jet shower lose energy the total energy of the associated jet can drop below our $p_{\rm T}^{\rm jet} = 30$ GeV cut, meaning that energy loss leads to a reduction of the Z-jet yield as a fraction of the number of Z-bosons. This makes the integral under the colored bands in Fig. 6-4 less than that under the violet dots there, and it pushes the colored band in Fig. 6-5 below the violet dots. The qualitative behavior and magnitude of this reduction is comparable to the reduction in the analogous photon-jet observable, see Fig. 6-2.

Finally, in Fig. 6-6 we analyze the spectrum of jets produced in association with a Z-boson. We show the ratio of the spectrum of associated jets in Pb-Pb collisions to that in p-p collisions, I_{AA}, for two different ranges of Z-boson transverse momenta, 60 GeV$<$ $p_{\rm T}^{\rm Z}$ $<$80 GeV and $p_{\rm T}^{\rm Z}$ $>$80 GeV. The effect of energy loss on this observable is again comparable to its effects on the analogous photon-jet observable, see Fig. 6-3.

In Section 6.4, we repeat the analysis of R_{JZ} and I_{AA} for jets produced in association with a Z-boson in our control models, where we use the expressions (4.7) and (4.10) for the rate of energy loss. We find that these observables exhibit little sensitivity to the form of dE/dx, meaning little sensitivity to the microscopic dynamics via which the partons in

the jet shower interact with the strongly coupled plasma.

In Sections 6.2 and 6.3, we have provided predictions for three photon-jet observables and three Z-jet observables in heavy ion collisions with $\sqrt{s} = 5.02$ ATeV obtained from our hybrid strong/weak coupling model, with fragmentation taken from PYTHIA and a rate of energy loss (4.2) as at strong coupling. We await the data that will come from LHC heavy ion Run 2 with considerable anticipation.

6.4 Model Dependence of Boson-Jet Correlations

In this Section, we study the sensitivity of the different photon-jet and Z-jet observables that we have considered in Sections 6.2 and 6.3 to the microscopic mechanism responsible for energy loss. To do so, we repeat our analysis with the strongly coupled form for the rate of energy loss (4.2) that we use in our hybrid model replaced by one or other of the expressions (4.7) and (4.10) that define our two control models, which are inspired by the radiative and collisional energy loss mechanisms. As in the strong coupling case, these expressions for dE/dx also contain a single parameter which is fitted to the single-jet production rate at one transverse momentum and centrality. The values of the parameters obtained from these fits are summarized in Table 5.1.

In Fig. 6-7 we show the results that we have obtained from the hybrid strong/weak coupling model and our two control models for the photon-jet observables that we have analyzed in heavy ion collisions with $\sqrt{s} = 2.76$ ATeV. The procedure for determining each of the observables is identical for all models and is described in Section 6.2. These plots make clear that the uncertainties in the present low-statistics data are too large to make it possible to use the photon jet imbalance or the spectrum of jets produced in association with isolated photons or the fraction of isolated photons with an associated jet to differentiate between microscopic models of the dynamics of energy loss. Within the current uncertainties, all the models agree with the CMS data displayed in these plots. The photon-jet imbalance in central collisions, top left panel of Fig. 6-7, does have modest power to discriminate between the strongly coupled model and the control models. This indicates that the higher statistics photon-jet data sets anticipated in LHC heavy ion Run 2 could shed

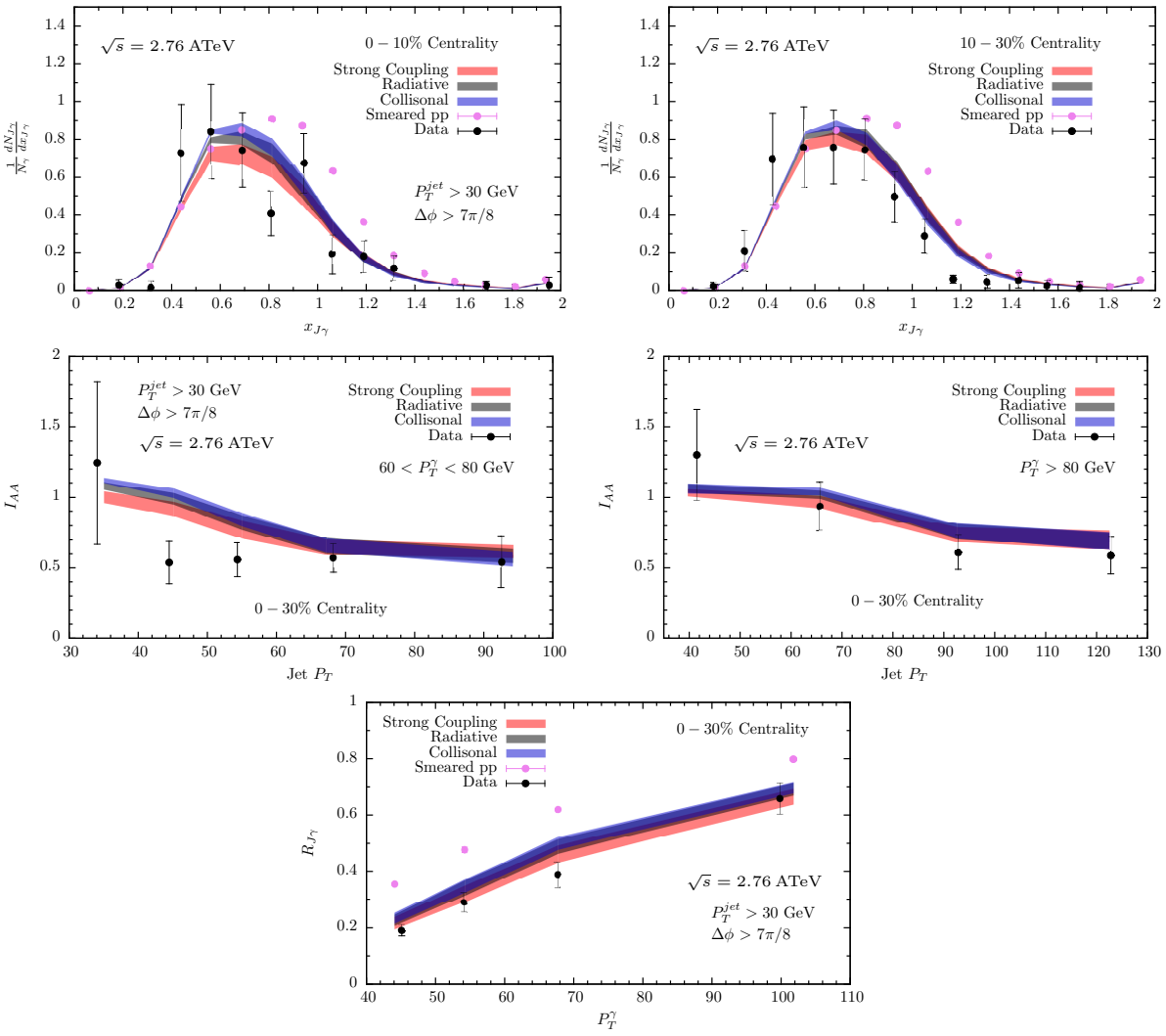

Figure 6-7: Computations of several photon-jet observables using three different models of the energy loss mechanism for heavy ion collisions with $\sqrt{s} = 2.76$ ATeV. The distributions of the transverse momentum imbalance of photon-jet pairs for two different centralities are displayed in the upper panels. The middle panel shows the ratio of the transverse momentum spectra of jets produced in association with an isolated photon in Pb-Pb collisions to that in p-p collisions for two different centralities. The lower panel shows the fraction of isolated photons produced in association with a hard jet with $p_{\mathrm{T}}{}^{\mathrm{jet}} > 30$ GeV at an azimuthal angle more than $7\pi/8$ away from that of the isolated photon. Data are taken from Ref. [145].

light on the microscopic dynamics via which jets lose energy, as well as on the quantitative validity of the simplifying assumptions inherent in our hybrid model.

To better compare our computations with future higher statistics data from LHC heavy ion Run 2, we also explore the model predictions of the different energy loss mechanisms for both photon-jet observables, displayed in Fig. 6-8, and Z-jet observables, displayed in Fig 6-9, in heavy ion collisions with $\sqrt{s} = 5.02$ ATeV. As at the lower collision energy, little discriminating power is observed. Again as at the lower collision energy, there is some separation among the predictions of our hybrid model with its strongly coupled rate of energy loss and the control models in the photon-jet and Z-jet momentum imbalance distributions in the most central collisions, displayed in the upper-left panels of Figs. 6-8 and 6-9, respectively.

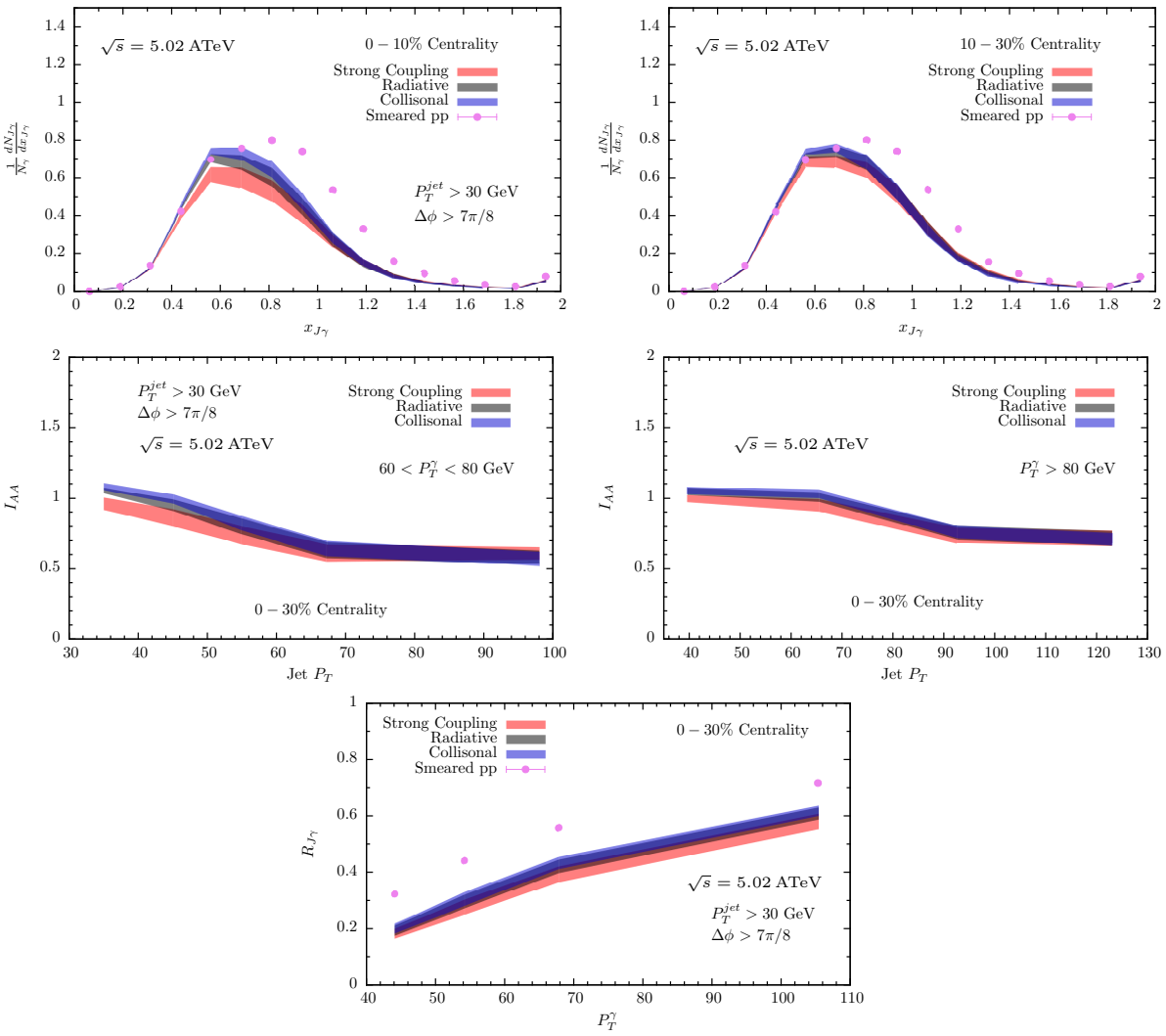

Figure 6-8: Predictions for several photon-jet observables computed with three different models of the energy loss mechanism in heavy ion collisions with $\sqrt{s} = 5.02$ ATeV. The distributions of the transverse momentum imbalance of photon-jet pairs for two different centralities are displayed in the upper panels. The middle panel shows the ratio of the transverse momentum spectra of jets produced in association with an isolated photon in Pb-Pb collisions to that in p-p collisions for two different centralities. The lower panel shows the fraction of isolated photons produced in association with a hard jet with $p_{\mathrm{T}}^{\mathrm{jet}} > 30$ GeV at an azimuthal angle more than $7\pi/8$ away from that of the isolated photon.

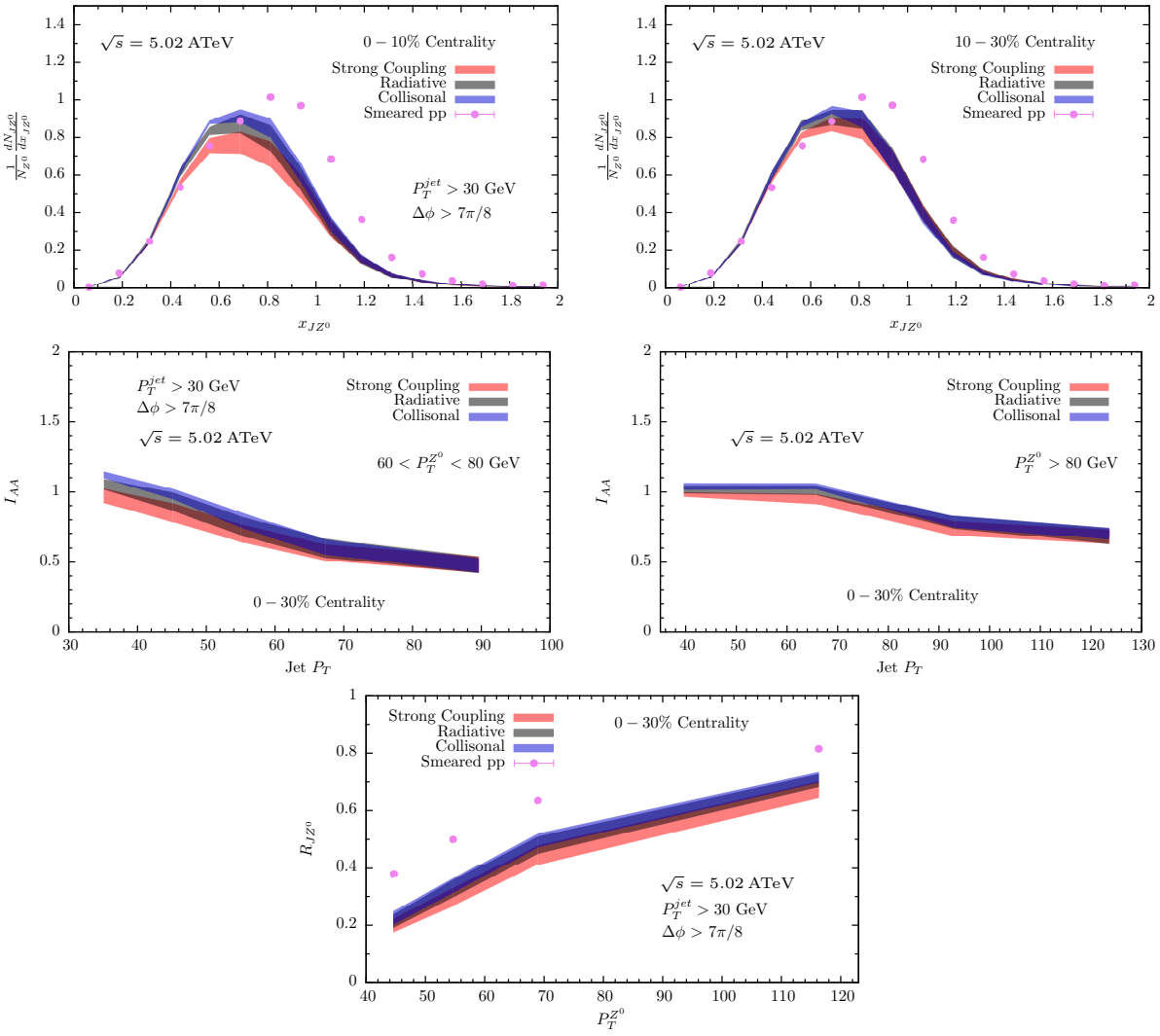

Figure 6-9: Predictions for several Z-jet observables computed with three different models of the energy loss mechanism in heavy ion collisions with $\sqrt{s} = 5.02$ ATeV. The distributions of the transverse momentum imbalance of Z-jet pairs for two different centralities are displayed in the upper panels. The middle panel shows the ratio of the transverse momentum spectra of jets produced in association with a Z-boson in Pb-Pb collisions to that in p-p collisions for two different centralities. The lower panel shows the fraction of Z-bosons produced in association with a hard jet with $p_{\mathrm{T}}^{\mathrm{jet}} > 30$ GeV at an azimuthal angle more than $7\pi/8$ away from that of the isolated photon.

6.5 Fragmentation Functions of Associated Jets: Boson-Jet and Dijet

We now turn to the analysis of a more differential class of jet observables, namely fragmentation functions. We saw in Fig. 5-6 of Section 5.3 that the predictions of our hybrid model and of our two control models for the ratio of the partonic fragmentation function of inclusive jets in PbPb collisions to that in p-p collisions are distinct for the three models. This motivates the hope that the higher statistics measurements expected from the coming LHC run may serve to distinguish between models. And, it motivates us to compute the predictions of all three models for the partonic fragmentation functions of jets produced in association with an isolated photon or a Z-boson. We shall present the results of these calculations in Section 6.5.1. We were initially surprised to see that the partonic fragmentation function ratio for jets produced in association with bosons turn out to be more similar for the three models we are considering than was the case for inclusive jets. Understanding this effect, which we shall do by the end of Section 6.5.1, leads us, in Section 6.5.2, to introduce a new observable constructed from the fragmentation functions of jets in dijet pairs in Pb-Pb collisions, without the need for any p-p reference. This turns out to be the observable that is most effective at differentiating among our three models of any observable that we have considered to date.

Unlike the more inclusive observables described in the previous Section, the hadronic fragmentation functions that experimentalists measure are quite sensitive to hadronization effects. However, the dynamics of hadronization, even in vacuum, are not under full theoretical control. In fact, the predictions of different Monte Carlo event generators for fragmentation functions can differ among themselves, and in comparison with p-p data, by as much as 20% as shown in Refs. [147, 148]. Since the modification of the fragmentation functions in Pb-Pb collisions with respect to those in p-p collisions is itself on the order of several tens of percent at most (see the measurements reported in Ref. [24, 30, 142]) and since there are differences in hadronization dynamics (in particular, differences in the patterns of color recombination) for jets in Pb-Pb and p-p collisions [127, 128, 129], it will be challenging to compare the ratios of *partonic* fragmentation functions in Pb-Pb colli-

sions to those in p-p collisions — ratios which we calculate in our models in Section 6.5.1 — to data. The in-medium effects of interest are comparable in magnitude to the known uncertainties coming from our lack of understanding of hadronization dynamics. This is strong further motivation for the importance of the observable that we introduce in Section 6.5.2: the ratio of the fragmentation function of inclusive jets in Pb-Pb collisions to that of the associated jets in dijet pairs. Since this is the ratio of the fragmentation functions of two different classes of jets in Pb-Pb collisions, with no need for a p-p reference, many hadronization uncertainties will cancel.

We shall restrict our calculations to partonic fragmentations throughout this Section, meaning that our calculations are not sensitive to hadronization and so are not affected by its challenges. The observable that we introduce in Section 6.5.2 is the one in this Section for which this will to the greatest degree possible also be true in experimental data. For this observable, as for those we calculate in Section 6.5.1, however, the fragmentation functions describing fragments with the lowest p_{T}'s cannot be described reliably by our hybrid model or by the two control models because none of these models include the contribution to the low-p_{T} component of a jet arising from the wake in the recoiling plasma that the jet plowing through it produces [149, 110, 90, 150, 151, 152].

6.5.1 Fragmentation Functions of the Associated Jets in Photon-Jet and Z-jet Pairs

Fragmentation functions are defined as the distribution of hadrons within a jet with a given fraction z of the total longitudinal momentum $p_{\parallel}$ of the jet. Longitudinal, here, means in the direction of the jet axis. In p-p collisions, where most of the activity in events with hard jets comes from hadrons produced via the fragmentation and subsequent hadronization of the virtual partons produced in an initial elementary partonic collision, fragmentation functions provide us with information about how the showering process via which the large virtuality of the initial partons relaxes takes place. Furthermore, since final state effects are negligible, $p_{\parallel}$ obtained from the energy of a jet reconstructed with a sufficiently large reconstruction radius provides a good proxy of the initial energy of the hard parton that

fragmented to form the jet. This means that the z-fraction of the final fragments are directly related to one of the QCD evolution variables. This is not the case in Pb-Pb collisions.

We have already mentioned one of the complications in Pb-Pb collisions: at low $p_{\rm T}$, some of the particles in a reconstructed jet did not originate from the initial hard parton that was produced in the initial elementary partonic collision. Some soft particles reconstructed in the jet come, instead, from the hadronization of moving quark-gluon plasma, set in motion by the momentum that the jet passing through it transfers to the medium through which it is passing. Operationally, this enters the analysis because in analyzing jets in Pb-Pb collisions it is necessary and standard to do a background subtraction to remove the hadrons formed from the quark-gluon plasma, and this background subtraction procedure is based upon the assumption that the momenta of these hadrons is uncorrelated with the direction of the jet. To the extent that this is the case, the background subtraction removes, on a statistical basis, particles in the jet cone that are not part of the jet itself. However, since the interaction of the jet with the plasma transfers momentum to the plasma, this back reaction (or recoil) effect means that the background subtraction procedure cannot remove all the particles from the medium: there is no way to disentangle all of them from the products of the jet shower; some of them must end up incorporated into jet observables. This means that, in Pb-Pb collisions, fragmentation functions at low $p_{\rm T}$ are sensitive to physical processes other than jet fragmentation. Addressing these additional physical processes requires a dynamical treatment of the response of the medium to the passage of the jet, which is beyond our current model implementation and will be studied in Chapter 7. For this reason, the results of our calculations become less reliable at small z. In this section, we will look at jets with $p_{\rm T} > 30$ GeV, meaning that $p_{\parallel} > 30$ GeV. So, $\ln(1/z) = 2.7$ or $\ln(1/z) = 3.5$ corresponds to fragments with $p_{\rm T} > 2$ GeV or $p_{\rm T} > 1$ GeV. We will plot our results out to larger values of $\ln(1/z)$, smaller values of z, but the effects of medium recoil that we are not including become more and more important for $\ln(1/z) \gtrsim 3$. In Section 6.5.2 where we consider inclusive jets and dijets, rather than jets produced in association with a boson, we will look at jets with $p_{\rm T} > 80$ GeV, meaning that our results there will be reliable out to somewhat larger values of $\ln(1/z)$.

There is a second complication in interpreting jet fragmentation functions in Pb-Pb

collisions, and this is that the $p_{\parallel}$ of a jet, as reconstructed from the final state, is less than the energy of the initial hard parton that fragmented into the jet because the partons in the jet have lost energy as they propagate through the strongly coupled medium produced in the Pb-Pb collision. At least some of the "lost" energy (according to the data [21, 153], a significant amount of it) ends up as soft particles moving at large, random, angles relative to the jet axis, and is not included when the jet is reconstructed. Therefore, even when they are reconstructed with a large reconstruction radius, the total energy of the quenched in-medium jets is smaller than the total energy of the hard partons originating from an elementary partonic collision. This means that when a jet is reconstructed in a Pb-Pb collision, it is impossible to make an experimental determination of the energy of the initial hard parton. Consequently, if one constructs a fragmentation function using the standard definition of z, namely the ratio between the momentum of an individual hadron to the $p_{\parallel}$ of the whole jet as reconstructed, this z is not directly related to the evolution variable in a DGLAP shower and, more generally, is simply hard to interpret. We will nevertheless report the predictions of our hybrid model and the two control models for fragmentation functions computed in this standard way, for comparison to future data.

Because we are looking at jets produced in association with a photon or Z-boson, however, there is an obvious alternative. We can define z_γ or z_Z (we shall denote these variables generically as z_B) as the ratio of the momentum of an individual hadron in the jet to the momentum of the γ or Z-boson, using the momentum of the electroweak boson in the event (which cannot have lost any energy since it does not interact with the quark-gluon plasma) as a proxy for the momentum of the initial hard parton that later fragmented and lost energy, forming the jet that the experimentalists reconstruct[7]. This is an improvement but it is not a panacea: we have seen in the previous Section that even in p-p collisions there is a broad distribution of the momentum imbalance between a boson (photon or Z) and the associated jet in a boson-jet event. One significant contributor to this imbalance is the fact that in many events the elementary hard scattering process produces one photon or Z plus more than one hard parton, not just one. Regardless, this imbalance is entirely due to perturbative vacuum QCD physics, not to any in-medium effects. This means that even when

[7] See Ref. [149] for a similar definition of the scaling variable.

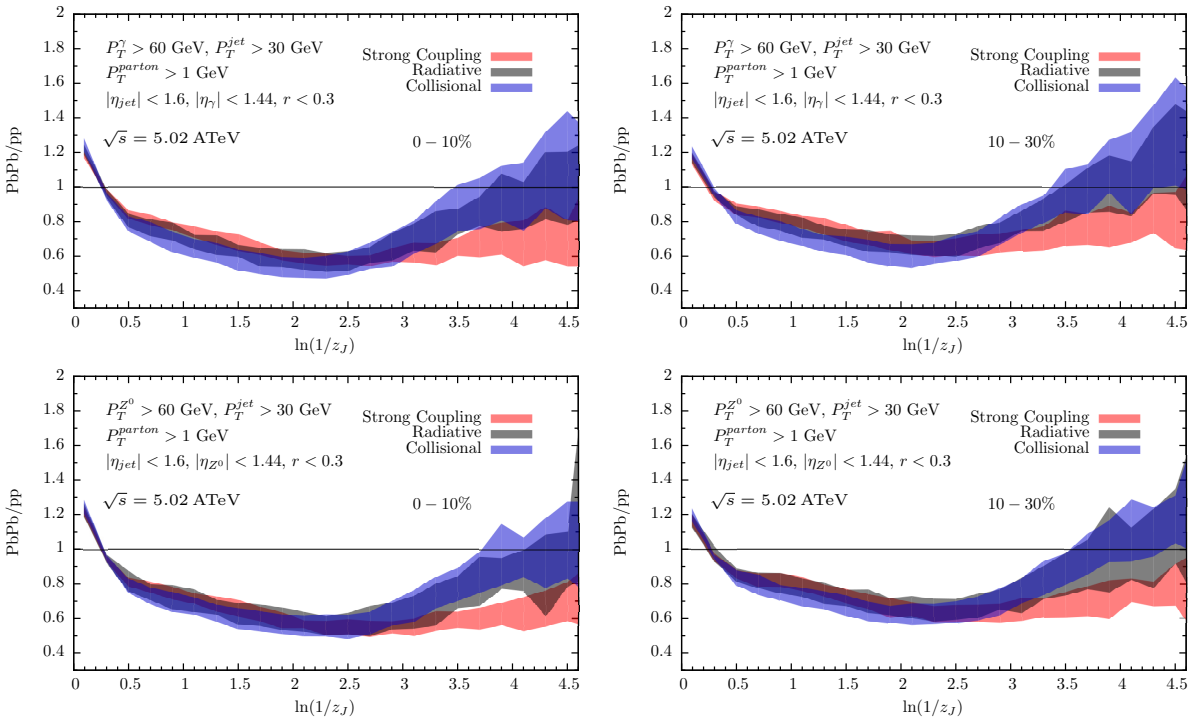

Figure 6-10: Predictions of our hybrid model, with strongly coupled energy loss for the partons in a PYTHIA shower, as well as our two control models for the partonic fragmentation function ratios (fragmentation function for jets in Pb-Pb collisions over that for jets in p-p collisions) for jets produced in association with an isolated photon (upper panels) or a Z-boson (lower panels) in Pb-Pb collisions at $\sqrt{s} = 5.02$ ATeV at two centralities (left and right panels). The fragmentation functions are constructed with respect to the variable $z_J = p_{\parallel}^{\text{parton}}/p_{\parallel}^{\text{jet}}$.

we construct fragmentation functions using z_γ or z_Z, we are not reliably dividing by the actual momentum of the initial hard parton that fragmented into the jet we are looking at. Still, by using z_γ or z_Z in Pb-Pb collisions we are using a variable that is as good a proxy for what we want as is the case in the standard fragmentation function in p-p collisions.

We first compute the fragmentation functions constructed with respect to the reconstructed energy of the jet produced in association with a photon or Z-boson. (We use the standard variable z, but here we denote it z_J to emphasize that its denominator is the momentum of the reconstructed jet. It is defined by $z_J \equiv p_{\parallel}^{\text{parton}}/p_{\parallel}^{\text{jet}}$.) In Fig. 6-10 we plot the ratio of the fragmentation functions in Pb-Pb to p-p as obtained in our framework for jets of $p_{\text{T}} > 30$ GeV produced in association with isolated photons (upper panels) and Z-bosons (lower panels) with $p_{\text{T}} > 60$ GeV. We have performed these simulations for two different

Pb-Pb centralities, $0-10$ %, shown on the left panels and $10-30$ %, shown on the right. Both photons and Z-bosons are required to have $|\eta| < 1.4$ while the jets are constrained to $|\eta_{\rm jet}| < 1.6$. The energy and direction of the jet axis are reconstructed with the anti-k_T algorithm with radius $R = 0.3$. Following the experimental analyses of inclusive fragmentation functions in Ref. [30], these fragmentation functions are constructed by including all particles surrounding the jet axis within an angular distance in η-ϕ space of $r = 0.3$. Since our simulations do not include the underlying event, these correspond to particles from the hard scattering process that remain correlated with the jet direction. (As noted above, in the analysis of experimental data a background subtraction is done, but soft particles from the plasma that is in motion following the jet will not be subtracted. This means that our calculations should not reproduce the data-to-come at large values of $\ln(1/z_J)$.)

The general features of the fragmentation function ratios plotted in Fig. 6-10 are very similar to those that we found for inclusive jets in Chapter 5. All the models display an enhancement of the hardest part of the fragmentation function in Pb-Pb collisions relative to p-p collisions. This is a generic behavior of any mechanism that removes soft particles from the jet, either via energy loss as here or via deflecting them into a direction far from that of the jet [106]. Removing soft particles increases the fraction of jets with a few hard fragments, which leads to the increase in the hard part of the fragmentation function. For all models there is also a depletion in the Pb-Pb fragmentation function at intermediate z_J. This is the expected result from quenching, which tends to reduce the energy of the fragments that propagate in plasma. Remarkably, for the energy range of bosons and jets explored in those figures, and with our current uncertainties, the pattern of fragmentation at large and intermediate z_J is indistinguishable among the three models we explore, despite their very different path length and energy dependences. We comment further on this below. At smaller values of z_J, the hybrid model with its strongly coupled energy loss suppresses soft fragments more than the control models. However, this separation between models occurs in a regime where the fragments have momenta smaller than 2 GeV, meaning that our calculations of fragmentation functions are not reliable there. Adding in the contributions from a medium that has picked up momentum from the jet passing through it, meaning that it is not completely removed by the background subtraction, would push the Pb-Pb

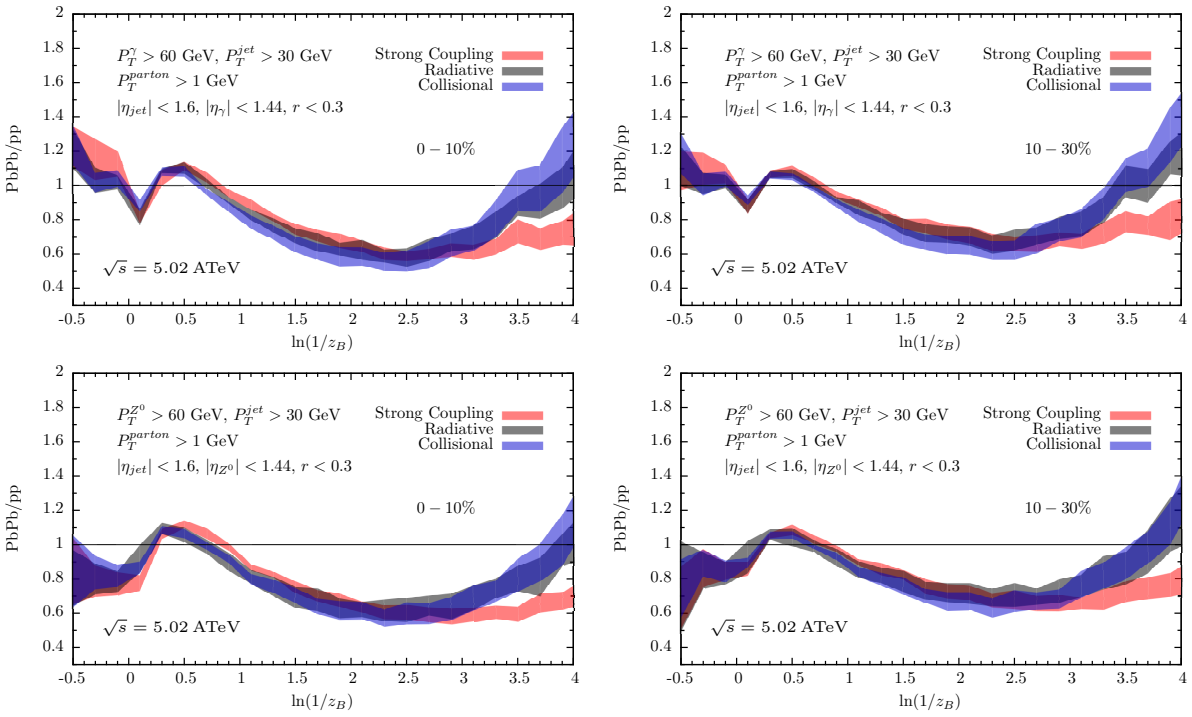

Figure 6-11: Predictions of our hybrid model and our two control models for the partonic fragmentation function ratios (Pb-Pb over p-p) for jets produced in association with a boson as a function of $z_B = -\mathbf{p}_T^{\rm parton}\mathbf{p}_T^B/(p_{\rm T}{}^B)^2$ for two different centralities for photon-jet (upper) and Z-jet (lower) events in Pb-Pb collisions at $\sqrt{s} = 5.02$ ATeV.

fragmentation functions up in this soft region by an amount that our model does not permit us to estimate at present.

In Fig. 6-11 we reanalyze the fragmentation function ratios, this time using the boson momentum z_B to define the scaling variable according to $z_B \equiv -\mathbf{p}_T^{\rm parton}\mathbf{p}_T^B/(p_{\rm T}{}^B)^2$, with $\mathbf{p}_T^B$ the transverse momentum of the isolated photon or Z-boson.[8] As already mentioned, our main motivation for redefining the scaling variable is to have a better proxy for the jet energy prior to quenching. If all bosons were prompt, their momentum would be insensitive to in-medium effects and energy loss would only affect the numerator of z_B. For those prompt bosons, the mismatch between the boson and the initiator parton of the jet originates entirely in vacuum processes. This is the case for Z-jet correlations, where the possibility of producing a Z in a jet shower is highly suppressed. In contrast, in the isolated photon

[8]Because of the fluctuations of the rapidity of the centre of mass of the elementary partonic collision that leads to boson-jet events, the rapidity of the boson and the jets do not need to be correlated, unlike the transverse momentum. For this reason, to construct z_B we have chosen to use only transverse momenta and chosen not to project the momenta of fragments along the boson direction.

sample we use, there is a small fraction of fragmentation photons even after we make our isolation cut, and for these photons energy loss effects are present via the quenching of their parent parton. Therefore, for photons, there is also a small dependence of the denominator of z_B on quenching; the effect of this small dependence on the fragmentation function ratio depends on the z_B range.

Note that as a consequence of the broad distribution of the boson-jet imbalance even in p-p collisions, z_B can be larger than one: there are jets with $p_{\rm T}$ larger than the momentum of the boson they are associated with. Those events populate the region of negative $\log 1/z_B$ in Fig. 6-11. In this region, all models lead to an enhancement of the in-medium fragmentation function of jets associated to photons. At first this seems puzzling, but there are in fact two reasons for this effect. The first is the fact that jet quenching does reduce the energy of fragmentation photons, as their parent partons lose energy. The second reason comes from imposing an isolation cut on photons in the events in our calculations, which do not include the particles corresponding to the medium. Since quenching affects all partons in our events, prompt photons in events with more than one jet are more isolated in our Pb-Pb simulations than in vacuum. This leads to an enhancement of the fragmentation function ratio for jets produced in association with isolated photons in the region of $x_J > 1$. However, it is not clear to us whether this effect will persist in a full simulation of photon-jet events in which particles from the Pb-Pb background are incorporated in the sample. We leave the study of the fate of this enhancement for future work. For the Z-jet correlation neither of these two effects are present, and the negative $\log z_B$ region is slightly suppressed, as expected.

The ratio of fragmentation functions also exhibits a non-trivial structure in the vicinity of $\log 1/z_B \sim 0.5$ ($z_B \sim 0.6$). This structure is correlated with the position of the maximum of the in-medium boson-jet imbalance in Figs. 6-1 and 6-4, $x_{J\gamma} \sim 0.6$ and $x_{JZ} \sim 0.6$. Since the maximum of the in-medium imbalance distribution is shifted towards smaller x values, the non-monotonic behavior of the fragmentation function ratio in this region reflects the behavior of the imbalance distribution. Indeed, the relative abundance of associated jets with $x_{J\gamma} \sim 0.6$ or $x_{JZ} \sim 0.6$ is enhanced in Pb-Pb collisions with respect to p-p. The fact that all three models exhibit the same behavior is a consequence of the

coincidence of the imbalance distribution in the three models.

As for fragmentation functions constructed with the variable z_J, here too the strongly coupled model only separates from the control models for soft particles where the physics of how the medium responds to the passage of the jet, physics that none of our models includes, becomes important.

In summary, the analysis of the fragmentation functions of jets produced in association with photons and Z-bosons indicates that mechanisms of energy loss that do not increase the number of hard fragments in jets, like the ones we have explored, lead to robust modifications to the fragmentation pattern of these jets. This also means that this type of observable is not very sensitive to the microscopic mechanism of parton energy loss.

We close this section by recalling our initial motivation — the separation between the predictions of our models for the fragmentation functions of inclusive jets seen in Fig. 5-6 — and asking why that separation between model predictions is less in the fragmentation functions for jets produced in association with photons and Z-bosons seen in Figs. 6-10 and 6-11. The answer comes in understanding the selection effects in a sample of "inclusive jets". Because the jet production spectrum is a steeply falling function of $p_{\rm T}$, and because usually two or more jets are produced in an event, most of the jets in a sample of inclusive jets are the most energetic jet in an event. In selecting a sample of inclusive jets, one is preferentially selecting jets that are the jet in their event that has lost the least energy. In contrast, when one selects jets by first identifying an isolated photon or Z-boson and then reconstructing an associated jet there is no such selection effect. This means that, on average, the inclusive jets whose fragmentation functions are shown in Fig. 5-6 have travelled through the medium over a shorter path-length and, again on average, they are jets that fragmented less. Fewer fragments, i.e. a jet with a lower jet mass and a smaller opening angle and a harder fragmentation function, means that within the jet there are fewer partons losing energy in the medium, and therefore means less energy loss. Both these effects are likely small compared to the event-by-event variation. But, on average, inclusive jets contain somewhat fewer fragments[9] and traverse somewhat less plasma. What

[9]There are actually two reasons why they contain somewhat fewer fragments. First, as we shall see only in the next Section, even in p-p collisions the higher energy jet in a dijet pair — and this is what most jets in an inclusive jet sample are — tends to have a harder fragmentation function. And, second, jets with fewer,

are the consequences in our models of the fact that in going from Fig. 5-6 to Figs. 6-10 and 6-11 there is an increase in path length? The path-length dependence of dE/dx in (4.2) is stronger than in the control models (4.7) and (4.10) meaning that in the mid-range of z where we see the effects of quenching (say $1 < \log 1/z < 3$) we expect the increase in path length to push the predictions of our hybrid strongly coupled model down relative to the control models. What are the consequences of the fact that in going from Fig. 5-6 to Figs. 6-10 and 6-11 the jets become wider and there is some reduction in the energy of the partons within them? In (4.2), a reduction in the energy of the partons means a reduction in the stopping length $x_{\rm stop}$ and an increase in dE/dx. So, for this reason also we expect to see the predictions of our hybrid strongly coupled model pushed down relative to those of the control models. And, this is indeed what we see. Unfortunately, the predictions of the hybrid model get pushed down just to the extent that in Figs. 6-10 and 6-11 they are essentially on top of the predictions of the control models.

In the next Section, we show that it is possible to select a sample of jets in which the predictions of the hybrid strongly coupled model for the fragmentation functions in the mid-range $1 < \log 1/z < 3$ are pushed down even farther.

6.5.2 Fragmentation Functions of the Associated Jets in Dijet Pairs

Motivated by the results and discussion above, we now turn our attention to the fragmentation functions of the associated (less energetic) jets in dijet events. Whereas in the inclusive jet sample of Fig. 5-6 we have selected jets that are likely to be those among the jets in their event that have been quenched the least, by selecting associated jets in dijet events we will likely be selecting those that have been quenched the most. That means we will be selecting those that have, on average, traversed a longer path-length of medium and those that were produced, on average, with a larger jet mass and jet opening angle and that, on average, contained more, and therefore lower energy, fragments before quenching.

In the left panel of Fig. 6-12, we show the ratio of fragmentation functions for jets of $80 < p_{\rm T} < 300$ GeV with $0.3 < |\eta| < 2$ produced in association with a jet of $p_{\rm T} > 120$

harder, fragments lose less energy [155] in the plasma produced in a Pb-Pb collision and so are even more likely to end up being the higher energy jet in a dijet pair.

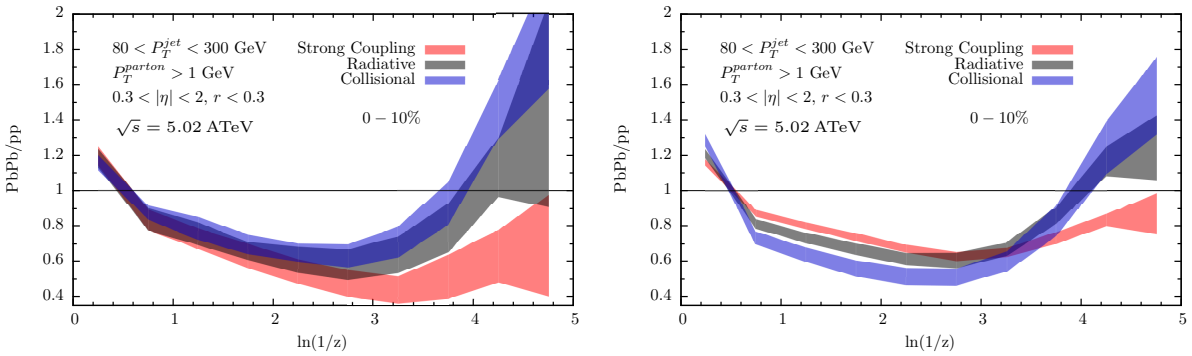

Figure 6-12: Left: Model predictions for the Pb-Pb to p-p ratio of fragmentation functions of associated jets (lower energy jets) in dijet events at $\sqrt{s} = 5.02$ ATeV with a leading jet of $p_{\rm T} > 120$ GeV. Right: Same for inclusive jets with the same range of $p_{\rm T}$ and η as the associated jets in the left panel. The right panel is similar to Fig. 5-6, but is for a different $p_{\rm T}$ range and is for the higher LHC heavy ion Run 2 collision energy.

GeV in Pb-Pb collisions to that in p-p collisions. By the associated jet in a dijet pair we will always mean the jet with the lower energy. For comparison, in the right panel of Fig. 6-12 we have analyzed inclusive jet fragmentation in a lower energy range, such that the momentum of the inclusive jets is in the same range as the momentum of the associated jets in the left panel of Fig. 6-12. Although by careful comparison to Fig. 5-6 we see that the modification pattern seems to be slightly dependent on the jet energy, the basic features in the right panel of Fig. 6-12 and in particular the ordering of the predictions of the three models, is the same as in Fig. 5-6. The inclusive jets are selected in a way that makes them likely to be the less quenched jets in their event with, on average, a shorter path length and fewer fragments. The jets in Section 6.5.1, selected via having been produced in association with photons or Z-bosons, have no such selection effects. And, the associated jets in the left panel of Fig. 6-12 are selected in a way that makes them likely to be the more quenched jets in their event with, on average, a longer path length and more fragments. Sure enough, we see that the predictions of our hybrid strongly coupled model — with a dE/dx that depends strongly on path-length and that increases at lower energies as $x_{\rm stop}$ decreases — are pushed lower than those of the control models in the left panel of Fig. 6-12.

The model-dependence of the fragmentation function ratios seen by comparing the left and right panels of Fig. 6-12 is striking: the ordering of the predictions of the three models is opposite in the two panels, with the hybrid strongly coupled model predicting the least

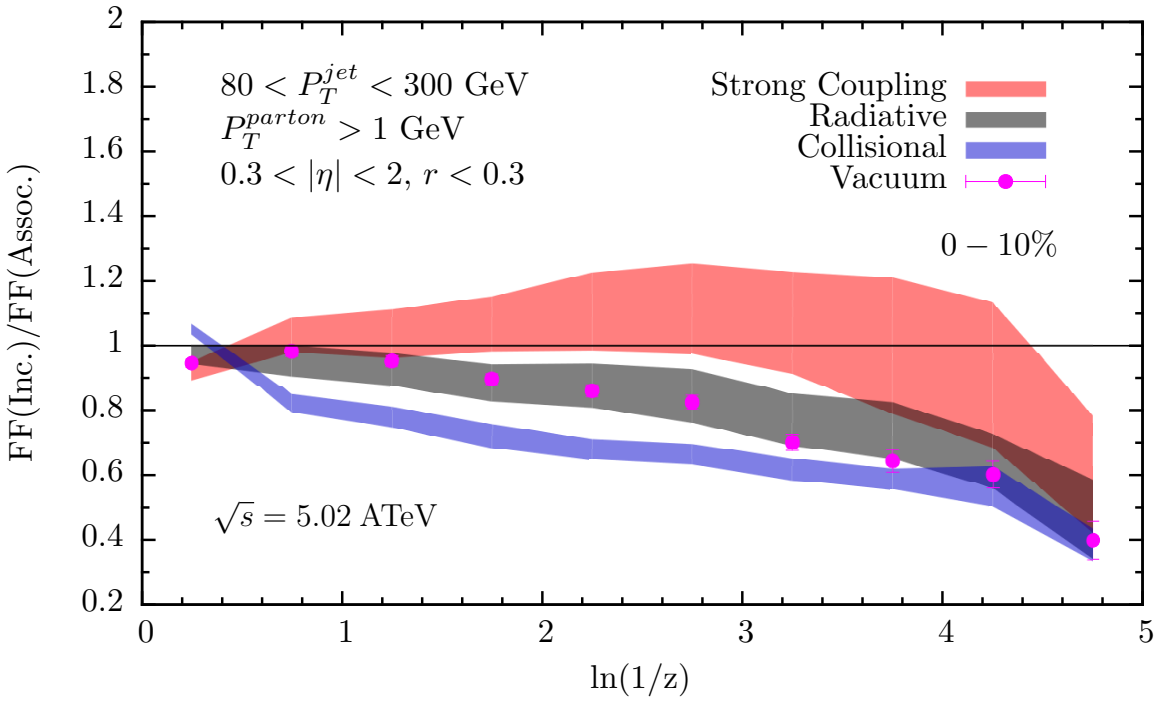

Figure 6-13: Model predictions for the ratio of the fragmentation functions of inclusive jets to the fragmentation functions of associated jets in dijet events whose most energetic jet has $p_{\mathrm{T}} > 120$ GeV in Pb-Pb collisions at $\sqrt{s} = 5.02$ ATeV. Both the inclusive jet and associated jet samples are constrained to the same η and p_{T} range, see the text. We see a striking, and robust, separation between the predictions of our hybrid strongly coupled model and our two control models. We also show the same ratio, constructed with the same kinematic cuts, for inclusive and associated jets in p-p collisions. The ratio in p-p collisions should not be compared to that in Pb-Pb collisions: each stands on its own and has its own implications. (Comparisons between Pb-Pb and p-p are shown in Fig. 6-12.) Here, the p-p results illustrate the differences between jets selected inclusively and jets selected by association with a leading jet in vacuum, with no jet quenching. And, the comparison between the Pb-Pb results from the different models shows how the interplay between these differences and the path-length and energy dependence of different expressions for dE/dx yields predictions for this ratio that depend sensitively on the underlying microscopic dynamics of jet quenching.

depression of the fragmentation function of the inclusive jets and the most depression of the fragmentation function of the associated jets. Seeing this motivates us to introduce a new observable in Fig. 6-13 in which we, in effect, take the ratio of the right panel of Fig. 6-12 to the left panel of Fig. 6-12. That is, we propose to compare the fragmentation function of inclusive (which is to say leading) jets to the fragmentation function of associated (lower energy) jets in Pb-Pb dijet events. To avoid trivial kinematic differences between the energies of the inclusive and associated jets, we have constructed this ratio with jets in the same interval of $p_{\rm T}$ and rapidity, $80 < p_{\rm T} < 300$ GeV and $0.3 < |\eta| < 2$. As in Fig. 6-12, the associated jets whose fragmentation functions constitute the denominator in the ratio plotted in Fig. 6-13 are produced in association with leading jets of $p_{\rm T} > 120$ GeV. (We have not investigated other choices of leading jet $p_{\rm T}$.) The predictions of our hybrid strongly coupled model and of our two control models for this new observable are displayed in Fig. 6-13. This observable yields the largest separation between the predictions of our models of any observable that we have investigated. This means that it is particularly sensitive to the underlying microscopic dynamics behind the modification of jets in medium.

The new observable that we have introduced in Fig. 6-13 has the added virtue that its construction does not require fragmentation functions from jets in p-p collisions. It is the ratio of the fragmentation functions of differently selected Pb-Pb jets with the same kinematics. This means that none of the uncertainties coming from the differences in the way hadronization occurs in Pb-Pb collisions and p-p collisions come into play. Our calculations behind Fig. 6-13 are, like those in Section 6.5.1, calculations of partonic fragmentation functions. Here, though, we expect that the ratio of fragmentation functions displayed in Fig. 6-13 should be a better predictor for the same ratio of the hadronic fragmentation functions that experimentalists can measure than in the case of any of the other fragmentation function ratios that we have constructed because much of the uncertainty in our understanding of hadronization should cancel in this ratio. Of course, in the softest region, at the smallest z's, it continues to be the case that we are leaving out contributions to the fragmentation functions from the moving quark-gluon plasma, set in motion by the jet passing through it. This effect should at least partially cancel in the ratio plotted in Fig. 6-13; this is yet one more advantage of using the ratio of fragmentation functions of differently selected

jets with the same kinematics in the same Pb-Pb collisions, without introducing jets from p-p collisions.

In Fig. 6-13 we have also plotted (as purple dots) the same ratio of the fragmentation function of inclusive jets to that of associated jets for p-p collisions from PYTHIA, with the same kinematic cuts as in our Pb-Pb analysis. We show this solely to confirm that even in the absence of any medium there is a difference between the inclusive jets and the associated jets. Selecting inclusive jets selects jets with fewer and therefore harder fragments. Selecting associated jets selects jets with more and therefore softer fragments. In Pb-Pb collisions, then, in the presence of a medium the differences between the rates of energy loss come into play as we have discussed. This effect, plus the difference between the path lengths seen by inclusive and associate jets on average, are amplified by the different path-length and energy dependence of the rates of energy loss in our hybrid strongly coupled model and our two control models. The result is the large separation between the predictions of the models for the ratio plotted in Fig. 6-13, making this ratio so discriminating. We look forward to seeing experimental measurements of this ratio; they have great potential to teach us about the microscopic dynamics that results in the observed modification of jets in heavy ion collisions.

6.6 Summary of Results

In these first two Chapters we have explored a broad range of jet observables in Pb-Pb collisions at LHC energies within the context of the hybrid strong/weak coupling model that we introduced in Section 4.1. This is a phenomenological approach to the physics of jet quenching in which we aim to synthesize the very different types of physical processes involved in the production, branching, and subsequent in-medium dynamics of jets in heavy ion collisions. In particular, our model separates the short distance physics which controls the production and hard branching evolution of jets, which behaves as in vacuum, from the longer distance processes that control the interaction of the jet shower with the strongly coupled fluid produced in energetic heavy ion collisions. Our goal is to describe the short distance physics with standard tools for describing the weakly coupled physics of jets in

vacuum, in particular with PYTHIA, and to describe the longer distance processes using insights from calculations done using strong coupling methods. In particular, to model the long distance physics we adopt results obtained by analyzing the rate of energy loss dE/dx of an energetic massless parton propagating through the hot liquid plasma of strongly coupled $\mathcal{N} = 4$ SYM theory, as obtained via gauge/gravity duality. We apply these results in QCD upon assuming that the differences between the hot liquid plasma phases of the two theories can be absorbed in a single parameter which controls the stopping distance of energetic excitations in plasma. We fitted this one model parameter to jet R_{AA} data in Section 5.1. Our model, now fully specified, yields a very good description of the suite of inclusive jet observables and dijet observables discussed in Chapter 5 and, as our explicit analysis in this Chapter shows, of all currently available data on photon-jet correlations. All these observables in sum span a wide range of energies, originate from different hard production processes with different primordial spectra, and correspond to jet samples with different selection biases, different ratios of quark jets to gluon jets, different fragmentation patterns and jet mass distributions, and that traverse different distributions of path lengths. Nevertheless, we have obtained a satisfactory description of all of these observables using our simple, hybrid, implementation of strongly coupled dynamics — namely by taking jets from PYTHIA and applying the strongly coupled rate of energy loss dE/dx parton-by-parton to the partons in a parton shower.

Although at one level we are pleased by the now increasingly many successes of our hybrid model approach, at another level they are frustrating. Our model is simple, gluing together two rather different descriptions of physics at different scales and in so doing incorporating much unknown physics into just one parameter. Of course the first goal in creating such a model is to capture some of the physics correctly, and it seems that we have done that. However, it could be even more interesting to see the model breaking down and to use ways in which it fails to describe some feature of some experimental data to understand which of the aspects of the physics that the model leaves out are important, and how, and why, and where. The string of successes in the comparison between the results of our model calculations and experimental data preclude investigations of this nature at present.

All that said, our explicit analysis of two control models with parametrically different expressions for dE/dx cautions us that we should not rush to conclude from the successes of our hybrid model that the experimental measurements of the various jet, dijet and photon-jet observables favor the strongly coupled form for dE/dx over other possibilities. Rather, we must acknowledge that these observables are not strongly sensitive to the parametric form of the rate of energy loss dE/dx. The experience that we have gained from our analysis suggests that as long as the vacuum-like branching processes that are at the core of jet dynamics are described well, any mechanism that is able to quench particles, in particular the softer partons in a jet, can capture the bulk features of the measured distributions of jet observables, including the various dijet and photon-jet asymmetries and correlations, as long as the parameter that governs the overall magnitude of dE/dx is chosen appropriately.

Nevertheless, it is certainly heartening and perhaps even remarkable that the range of values of the one parameter in our hybrid strong/weak coupling model, $\kappa_{\rm sc}$, that we find provides a good description of so much jet data agrees so well with *a priori* expectations. $\kappa_{\rm sc}$ should be smaller than but of order one, exactly as we have obtained. A stopping length for energetic partons in the strongly coupled QGP of QCD that is three to four times longer than that in the strongly coupled $\mathcal{N} = 4$ SYM plasma with the same temperature, as we find, is an eminently reasonable result.

These conclusions are all conclusions that we reached in Chapter 5. The analyses of photon-jet observables presented in this Chapter serves to reinforce them in many ways.

Looking ahead, we hope that among the many calculations from our hybrid model that we have presented the ones that will be most important will be the many predictions that we are making for experimental measurements that are anticipated in the near future. These can be grouped into three categories, the first two of which are:

- We have provided the predictions of our hybrid model for inclusive jet observables, dijet observables, and photon-jet observables in heavy ion collisions with collision energy $\sqrt{s} = 5.02$ ATeV, in anticipation of LHC heavy ion Run 2. This is particularly important for the photon-jet observables. The present data have low statistics, and correspondingly large error bars, making the fact that our hybrid model describes them well less impressive than it could be. In the run to come, the statistics will

be greater by about an order of magnitude, meaning that the error bars should be significantly smaller, making the confrontation between the predictions of our model and these measurements much more constraining.

- We have provided the predictions of our hybrid model for Z-jet observables, which we hope will be tested in future LHC runs.

Confrontation between these predictions and the data to come should serve either to further strengthen our confidence in the approach to jet quenching that we have introduced or to identify and quantify ways in which it fails, ideally pointing toward which aspects of the physics that we have left out are most important and guiding the improvement of the model. It is also possible that as the experimental uncertainties shrink measurements of these observables could serve to differentiate between the different assumptions about the dynamics of parton energy loss, and consequent different forms for dE/dx. However, the distinctions between the predictions of our hybrid model and our two control models for these observables are small, limiting the discriminating power of these observables even as the experimental uncertainties shrink.

It seems clear that in order to find observables that provide more discrimination among the different possible dynamical processes via which the partons in a shower lose energy as they traverse the strongly coupled plasma we will need to investigate intrajet observables. Utilizing those observables that involve the angular shape of jets must wait, as it will require adding further physics to the model, including for example the transverse momentum picked up by the shower partons as they interact with the medium, and so must involve the addition of at least one new parameter to the model. There is good motivation for such investigations, which we will address in Chapter 7. With the one parameter model that we have constructed here, the class of intrajet observables that we may be able to describe is those constructed from fragmentation functions:

- The third category of predictions that we have made are predictions for various ratios of fragmentation functions. We have taken advantage of having a tool with which we can compute multiple observables (here, fragmentation functions for jets in p-p collisions, inclusive jets and jets in dijet pairs in Pb-Pb collisions, and jets produced

in association with photons or Z-bosons in either Pb-Pb or p-p collisions) in varying kinematic regimes to search for new discriminating observables which are particularly sensitive to differences between mechanisms of energy loss. We have provided the results of our hybrid model calculations for ratios between partonic fragmentation functions in photon-jet and Z-jet events in Pb-Pb collisions to those in p-p collisions, but for reasons that we have understood qualitatively these turn out not to be particularly discriminating. Also, these predictions are sensitive to differences between hadronization dynamics in Pb-Pb and p-p collisions that are not under good theoretical control at present, reducing the reliability of our predictions for these ratios. The most discriminating observable that we have found is the ratio of the fragmentation function of inclusive jets in Pb-Pb collisions to the fragmentation functions of jets in the same kinematic regime, in the same collisions, that are the lower energy jets in a dijet pair. (We refer to the latter as associated jets.) Unlike most jet observables, this measurement does not require any p-p reference data. And, since the ratio we propose is constructed from jets in the same kinematic regime in the same PbPb collisions, differing only in how they were selected, we expect that many of the theoretical uncertainties associated with the modification of hadronization in medium should cancel. This makes the ratio of partonic fragmentation functions that we compute a better proxy to the ratio of fragmentation functions that experimentalists will measure. Furthermore, we find that the predictions of our hybrid strong/weak coupling model and our two control models for this ratio, see Fig. 6-13, are well separated over a wide range of z, making the discriminating power of this observable robust even after the softening of the fragmentation functions expected after hadronization. And, perhaps best of all, we have a good qualitative understanding of why this ratio is such a discriminating observable. First, in Pb-Pb collisions as in vacuum inclusive jets tend to contain fewer, harder, fragments than associated jets on average. Second, the distribution of the path length of the medium through which a sample of inclusive jets has propagated is, on average, shorter than that for a sample of associated jets. Both these effects mean that, on average, the inclusive jets have lost less energy than the associated jets. And, we have shown that both these effects push the predictions

of our hybrid strong/weak coupling model and our control models apart. Measurement of this ratio of fragmentation functions should be a particularly effective way to gain information about the dynamics via which energetic partons lose energy as they traverse strongly coupled plasma. The experimental determination of this ratio in the imminent LHC heavy ion Run 2 can therefore shed light on the microscopic dynamics of jets in quark-gluon plasma.

6.7 Improvements to our Current Implementation

In this Section we summarize the main simplifications taken in our implementation, some of which have already been addressed throughout the presented work and will be tackled in Chapter 7. Such improvements are well motivated indeed, given the increase in the quantity and quality of data on jet observables at both the LHC and RHIC anticipated in the near future.

Some of the improvements that should be investigated come from the phenomenological aspects of our model. The effects of adding hadronization to the model should be studied, as although this would open up new uncertainties it would also open up the possibility of comparing to new observables. As we have discussed in Section 5.3, it would be of considerable interest to try to *follow the energy lost by the quenched jet* and to investigate the degree to which the fraction of the 'lost' energy that happens to become soft particles within the jet cone is or is not subtracted during the jet reconstruction procedure used in the analysis of experimental data.

A particularly important effect that we have not included in our computation is the kicks in transverse momentum (transverse to the initial jet direction) that the fragments in the shower will all pick up as they propagate through the medium, losing energy. For simplicity, we have assumed that all the in-medium partons maintain their direction of propagation. The inclusion of *transverse momentum broadening* would have little effect on $R_{\rm AA}$, which is dominated by the hardest fragments, and therefore would not have much effect on the extracted value of $\kappa_{\rm sc}$. However, as stressed in Ref. [106], it would increase the dijet

imbalance somewhat, since some of the soft fragments would get kicked out of the jet cone. We should mention, however, that this effect is unlikely to be pronounced because partons in the shower that become soft due to energy loss are very likely already being removed from the jet via the consequent large Bragg-like increase in dE/dx in (4.2). Including transverse momentum broadening would make it possible to interpret other interesting observables. For example, in our present calculation our dijets are just as back-to-back as dijets in proton-proton collisions. This is consistent with present data on the distribution of the azimuthal angle separating jets in a dijet pair [20, 21, 22] and the distribution of the azimuthal angle separating the photon and the jet in gamma-jet events [23]. However, at present it would not be sensible for us to compare our model to these data since there is no way within our model for these angular distributions to be different in Pb-Pb collisions than in proton-proton collisions. After adding transverse momentum broadening to our model, we could then use the data that (at present) show no significant change in the distribution of the dijet or photon-jet azimuthal separation angle from proton-proton to Pb-Pb collisions to constrain the new component of the model. We can further imagine using this data and a suitable variant of our hybrid model to separately constrain the probability that a hard parton is scattered by a large angle, thus looking for evidence of the presence of point-like quark and gluon quasiparticles [154]. So, incorporating transverse momentum broadening into our hybrid approach would result in a loss in minimalism and an increase in the number of parameters that would need to be fitted to data but it would mean that the model could be confronted with data on further observables, including the distributions we have just mentioned or, for example, various measures of jet shapes.

Another feature of the dynamics of energy loss that we have not implemented is the effects of finite resolution on the interaction between the shower and the medium. In a finite medium, the separation of the jet fragments in the transverse direction in position space as they propagate through the plasma must be finite. As has been explicitly shown for radiative processes [155], structures with a transverse size smaller than a given resolution scale must act *coherently* as seen by the medium. This reduces the effective number of propagating partons seen by the medium, and makes the 'effective partons' harder than anticipated. If $\kappa_{\rm sc}$ is left unchanged, these dynamics would tend to increase $R_{\rm AA}$, reduce

the dijet asymmetry and make the fragmentation functions more similar to their vacuum counterparts. Of course, including these effects would result in a larger fitted value of $\kappa_{\rm sc}$.

There has been recent progress in the implementation of the effects of finite transverse resolution at strong coupling by the study of the propagation of a string with a kink near one of its endpoints in AdS-BH [156]. This configuration is the strongly coupled analogous of a three jet event, and by opening the angle of the kink the authors can gauge when the energy loss of the quark-gluon half of the string becomes comparable to the energy loss of a fully decoupled system. In this way the resolution power of the strongly coupled plasma can be determined and it would be of great interest to incorporate this effect into our hybrid model, a task we will leave for future work.

We will in this thesis nevertheless perform a relevant calculation in Part III involving multi gluon emission, and also by studying the different limits in which these emissions occur we can assess the relevant times at which the medium is capable of resolving the multipartonic system. The results presented there support the picture in which in medium jets are regarded as a collection of effective emitters, an effect that as said above could have important phenomenological consequences and could be put to test within the framework of our hybrid model for jet quenching.

In the next and last Chapter of this Part of the thesis we will improve our hybrid model by considering the effect of transverse momentum broadening that the jet experiences as a result of its interaction with the thermal color bath, which is *a priori* expected to modify the transverse energy distribution of jets, as can be quantified by the use of the jet shapes observable. We will also estimate the implications of medium response to the energy deposited by the jet, which makes the plasma locally hotter and faster and therefore induces background correlations with the jet direction, an effect that is expected to be most visible when analyzing the more challenging intra-jet observables. Dedicated analysis of the study of the "lost energy" published by the CMS collaboration also represent an essential tool with which to compare our assumptions about the jet/plasma interplay and allow for a detailed examination of the spectra and angular distribution of the thermalized energy.

Chapter 7

Transverse Momentum Broadening and Medium Response

In this Chapter we extend the hybrid strong/weak coupling model for jet quenching, which combines perturbative and non-perturbative physics in a phenomenological way, by including dynamics beyond pure energy loss. Colored projectiles in the quark-gluon plasma get broadened through transverse kicks while transferring energy to the thermal system. The jet passage modifies the hydrodynamic background, locally making it a bit hotter and faster. Such effect can be estimated by assuming small perturbations and quantified by matching the excited stress energy tensor to the total lost momenta by the individual partons of the shower. The energy flow from the jet to the medium translates into soft radiation at large angles, which is correlated with the jet direction. We find that including these physics is crucial to understanding the internal, soft structure of high energy jets and its connection with the rest of the system

7.1 Broadening

The first physical process we will supplement our hybrid model with is the implementation of transverse momentum broadening of the propagating partons in the plasma. The multiple soft exchanges that a parton suffers when traversing a medium leads to a random change of its momentum. In addition to energy loss, which for very energetic particles may

be viewed as mostly affecting the momentum of the parton along its direction of motion, elastic-like processes can change the direction of propagation, supplementing the parton with some additional momentum perpendicular to its original direction of propagation. If the parton suffers multiple soft exchanges, this transfer of momentum may be thought of as a gaussian (white noise like) stochastic process. As a consequence, the transverse momentum distribution of partons after traversing a medium of a fixed length L is approximately gaussian, with a width that scales with the medium length, $Q_\perp^2 = \hat{q}L$. In this relation, $\hat{q}$ is the momentum broadening parameter, which codifies the typical square momentum that the medium transfer to the probe per unit length. In perturbative (radiative) energy loss computations, this medium parameter determines the intensity of radiation of medium induced gluons by the parton while it ploughs through the plasma. Therefore, in this limit the energy loss and broadening processess are correlated. At strong coupling, the transverse momentum broadening was first determined in in different limits in [157, 96, 158]. However, unlike perturbation theory, a strong correlation between the dynamics responsible for broadening and for the induced energy loss of probes in the plasma has never been stablished (for some attempts to relate these mechanism based on a parton based interpretation of strong coupling, see [114, 76]).

In this Section, we will discuss the effect of broadening in our model. Since our construction is designed to account for the effects of a strongly coupled medium in jet observables, we will assume no a priori relation between the broadening parameter and the energy loss. This amounts to introducing an additional parameter, $\hat{q}$, that we attempt to fix to data. Quite surprisingly, we will observe a remarkable insensitivity of many jet observables to this process, which makes it very difficult to extract the precise value of this medium parameter from these computations. We will introduce a new observable which exhibits sensitivity to in-medium broadening as a possible way to constrain the value of the momentum broadening parameter $\hat{q}$ from experimental data.

7.1.1 Introduction of Broadening in the Hybrid Approach

Our implementation of broadening will rely in the multiple soft exchange approximation, characterised by a gaussian distribution of transverse exchanges. Since the medium is dynamical, with a strong longitudinal and transverse expansion that makes the energy density and velocity at each point of the fluid to change with time, we will assign at each point a local transverse momentum broadening parameter. We will assume that the local value of this parameter is determined solely by the local temperature at the point. Many other jet quenching studies follow a similar approach but, instead, assume a simple scaling of $\hat{q}$ with the local energy density. Nevertheless, strong coupling computations indicate that, at least for theories with a gravity dual, the momentum broadening parameter scales with temperature as

$$\hat{q} = KT^3 \,. \tag{7.1}$$

with K a theory-dependent constant. For very energetic particles, in the infinitely strongly coupled large N limit of $\mathcal{N} = 4$ SYM, $K = K_{\mathcal{N}=4} \simeq 24$ (for $\lambda = 10$) as extracted from [157]. Following the spirit of our hybrid approach, we will assume that all the difference in degrees of freedom and symmetries between $\mathcal{N} = 4$ and SYM can be recast in the value of K. Therefore, we will treat K as and additional free parameter of our setup and explore its consequences in jet data. For comparison, the $\hat{q}$ extracted by the jet collaboration [115] based on a perturbative analysis of high-momentum particle suppression yields $K_{pert} \simeq 5$.

Most computations of in-medium energy loss and broadening of jets are performed in the limit of a static fluid at rest. However, we will study the interactions of jets with a strongly expanding medium which is well described by hydrodynamics. Similar to our treatment of energy loss in expanding plasma in previous Chapters, we will extend the computation to a dynamical medium by applying the static medium results in the local fluid rest frame. As usual, this approximation assumes that gradient correction effects in this quantity are small. This prescription implies that all the momentum degradation of the particle is computed in the fluid rest frame of the local cell the parton traverses at a given time. In particular, the momentum degradation in the longitudinal direction is ascribed to energy

loss, as detailed in Section 4.3, while the broadening of momentum by soft exchanges affects momentum components transverse to the parton in this frame. Therefore, in general the direction in which the momentum is broadened may not be transverse to the parton propagation in the collision rest frame. The detailed transformation and approximations between the fluid frame and the collision frame can be found in Apendix A.

Following our Montecarlo approach, we perform a full simulation of jets in medium. For the analysis performed in this section, we studied 500.000 jet events, generated and evolved with PYTHIA 8.183. Hard processes are distributed in the transverse plane according to binary collisions. Those jets are embedded in the hydrodynamic background of Ref. [131, 132]. We follow the trajectories of all the particles generated by the jet shower as they traverse the hot matter created in the collision. During the life time of each particle, we discretise its trajectory and at each point we add to its momentum a random transverse momentum according to a gaussian distribution of width $\hat{q}dt_F$ with dt_F the length of the discretised time interval in the fluid frame[1]. Following our prescription above, the addition of momentum is performed such that the partons are kept on mass shell. As a consequence, broadening dynamics alone leads to a small quenching of jets. This forces us to evaluate the impact of these new dynamics on the quenching parameter of our model $\kappa_{\rm sc}$, which we evaluate in the next Section.

7.1.2 Insensitivity of Jet Observables to Broadening

As already mentioned, the small degradation of energy introduced by our implementation of broadening, leads to a small increases on the energy loss suffered by jets when traversing the medium for a fixed value of $\kappa_{\rm sc}$. To test this sensitivity, and following our previous work, we have refitted the value of $\kappa_{\rm sc}$ for the different values of the K broadening parameter. As shown in Fig. 7-1, the effect of broadening is small. In this plot, the width of the band is controlled by the theoretical uncertainties of the model, as well as the uncertainty of the data point used to fix the model. For typical values of K between the perturbative estimate and the strong coupling of $\mathcal{N} = 4$, $K \simeq 5,\ 24$ respectively, the effect of broadening implies a reduction of less than 5% in the value of $\kappa_{\rm sc}$ reported in our previous work, which

[1] We have checked that our results do not depend on the choice of dt_F

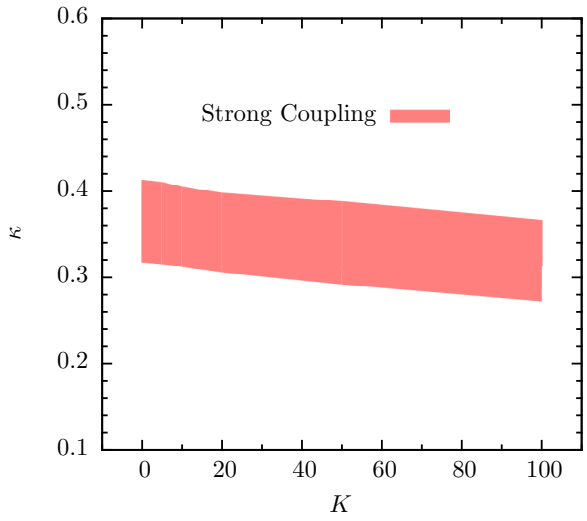

Figure 7-1: Strong coupling energy loss parameter κ_{SC} dependence on broadening parameter K.

is significantly smaller than the theoretical uncertainties expressed by the width of the band in this plot. As a test of sensitivity, we have extended our computations to unrealistically large values of K, more than 3 times larger than the value in $\mathcal{N} = 4$ SYM. Even at those extreme values, K $\kappa_{\rm sc}$ is only reduced by about 10%.

Having fixed the dependence of the quenching parameter $\kappa_{\rm sc}$ on the broadening parameter K, we can explore its effect in different observables. We first consider the suppression factor of jets as a function of the jet reconstruction parameter R in the anti-k_t algorithm. This parameter controls the (anti-k_t) distance of particles from the jet axis that are considered as part of the jet. The larger the parameter R the larger the size of the jet in η-ϕ plane. Because of this, the dependence of the suppression factor on the jet size has been traditionally considered as a measure of the modification for the angular distribution of jet energy as a consequence of in-medium interactions. According to this expectations, broadening effects should have an imprint in this observables, since the soft exchanges with the medium transport jet fragments at large angles away from the jet. However, this is not what we observe in our simulation.

In Fig. 7-2 we show the R dependence of $R_{\rm AA}$ for $K = 0$, *i. e.* no broadening (left), and for $K = 50$ (right) for jets $|y| < 2$. For comparison, we show the suppression of anti-k_t jets with R=0.3 as measured by CMS in the same interval of momentum and rapidity. The

left most data point is the one we use to constrain the value of $\kappa_{\rm sc}$ in both cases. Therefore, these two simulations have different values of $\kappa_{\rm sc}$ although the difference is small, as already explained. In both simulations, although the suppression factor shows a very weak dependence on the reconstruction radius R, wide (large R) jets tend to be more suppressed than narrow (small R) jets. Within our model, this trend is easy to understand. When comparing jets at the same energy, wide jets possess more fragments that narrow jets. Since the larger the number of partons traversing the medium the larger the lost energy, wide jets are naturally more suppressed. The same qualitative dependence of the suppression factor with the jet size has been recently observed in holographic computations [89, 159]. Measurements of the R-dependence of $R_{\rm AA}$ by the CMS collaboration at this high energy show very little sensitivity to the jet radius, similar to our simulations, although experimental uncertainties do not allow us to constrain the small decrease of the suppression factor with R.

In spite of the extreme broadening introduced by having $K = 50$, the R dependence of this observable is almost identical in the two panels of Fig. 7-1. The origin of this independence on K lies in the strong quenching of jets by the plasma. Since this quenching implies a large energy loss, all soft fragments which could be easily decorrelated from the jet axes by multiple scattering are strongly quenched, reducing their energy to medium scale. For this observable, the medium acts as a filter, which suppresses all soft fragments; the jet sample that dominates the inclusive spectrum is then biased to contain few or just one hard parton (at scale Q_0) while propagating through the plasma. For those jets, therefore, the extreme broadening only leads to a rotation of the jet axis, but does not change the intrajet distribution nor the energy loss.

The strong modification of the intrajet structure is clearly illustrated by the analysis of jet shapes in quenched jets. Jet shapes are defined as the fraction of the jet energy reconstructed with a given anti-k_t parameter R contained in an annulus of width δr (in $\eta - \phi$ space) surrounding the jet axis. Following the analysis in [27], we construct the

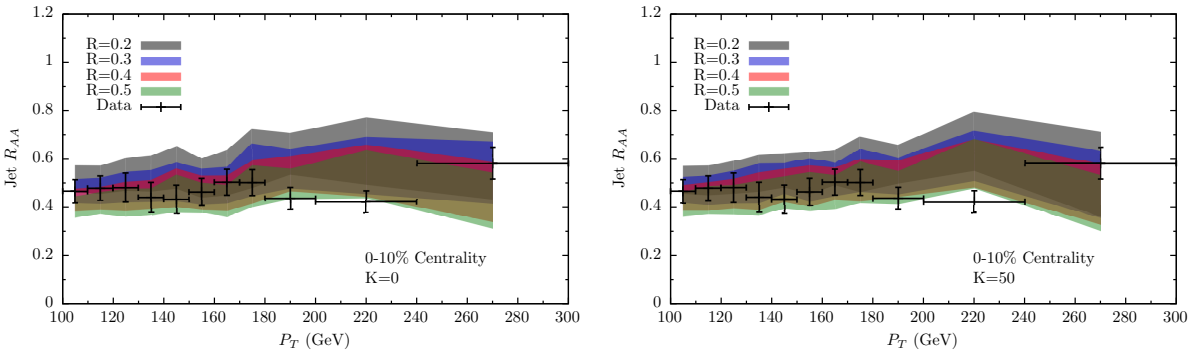

Figure 7-2: Dependence of RAA on jet radius R for $K = 0$ (no broadening, left panel) and $K = 50$ (right panel). We also show the CMS data from [139] which we use to refit $\kappa_{\rm sc}$ for the different values of K.

differential jet shapes as

$$\rho(r) \equiv \frac{1}{N_{\rm jets}} \frac{1}{\delta r} \sum_{\rm jets} \frac{\sum_{i \in r \pm \delta r/2}^{r_{\rm max}=R} p_t^{i,{\rm track}}}{p_t^{\rm jet}} \,, \tag{7.2}$$

where the tracks in the sum don't necessarily have to belong to the jet constituents defined through the anti-k_t clustering. For this reason the final jet shape distribution is multiplied by the event averaged factor $\left\langle p_t^{\rm jet} / \sum_{i=0}^{N_{\rm bins}} p_t^{\rm track}(r_i) \right\rangle$ so that it is normalized to one. The sum over jets includes all jets with $p_t^{\rm jet} > 100$ GeV and $0.3 < |\eta| < 2$. We show the result of this analysis in Fig. 7-3, where we compare the quenched to the unquenched (p-p) jet shape for two different centrality classes and for different values of K. For reference, we also show the experimental results for this ratio, as measured by the CMS collaboration [27].

The strong suppression of strong fragments described above is clearly illustrated by the suppression of the jet shape at large r. Jet shapes are strongly peaked at small r values; for jets with R=0.3, with most (96%) of the jet energy concentrated in $r < 0.2$. As r increases, the jet energy is distributed in softer and softer fragments. As we can see, the strong in-medium quenching strongly depletes the large r contribution of the jet shape, as compared to the vacuum shape. This depletion is almost independent of the jet broadening parameter. Similarly, the small r behaviour of the jet shape is almost identical to the vacuum

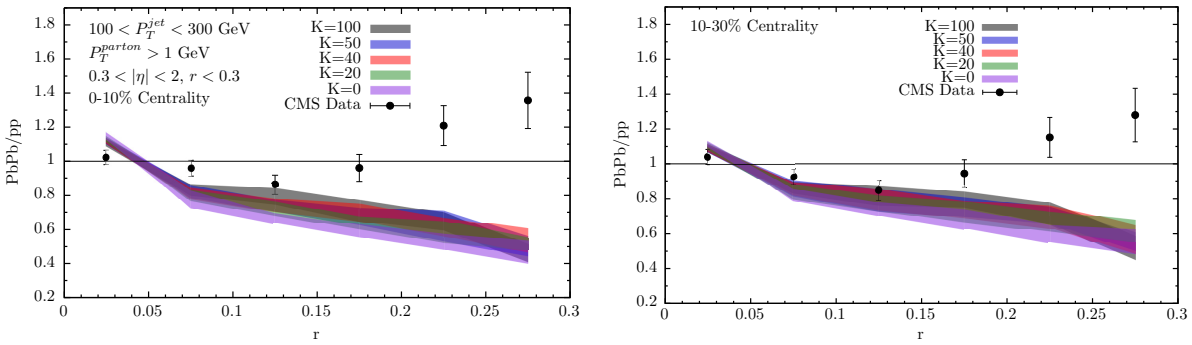

Figure 7-3: Left: Jet shapes ratio of PbPb/pp for different values of the broadening parameter K as compared to CMS data [27] for 0-10% centrality (left) and 10-30% centrality (right).

one, which shows that jets with only one fragment propagating through the plasma only suffer an overall energy shift. We have in fact tested that the final jet energy distribution is well approximated by the shape distribution of jets which only possess one fragment during in-plasma propagation, showing that multi-partonic structures are strongly suppressed. Therefore, the effect of broadening is only to tilt the jet axis of those single parton jets, which does not alter the final shape distribution. Since those single partons are as energetic as the jet, the deflected angle is small, even for the extreme values we consider in the Fig. 7-2.

It is also important to note that the trend of our numerical simulations is opposite to the experimental measurement. Indeed, the results of [27] indicate an enhancement of soft particles at large angles as a result of the in-medium interaction. This enhancement, which has little contribution to the overall jet energy, points to the existence of soft modes correlated with the jet axis. Within our current implementation, which is dominated by the extreme assumption that all the lost energy is thermalised immediately after the collision, no such enhancement is produced. Nevertheless, the collective reaction of the medium to the deposited jet energy leads to an additional source of correlations in the emission of particles from the fireball. In the next Section we will explore the influence of this dynamics on shape observables.

7.1.3 A Broadening-Sensitive Observable

Before describing the recovery of the jet energy, we would like to finish our study of broadening by identifying an observable with potential direct sensitivity of the broadening parameter $\hat{q}$ (or K in our implementation). The main reason for the insensitivity to broadening of the observables discussed in the previous section is that they are dominated by energetic partons in the plasma, whose direction is altered very little by the soft in-medium exchanges. Similarly, as we have observed, soft particles in plasma are strongly suppressed. This does not mean that reconstructed jets do not possess soft particles, but rather that those particles are only produced by the fragmentation of the hard partons outside the medium, and therefore equally insensitive to the in-medium broadening. For this reason, in this Section we introduced an observable which focusses in semi-hard partons, sufficiently soft to be deflected by soft exchanges, but sufficiently hard to survive in-medium propagation.

This new observable is, in essence, a more differential version of a jet shape. Instead of determining the r distribution of all the jet energy, we focus on the distribution of jet energy carried by particles in a certain interval of transverse momentum. Denoting this observable as $\Psi_{p_{\rm T}}(r)$,

$$\Psi_{p_{\rm T}}(r) \equiv \frac{1}{N_{\rm jets}} \frac{1}{\delta r} \sum_{\rm jets} \frac{\sum_{i \in r \pm \delta r/2}^{r_{\rm max}=2R} p_t^{i,\rm track}}{p_t^{\rm jet}} \,, \tag{7.3}$$

where the particles in the sample are constrained to have a transverse momentum in the range $10 < p_{\rm T} < 20$ GeV and the jets satisfy the same cuts as the ones entering $\rho(r)$. Analogously to the standard jet shapes we multiply the final distribution by the factor $\left\langle p_t^{\rm jet} / \sum_{i=0}^{N_{\rm bins}} p_t^{\rm track}(r_i) \right\rangle$, with the difference that now it doesn't normalize it to one due to the restricted $p_{\rm T}$ range of the selected tracks.

In Fig. 7-4 we show the prediction of our model for this observable for several values of the broadening K, selecting particles in the interval $10 < p_{\rm T} < 20$ GeV. The selection of these cuts follows two requirements: on the one hand, partons must be hard with respect to the medium temperature to ensure that no possible collective effects affect the measurement; this is safely achieved by th lower $p_{\rm T}$ cut of 10 GeV. On the other hand, the partons

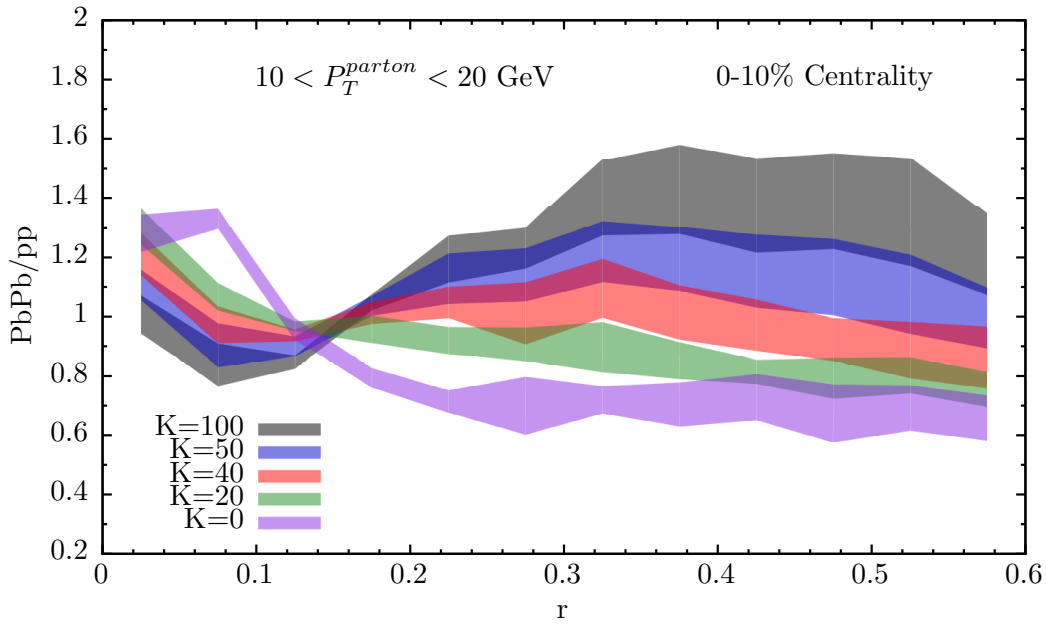

Figure 7-4: Special version of jet shapes ratio where the parton p_T cuts are $10 < p_T < 20$ GeV.

of this observable cannot be too hard, so that the in-medium deflection significantly alters their direction of propagation; we have found that the upper cut of $p_{\rm T} < 20$ GeV serves this purpose well. Therefore, unlike the less differential observables described in the previous section, $\Psi_{p_{\rm T}}(r)$ shows significant sensitivity to the value of K. Indeed, as K grows, the partons in this momentum range are more and more transported to distances farther away from the jet, populating the large r region and depleting the collinear ($r = 0$). Certainly, this observable is strongly sensitive to hadronisation effects, which are not under good theoretical control. Nevertheless, the observed sensitivity to in-medium broadening, absent in any of the other observables studied, encourages us to suggest the exploration of this measurement for a direct extraction of the in medium broadening.

7.2 Medium Back-reaction

In this Section we will incorporate another important feature to our description of quenching dynamics in plasma: the conservation of the lost energy. In our implementation up to now, the energy lost by energetic partons was assumed to be completely decorrelated from the jet axis and to be quickly transformed into a medium effect. This assumption was

motivated by the holographic analysis of the stress tensor associated to an energetic parton performed in [90, **?**], which showed that, indeed, after a short time of order $1/T$ all the energy dumped into the medium was rapidly converted into a hydrodynamic excitation of the system. These results showed in a field theory computation, $\mathcal{N} = 4$ SYM, that the collective response of the plasma to the jet passage, first described in [160, 110, 161, 162] did indeed take place, in spite of the fact that the probes of the system are small compared to medium scale. As a consequence of this back-reaction, the quark-gluon plasma does not behave only as a passive absorber of QCD jets, but its dynamics are altered as a consequence of the addition of the energy and momentum supplemented by the jet. In this Section we will provide a simple account of this collective response by providing a simplified description of this back-reaction without introducing additional parameters into the model.

The mechanism we will describe is not exclusive to strong coupling, although this scenario provides a natural realization for this collective response. Even in perturbative QCD analysis, the interaction and subsequent radiation of the medium induced gluons responsible for energy loss at strong coupling lead to a rapid degradation of the emitted gluon momenta. This degradation may be viewed as a rapid transfer of energy from hard (jet) modes to soft (medium) modes and it has been described recently in detail in [107, 163, 164, 152]. From the point of view of the radiative energy loss, the extreme assumption we will do is that no (experimentally sensitive) information of the short time distribution of energy associated to the energy loss survives the strong interaction with the medium. Note that this is well supported at strong coupling, while the perturbative distributions in a dense system, in which the multiple soft scattering approximation is valid, still exhibit some sensitivity to this initial distribution. For perturbative based analysis in which the system is treated as dilute, and therefore emitted gluons do not suffer significant interactions, the back-reaction dynamics we describe in this Section are irrelevant.

7.2.1 The Spectrum of Medium Particles Associated to Quenched Jet Energy

Following the discussion above, in this Section we will describe a simple implementation of the back-reaction of the plasma to the passage of an energetic source. We will characterize the medium response to the transfer of momentum by analyzing the induced velocity and temperature variations of the hydrodynamic behaviour of the quark-gluon plasma fluid. Since the total energy deposited by a typical jet in heavy ion collisions ($\mathcal{O} \sim 20$ GeV), is small when compared to the total energy per unit rapidity of the event ($\mathcal{O} \sim 1$ TeV), similarly to [160, 110, 161, 162] we will treat the incorporation of additional momentum to the medium as a small perturbation (for studies on the non-linear response of the plasma see [165, 166, 150, 167]). For simplicity, we will also assume that the unperturbed fluid is well described by a boost invariant flow. Although in our simulations of the lost energy we take into account transverse flow, in this first study of back-reaction effects we will neglect the effect of the background fluid velocity in the transverse plane. Consequently with this assumption, we will also assume that the freeze-out of the hot plasma occurs at at fixed proper time hyper surface. Within this approximations, we will be able to give a simple expression of the modified emission spectrum associated to the jet passage determined solely by the amount of energy and momentum lost by the jet.

In a boost invariant fluid with no transverse velocity, the disturbance associated to the jet may be characterised by a perturbation of the velocity field

$$\delta u^{\mu} = \left(0, \delta u^{i}, \delta u^{\eta}\right), \tag{7.4}$$

where δu^{i} goes through $i = 1, 2$ and δu^{η} are the variations of the velocity field in the transverse plane and space-time rapidity directions. The disturbance is also determined by the change in temperature of the plasma δT . These perturbed fields may not be boost invariant and in general will depend in all space-time directions. Within our assumptions, variations along the proper time direction are quadratic in fluctuations. At a fixed proper

time τ, the total momentum stored in the perturbation of the plasma is

$$\Delta P^i_\perp = w\,\tau \int d^2x_\perp\, d\eta\, \delta u^i_\perp\,, \qquad \Delta P^\eta = \tau w \int d^2x_\perp\, d\eta\, \delta u^\eta \tag{7.5}$$

where we have used that the variation of the fluid stress tensor is $\delta T^\tau_a = w\delta u_a$ with $w = \epsilon + p$ the enthalpy for $a = 1, 2, \eta$. Similarly, for an almost perfect fluid with small shear viscosity we may neglect non-dissipative effects on entropy production and compute the increase in entropy associated to the perturbation from the flux of the entropy current across the fixed τ hyper-surface

$$\Delta S = \frac{\tau s}{c_s^2} \int d\eta\, d^2x_\perp\, \frac{\delta T}{T}\,, \tag{7.6}$$

where s and c_s are the entropy density and speed of sound of the unperturbed fluid which, within the boost invariant assumption, only depend on the proper time τ.

Both Eq. (7.5) and Eq. (7.6) are valid at all fixed time hyper-surface and, in particular, in the freeze-out hyper-surface. At this time, both these expressions determine all the momenta and entropy produced by the source of the disturbance. Following our assumption that all the momentum lost by the jet decorrelates completely from the shower and incorporates into the plasma, $\Delta P^i_\perp$ and ΔP^η equal the transverse momentum and momentum rapidity lost by the jet in the plasma respectively. Since in our implementation of energy loss we have assumed that the rapidity of the jet remains approximately constant, we set $\Delta P^\eta = 0$.

The entropy production associated to the jet passage may also be constrained by the total energy carried by the particles produced by the perturbation. To do so, we will employ the standard Cooper-Frye prescription in order to determine the perturbed spectrum

$$E\frac{dN}{d^3p} \;= \tfrac{1}{(2\pi)^3} \textstyle\int d\sigma^\mu\, p_\mu\, f(u^\mu p_\mu)\,. \tag{7.7}$$

Assuming for simplicity a Boltzmann distribution $f(E) = \exp\{-E/T\}$, and expanding

to leading order in the perturbation we get

$$
\begin{aligned}
E\frac{d\Delta N}{d^3p} =& \frac{1}{(2\pi)^3}\,\tau \int d^2x_\perp\, d\eta\, m_T \cosh(\mathrm{y}-\eta)\, \mathrm{e}^{-\frac{\mathrm{m_T}}{\mathrm{T}}\cosh(\mathrm{y}-\eta)} \\
& \times \Big\{ p^i_\perp \frac{\delta u^i_\perp}{T} + \tau^2 p^\eta \frac{\delta u^\eta}{T} + \frac{m_T}{T}\frac{\delta T}{T}\cosh(\mathrm{y}-\eta) \Big\},
\end{aligned}
\tag{7.8}
$$

where $m_T = \sqrt{m^2 + p_T^2}$ is the transverse mass of the emitted thermal particle. Note that this expression is only valid for particles of momentum p comparable to the decoupling temperature T. Even if the perturbation is small, its effect on the thermal distribution of particles significantly away form the typical momentum is exponentially enhanced.

The expression in Eq. (7.8) is general and independent on the space-time dependence of the perturbed hydrodynamic fields. To proceed further we will assume that during the space-time evolution of the perturbation over the boost invariant background, the space-time rapidity of the disturbance remains approximately constant. Since high-energy jets propagate at a fixed space-time rapidity η_j equal to their momentum rapidity y_j, $\eta_j = y_j$, the previous assumption implies that the perturbation is narrow around the momentum rapidity of the jet, which allows us to perform the η integration in Eq. (7.8) by replacing $\eta \to y_j$. Imposing that the momentum of the emitted particles equals the lost momentum of the jet

$$
\Delta E = \int d^3p\, \frac{d\Delta N}{d^3p}\, E\,, \qquad \Delta P_{\perp,i} = \int d^3p\, \frac{d\Delta N}{d^3p}\, p_{\perp,i}\,,
\tag{7.9}
$$

and together with Eq. (7.5) and Eq. (7.6) we can fix the relation of the produced entropy and the energy lost as well as the enthalpy of the gas after decoupling and express the spectrum of particles emitted off the boosted, heated up fluid cell as

$$
\begin{aligned}
E\frac{d\Delta N}{d^3p} =& \frac{1}{32\pi}\,\frac{m_T}{T^5}\cosh(\mathrm{y}-\mathrm{y_j})\, \mathrm{e}^{-\frac{\mathrm{m_T}}{\mathrm{T}}\cosh(\mathrm{y}-\mathrm{y_j})} \\
& \times \Big\{ p_\perp \Delta P_\perp \cos(\phi-\phi_j) + \frac{1}{3} m_T\, \Delta M_T \cosh(\mathrm{y}-\mathrm{y_j}) \Big\}.
\end{aligned}
\tag{7.10}
$$

where p_T, m_T, ϕ and y are the transverse momentum, transverse mass, azimuthal angle and rapidity of the emitted thermal particle, ΔP_T and $\Delta M_T = \Delta E/\cosh y_j$ are the trans-

ferred transverse momentum and mass from the source with ϕ_j and y_j its azimuthal angle and rapidity. Note that this spectrum is the correction to the one body distribution of particles emitted by the hot plasma. As a consequence, this distribution may be negative, as it may occur for the emission of particles opposite to the jet direction in the transverse plane. Those negative values simply mean that the perturbed thermal source emits less particles in the direction opposite to the jet propagation than the unperturbed one. This is a consequence of the global push of the fluid along the direction of lost momentum.

This closed expression, which only depends on the momentum lost by the jets in the plasma and on the kinematics of the jet, will be the basis for our analysis of back-reaction. Under the physical assumptions employed in this derivation, this spectrum allow us to provide an estimate on the effect of collective response of the plasma to the jet passage without having to model explicitly the complicated process of relaxation of the energy lost by the jet. As stated, this expression is only valid for thermal particles emitted with a momentum comparable to the mean momentum in the fluid cell and it significantly deviates for semi-hard particles produced in the plasma. Nevertheless, we will use this expression also for that range as a first estimate. In the next Section we will explain how we have implemented this spectrum in our analysis of jets propagating within hot QCD plasma.

7.2.2 Implementation of Back-Reaction, Background Model and Jet Hadronisation

The implementation of the simplified expression Eq. (7.8) for the spectrum of back-reacted particles demands further modelling for a proper description in heavy ion collisions, which we now address. The three main aspects that we will need to incorporate into our description are the effect of radial flow and chemical composition of the fireball, the implementation of a background to properly account for the negative contribution from the induced spectrum, and the generation of particles consistent with the one body distribution Eq. (7.8). Furthermore, since the particles produced after decoupling are hadrons, we will also need to consider the hadronisation of our quenched jet samples, which we have not included in our previous implementation of the hybrid model. In this section we will discuss these four

aspects sequentially.

As we have stated, our derivation of Eq. (7.8) neglects the effect of the flow fields of the unpertubed fluid in the transverse direction and, as a consequence, the effect of radial and azimuthal flow. The effect of the latter is small in most central collisions, but the former has important consequences for the spectrum of particles produced by the fireball. As it is well known, the radial boost of the velocity field leads to a spectrum which is harder than that of a fixed temperature source at the decoupling temperature, as a consequence of a thermal blue shift. Another consequence of radial flow is the different spectrum of particles which have different masses, getting the more massive hadrons a harder spectra than the lighter ones. Because of the thermal blue shift, Eq. (7.10) produces a much softer spectrum than the experimentally measured one, which significantly affects the influence of back-reaction dynamics on jet observables. Because of the different spectrum of massive particles, Eq. (7.10) also underestimates significantly the number of particles with an energy few times the temperature. For this reasons, we will correct in part the deficiencies of the model by employing in our implementation of Eq. (7.10) effective temperatures which differ from the decoupling temperature and that are species dependent. To gauge the effect of the chemistry, we will consider the plasma to be composed mainly by pions and protons, leaving a more detailed study of the hadrochemestry of back-reaction to future work. By fitting the measured particle spectra [168] to a spectrum consistent with Eq. (7.8), we will use the following (momentum dependent) temperatures for pions and protons

$$T_\pi(p_\mathrm{T}) = 0.21\, {p_\mathrm{T}}^{0.28}\,\mathrm{GeV} \qquad \mathrm{T_p(p_T)} = 0.4\,\mathrm{GeV} \tag{7.11}$$

with T_π forced to lie within the range $[0.19, 0.4]$ GeV for any p_T together with a proton to pion ratio of 0.05. This values provide a good description of both the proton and pion spectrum in the region of $p_\mathrm{T} < 3$ GeV (up to the region of very small momentum $p_\mathrm{T} \sim 0.5$ GeV where the measure yield contains a large contribution from resonant decays and we get maximum deviations of 10%), and therefore are well described by the boosted thermal distribution at that momentum.

As we have already discussed, a characteristic feature of Eq. (7.10) is that for jets with

small ΔM_T, the perturbed spectrum of particles emitted at large azimuthal angle with respect to the jet direction becomes negative. This reflects the fact that a boosted fluid cell will emit less particles along the opposite direction of the boost when compared to the non-perturbed case. This negative contribution therefore depletes momentum in that region of azimuth as compared to analysis performed assuming an unperturbed background. To best determine the implications of the effect, we will embed our jet sample in an oversimplified background, whose sole purpose is to provide sufficient thermal particles as to neutralise the negative contribution in the induced spectrum. The background is constructed by generating an ensemble of pions and protons which is flat in ϕ and η that reproduces the measured particle yield and spectra, without including azimuthal flow. As we will stress in the next Section, the addition of this contribution will force us to introduce a background subtraction procedure in our analysis of in-medium jets. We will describe this procedure in detail in Section 7.2.3.

On an event by event basis, we determine the lost momentum by all the partons in the jet shower[2] as well as in initial state radiation following our hybrid strong/weak coupling model as described in Section 4.3 . Since each of the propagating partons loses energy into the medium, each of them generates its own wake induced by its lost momentum. In the linearised approximation we have employed, the multiple generated wakes do not alter each other, and the final spectrum is the superposition of the spectrum generated by each propagating parton. At hadronisation, each of the induced wakes generates an ensemble of particles consistent with the one body distribution Eq. (7.10) computed from the kinematics of each parton and its lost momentum. This ensemble in general contains particles in the region of azimuthal angle in which Eq. (7.10) becomes negative, which we will call negative particles. These negative particles are neutralised by removing a particle from the background which is sufficiently close in $\eta - \phi$ space and in transverse energy [3].

[2]For the back-reaction analysis we include all particles of the jet shower, independently on whether they belong to jets of a fixed reconstruction radius.

[3]Negative particle neutralisation proceeds as follows: by looking into the particles surrounding the negative one within a cone of $R \sim 0.3$, start a loop looking for the best candidate in terms of E_T and angular position in $\eta - \phi$ plane, which means that we want to minimize ΔE_T and Δr, the difference in transverse energy and angular position with respect to the negative particle respectively. Select as a provisional candidate an arbitrary background particle, setting a ΔE_T^{min} and a Δr^{min}, then update candidate if the next particle in the loop satisfies one of the following two conditions: 1) $\Delta E_T < \Delta E_T^{min}$ and $\Delta r < \Delta r^{min} + 0.05$;

To take into account the effect of fluctuations into the reconstructed in-medium jets, we generate the back-reacted ensembles via a simple Metropolis algorithm designed to satisfy the conservation of the lost jet energy. The procedure contains the following steps. First we generate an independent list of particles from the one body distribution Eq. (7.10) until the sum of their energies reaches the lost energy. This ensemble randomly selects pions and protons such that the average ratio coincides with the average measure yield. Whenever a negative particle is produced, as defined above, its contribution to the net energy and momentum of the ensemble is negative. This initial list also sets the number of negative particles. From this initial ensemble, whose four-momentum in general will not coincide with the lost jet momentum, we randomly select a particle which we substitute with a new particle according to Eq. (7.10). If the change improves four-momentum conservation, it is accepted. Otherwise, the change may be accepted with a probability distribution

$$W(p^{\mu}_{\text{new ensemble}}) = e^{-\left(p^{\mu}_{\text{new ensemble}} - \Delta P^{\mu}\right)^2} / e^{-\left(p^{\mu}_{\text{ensemble}} - \Delta P^{\mu}\right)^2}, \tag{7.12}$$

where $p^{\mu}_{\text{new ensemble}}$ is the four momentum of the candidate ensemble, $p^{\mu}_{\text{ensemble}}$ the one of the previous ensemble, and ΔP^{μ} is the lost four-momentum of the hard event. The procedure is repeated until each of the four components of p_{ensemble} is within 400 MeV of the total lost momentum[4]. The ensemble generated after this procedure conserves energy and momentum (within the tolerance above) and possess a one body distribution identical to Eq. (7.10), which we have explicitly checked.

Since the medium response manifests itself in the form of modified distributions for hadrons, namely pions and protons in our approach, we are forced to consider the hadronisation of jet showers to properly account for the effect of medium back-reaction in final observables. Hadronisation leads, generically, to a softening of the typical jet fragments; a failure to introduce these dynamics would significantly underestimate the effect of thermal source since the typical partonic fragment is much harder than its associated hadrons. Nevertheless, because of its non-perturbative nature, hadronization in vacuum still remains a

or 2) $\Delta E_T < \Delta E_T^{min} + 0.1$ GeV and $\Delta r < \Delta r^{min}$. We have checked that by this procedure we can simultaneously satisfy the transverse energy and angular coincidence conditions to a very reasonable degree

[4]We have explicitly checked that changing this threshold does not significantly change our results

fundamental problem and presents serious challenges for its phenomenological modelling. Furthermore, the modification of the models that are successfully applied to vacuum QCD processes due to the presence of a heavy ion environment is not yet understood. As an example, the change of colour flows in the jet shower as a result of soft exchanges with the medium has been argued to lead to significant effects in certain regions of phase space [128], but its overall description remains yet unclear. Because of all these uncertainties, in this work we will adopt a simplified model for the in-medium hadronisation, which has been widely use in the literature. The main assumption is that hadronisation of high energy jets occurs in the same way as in vacuum, keeping, in particular, the same colour correlations in spite of the in-medium exchanges. Although several different prescriptions exist, in this work we will employ the Lund string model as implemented in PYTHIA acting on the medium-modified shower generated by our hybrid approach. We defer the analysis of the impact of different models for future work.

7.2.3 The Effect of Back-Reaction in Jet Observables

After the implementation of energy loss of hard processes via the hybrid model described in Section 4.3, the medium response to the energy lost in the plasma and the thermal-like background in which the quenched hard events are embedded, as described in Subsection 7.2.2, we obtained a full event simulation from which to extract medium modified observables. In contrast to our previous work from previous Chapters, the inclusion of a background forces us to implement a background subtraction procedure, making our analysis of quenched events much closer to the actual analysis of jet data at the LHC. The medium response to the jet passage makes this complicated procedure absolutely necessary. For hard jets produced together with an uncorrelated (to the jet) background, several stablished techniques (see for example [169, 170, 171]) allow for a systematic removal of the effect of background particles from jet observables. This procedure, generally referred to as background subtraction, is routinely applied to jet measurements at the LHC and, at least in p+p collisions, efficiently removes the effect of large soft (non-pertrubative) backgrounds from theoretically controlled hard processes. However, in a heavy ion environment, a strong

medium response as the one describe above correlates part of the background with the jet direction, which makes the outcome of the subtraction procedure unclear. To gauge the effect of the dynamical medium in jet samples analysed as if the background was uncorrelated to the jet, we will implement a full background subtraction procedure to analyse the events produced within our framework. In particular we have implemented a version of the so called noise/pedestal background subtraction procedure [172, 25]; the details of our implementation can be found in Appendix D.

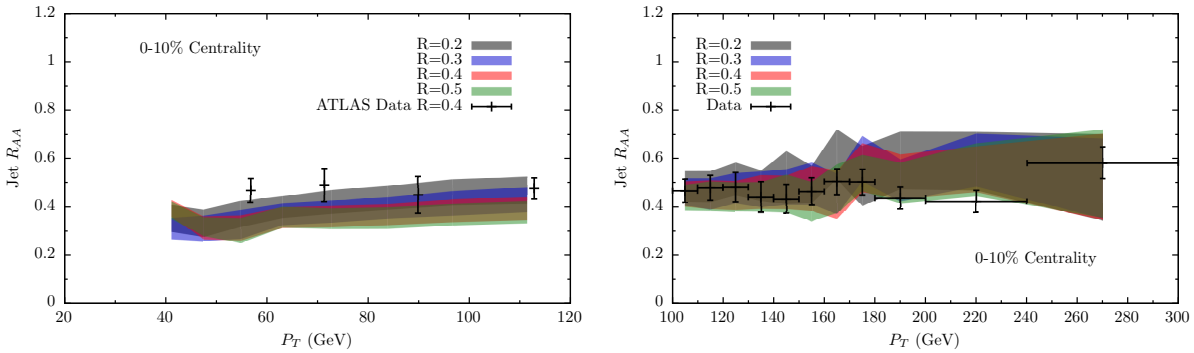

Figure 7-5: Dependence of R_{AA} on the jet radius R for $K = 0$ with the inclusion of back-reaction effects. The left plot shows this observable for $40 < p_T^{jet} < 100$ GeV, while the right one has $100 < p_T^{jet} < 300$ GeV.

As in Section 7.1, we first consider the R-dependence of jet suppression. In Fig. 7-5 we show jet $R_{\rm AA}$ as a function of $p_{\rm T}$ for central events for a long interval of jet momenta and for different anti-k_t radii. In the right panel, we show our results for $100 < p_{\rm T} < 300$ GeV in comparison with CMS measurements of $R_{\rm AA}$ for $R = 0.3$ jets. Note that, similarly to broadening, back-reaction alters the jet suppression factors, which made us re-tune our model. Nevertheless, this retuning only modifies the value of $\kappa_{\rm sc}$ at the percent level, which is much smaller than the theoretical uncertainty reported in previous Chapters. As for broadening, $R_{\rm AA}$ in this region shows a very small dependence on reconstruction radii, consistent with LHC data [139].

Due to the same filtering of multi-partonic jets in medium described in Section 7.1, the suppression factor $R_{\rm AA}$ shows a small decrease, with increasing jet radius. However, this effect is milder than in the broadening case, since back-reaction puts part of the lost energy from hard partons back into the jet cone by correlating medium particles with the jet

axis. Nevertheless, the wide angular distribution of the spectrum of back-reacted particles, Eq. (7.10), implies that even for the relatively large radius of $R = 0.5$ explored in Fig. 7-5, the recovered energy is small. For even larger reconstructed jet radius, the full jet energy is recovered and $R_{\rm AA}$ approaches unity. However, for those large radius, fluctuations in the background make the reconstruction algorithm we have implemented uncertain[5].

In the right panel of Fig. 7-5 we show the jet $R_{\rm AA}$ for smaller jet $p_{\rm T}$ for different values of R. As previously reported in the left panel of Fig.5-2, the suppression factor shows a mild increase with $p_{\rm T}$, in agreement with ATLAS data. In spite of the lower energy, the effect of back-reaction in the explored range of radius is small, similarly to higher momentum jets. This is in apparent contrast with $R_{\rm CP}$ measurements reported by ALTAS in [25], which indicate that the suppression of jets decreases with radius in this range of momenta [6], although with sizeable systematic uncertainties. Nevertheless, this contrast points towards possible improvements of our model[7], which we will discuss in Section 7.3.

To further study the R dependence of jet suppression in our model, and motivated by the ALICE analysis reported in [35], in Fig. 7-6 we show the ratio of spectra of jets in Pb-Pb collision at different radii to that of $R = 0.2$. For comparison, we show the same ratio in p+p collisions as simulated by PYTHIA. An important advantage of this observable is that it is constructed with Pb-Pb data only. This leads to a significant reduction of the theoretical uncertainties in our model, since the errors of the spectra at different radii are correlated. This is the reason why the widths of the theoretical predictions displayed in Fig. 7-6 are significantly narrower than those of $R_{\rm AA}$. Because of this cancellation of uncertainties, this observable clearly shows that within the range of R studied, wider jets lose more energy than narrower jets. In vacuum, the number of jets with a given $p_{\rm T}$ increases as R increases, since wider jets include a larger fraction of the initial partonic energy. Therefore, the ratio of spectra of jets of R=0.2 to that of jets with a given R decreases with R. In the medium, this general trend is also observed. However, this ratio reduces more slowly with increasing R.

[5]We have explicitly tested the recovery of jet energy by embedding our simulations in a homogenous background with no fluctuations.

[6]Since ATLAS repots $R_{\rm CP}$ as opposed to $R_{\rm AA}$, in Fig. 7-5 and since our simulations do not reproduce the suppression in peripheral events due, in part, to the lack of energy loss in the hadronic phase (see [173, 174]) we do not directly compare to those data

[7]Note that the background subtraction method implemented in this work is not completely equivalent to the one implemented in [25].

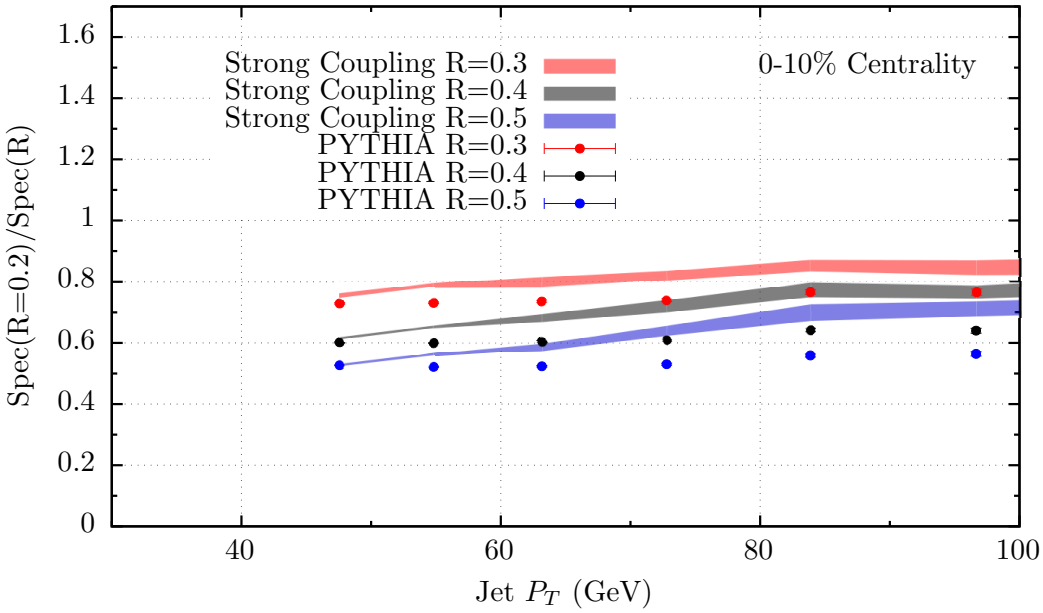

Figure 7-6: Ratio of the spectrum of jets with radius R over jets with radius 0.2 as a function of the reconstructed jet p_t. The colored bands correspond to the hybrid model and the dots are the vacuum simulations as described by PYTHIA. The shift upwards of the PbPb results are due to the fact that in our model wider jets lose more energy.

Since energy loss affects all radii, and in particular, both the numerator and the denominator in Fig. 7-6, the fact that all spectra are more similar in medium than in vacuum shows that wider jets lose more energy.

Another interesting feature of this observable is that the deviation between the vacuum and medium ratios increases as the momentum of the jet increases. This fact is a consequence of the strong suppression of jets with several in-medium partons. Low $p_{\rm T}$ jets contain, on average, a smaller number of partons propagating simultaneously in medium. Therefore, the low $p_{\rm T}$ region is dominated by jets that at medium scale are formed by only one parton, for which the energy loss is independent of the reconstruction radius. As the $p_{\rm T}$ becomes larger, the average number of partons per jet increases, and the medium filters out the contribution of jets with high partonic content, which are more abundant the larger the jet radius. Although a direct comparison with the semi-inclusive jet measurements performed by ALICE is not possible, our analysis highlights the potential that this type of measurements have in discerning the mechanisms of jet quenching.

Paralleling the discussion in Section 7.1 we now turn to jet shapes ratio, shown in Fig.

7-7 for two different centralities, to further explore the angular structure of the suppression mechanism. To gauge the effect of hadronisation and background subtraction on one hand, and back-reaction on the other, in both panels we show the jet shape computed at hadronic level with and without back-reaction. As discussed in the broadening section, the hybrid model is very effective at quenching the many soft and medium partons populating the jet. As a consequence, without back-reaction the effect of energy loss is to increase the importance of narrow jets in the quenched jet sample, leading to a depletion of the modified jet shape at large transverse distances. Note that the only difference between the non back-reacted simulations in Fig. 7-7 and the $K = 0$ simulations displayed in Fig. 7-3 is hadronisation and jet reconstruction. The partonic distributions in Fig. 7-3 give rise to narrower distributions than the hadronic ones displayed in Fig. 7-7, a natural consequence of the non-trivial angular distribution of the Lund strings connecting the hard partons in the jet. The sizeable contribution of hadronisation effects in this observable agrees with the general analysis of narrow jets performed in [175].

Despite the hadronic uncertainties, the measured jet shape distribution shows a remarkable increase of the jet energy at large r, *i. e.* at large angular distance from the jet axis. It is important to keep in mind that the large enhancement displayed in the ratio of jet shapes does not mean that in-medium jets become significantly wider than vacuum jets. Bot for PbPb and pp most of the jet energy is concentrated at small r. However, in PbPb jets the fraction of the jet energy contained in the region of $r > 0.2$ is larger than in pp, but in both cases this fraction is small. The measured jet shapes points towards the existence of in-medium dynamics that can transport small fractions of jet energy to large angles. The hadronisation of the wakes associated to the hydrodynamic response to the deposition of energy provides such a mechanism. Although within our current implementation of back-reaction effects we obtain a clear enhancement of jet shape at large angle with respect to the non back-reacted case, it is clear from Fig. 7-7 that this energy transport to large angles is insufficient to describe LHC data. As we will elaborate in Section 7.3, the jet shape analysis is most sensitive to semi-hard particles in the region of $p_{\rm T} > 1$ GeV, in which the small field approximation of Eq. (7.10) is not valid. Nevertheless , the discrepancy of our simulations with data may point to the existence of a more efficient mechanism of energy

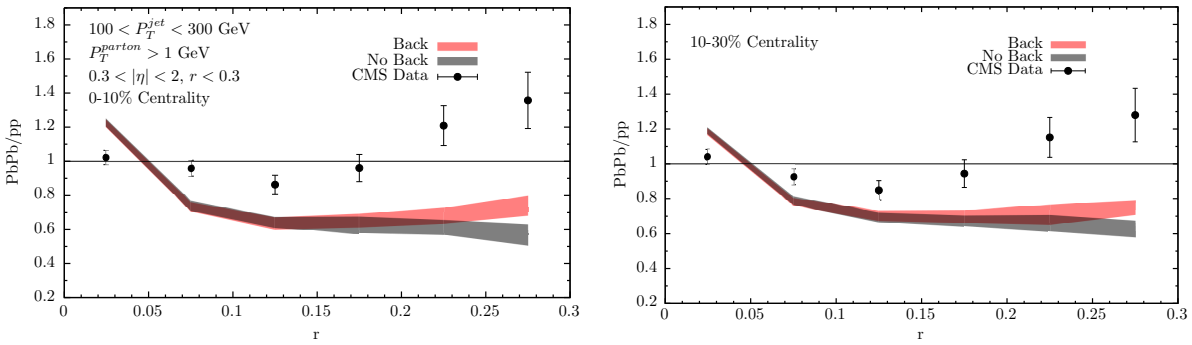

Figure 7-7: Jet shapes ratio of PbPb/pp comparing our system with and without back-reaction effects for 0-10% centrality (left) and 10-30% centrality (right).

transport at large angles into semi-hard partons. We defer this discussion to Section 7.3.

We now turn to an intrinsically hadronic observable: jet fragmentation functions. These show the distribution of relative momentum of the tracks along the jet axis with respect to the total jet momentum, $z \equiv \cos\theta\, p_{track}/p_{jet}$. Unlike in previous Chapters where we only analyzed partonic fragmentation functions, the inclusion of hadronisation allows us to do a direct comparison with experimental measurements. However, we must keep in mind that the hadronisation process is not under good theoretical control and that we have only implemented a simplified prescription which assumes no changes in the colour flow of in-medium jets. The study of different prescriptions for hadronisation within our model will be studied elsewhere.

Results for jet fragmentation functions are shown in Fig. 7-8 for 0-10% and 10-30% centrality. Both panels display the ratio between PbPb over pp (hadronic) fragmentation functions compared to data. We include two bands, one for the simulation with back-reaction and the other without it. Since the fluctuations in our simplified background do not coincide with those of an actual heavy ion collision, we need to correct for the difference in jet energy resolution, as described in Appendix D, in order to do a fair comparison with CMS data [27]. To subtract the background we use the η reflection procedure described in [27], which is the reason why the η cut has to be greater than the jet radius $R = 0.3$.

By comparing the results of our simulations with and without back-reaction, the jet fragmentation functions clearly show which is the effect of the medium response. The hard part of the jet is practically independent of the background dynamics, with an al-

most identical distribution of hard fragments[8]. Both simulations show and enhancement of hard fragments at large z (small $\log 1/z$) values. Such enhancement is due to the already discussed filtering of the small energy partons of the jet responsible for the narrowing of the jet shape distribution, which also hardens the jet. Such enhancement seems therefore generic to any mechanism of energy loss which reduces significantly the soft components of jets (see [176] for a similar effect in a perturbative-based jet quenching Monte Carlo [177, 178]). The small-z part of the fragmentation function is sensitive to back-reaction effects. The emission of soft particles by the jet-induced wake compensates the suppression of soft fragments due to energy loss and leads to an overall enchantment of soft tracks in the PbPb jets with respect to pp jets. The comparison between back-reacted and no back-reacted simulations also shows the range of momenta at which back-reaction becomes effective, $p_{\rm T} \sim 2.5$ GeV, where our approximate approach to the wake distribution Eq. (7.10) significaly underestimates particle production.

The back-reacted fragmentation function is in general qualitative agreement with the measured modifications by CMS. At large z, the central value of the measured data points do not show an enhancement, although the uncertainties are large. At small z a soft enhancement with respect to pp jets is observed, which is similar to that introduced by medium back-reaction, although the experimental data shows a larger magnitude for such effect starting at larger values of z than in our simulations. A better description of back-reaction dynamics and a better understanding of hadronisation of medium-modified jets could bring our simulations to a much closer agreement with this challenging observable. Nevertheless, it is worth mentioning that the disagreement between the PYTHIA Monte Carlo simulations of p-p events and the fragmentation functions of the small R jets can be as large as 30%, a number which is comparable to the size of medium modifications themselves. Despite this fact, it is interesting to note that back-reaction dynamics have a large impact into the small z description of jet fragmentation function. In the next Section we will explore other observables which are more sensitive to the soft particles emitted as a consequence of medium response.

[8]The small differences between the two simulations can be understood as the small change in reconstructed jet momentum associated to the addition of soft particles to the jet.

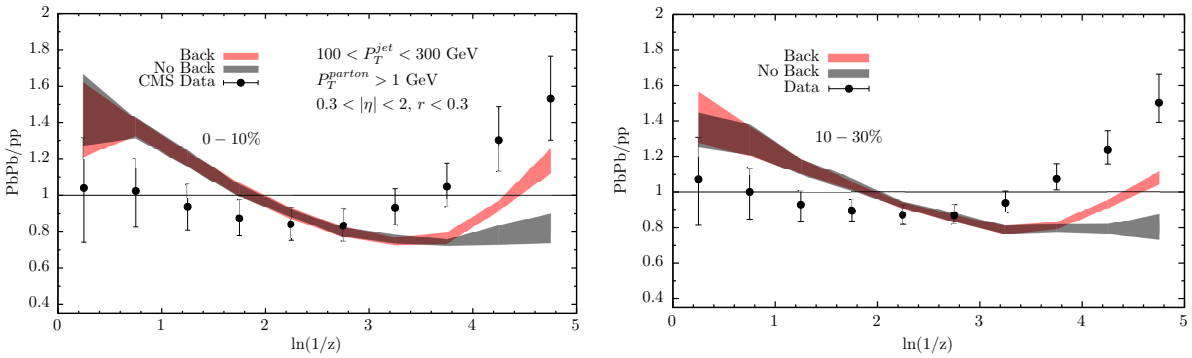

Figure 7-8: Jet fragmentation functions ratio of PbPb/pp comparing our system with and without back-reaction effects for 0-10% centrality (left) and 10-30% centrality (right).

7.2.4 Recovering the jet energy and missing $p_{\rm T}$

As we have seen, medium back-reaction has important consequences for the distribution of soft particles in hard di-jet (and in general multi jet) events. However, an important feature that makes the inclusion of these effects superior to other implementations that do not take into account the response of the medium is full energy conservation in the overall event. As we have stressed, one of the main assumptions of our model, supported by strong coupling computations, is that all the lost energy by the jet is quickly incorporated into the collective motion of the quark-gluon plasma and it is therefore recovered in the form of soft particles with a wide angular distribution given by Eq. (7.10). In this section we will study the spectrum and angular distribution of the lost energy by studying the so called "missing $p_{\rm T}$" observables introduced recently by CMS [179] which we will describe below. Note that this is an intrinsically hadronic observable, and therefore, hard to control theoretically without significant modelling. Nevertheless, we will observe several qualitative features of our implementation which are common to the experimentally measured distribution which indicates that our treatment, although simplified, captures the main aspects of the collective reaction of the plasma to the deposited jet energy.

Following [179], the missing $p_{\rm T}$ analysis consists in studying the conservation of momentum in heavy ion events which include hard jets of a given anti-k_t radius. In this analysis, the momenta of each of the particles of the event is projected along the jet axis,

as determined by the anti-k_t algorithm. This projection is given by

$$\not{p}_{\mathrm{T}}^{\parallel} = -p_{\mathrm{T}} \cos\left(\Phi_{\mathrm{Dijet}} - \Phi\right) \ , \tag{7.13}$$

where p_{T} is the transverse momentum of the track, while Φ and Φ_{Dijet} are the azimuthal angles of the track and dijet respectively. The dijet angle is defined as the bisection between the azimuthal angles of the dijet pair. With this convention, $\not{p}_{\mathrm{T}}^{\parallel}$ is positive for tracks in the subleading jet hemisphere and negative otherwise. By momentum conservation, the sum of all the $\not{p}_{\mathrm{T}}^{\parallel}$ in an event is zero. However, in the experimental analysis only charged tracks with $|\eta| < 3$ are considered, and therefore, the net $\not{p}_{\mathrm{T}}^{\parallel}$ does not cancel identically. Nevertheless, studying the approximate cancellation of this momentum component as a function angular distance from the jet we can extract valuable information about the distribution of the lost jet energy. Note that in this analysis, the jet reconstruction algorithm is only used to select the event sample and to determine the jet axis and no background subtraction is performed.

We start by computing the $\not{p}_{\mathrm{T}}^{\parallel}$ distribution sliced in Δ bins, where Δ is the distance in $\eta - \phi$ plane of the track with respect to the dijet angle in the hemisphere of the jet to which it is closest. We consider di-jet pairs with leading and subleading transverse momenta ${p_{\mathrm{T}}}^{L} > 120$ GeV and ${p_{\mathrm{T}}}^{S} > 50$ GeV respectively and with both jets within $|\eta| < 2$. These two jets are required to be back-to-back, which translates into $\Delta\phi > 5\pi/6$. Finally, after identifying the di-jet pair, only those di-jets with both jets $|\eta| < 0.6$ are considered. The result of this analysis is shown in Fig. 7-9 for our full simulations including medium response (right) and, for comparison, without medium back-reaction (left). In both plots, the net $\not{p}_{\mathrm{T}}^{\parallel}$ at each Δ of all charged tracks with $|\eta| < 3$ is given by the solid points; the contribution to this net momentum of tracks in different momentum bins are codified by the coloured histograms. In both plots, the solid line shows the accumulative sum in Δ of $\not{p}_{\mathrm{T}}^{\parallel}$, for all p_{T} bins in our PbPb simulation; for comparison, the dashed line shows the same sum for the $p - p$ events as determined by our PYTHIA tune. Note that the $\not{p}_{\mathrm{T}}^{\parallel}$ distribution generated by the PYTHIA tune we use is not identical to the p-p measurements reported in [179]. This small discrepancy illustrates the difficulty in quantitatively describing this hadronic observable.

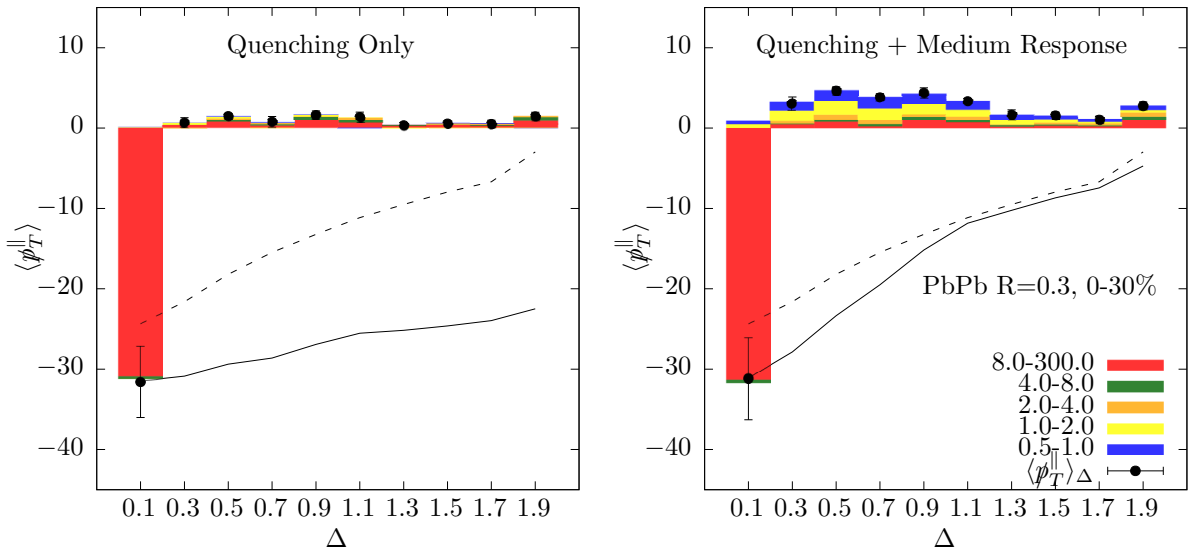

Figure 7-9: Missing p_T plots A_J inclusive as a function of Δ in PbPb collisions for $R = 0.3$ jets with quenching only (left) and quenching plus medium response (right). The inclusion of back-reaction clearly shows how the energy is recovered due to soft particles in the subleading jet hemisphere, in consonance with experimental results, implying that the absence of the effect gives a flawed physical description of jet quenching.

The comparison of the two panels clearly shows the effect of medium back-reaction. While the accumulated $\not{p}_{\mathrm{T}}^{\parallel}$ tends to zero as Δ increases for the simulations in the left panel, in the right panel it saturates at a fixed value similar to 20 GeV. This saturation value indicates the average energy lost by the dijet pair, which compares well with the simple estimates in [106]. The medium response transforms the lost energy into softer particles in the range of $\sim 0.5 - 2$ GeV, which move preferentially along the direction of the most quenched jet, the subleading jet, as shown by the enhancement of soft $\not{p}_{\mathrm{T}}^{\parallel}$ observed in the left panel of the figure. The figure also shows explicitly the wide angular region in which the lost jet energy is distributed, since the soft enhancement survives up to large distances $\Delta \sim 1$. As already explained, back-reaction dynamics do not change the hard part components of the jet and therefore, the red histogram is almost identical in both panels, signaling that most of the hard fragments lie in the leading jet hemisphere. The experimentally measured distributions are very similar to our simulations. Nevertheless, our implementation of medium back-reaction in-general gives a larger fraction of softer particles in the subleading jet hemisphere and an underestimate of the distribution of semi-hard, $2 < \not{p}_{\mathrm{T}}^{\parallel} < 8$ GeV

particles. We will defer the discussion of the origin of this discrepancy to Section 7.3.

We now study the dependence of the $\not{p}_{\rm T}^{\parallel}$ distribution on the di-jet asymmetry $A_J = ({p_{\rm T}}^L - {p_{\rm T}}^S)/({p_{\rm T}}^L + {p_{\rm T}}^S)$. In Fig. 7-10 we show the integrated value of $\not{p}_{\rm T}^{\parallel}$ over the angular separations Δ for di-jet events reconstructed with anti-k_t R=0.3 in bins of the di-jet asymmetry for two different centralities. The larger the di-jet asymmetry the larger the momentum imbalance between the leading and associated jet. In Pb-Pb collisions, events with a larger momentum imbalance are associated, in average, with larger in-medium losses of the subleading jets. Nevertheless, the wide A_J distribution in $p-p$, which is controlled by strong radiative processes associated to the production of hard di-jet events also leads to a non-trivial $\not{p}_{\rm T}^{\parallel}$ distribution in those events, independent of the exchanges with the plasma. To focus on in-medium effects, in Fig. 7-10 the (vacuum) p-p distribution is subtracted from the Pb-Pb one. As in the previous plot, the contribution of the different particle momentum ranges is shown by the coloured histograms and the solid points correspond to the contribution of all bins. The error bar shows the theoretical uncertainty.

These distributions clearly show both the effect of energy loss and medium back-reaction in the event. On the one hand, for both centralities and for all values of A_J, particles of momentum $p_{\rm T} > 2$ GeV are enhanced in the direction of the leading jet and suppressed in the direction of the associated jet, as compared to p-p, as shown by the negative value of the different histograms in the figure. This is a natural consequence of energy loss, since the associated jet loses on average more energy than the leading jet, which suppresses the momentum of the fragments that form the jet. Consistently with this interpretation, the net negative contribution of this region of momenta increases with increasing asymmetry and centrality. Soft particles are, on the contrary, enhanced in the subleading jet direction in Pb-Pb with respect to p-p. Within our implementation, the emission of particles correlated to the jet axis in this momentum range is totally controlled by medium back-reaction. The collective response of the plasma is oriented along the direction of the net deposition of momentum, which coincides with the subleading jet direction. The amount of $\not{p}_{\rm T}^{\parallel}$ in soft momenta completely balances the momenta in hard particles and, therefore, the number of soft fragments in the subleading jet direction increases with centrality and A_J. These

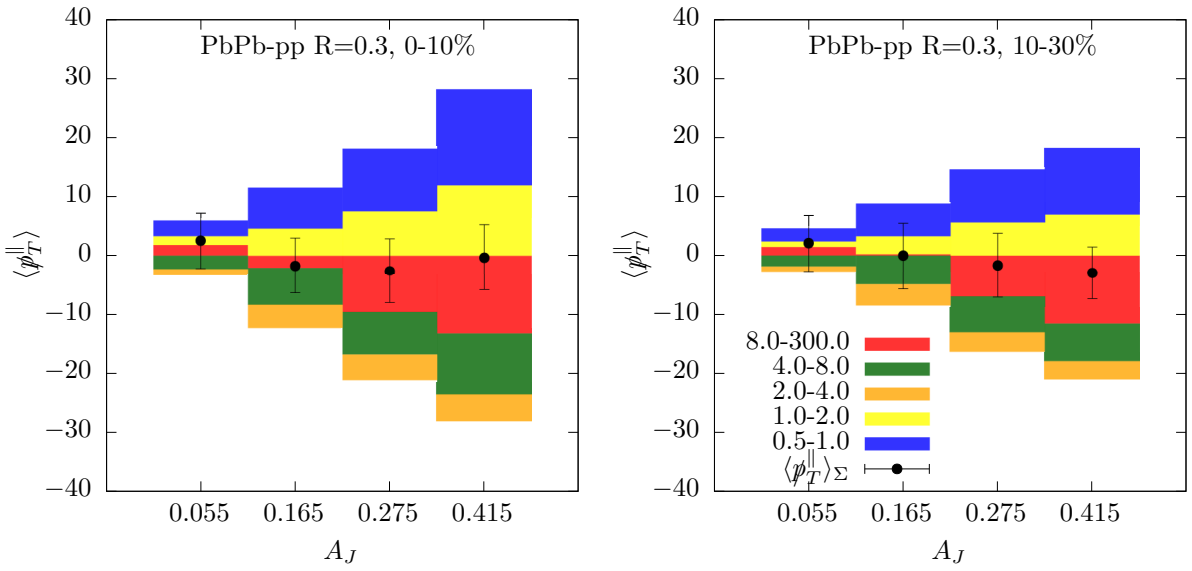

Figure 7-10: Missing $p_{\rm T}$ plots of the difference between PbPb and pp collisions, Δ inclusive as a function of A_J for $R = 0.3$ jets for 0-10% (left) and 10-30% centrality class. Quenching suppresses the hard particle contribution in the subleading jet hemisphere, whose energy has been thermalized and transformed into softer hadrons. The effect is somewhat milder in the more peripheral centrality class as it is expected due to the smaller size of the fireball.

features are also present qualitatively in the missing-$p_{\rm T}$ measurements reported by the CMS collaboration [179], although, as already stressed, the precise momentum breakdown of the $\not{p}_{\rm T}^{\parallel}$-distribution differs from our computations, specially in the semi-hard region.

Finally, we turn to the dependence of the $\not{p}_{\rm T}^{\parallel}$ distribution in the reconstruction radius R. In Fig. 7-11 we show the $\not{p}_{\rm T}^{\parallel}$ distribution as a function of the angular separation Δ for different values of the jet reconstruction parameter. In analogy with the jet asymmetry dependence of $\not{p}_{\rm T}^{\parallel}$, we show the difference between Pb-Pb and p-p events, to focus on the medium contribution to the $\not{p}_{\rm T}^{\parallel}$ distribution. As in the previous plots, the colour histograms show the contribution of different $p_{\rm T}$-ranges and the solid points the average value per Δ-bin. The error bars include the theoretical and experimental uncertainties. As shown in Fig. 7-9, momentum conservation is (approximately) recovered when summing over all Δ bins.

As already mentioned, in this analysis the reconstruction algorithm is only employed to determine the sample of events over which the $\not{p}_{\rm T}^{\parallel}$ distribution is computed as well as the jet axis. By varying the anti-k_t R, while keeping the momentum cuts on the di-jet fixed, we include jets with softer fragmentation patterns. In the leading jet direction, the

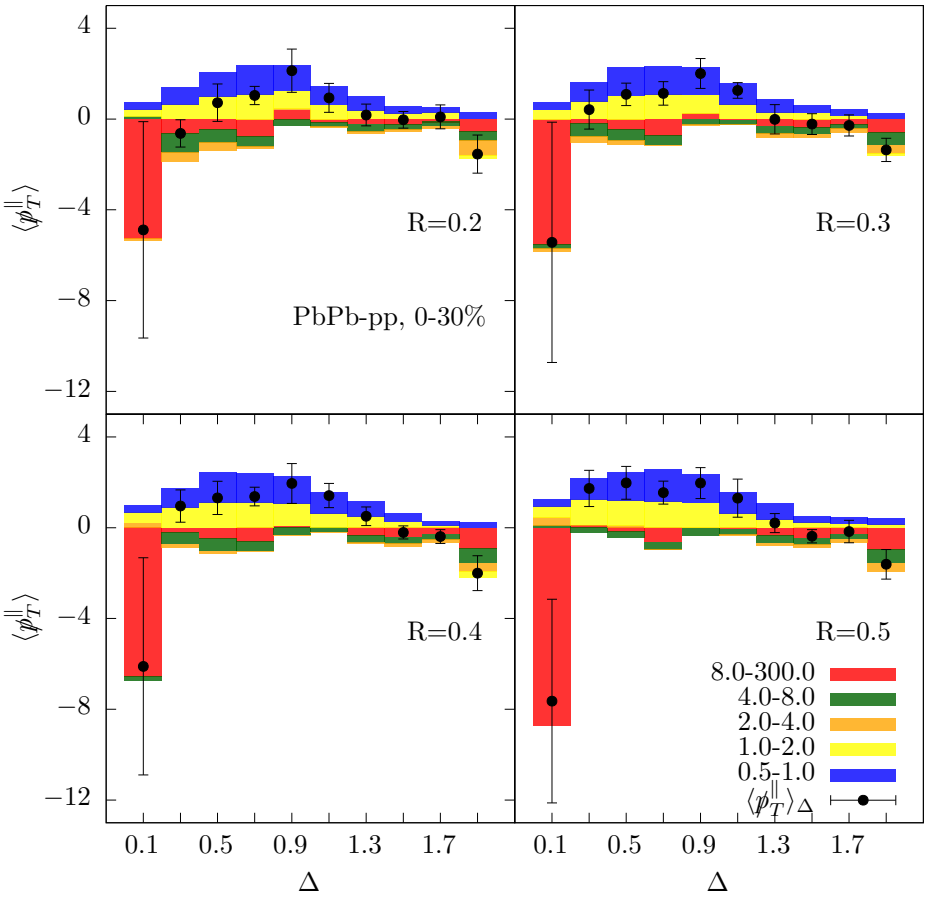

Figure 7-11: Evolution in R of the missing p_T observable, A_J inclusive and sliced in Δ, for the difference between PbPb and pp collisions. There is some hint of R dependence, despite the big error bars (specially for the first Δ bin), that signals the fact that wider jets contain more partons which feed the soft particle content by interacting with the plasma.

bias introduced by the filtering mechanism described in the previous sections enhances the contribution of jets with small partonic partonic activity, suppressing the R dependence of the different observables. The associated jets are, however, less sensitive to this bias and their partonic activity increases with R. Since jets with a larger number of fragments lose more energy, the enhancement of hard fragments along the leading jet direction at small Δ grows with R. Despite the large error bars both in our predictions and in data, this enhancement is present in both the Fig. 7-11 and in experiments [179]. Beyond the first Δ bin, as shown by the comparison in Fig. 7-9, the distribution of $\not{p}_{\rm T}^{\parallel}$ in the medium is dominated by medium effects. The large Δ dependence of the $\not{p}_{\rm T}^{\parallel}$ distribution shows very little sensitivity to R, which may be understood as a consequence of the wide angular region in which energy is recovered, controlled by Eq. (7.10). Remarkably, all these features are in qualitative agreement with the experimental distributions reported in [179].

As we have seen, the combination of energy loss and medium back-reaction is able to reproduce many qualitative features of the different missing $p_{\rm T}$ distributions reported by the CMS collaboration. At the quantitative level, however, the agreement is not complete. In the next Section we will discuss the possible sources of this disagreement which will motivate possible future directions for improving our understanding of jets in strongly coupled plasma.

7.3 Discussion

In this Chapter we have described the origin, implementation and observable consequences of two important effects for our hybrid model of jet quenching: transverse momentum broadening and medium response to the jet passage.

Our discussion of transverse momentum broadening is based on a gaussian-like noise term associated to Brownian motion. This approximation captures the bulk of the momentum-transfer distribution but neglects rare large angle momentum transfers, which may be potentially used to determine at which scale the medium fluctuations behave as quark and gluon quasi-particles [154]. Quite surprisingly, we have found that the transverse momentum transfers have small impact on typical jet observables such as the jet spectrum and jet

shapes, even for large values of the new free parameter $K \equiv \hat{q}/T^3$. The reason is that the strong quenching described by our hybrid approach removes many of the softer partons within the jet as it propagates in the medium. This "filtering" effect bias the quenched jet distribution to configurations in which jets only have one fragment, for which the broadening leads to an overall change in direction. This effect, which is easily captured by a Montecarlo implementation of jet dynamics, makes intra-jet observables, such as jet-shapes, insensitive to the momentum transfer. This insensitivity also difficults the direct extraction of the jet quenching parameter from traditional jet observables. By restricting the $p_{\rm T}$-range of the tracks entering the analysis to be $10 < p_{\rm T}^{\rm parton} < 20$ GeV, we have proposed a special kind of jet shape which exhibits a sensitivity of K (see Fig. 7-4) and which could be used to determine the broadening parameter experimentally.

Unlike broadening, intrajet observables are sensitive to the collective response of the plasma to the jet passage. Motivated by holographic computations, our implementation of energy loss assumes that all energy and momentum is incorporated into hydrodynamic motion. As explicitly demonstrated by the computations in [90, **?**], this leads to the generation of hydrodynamic wakes, which make effective the overall energy and momentum conservation of the event. We have only performed an approximate analysis of this response, based on the assumptions of perturbations on top of a boost invariant fluid. This simplification has allowed us to determine the spectrum of the particles generated from the hadronic decay of the wake that each energetic parton generates due to its interaction with the plasma, without having to incorporate additional parameters to the model. By comparing our computations with and without medium back-reaction we have stablished that indeed, this collective effects have important consequences for jet-shapes, fragmentation function and missing-$p_{\rm T}$ observables as discussed in Sections 7.2.3 and Section 7.2.4.

The comparison of our simplified approach with intrinsically hadronic observables, such as jet fragmentation functions or $\not{p}_{\rm T}^{\parallel}$ distribution is encouraging. As we have discussed, our simplified approach to medium back-reaction and hadronisation is able to describe many of the qualitative features of the measured distributions, such as the soft enhancement of fragmentation functions, the wide angular distribution of the lost jet energy, or the A_J and R dependence of the $\not{p}_{\rm T}^{\parallel}$ distribution. The medium response of the plasma to

the deposited energy is an effective mechanism to transport the lost energy to large angles, as suggested by data. It is also an unavoidable consequence of a large deposition of energy into soft modes, as expected at strong coupling, but also in a dense perturbative medium [107, 163, 164, 152]. However, a quantitative comparison with those observables demands a more sophisticated incorporation of medium response.

In all those observables, the main source of discrepancy between our simulation and the experimentally measured distribution is a consequence of the incorrect description of semi-hard particles $2 < p_{\rm T} < 8$ GeV. This is precisely the region in which our simplified implementation of medium response is less accurate. Indeed, even if the modifications of the flow field induced by the deposited energy are small, their effect in the final particle production can be large in the tail of the thermal distribution. Technically, this is a consequence of the exponential dependence on the flow fields of the final particle spectrum, Eq. (7.7). For particles with a typical momentum significantly larger than the medium temperature, this exponential dependence leads to two main effects: 1) a significant (exponential) enhancement of the overall yield of semi-hard particles, as a consequence of the larger temperature of the fluid cell; and 2) a narrower distribution of the emission pattern along the direction of the energy deposition [162]. Both these effects tend to increase the contribution of semi-hard partons from the medium response along the jet direction, which can potentially bring the $\not{p}_{\rm T}^{\parallel}$ distribution closer to data. Similarly, an enhanced contribution of these semi-hard partons could potentially increase the effect of medium back-reaction in jet shape distributions, incrementing the fraction of the jet energy at large r. However, unlike our simplified expression Eq. (7.10), the correct description of this semi-hard region depends explicitly on the space-time dependence of the momentum deposition [162]. It would be interesting to investigate the effect of the full flow profile as predicted by holographic computations [90, **?**] in the final particle production spectrum.

The observed quantitative disagreement may point towards a different physical mechanism as a source of the medium modification of jet properties. A salient example of a mechanism able to increase the rate of semi-hard partons correlated to the jet is medium induced gluon radiation, the dominate mechanism for perturbative energy loss. In a purely perturbative approach, most of the jet energy degradation is due to the emission of additional

semi-hard gluons. As already mentioned, in a dense medium in which the emitted gluons re-scatter and radiate prior to escaping the collision zone, a very quick degradation of the primordial radiation spectrum down to medium has been observed [107, 163, 164, 152], which leads to a rapid thermalization of the emitted energy [152]. These approaches also lead to a qualitative agreement with $\not{p}_{\mathrm{T}}^{\parallel}$-distribution [163] but fail to reproduce the soft enhancement of fragmentation function [180]. Approaches that treat the medium as dilute, such that the emitted gluons do not re-scatter, are able to reproduce the large r-enhancement of jet shapes [181], since the emitted gluons remain correlated with the jet direction; it would be interesting to analyse the $\not{p}_{\mathrm{T}}^{\parallel}$-distribution in those approaches. Since our approach is based on the assumption that the physics of jet energy loss are strongly coupled, we will not consider this mechanisms further.

Another physical process which has not been incorporated into our approach is finite resolution effects. In the current implementation of jet medium interaction, we have assumed that irrespective of the transverse separation of the partonic shower, all partons can interact with the medium (provided they are formed sufficiently early). However, on physical grounds, when two or more colour sources propagate through the plasma sufficiently close to one another, their interaction with the system must be indistinguishable from the interaction of an equivalent colour source with a colour charge equal to the net change of the partonic system. This physics has been observed in the interference pattern of gluon emissions in a (perturbative) QCD antenna [124, 125, 126], and also in analysis of jet proxies at strong coupling via holography [89, 156]. The main effect that the inclusion of these dynamics would have into our model is that for narrow jet fragmentation patterns, the coherence in-medium loss of the partonic system as a single effective emitter does not alter the internal structure of the jet, independently of how soft the fragments are. Therefore, these coherence effects could improve the quantitative comparison of our model with jet shapes and fragmentation functions data. A natural future extension of the work of this thesis is to assess the relevance of such an effect by its inclusion in a full Monte-Carlo evolution such as the one we have already developed. To best understand these effects, in Part III of this thesis we will determine the two gluon emission rate for an energetic parton traversing a thin QGP. This academic problem is simple enough to be doable analytically

while at the same time allows for the coherence physics we are after to emerge, supporting the effective emitters picture and validating our computational framework which we will exploit in future extensions of our work.

Part III

Jet Formation and Interference in a Thin QCD Medium

Chapter 8

Two-Gluon Emission Rate from a Hard Parton in a Thin QGP

In heavy-ion collisions, an abundant production of high-energy QCD jets allows to study how these multiparticle sprays are modified as they pass through the quark-gluon plasma. In order to shed new light on this process, we compute the inclusive two-gluon rate off a hard quark propagating through a color deconfined medium at first order in medium opacity. We explicitly impose an energy ordering of the two emitted gluons, such that the "hard" gluon can be thought of as belonging to the jet substructure while the other is a "soft" emission (which can be collinear or medium-induced). Our analysis focusses on two specific limits that clarify the modification of the additional angle- and formation time-ordering of splittings. In one limit, the formation time of the "hard" gluon is short compared to the "soft" gluon formation time, leading to a probabilistic formula for production of and subsequent radiation off a quark-gluon antenna. In the other limit, the ordering of formation is reverted, which automatically leads to the fact that the jet substructure is resolved by the medium. We observe in this case a characteristic delay: the jet radiates as one color current (quark) up to the formation of the "hard" gluon, at which point we observe the onset of radiation of the new color current (gluon). Our computation supports a picture in which the in-medium jet dynamics are described as a collection of subsequent antennas which are resolved by the medium according to their transverse extent.

For typical medium-induced gluons, all correlations are suppressed as their formation

time over the medium length [182], see also [183]. For large media, this allows to treat multiple medium-induced branchings in terms of a cascade [107, 184], see also [185, 186]. The large separation of scales, related in turn to the medium length and the mean free path, can also potentially lead to significant radiative corrections to transverse momentum broadening and energy loss in the medium [187, 118, 188] and, in general, to medium transport coefficients [117, 118]. See also [189, 190] for related work in next-to-leading order corrections to the medium-induced spectrum. The emission spectrum of two gluons with comparable formation times was analysed for the case of a dense medium in [191]. These approaches, however, consider the gluon transverse momenta to be of the order of the medium scale and therefore do not explicitly study the interplay between emissions of the former kind and genuine vacuum emissions, either short- or long-distance ones, which can take place in the context of high-energy jets. In this Chapter of the thesis, we aim at providing further analytical insight into these situations, complementary to the numerical analysis of the rate at first order in medium opacity presented in [192].

The study of coherence effects for in-medium jets is a relatively new subject. In [124, 125, 193, 126, 194, 195] the single gluon emission rate off two classical colour currents was computed in different approximations. The main finding of these studies may be summarised as the emergence of a new scale, the medium resolution scale, which controls the ability of the medium to resolve the number of colour emitters that traverse the plasma. If the transverse separation of the colour sources is larger than this scale, the medium is able to interact independently with each of the sources, and the medium-induced radiation spectrum consists of the superposition of the induced spectrum from each of the colour currents. If the transverse separation is small compared to this scale, the system interacts coherently with the propagating currents and the medium-induced spectrum coincides with that of a single colour charge in the overall colour representation of the system of currents. The phenomenon of medium resolution has also been recently found in the dynamics of energetic colour objects plunging through infinitely strongly coupled gauge theory plasmas [156]. These findings lead to the suggestion of a new picture for jet dynamics in heavy-ion collisions where, from the point of view of the medium, the jet shower is organised in terms of effective emitters, according to the medium resolution scale [155].

In this Chapter we study the coherent branching of soft gluons in jet showers by directly analysing the double-inclusive gluon emission rate. The two gluons have well separated energies, which are both much smaller than the quark energy. We will model the medium as a single scattering centre which interacts once with a jet shower at a given distance from the hard production vertex that generates the shower. This medium model corresponds to the leading order in opacity expansion for a medium which can be situated at any distance from the hard vertex. Since we can place the interaction at will, this scattering centre may be also viewed as a chronometer, which tests the jet shower at different times. The double inclusive emission rate in the $N = 1$ opacity approximation was analysed in [192] for realistic values of the medium parameters. However, our computation is not aimed at describing the gluon emission rate in a realistic model of the hot matter produced in ultra-relativistic heavy-ion collisions but rather to understand how in-medium interactions generically affect the gluon radiation pattern.

8.0.1 Computing the Amplitude and Cross Section

We start by definining the momenta of the quark, the "hard" and the "soft" gluons which are given by $P = (p^+, 0, \mathbf{0})$, $K_H = (k_H^+, k_H^-, \boldsymbol{k}_H)$ and $K_S = (k_S^+, k_S^-, \boldsymbol{k}_S)$, respectively. In our computation we assume the following energy ordering $p^+ \gg k_H^+ \gg k_S^+$. This is the conventional ordering of a vacuum shower leading to the double-logarithmic enhancement of gluon emissions. In the presence of the medium, such an ordering allows us to study how the hard jet substructure builds up in the presence of a probing, soft gluon which can be either collinear or medium-induced.

We also assume that the energy of both gluons is much larger than the typical momentum transfer from a medium exchange q, $k_S^+ \gg q$. In order to consistently neglect the radiation from the scattering centre, we will focus solely on collinear emissions with respect to the quark; this means that the emission angles of both of the gluons, $\theta_H = k_H/k_H^+$ and $\theta_S = k_S/k_S^+$, are small. However, we will make no assumptions about the relative magnitude of the emission angles θ_H/θ_S. To account for all relevant medium effects, we will allow the transverse momentum of one of the gluons, k_S, to be of the order of the

in-medium momentum transfer q. The gluonic fields of the medium can be effectively described by a collection of static scattering centres as already described in Section 2.3.

These assumptions simplify significantly the computation of the emission amplitudes. Since we are focusing in the rate in which both the gluons and the quark possess a much larger energy than the medium momentum transfer, we can use an eikonal approximation for the QCD Feynman rules that allows us to exploit this separation of scales at amplitude level. For ease of computation we will work in the mixed representation where the minus-component of the momenta is Fourier transformed to configuration space. Although the eikonal Feynman rules are well-known, we have re-derived them in Appendix B to clearly state our approximations and for the readers convenience. To discuss how we have organised our computation, we proceed to list the main ingredients.

In the eikonal limit, the quark and triple-gluon vertices conserve spin and helicity, respectively. It is useful to absorb the spin and polarization of the propagating degrees of freedom of adjacent propagators into properly contracted vertices, see Appendix B. In our present calculations, we will be using two types of eikonal emission vertices which are justified by the ordering of energies we have assumed. First, emissions of gluons off the energetic quark come with the factor

$$V_{G}^{a,i}(p^+;\boldsymbol{k}_I,k_I^+)\equiv V_{G}^{a,i}(\mathbf{0},p^+;\boldsymbol{k}_I,k_I^+)=2ig\,t^a\frac{p^+}{k_I^+}\,k_I^i\,, \tag{8.1}$$

where $I=H,S$, while the gluon splitting brings a factor

$$\Gamma_{G}^{abc,i}(\boldsymbol{k}_H,k_H^+;\boldsymbol{k}_S,k_S^+)=2g\,f^{abc}\frac{1}{z}\kappa_S^i\,, \tag{8.2}$$

where we have defined $z\equiv k_S^+/k_H^+$ and

$$\boldsymbol{\kappa}_S\equiv\boldsymbol{k}_S-z\,\boldsymbol{k}_H \tag{8.3}$$

is the relative momentum of the emission. Both effective vertices are transverse vectors and are proportional to the relevant colour factor. The four-gluon vertex does not exhibit the $1/z$ enhancement of Eq. (8.2), and it is therefore negligible in this kinematic limit. The

same argument holds for the gluon splitting into a quark-antiquark pair.

The momentum in Eq. (8.3) deserves some discussion. Naively, the strong ordering in the energy of the gluon suggests that we may drop the apparently subleading contribution $z\boldsymbol{k}_{H}$ in the definition of $\boldsymbol{\kappa}_{S}$. However, this can only be done if $\boldsymbol{k}_{H}$ and $\boldsymbol{k}_{S}$ are of the same order. This is the case when both gluons are medium-induced. However, in this work we will be interested in exploring the emission rate when the angles in transverse space θ_{H} and θ_{S} are comparable, which implies that k_{H} is parametrically (in $1/z$) larger than k_{S}.

Since there is only one non-vanishing component of the medium potential, the effective interaction vertices become scalars, and read

$$u_{Q}^{a}(p^{+}) = 2ig\, t^{a}\, p^{+}\,, \tag{8.4}$$

$$u_{G}^{abc}(p^{+}) = 2g\, f^{abc}\, p^{+}\,, \tag{8.5}$$

where we have amputated the medium field in the definition of the vertex; for details see Appendix B.

Having absorbed all spinor and helicity structures into the vertices, the internal partons are simply described by scalar propagators. Keeping the leading energy correction on the position of the poles, the propagation of the gluons in the mixed representation, see Eq. (B.9), may be expressed as

$$D_{G}(x^{+};\boldsymbol{k}_{I},k_{I}^{+}) \equiv D(x^{+};\boldsymbol{k}_{I},k_{I}^{+}) = \frac{\Theta(x^{+})}{2k^{+}} \exp\left[-i\frac{\boldsymbol{k}_{I}^{2}}{2k_{I}^{+}}x^{+} - \epsilon x^{+}\right]\,, \tag{8.6}$$

where again $I = H, S$ and $\Theta(x)$ is the Heaviside theta-function. The propagation of the quark is identical to that of the gluon; however, since we are taking the quark to have a much larger energy, we will adopt the strict eikonal limit, $k_{H}/p^{+}, k_{S}/p^{+}, q/p^{+} \ll 1$,

$$D_{Q}(x^{+};p^{+}) \equiv D(x^{+};\boldsymbol{0},p^{+}) = \frac{\Theta(x^{+})}{2p^{+}} e^{-\epsilon x^{+}}\,. \tag{8.7}$$

The ϵ-prescription in the propagators above suppresses the propagation of modes in the distant past and future. Finally, all in-coming and out-going particles have to be multiplied by the appropriate phases, embodying energy-momentum conservation, and by spinor or

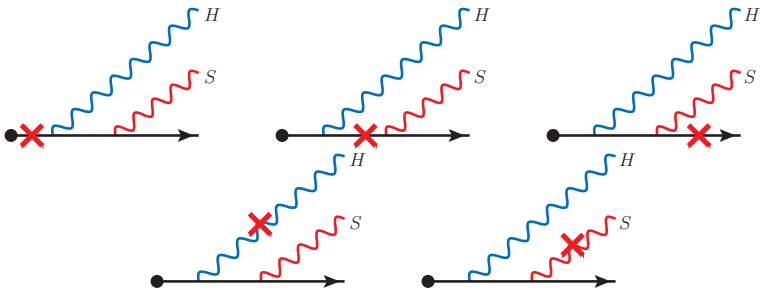

Figure 8-1: Two-gluon emission off a quark with $N = 1$ interactions with the medium. We also include the diagrams with the substitution $H \leftrightarrow S$.

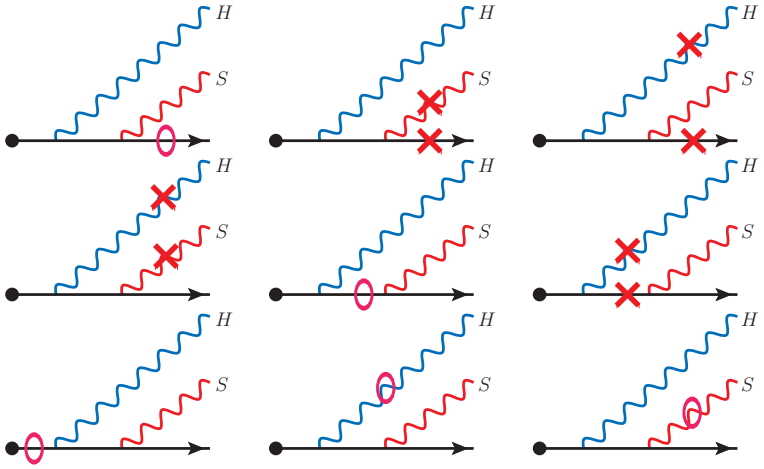

Figure 8-2: Two-gluon emission off a quark with $N = 1$ unitarity corrections. We also include the diagrams with the substitution $H \leftrightarrow S$.

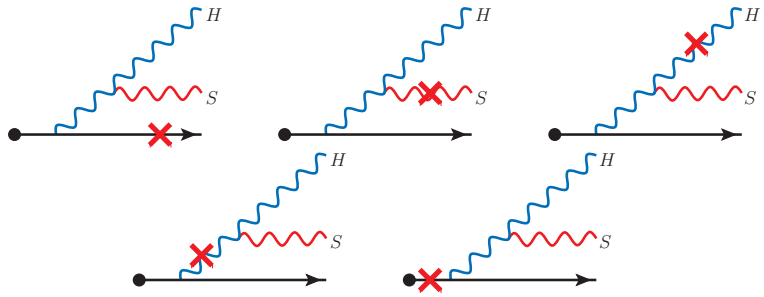

Figure 8-3: Sequential two-gluon emission off a quark and with $N = 1$ interactions with the medium.

polarization vectors for quarks and gluon, respectively; see Appendix B for more details.

These eikonal rules are the building blocks with which we construct the double gluon emission rate. Neglecting the four-gluon vertex, the full computation of this process in-

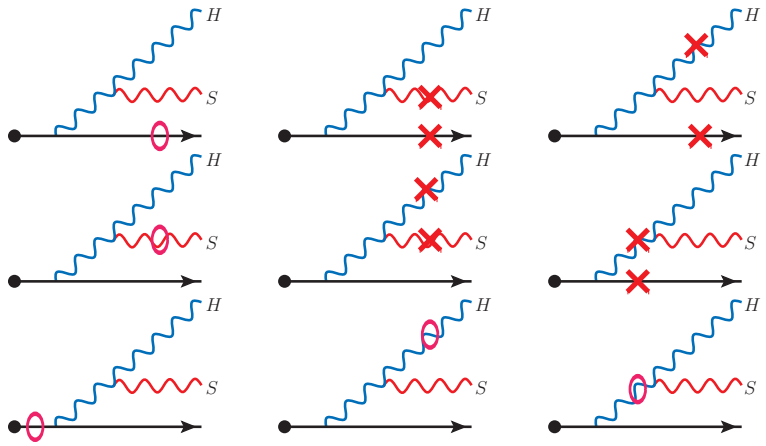

Figure 8-4: Sequential two-gluon emission off a quark with $N = 1$ unitarity corrections.

volves the calculation of 15 real amplitudes, summarised in Figs 8-1 and 8-3. Also, a total 23 additional non-vanishing virtual corrections, or double-Born diagrams, which involve the interference between double scattering amplitudes with vacuum diagrams, need to be considered. These are summarised in Figs. 8-2 and 8-4. All relevant Feynman rules are summarised in Appendix B.3. After squaring the real diagrams, the full rate is composed of 248 combinations.

Given the large number of diagrams that needs to be computed and squared, in this work we have used an automated procedure to compute this cross section. We have coded the Feynman rules outlined in the previous section in Mathematica, where we perform all integrations, sums and colour algebra via symbolic computations. The amplitude of these processes can be written as

$$\mathcal{M}^{ab}_{(0)\,\lambda\lambda'} = \varepsilon^i_\lambda(\boldsymbol{k}_H)\varepsilon^j_{\lambda'}(\boldsymbol{k}_S)\sum_k m_k^{ab,ij}\,, \tag{8.8}$$

$$\mathcal{M}^{ab}_{(1)\,\lambda\lambda'} = \int_{x^+}\int_{\boldsymbol{q}} \varepsilon^i_\lambda(\boldsymbol{k}_H)\varepsilon^j_{\lambda'}(\boldsymbol{k}_S)\mathcal{A}^c(x^+;\boldsymbol{q})\sum_k m_k^{abc,ij}(x^+;\boldsymbol{q})\,, \tag{8.9}$$

$$\mathcal{M}^{ab}_{(2)\,\lambda\lambda'} = \int_{x^+,x'^+}\int_{\boldsymbol{q},\boldsymbol{q}'} \varepsilon^i_\lambda(\boldsymbol{k}_H)\varepsilon^j_{\lambda'}(\boldsymbol{k}_S)\mathcal{A}^c(x^+;\boldsymbol{q})\mathcal{A}^d(x'^+;\boldsymbol{q}')\sum_k m_k^{abcd,ij}(x^+,x'^+;\boldsymbol{q},\boldsymbol{q}')\,, \tag{8.10}$$

where the basic building blocks are the amputated amplitudes $m_k^{abXY,ij}(\ldots)$. The first two superscripts $\{a,b\}$ relate to the colour structure and the latter two $\{i,j\}$ relate to the indices

of the two out-going transverse momenta, with $\{\lambda, \lambda'\}$ being their respective polarizations. The superscripts X and Y and the number of arguments relate to the number of insertions of the medium field. In the argument of the function we have suppressed the kinematics of the emitted gluon. The subscript k simply designates the particular diagram under consideration, and the sum runs over all diagrams in Figs. 8-1 and 8-3 for Eq. (8.9) and Figs. 8-2 and 8-4 for Eq. (8.10). The vacuum terms are also trivially found from these diagrams. Thus, Eq. (8.8) is the sum of all vacuum amplitudes, Eq. (8.9) is the sum of diagrams with one medium insertion, and Eq. (8.10) is the sum of all non-vanishing amplitudes with two medium insertions. We will refer to $\mathcal{M}_{(1)}$ as medium-real diagrams, and $\mathcal{M}_{(2)}$ will be referred to as medium-virtual diagrams.

Of course, all the amplitudes in Eqs. (8.8)-(8.10) are also proportional to the amplitude of the hard process that created the out-going quark. Since this simply factorises into the Born cross-section for quark production, we will always suppress it.

To illustrate the procedure, we describe here how to compute one of the amputated amplitudes, namely the upper left diagram of Fig. 8-1, which reads

$$m_1^{abc,ij}(x^+;\boldsymbol{q}) = \int_{x_H^+,x_S^+} e^{ik_H^- x_H^+ + ik_S^- x_S^+}\, V_G^{a,i}(p^+;\boldsymbol{k}_H,k_H^+)\, D_Q(x_S^+ - x_H^+;p^+) \\ \times V_G^{b,j}(p^+;\boldsymbol{k}_S,k_S^+)\, D_Q(x_H^+ - x^+;p^+)\, u_Q^c(p^+)\, D_Q(x^+ - x_0^+;p^+)\,, \quad (8.11)$$

where the gluons are on-shell: $k_H^- = \boldsymbol{k}_H^2/(2k_H^+)$ and $k_S^- = \boldsymbol{k}_S^2/(2k_S^+)$. In order to alleviate the notation, we have also defined the integrals

$$\int_{x^+} = \int_{-\infty}^{\infty} \mathrm{d}x^+\,, \quad (8.12)$$

$$\int_{\boldsymbol{q}} = \int \frac{\mathrm{d}^2\boldsymbol{q}}{(2\pi)^2}\,, \quad (8.13)$$

and usually we will set $x_0^+ = 0$ if not stated otherwise.

In this amputated amplitude, i and j are transverse space indices that denote the transverse momentum component of the soft and hard gluons, while a and b are their respective colour indices. The positions x_H^+, x_S^+ and x^+ denote the position in configuration space

where the hard and soft emissions and the scattering with the medium take place. Finally, the two phase factors appearing in the integrand are a consequence of the external leg insertion. To deal with the colour algebra we use the ColorMath package [196].

Following these simple rules, we introduce all amplitudes in Mathematica, which we also use to square them. The x_H^+ and x_S^+ integrals in the amputated amplitude, see Eq. (8.11), and the transverse momentum multiplication are performed symbolically. Formally, we take advantage of the medium average Eq. (2.25) to write for the square of the medium-real amplitudes

$$\begin{aligned}\left\langle\left|\mathcal{M}_{(1)}\right|^2\right\rangle &= \int_{x^+,x'^+}\int_{\boldsymbol{q},\boldsymbol{q}'}\langle\mathcal{A}^c(x^+;\boldsymbol{q})\mathcal{A}^{*\,c'}(x'^+;\boldsymbol{q}')\rangle\sum_{k,k'} m_{(k)}^{abc,ij}(x^+;\boldsymbol{q})m_{(k')}^{*abc',ij}(x'^+;\boldsymbol{q}') \\ &= \mu_D^2\int_{x^+}\int_{\boldsymbol{q}} n(x^+)\mathcal{V}(\boldsymbol{q})\sum_{k,k'} m_{(k)}^{abc,ij}(x^+;\boldsymbol{q})m_{(k')}^{*abc,ij}(x^+;\boldsymbol{q})\,, \end{aligned} \tag{8.14}$$

where the sum of all repeated indices is assumed and we have used $\sum_\lambda \boldsymbol{\varepsilon}_\lambda^i(\boldsymbol{k})\boldsymbol{\varepsilon}_\lambda^j(\boldsymbol{k}) = \delta^{ij}$ in order to contract the transverse indices. A similar strategy can be followed for the medium-virtual amplitudes, which are added by multiplying them with the vacuum amplitudes such that

$$\begin{aligned}\langle\mathcal{M}_{(2)}\mathcal{M}_{(0)}^*\rangle &= \int_{x^+,x'^+}\int_{\boldsymbol{q},\boldsymbol{q}'}\langle\mathcal{A}^c(x^+;\boldsymbol{q})\mathcal{A}^{c'}(x'^+;\boldsymbol{q}')\rangle\sum_{k,k'} m_{(k)}^{abcc',ij}(x^+,x'^+;\boldsymbol{q},\boldsymbol{q}')m_{(k')}^{*ab,ij} \\ &= \mu_D^2\int_{x^+}\int_{\boldsymbol{q}} n(x^+)\mathcal{V}(\boldsymbol{q})\sum_{k,k'} m_{(k)}^{abcc,ij}(x^+,x^+;\boldsymbol{q},-\boldsymbol{q})m_{(k')}^{*ab,ij}\,. \end{aligned} \tag{8.15}$$

In particular, when calculating contact terms (i.e. diagrams with two insertions on the same propagator, denoted with a circle in Figs. 8-2 and 8-4) we use the half-value prescription for the Heaviside function, $\Theta(0) = 1/2$, which yields the correct answer for the double-Born diagrams. The full medium-induced spectrum at first order in opacity is then

$$\begin{aligned}\langle|\mathcal{M}_{1\text{OP}}|^2\rangle &= \left\langle\left|\mathcal{M}_{(1)}\right|^2\right\rangle + 2\text{Re}\langle\mathcal{M}_{(2)}\mathcal{M}_{(0)}^*\rangle \\ &= \mu_D^2\int_{x^+}\int_{\boldsymbol{q}} n(x^+)\mathcal{V}(\boldsymbol{q})\,w(x^+;\boldsymbol{q})\,, \end{aligned} \tag{8.16}$$

where

$$w(x^+;\boldsymbol{q}) = \sum_{k,k'} \Big[m^{abc,ij}_{(k)}(x^+;\boldsymbol{q}) m^{*abc,ij}_{(k')}(x^+;\boldsymbol{q}) + m^{abcc,ij}_{(k)}(x^+,x^+;\boldsymbol{q},-\boldsymbol{q}) m^{*ab,ij}_{(k')} + m^{ab,ij}_{(k)} m^{*abcc,ij}_{(k')}(x^+,x^+;\boldsymbol{q},-\boldsymbol{q}) \Big] . \tag{8.17}$$

The spectrum of emitted gluons is then

$$\frac{\mathrm{d}^2 N_{\text{1OP}}}{\mathrm{d}\Omega_{k_H}\,\mathrm{d}\Omega_{k_S}} \equiv \frac{1}{\sigma_q^{\text{Born}}} \frac{\mathrm{d}^2\sigma_{\text{1OP}}}{\mathrm{d}\Omega_{k_H}\,\mathrm{d}\Omega_{k_S}} = \frac{1}{2p^+} \langle |\mathcal{M}_{\text{1OP}}|^2 \rangle , \tag{8.18}$$

where the factor $1/(2p^+)$ is the quark flux and the phase space for the gluons is given by $\mathrm{d}\Omega_k \equiv (2\pi)^{-3}\mathrm{d}^2\boldsymbol{k}\,\mathrm{d}k^+/(2k^+)$. Unitarity is enforced by demanding that the full $\langle |\mathcal{M}_{\text{1OP}}|^2 \rangle \to 0$ when the medium momentum exchange vanishes, $q \to 0$. In other words, an exact cancellation of medium-real and medium-virtual diagrams takes place in this limit, such that no double-counting with the pure vacuum cross section is allowed. We have explicitly checked that our expressions respect this condition.

8.1 Analysis of the Induced Rate

The strategy of computing the full amplitude in an automatised form allows us to deal with the many diagrams we have computed in a simple and effective way. However, the answer that this computation yields is lengthy and we have not been able to reduce it to a simple form. Therefore, in this section we will explore two particularly interesting limits of this expressions in which we have managed to express the answer in a closed form. This analysis is complementary to the numerical analysis of the full rate performed in [192].

Prior to taking these two limits, some general considerations about the full square matrix are in order. The analysis of the colour structure of both the real and virtual contributions allows us to separate the full answer into only two non-vanishing colour structures (after averaging over colours). The total rate may be expressed as

$$w(x^+;\boldsymbol{q}) = C_F^2 C_A w_Q(x^+;\boldsymbol{q}) + C_F C_A^2 w_G(x^+;\boldsymbol{q}) , \tag{8.19}$$

where the elements w_Q and w_G are functions of the kinematic variables. This general structure admits a simple interpretation. The full rate may be understood as the sum of two different physical processes: i) the emission of two gluons off the high-energy quark, w_Q; and ii) the emission of a hard gluon off the high-energy quark which, in turn, emits an additional soft gluon w_G. These emissions can occur either as originated from the initial virtuality of the hard vertex that creates the energetic quark or as a result of the interaction of the system with the medium. Note that in the infinite quark energy limit, the change of momentum of the quark as a result of the interaction and emission processes is negligible. This implies that, effectively, only the gluon scatters and terms proportional to C_F^3 are suppressed by powers of the quark energy.

The expressions for w_Q and w_G may also be organised according to their dependence on the position of the scattering centre, x^+. In general, we can express these two terms as

$$w_I(x^+;\boldsymbol{q}) = \sum_{i=1}^{N_I} \mathcal{P}_I^{(i)}(\boldsymbol{q})\Big\{1-\cos\left[x^+/\tau_I^{(i)}(\boldsymbol{q})\right]\Big\} \tag{8.20}$$

where $I = Q,\, G$, $N_Q = 2$ and $N_G = 19$ is the number of independent terms for the two distinct colour structures and the functions $\mathcal{P}_Q^{(i)}$, $\mathcal{P}_G^{(i)}$, $\tau_Q^{(i)}$, $\tau_G^{(i)}$ are rational functions of products of the four momenta of the three partons as well as of the transferred momenta. These are, in general, complicated expressions which we have not been able to simplify to a compact form, and shall therefore not be presented here. In the following subsections we will show instead the results obtained by the consideration of two distinct kinematic limits.

It is interesting to note that all the dependence of the full rate, Eq. (8.20), on the position of the scattering centre, x^+, occurs in the form of cosine-like phase factors. These phases indicate interference effects between the vacuum production of the quark, at $x_0^+ = 0$, and the medium scattering processes. For single gluon emission these interferences are well known, and are the precursors of the Landau-Pomeranchuk-Migdal (LPM) effect. In the context of radiation induced by a single scattering, this effect can be understood as the frustration of the induced radiation when the scattering centre is placed too close to the hard vertex, at a distance shorter than the formation time of the emitted gluon, $\tau = 2k^+/(\boldsymbol{k}-\boldsymbol{q})^2$. While in the single emission rate all the cross section is characterised by this single time-

scale, in the double-gluon emission rate several time-scales appear.

This distinct x^+ dependence of the total rate allows us to treat differently the kinematic factors $\mathcal{P}_I^{(i)}$ and the formation factors $\tau_I^{(i)}$ when expanding the rate in different kinematic regions. The limits we will explore invoke certain assumptions about the momenta of the partons and the transferred momenta, for any medium length L. In fact, the dependence of any scale related to the medium length only enters in the computation via the phase factors, as L appears in the limits of integration of x^+. Therefore, interferences are solely dependent on the relative magnitude of the formation factor $\tau_I^{(i)}$ and the medium length. For this reason, when taking kinematic limits, it is consistent to expand the kinematic factors $\mathcal{P}_I^{(i)}$ and $\tau_I^{(i)}$ to different orders since apparently subleading terms in $\tau_I^{(i)}$ may be enhanced by the medium length. In the next two subsections we will specify the limits we explore and describe this approximation in more detail.

8.1.1 Expansion Parameters

We now specify the parameters which we use to expand the symbolically computed cross section. First of all, as it is clear from the Feynman rules in sec. 8.0.1, the energy of the quark disappears from the final rate, since there is a cancellation between the p^+-dependence of the eikonal vertices and the eikonal quark propagators. This is only true in the strictly infinite quark energy limit that we adopt. Secondly, the structure of these rules also indicates that the rate depends on the energies of both emitted gluons via the combination

$$z = \frac{k_S^+}{k_H^+}\,, \tag{8.21}$$

which, by assumption, is small.

We analyse the double emission rate as a function of the emission angles of the two gluons. Assuming both these angles are small, these are trivially related to the momentum of the emitted gluons via

$$\theta_H = \frac{k_H}{k_H^+}\,, \qquad \theta_S = \frac{k_S}{k_S^+}\,. \tag{8.22}$$

In terms of these angles, the variable $\boldsymbol{\kappa}_S$, defined in Eq. (8.3), is independent of z. To make this scaling explicit, we may write $\boldsymbol{\kappa}_S$ as

$$\boldsymbol{\kappa}_S = k_S^+ \left(\theta_S \, \mathbf{n}_S - \theta_H \, \mathbf{n}_H\right) \tag{8.23}$$

with $\mathbf{n}_S$ ($\mathbf{n}_H$) the unit transverse vector along the direction of $\boldsymbol{k}_S$ ($\boldsymbol{k}_H$). This form motivates us to organise the computation in terms of the (dimensionless) ratio of angles

$$r = \frac{\theta_H}{\theta_S} \, . \tag{8.24}$$

In addition to the momenta of both gluons, the medium interaction introduces an additional dimension-full quantity, namely the momentum transferred by the scattering centre, $\boldsymbol{q}$. In order to properly take limits of the full rate, we need to consider the relative magnitude of this momentum transfer to other dimension-full quantities in the rate. Motivated by the fact that the single-gluon medium-induced rate is dominated by gluons with transverse momenta of order the transferred momentum, we choose to organise our computation in terms of the (dimensionless) ratio

$$\tilde{q} = \frac{q}{k_S} = \frac{1}{z\theta_S} \frac{q}{k_H^+} \, . \tag{8.25}$$

This ratio ensures that, as long as we keep $\tilde{q}$ finite, the softest gluon in the amplitude may be medium-induced. This choice of scaling introduces a non-trivial dependence of the emission rate on the variable z. This may be best illustrated by considering the ratio between the transferred momentum and the transverse momentum of the hard gluon

$$\frac{q}{k_H} = \tilde{q} \, \frac{z}{r} \, . \tag{8.26}$$

Although by construction we have assumed that z is small in the Feynman rules, the introduction of the scaling Eq. (8.25) leads to a different behavior depending on the relative magnitude of z and r. By keeping $\tilde{q}$ fixed, the limit $z \ll r$ implies that the transverse momentum of the hard gluon is much greater than the medium momentum transfer; com-

plementary, for the limit in which $r \ll z$ the transverse momentum of the hard gluon is much smaller than the momentum transfer. These are the two limits that we will explore in the next subsection. We will leave the analysis of the region $r \sim z$, in which the transverse momentum of both gluons are comparable to the medium transfer, for future work.

These two particular limits also have a close relation to two distinct space-time pictures of the emissions. In the limit of small z, the hard gluon is formed early in the medium. The two hardest partons, the quark and the hard gluon, will therefore form an effective dipole, or antenna, that is probed by the emission of the softest parton in the cascade. This situation is close in spirit to the one studied in [124, 125, 193, 126, 194, 195]. In the opposite limit, the formation times of the soft gluon is shorter than the hard one, allowing it to be emitted earlier in the cascade. This is a novel situation that we study for the first time in detail.

8.1.2 Emission Rate in the Soft Limit

We start by studying the double induced gluon rate in the limit $z \ll r$, i. e.,

$$z \to 0\,, \quad \text{with} \quad \left\{r,\, \tilde{q},\, \theta_S, k_H^+\right\} \text{ fixed}\,. \tag{8.27}$$

As already discussed, in this limit Eq. (8.26) implies that k_H decouples from the medium scale. This means that the medium-induced rate of the hard gluon is power suppressed and, to leading order in z, the rate of emission of this gluon is dominated by the vacuum processes associated to the hard vertex. Note also that the (vacuum) formation times of the two gluons are strongly ordered,

$$\frac{\tau_H}{\tau_S} = \frac{z}{r^2}\,, \tag{8.28}$$

with $\tau_H = 2k_H^+/\boldsymbol{k}_H^2$ and $\tau_S = 2k_S^+/\boldsymbol{k}_S^2$ the vacuum formation times of the hard and soft gluons, respectively. Therefore, at leading order in z, the hard gluon is effectively emitted from the hard vertex since it is formed at an arbitrarily short time.

We expand the prefactors $\mathcal{P}_Q^{(i)}$ and $\mathcal{P}_G^{(i)}$ in Eq. (8.20) to leading order in z, which means that we only keep terms that diverge as z^{-2}. In this limit, only 1 out of the 2 $\mathcal{P}_Q^{(i)}$ and

10 out of the total 19 $\mathcal{P}_G^{(i)}$ terms remain. The phase factors of those terms, $\tau_Q^{(i)}$ and $\tau_G^{(i)}$, possess different leading z behavior, z^{-1}. Following the discussion around Eq. (8.20) (on the presence of a new scale, the position of the scattering centre from the hard vertex, x^+) induces us to expand the phase factors $\tau_Q^{(i)}$, $\tau_G^{(i)}$ to a different z-order than the prefactors $\mathcal{P}_Q^{(i)}$ and $\mathcal{P}_Q^{(i)}$. Performing this limit, several cancellations occur and we ultimately were able to bring the cross section to a closed form.

Following the notation of Eq. (8.19), the term associated to the emission of the two gluons by the quark, proportional to the colour factor $C_F^2 C_A$, is in the leading z-limit given by

$$w_Q(x^+;\boldsymbol{q}) = \frac{4g^2}{\boldsymbol{k}_H^2} \times \left(-8g^4\right) \frac{\boldsymbol{k}_S \cdot \boldsymbol{q}}{(\boldsymbol{k}_S+\boldsymbol{q})^2\, \boldsymbol{k}_S^2} \left\{1 - \cos\left[\frac{(\boldsymbol{k}_S+\boldsymbol{q})^2}{2k_S^+} x^+\right]\right\}, \tag{8.29}$$

where we have expressed all the factors in terms of products of the final momenta. This expression admits a simple physical interpretation. This part of the cross section is the product of the vacuum probability of emitting a gluon off the hard quark (in the soft limit), $\sim 1/\boldsymbol{k}_H^2$, times the $N = 1$ opacity spectrum for the medium-induced emission of a soft gluon by the same quark [42, 41] (which is the expression we obtained for single gluon emission in Section 2.3.5). For later convenience, let us define the vectors,

$$\boldsymbol{A}_q = \frac{\boldsymbol{k}_S+\boldsymbol{q}}{(\boldsymbol{k}_S+\boldsymbol{q})^2}\,, \quad \boldsymbol{B}_q = \frac{\boldsymbol{k}_S}{\boldsymbol{k}_S^2}\,, \quad \boldsymbol{L}_q = \boldsymbol{A}_q - \boldsymbol{B}_q\,, \tag{8.30}$$

where the latter vector is often referred to as the Lipatov vertex. In terms of these functions, the $N = 1$ opacity expression for the single gluon emission may be expressed as [42, 41]

$$\frac{-\boldsymbol{k}_S \cdot \boldsymbol{q}}{\boldsymbol{k}_S^2 (\boldsymbol{k}_S+\boldsymbol{q})^2} = \frac{1}{2}\left(\boldsymbol{L}_q^2 + \boldsymbol{A}_q^2 - \boldsymbol{B}_q^2\right). \tag{8.31}$$

We will refer back to this decomposition in sec. 8.2.

We now turn to the $C_F C_A^2$ contribution in the same limit. After expanding the prefactors and the phase factors in the manner described above, we find convenient to express the full

answer in terms of the vectors

$$\boldsymbol{A}_g = \frac{\boldsymbol{\kappa}_S + \boldsymbol{q}}{(\boldsymbol{\kappa}_S + \boldsymbol{q})^2}\,, \quad \boldsymbol{B}_g = \frac{\boldsymbol{\kappa}_S}{{\boldsymbol{\kappa}_S}^2}\,, \quad \boldsymbol{L}_g = \boldsymbol{A}_g - \boldsymbol{B}_g\,, \tag{8.32}$$

where $\boldsymbol{\kappa}_S$ has been defined in Eq. (8.3). These functions are analogous to those of Eq. (8.31) but, since they are functions of $\boldsymbol{\kappa}_S$ they may be viewed as the transverse momentum of the soft gluon as measured with respect to the hard one. In terms of these functions, the contribution to the cross section in which the hard gluon emits the soft one is given by

$$\begin{aligned} w_G(x^+;\boldsymbol{q}) = \frac{4g^2}{\boldsymbol{k}_H^2} \times 4g^4 \Bigg\{ & \left(\boldsymbol{L}_g^2 + \boldsymbol{A}_g^2 - \boldsymbol{B}_g^2 - \boldsymbol{A}_q \cdot \boldsymbol{L}_g\right) \left\{1 - \cos\left[\frac{(\boldsymbol{\kappa}_S + \boldsymbol{q})^2}{2k_S^+} x^+\right]\right\} \\ & - \boldsymbol{L}_q \cdot \boldsymbol{A}_g \left\{1 - \cos\left[\frac{(\boldsymbol{k}_S + \boldsymbol{q})^2}{2k_S^+} x^+\right]\right\} \\ & + \boldsymbol{L}_q \cdot \boldsymbol{L}_g \left\{1 - \cos\left[\left(\frac{(\boldsymbol{\kappa}_S + \boldsymbol{q})^2}{2k_S^+} - \frac{(\boldsymbol{k}_S + \boldsymbol{q})^2}{2k_S^+}\right) x^+\right]\right\} \\ & + \mathcal{C}\left(k_H^+, \boldsymbol{k}_H; k_S^+, \boldsymbol{k}_S\right) \sin\left[\frac{\boldsymbol{k}_S^2}{2k_S^+} x^+\right] \sin\left[\frac{\boldsymbol{q} \cdot \boldsymbol{k}_H}{k_H^+} x^+\right] \Bigg\}\,, \end{aligned} \tag{8.33}$$

where we have defined the function[1]

$$\mathcal{C}\left(k_H^+, \boldsymbol{k}_H; k_S^+, \boldsymbol{k}_S\right) = -\frac{1}{4} \frac{k_S^+}{k_H^+} \frac{\boldsymbol{\kappa}_S \cdot \boldsymbol{k}_H}{\boldsymbol{k}_H^2\, \boldsymbol{k}_S^2\, {\boldsymbol{\kappa}_S}^2} \tag{8.34}$$

Since $\mathcal{C}$ does not depend on $\boldsymbol{q}$, after integration over transferred momenta with the isotropic distribution $\mathcal{V}(\boldsymbol{q})$ in Eq. (2.25), the last term of Eq. (8.33) vanishes. Therefore, similarly to Eq. (8.33), this contribution to the full rate is also proportional to the vacuum probability of emitting a hard gluon, $\sim 1/\boldsymbol{k}_H^2$. Combining Eq. (8.29) and Eq. (8.33) we may express the full answer for the double-inclusive gluon rate as

$$\left\langle \left|\mathcal{M}_{1\text{OP}}\right|^2 \right\rangle \Big|_{z \ll r} = \mathcal{P}_{\text{vac}}\left(k_H\right) \times \mathcal{P}_{\text{ant}}^{(1)}\left(k_S\right)\,, \tag{8.35}$$

[1] In spite of the explicit fraction k_S^+/k_H^+ in Eq. (8.34), this term is of the same z-order as the rest of the terms in Eq. (8.33).

where $\mathcal{P}_{\text{vac}}$ is the vacuum $q \to q + g$ splitting function in the soft limit

$$\mathcal{P}_{\text{vac}}(k_{\scriptscriptstyle H}) = \frac{2C_F\, g^2}{k_{\scriptscriptstyle H}^2}\,, \tag{8.36}$$

and $\mathcal{P}^{(1)}_{\text{ant}}$ is the emission rate of soft gluons off a hard quark-gluon dipole at first order in medium opacity, which we have derived in Appendix C using the method of classical currents employed in [194]. $\mathcal{P}^{(1)}_{\text{ant}}$ is given in Eq. (C.15) and Eq. (C.17), which we reproduce here for the readers convenience,

$$\begin{aligned}
\mathcal{P}^{(1)}_{\text{ant}} &= 4g^4 C_A \mu_D^2 \int_{x^+}\int_{\boldsymbol{q}} n(x^+)\mathcal{V}(\boldsymbol{q}) \\
&\times \Bigg\{ C_F(\boldsymbol{L}_q^2 + \boldsymbol{A}_q^2 - \boldsymbol{B}_q^2)\left\{1 - \cos\left[\frac{(\boldsymbol{k}_{\scriptscriptstyle S}+\boldsymbol{q})^2}{2k_{\scriptscriptstyle S}^+}x^+\right]\right\} \\
&\quad + C_A\Bigg[\left(\boldsymbol{L}_g^2 + \boldsymbol{A}_g^2 - \boldsymbol{B}_g^2 - \boldsymbol{A}_q\cdot\boldsymbol{L}_g\right)\left\{1 - \cos\left[\frac{(\boldsymbol{\kappa}_{\scriptscriptstyle S}+\boldsymbol{q})^2}{2k_{\scriptscriptstyle S}^+}x^+\right]\right\} \\
&\qquad - \boldsymbol{L}_q\cdot\boldsymbol{A}_g\left\{1 - \cos\left[\frac{(\boldsymbol{k}_{\scriptscriptstyle S}+\boldsymbol{q})^2}{2k_{\scriptscriptstyle S}^+}x^+\right]\right\} \\
&\qquad + \boldsymbol{L}_q\cdot\boldsymbol{L}_g\left\{1 - \cos\left[\left(\frac{(\boldsymbol{\kappa}_{\scriptscriptstyle S}+\boldsymbol{q})^2}{2k_{\scriptscriptstyle S}^+} - \frac{(\boldsymbol{k}_{\scriptscriptstyle S}+\boldsymbol{q})^2}{2k_{\scriptscriptstyle S}^+}\right)x^+\right]\right\}\Bigg]\Bigg\}\,,
\end{aligned} \tag{8.37}$$

which only depends on two dynamical time-scales,

$$\tau_{\scriptscriptstyle q} = \frac{2k_{\scriptscriptstyle S}^+}{(\boldsymbol{k}_{\scriptscriptstyle S}+\boldsymbol{q})^2}\,, \qquad \tau_{\scriptscriptstyle g} = \frac{2k_{\scriptscriptstyle S}^+}{(\boldsymbol{\kappa}_{\scriptscriptstyle S}+\boldsymbol{q})^2} \tag{8.38}$$

which are the formation times of the soft gluon when emitted collinear to the hard quark, $\tau_{\scriptscriptstyle q}$, and to the hard gluon, $\tau_{\scriptscriptstyle g}$.

The factorised form Eq. (8.35) admits a simple physical interpretation of the emission rate. In this limit, in which the hard gluon cannot be medium-induced, its production is totally dominated by vacuum physics, and its rate is determined by the vacuum splitting function. Since, as shown in Eq. (8.28), the formation time of the hard gluon is parametrically smaller than that of the soft gluon, the hard gluon is emitted early. From the point of view of the medium, the system behaves as a quark-gluon antenna right after the hard vertex. Therefore, the scattering centre interacts with this two-parton systems simultaneously.

The emission pattern includes several interferences effects, encoded in the intricate x^+ dependence of the rate, which are a result of the simultaneous propagation of this multi-parton system. We will discuss this pattern in detail in sec. 8.2.

8.1.3 Emission Rate in the Collinear Limit

We now explore a different limit for the emission rate in which the hard gluon is not forced to be emitted first. To do so, we will consider the emission rate in the limit in which the ratio of angles goes to zero first ($r \to 0$) and then look for terms leading in the ratio of energies $z \ll 1$. The scaling of the momentum transferred with the transverse momentum of the medium gluon, Eq. (8.25), implies that the order of limits does not commute, since, as expressed in Eq. (8.26), in this limit the transverse momentum of the hard gluon, $k_{\scriptscriptstyle H}$, becomes parametrically smaller than q. The limit we performed may be summarised as,

$$r \to 0,\, z \to 0, \quad \text{with} \quad \left\{\tilde{q},\, \theta_{\scriptscriptstyle S}, k_{\scriptscriptstyle H}^+\right\} \text{ fixed}\,. \tag{8.39}$$

It is easy to see from Eq. (8.28) that in this limit the formation time of the hard gluon is parametrically longer than that of the soft emission.

As before, we expand the pre-factors $\mathcal{P}_{\scriptscriptstyle Q}^{(i)}$ and $\mathcal{P}_{\scriptscriptstyle G}^{(i)}$ to leading order in r, which corresponds to r^{-2}. In this limit, only 1 out of the 2 terms in $\mathcal{P}_{\scriptscriptstyle Q}^{(i)}$ and 7 out of the 19 terms $\mathcal{P}_{\scriptscriptstyle G}^{(i)}$ are non-vanishing, and all of them depend on z as a power, z^{-2}. Unlike the previous case, not all the phase factors of the surviving terms possess the same leading r limit: 6 of the phase factors $\tau_{\scriptscriptstyle G}^{(i)}$ are $\mathcal{O}(r^0)$ and the remaining one is $\mathcal{O}(r^2)$. The presence of the additional scale x^+ allows us to keep the latter apparently suppressed time-scale, which becomes important at times of order r^{-2}. Nevertheless, in the leading r limit, all 6 terms with $\mathcal{O}(r^0)$ phases cancel identically, leading to

$$w_{\scriptscriptstyle Q}(x^+;\boldsymbol{q}) = \frac{4g^2}{\boldsymbol{k}_{\scriptscriptstyle H}^2} \times (-8g^4)\frac{\boldsymbol{k}_{\scriptscriptstyle S}\cdot\boldsymbol{q}}{\boldsymbol{k}_{\scriptscriptstyle S}^2\,(\boldsymbol{k}_{\scriptscriptstyle S}+\boldsymbol{q})^2}\left\{1-\cos\left[\frac{(\boldsymbol{k}_{\scriptscriptstyle S}+\boldsymbol{q})^2}{2k_{\scriptscriptstyle S}^+}x^+\right]\right\}\,, \tag{8.40}$$

$$w_{\scriptscriptstyle G}(x^+;\boldsymbol{q}) = \frac{4g^2}{\boldsymbol{k}_{\scriptscriptstyle H}^2} \times 4g^2\frac{q^2}{\boldsymbol{k}_{\scriptscriptstyle S}^2\,(\boldsymbol{k}_{\scriptscriptstyle S}+\boldsymbol{q})^2}\left\{1-\cos\left[\frac{\boldsymbol{k}_{\scriptscriptstyle H}^2}{2\,k_{\scriptscriptstyle H}^+}\,x^+\right]\right\}\,. \tag{8.41}$$

As in the previous limit, both terms of the emission amplitude are proportional to $\mathcal{P}_{\rm vac}$,

Eq. (8.36), which implies that the production of the hard gluon proceeds as in vacuum. This is a consequence of the fact that in this limit k_{H} is parametrically smaller than q. Due to LPM interference, the medium-induced rate is collinear finite [42, 41], implying that gluons with $k_{H} \ll q$ cannot be medium-induced and, therefore, have to have been generated in the hard vertex that creates the jet.

The soft gluon emission rate depends on two distinct time-scales. The emission rate of soft gluons off the quark, $w_{Q}(x^{+}; \boldsymbol{q})$, is identical in both limits, Eq. (8.29) and Eq. (8.40), which, as we have discussed coincides with the $N = 1$ opacity spectrum. This spectrum is controlled by the formation time of the soft gluon in medium τ_{q}. The contribution to the rate coming from emissions off the hard gluon, $w_{G}(x^{+}; \boldsymbol{q})$, is different in this limit. This rate no longer depends on the time-scale τ_{g}, as Eq. (8.33). The time-scale controlling interferences in Eq. (8.41) is the formation time of the hard gluon, $\tau_{H} = 2k_{H}^{+}/\boldsymbol{k}_{H}^{2}$.

The appearance of τ_{H} in the emission rate leads to a simple consequence. If the scattering centre interacts with the quark-gluon system prior to the formation of the hard gluon, $x^{+} \ll \tau_{H}$, the emission rate is dominated by radiation off the quark, since the Eq. (8.41) vanishes. After τ_{H}, the emission rate may be understood as the incoherent superposition of the radiation off the quark plus the radiation off the gluon. At these late times, the rate of emission off the hard gluon is given by the Gunion-Bertsch term [197],

$$\lim_{r\to 0} \boldsymbol{L}_{g}^{2} = \frac{\boldsymbol{q}^{2}}{\boldsymbol{k}_{S}{}^{2}\,(\boldsymbol{k}_{S}+\boldsymbol{q})^{2}}\,, \tag{8.42}$$

where $\boldsymbol{L}_{g}$ is defined in Eq. (8.32), which corresponds to the emission of a soft gluon of momentum $\boldsymbol{k}_{S}$ off a hard on-shell gluon generated infinitely far away from the scattering centre. This rate differs from the emission rate of the soft gluon off the quark, Eq. (8.40), which is the $N = 1$ spectrum.

This difference in the emission rate implies that after the formation of the gluon, this new source of colour does not radiate in-medium as an independent new source produced at τ_{H}, which would lead to an equivalent $N = 1$ spectrum off the hard gluon. The origin of the different rates at asymptotic late times may be understood from the analysis of the antenna spectrum, Eq. (8.37). First of all, we note that in the limit Eq. (8.39), the time-

scales that control the emission from the colour dipole are parametrically suppressed with respect to τ_H. In the small r limit

$$\frac{\tau_H}{\tau_q} = \mathcal{O}\left(\frac{z}{r^2}\right) , \quad \frac{\tau_H}{\tau_g} = \mathcal{O}\left(\frac{z}{r^2}\right) , \quad \frac{\tau_H}{\tau_q} - \frac{\tau_H}{\tau_g} = \mathcal{O}\left(\frac{z}{r}\right) . \tag{8.43}$$

Because of this separation of time-scales, the relevant limit of the antenna spectrum Eq. (8.37) is to consider $x^+ \to \infty$, which implies that all phase factors average out to zero. In this incoherent limit, together with Eq. (8.39), the part of the antenna spectrum proportional to C_A is

$$\lim_{r\to 0} \left(\boldsymbol{L}_g^2 + \left(\boldsymbol{A}_g^2 - \boldsymbol{A}_q \cdot \boldsymbol{A}_g\right) - \left(\boldsymbol{B}_g^2 - \boldsymbol{B}_q \cdot \boldsymbol{B}_g\right)\right) = \frac{\boldsymbol{q}^2}{\boldsymbol{k}_S{}^2 \left(\boldsymbol{k}_S + \boldsymbol{q}\right)^2} , \tag{8.44}$$

which coincides with the Gunion-Bertsch rate found in the two-gluon cross section.

This observation leads to a simple interpretation of the full double emission rate. If the scattering centre is placed early compared to τ_H, the interaction of the vacuum jet with the medium is identical to the interaction of a hard quark with the scattering centre; the emission of the hard gluon occurs after the scattering, and proceeds as in vacuum. If, on the contrary, the interaction with the scattering centre occurs at a time long compared to τ_H, then the hard gluon has time to form via vacuum processes, leading to the generation of an in-medium antenna. From this time on, it is the quark-gluon dipole the one that interacts with the medium. We will discuss the consequences of this interpretation in sec. 8.2.

8.2 Discussion

In this Chapter we have discussed two particular kinematic regions, summarised in Eq. (8.27) and Eq. (8.39), of the emission rate of two gluons in a thin (opacity $N = 1$) medium. These limits are particularly interesting because they allow us to cleanly separate vacuum and medium emissions. As we have discussed, in both those kinematic regions the emission of one of the gluons, the hard gluon, is dominated by vacuum-like processes produced at the hard vertex that creates a jet, while the soft gluon is medium-induced. By choosing this kinematics, we have focused on understanding how the multi-parton state associated

to the propagation of a jet in plasma interacts with a QCD medium. However, this limit prevents us from studying how the emission of new partons by medium-induced processes interferes with the evolution of the jet shower, which demands the analysis of the rate when both emitted gluons can be medium-induced. This is a more intricate analysis which we leave for future work. Other analyses of the rate of emission of two gluons of comparable momentum from an on-shell quark propagating in the plasma can be found in [192, 191].

As we have shown, within these regions the emission pattern of soft gluons is controlled by the emission spectrum off a hard quark-gluon dipole in medium, Eq. (8.37). This type of dipoles has been recently used to understand emissions by multiple colour sources in plasma and led to a rich interference structure [124, 125, 193, 126, 194, 195]. The particular case of opacity $N = 1$ for a colour singlet antenna was analysed in detail in [194]. Although the main lessons of the interference emission pattern of the quark-gluon antenna may be inferred from the analysis of the colour singlet antenna in [194], for completeness we discuss those features below.

The antenna emission rate is controlled by three distinct time-scales: the in-medium formation times of soft gluons emitted off the quark, τ_q, and off the gluon, τ_g, defined in Eq. (8.38) and a third time-scale, intrinsically multi-partonic, which combines kinematic information of both constituents of the antenna,

$$\tau_{\rm res}^{-1} = \frac{1}{\tau_q} - \frac{1}{\tau_g} = \frac{2\boldsymbol{q} - \boldsymbol{k}_S - \boldsymbol{\kappa}_S}{2}\,\mathbf{n}, \tag{8.45}$$

with $\mathbf{n} = \boldsymbol{k}_H/k_H^+$ a vector in transverse space whose modulus is the opening angle of the quark-gluon system, $\mathbf{n}^2 = \theta_H^2$. This time-scale controls the interference between medium-induced emissions of the two sources.

To understand how these interferences occur, let us first consider the induced spectrum off the quark-gulon dipole when the angle of the antenna θ_H is large. In this limit, the stimulated emissions off the quark and off the hard gluon are independent of one another. The medium-induced spectrum off each of the propagating sources is dominated by gluons emitted with a typical transverse momentum *with respect to the source* of order μ_D; this means that medium-induced gluons off the quark have $k_S \sim \mu_D$ while the induced gluons

off the hard gluon have $\kappa_S \sim \mu_D$. Therefore, the induced spectrums will be well separated from one another if the angle of the dipole $\theta_H \gg \theta_{\rm med}$, with $\theta_{\rm med} = \mu_D/k_S^+$ being the typical emission angle with respect to the emitting source. In this limit, as a consequence of Eq. (8.23), medium-induced gluons off the quark have $\kappa_S \approx k_S^+\theta_H \gg k_S$ and induced gluons off the hard gluon have $k_S \approx k_S^+\theta_H \gg \kappa_S$. This condition is sufficient to show that, up to corrections of order $\theta_{\rm med}^2/\theta_H^2$, the antenna spectrum Eq. (8.37), is the incoherent superposition of the stimulated spectrum off the quark and off the hard gluon.

Complementary, soft gluon emission off the antenna suffers from strong interferences for $\theta_H \ll \theta_{\rm med}$. In this limit, for typical induced gluons $\boldsymbol{\kappa}_S \approx \boldsymbol{k}_S \sim \mu_D$, which implies that $\tau_q \approx \tau_g$, $\boldsymbol{A}_q \approx \boldsymbol{A}_g$, $\boldsymbol{B}_q \approx \boldsymbol{B}_g$ and $\boldsymbol{L}_q \approx \boldsymbol{L}_g$. The antenna spectrum is reduced to

$$\begin{aligned} w_{\rm ant}^{(1)}\left(x^+;\boldsymbol{k}_S,k_S^+\right)\Big|_{\theta_H\ll\theta_{\rm med}} &= C_F\left[1-\cos\frac{x^+}{\tau_q}\right]\left(\boldsymbol{L}_q^2+\boldsymbol{A}_q^2-\boldsymbol{B}_q^2\right) \\ &+ C_A\left[1-\cos\frac{x^+}{\tau_{\rm res}}\right]\boldsymbol{L}_q^2\,, \end{aligned} \tag{8.46}$$

which is the medium-induced spectrum off the quark plus an additional interference term encoding the emission off the gluon. In the small dipole limit, for typical induced gluons Eq. (8.45) yields $\tau_{\rm res}^{-1} \sim \mu_D\theta_H$. Therefore, interferences between the two sources suppress the emission off the hard gluon if at the relevant observation time x^+ the transverse size of the dipole is $\lambda = \theta_H x^+ \ll \lambda_{\rm res}$, with

$$\lambda_{\rm res} = \frac{1}{\mu_D} \tag{8.47}$$

the *transverse resolution scale*, which in this dilute medium equals the inverse typical momentum transferred by the medium.

The characteristic time-scale for medium-induced radiation is the formation time of the emitted gluon, τ_q. At this time, the typical transverse size of the quark-gluon dipole is $\lambda \sim \lambda_{\rm res}\,\theta_H/\theta_{\rm res}$. Therefore, for induced gluons with $\theta_{\rm res} \gg \theta_H$ the transverse size of the dipole at emission is small compared to the transverse resolution scale and the spectrum is totally dominated by the emission off the hard quark. Nevertheless, the condition $\theta_{\rm res} \gg \theta_H$ depends on the frequency of the soft gluon, and at fixed θ_H only a fraction of the

induced spectrum, with $k_S^+ \ll \mu_D/\theta_H$, is suppressed by interference effects. Since LPM interference suppresses induced radiation with formation time larger than the medium length L, the medium-induced spectrum has a maximum frequency of emission, $\omega_{max} \sim \mu_D^2 L$ [41, 42, 43]. Therefore, if the dipole opening angle $\theta_H \ll 1/\mu_D L$, all the medium-induced spectrum off the gluon is cancelled by interference, and the full emission spectrum off the quark-gluon dipole is given by the medium-induced radiation off a hard quark. The multipartonic system interacts with the plasma as a single colour charge, the total charge of the system, as long as its maximal transverse size in the medium $\theta_H L \ll \lambda_{\rm res}$. As we have seen, the rich interference structure associated to the medium resolution scale $\lambda_{\rm res}$ emerges in the soft limit of the double gluon emission rate, Eq. (8.35), in which the emission of a hard gluon may be viewed as the production of an in-medium antenna.

The emergence of the antenna interference pattern suggests a simple organising principle to understand the dynamics of jet showers in medium based on the resolution scale, as already suggested in [155]. A basic element of this picture is that, similarly to vacuum, jet showers may be best understood as a collection of in-medium antennas, that are dynamically generated in the process of relaxation of the virtuality of the jet. Our computations in the small angle regime support this picture. As we have seen in sec. 8.1.3, the emission of soft gluons by a quark-gluon system generated in vacuum explicitly depends on the formation time of the gluon τ_H. While for short times $x^+ \ll \tau_H$ the emission pattern off the quark-gluon system is just that off a quark, after τ_H both the quark and the hard gluon contribute to the emission spectrum. This agrees with the common approximation of considering τ_H as the time in which the hard gluon decorrelates from the hard quark. Nevertheless, disregarding the trivial differences in colour factors, the emission spectrums of the quark and gluon are not identical. Therefore, a naive iteration of the medium-induced spectrum after the formation of the hard gluon leads to the incorrect emission rate.

As we have shown, the emission rate off the hard gluon is predicted from the antenna picture in the small angle limit, provided the antenna forms after τ_H. The physical origin of the discrepancy between the iteration of the $N = 1$ opacity spectrum, Eq. (8.40), and the antenna prediction is easy to understand. As it is well known, in the totally incoherent limit ($\tau_q \ll x^+$) the emission rate can be expressed as Eq. (8.31), which we reproduce here

for convenience,

$$\frac{-2\,\boldsymbol{k}_S\cdot\boldsymbol{q}}{(\boldsymbol{k}_S+\boldsymbol{q})^2{\boldsymbol{k}_S}^2}=\boldsymbol{L}_q^2+\boldsymbol{A}_q^2-\boldsymbol{B}_q^2\,, \tag{8.48}$$

which shows that the emission rate is the sum of the stimulated emission off an on-shell quark, $\boldsymbol{L}_q^2$, the medium broadening of a soft gluon produced in the hard vertex, $\boldsymbol{A}_q^2$, and a unitarity correction which subtracts strength from the vacuum emission rate of soft gluons off the quark, $\boldsymbol{B}_q^2$. The difference in the in-medium rate off the hard gluon lies precisely in a different $vacuum$ emission rate of soft gluons by the quark-gluon antenna. As shown in Eq. (C.12), because of the interference with the quark, the vacuum emission of soft gluons off the hard gluon is proportional to

$$\mathcal{P}^G_{\rm vac}\propto\left(\boldsymbol{B}_g-\boldsymbol{B}_q\right)^2\,, \tag{8.49}$$

where the dependence in $\boldsymbol{B}_q$ reflects the interference with the quark. This vacuum rate vanishes in the limit of $\theta_{\scriptscriptstyle H}\ll\theta_{\scriptscriptstyle S}$, since, on the formation time of the vacuum soft gluon, the transverse size of the quark-gluon dipole is negligible. This does not imply that the in-medium rate vanishes, since, in the limit Eq. (8.39), $\tau_{\scriptscriptstyle H}\sim 1/k_{\scriptscriptstyle H}^+\theta_{\scriptscriptstyle S}r^2$ and the dipole has a (parametrically) long time to separate, leading to a large transverse separation at formation time $\Delta=\theta_{\scriptscriptstyle H}\tau_{\scriptscriptstyle H}\sim z/rk_{\scriptscriptstyle S}$. As a result of vacuum interference, the emission off the gluon coincides with the emission off an on-shell gluon generated infinitely far away from the scattering centre, since no soft gluons are produced in vacuum in this kinematic lint.

The small angle approximation explored in sec. 8.1.3 is, however, insensitive to the the medium resolution scale $\lambda_{\rm res}$. For typical in medium radiation with $k_{\scriptscriptstyle S}\sim\mu_D$, at the time the hard gluon forms the transverse size of the dipole is $\lambda=\lambda_{\rm res}\,z/r\gg\lambda_{\rm res}$ and the antenna is totally resolved. For this reason, at times long compared to $\tau_{\scriptscriptstyle H}$ the two gluon emission rate, Eq. (8.40) and Eq. (8.41), coincides with the spectrum of a fully resolved ($x^+\to 0$) small angle antenna, Eq. (8.46). Unfortunately, the limit in which $r\to 0$ first is inadequate to explore the interplay between $\lambda_{\rm res}$ and the formation of the hard gluon. In future work we plan to address the limit $r\sim z\to 0$ to understand how the formation of the antenna affects the resolution of the colour structure of the propagating dipole.

Chapter 9

Conclusions and Outlook

In this thesis we have studied how high energetic excitations propagate through a non-abelian strongly coupled plasma. This new state of matter is produced at heavy ion collisions in our accelerators and allows us to study a stage of the evolution of our Universe that occurred during the first microseconds after the Big Bang. In this extreme conditions of temperature and density the ordinary matter that we are made of behaves as a an almost perfect fluid, the most perfect known by mankind up to now in fact. The theory of strong interactions is tested at an energy scale that even though it is high enough to melt hadrons, it does not get to the point where the coupling constant is low enough to allow a perturbative description. In the plasma, the partonic field content, the quarks and gluons, cease to be the relevant degrees of freedom and a microscopic description in terms of quasi-particles is not possible. A very useful tool to put to test the actual behaviour of this strongly coupled fluid is the analysis of jet modifications as a result of their interactions with the plasma.

In a first introductory part we have given the concepts needed to picture how heavy ion collisions develop as we are able to understand it today. We have introduced the techniques commonly used to describe parton propagation within a deconfined medium both from the weak coupling and strong coupling regime, and used them to obtain energy loss rate equations that describe the energy degradation of these probes in their passage through the plasma. At weak coupling, the main mechanism responsible for energy loss is induced gluon emission and interesting interference phenomena occur that lead to a dependence on

path length of L^2. These are known as coherence effects and their study becomes richer by considering multi-gluon emission, as it is done done in Part III. The strongly coupled picture uses holography to map a dressed excitation moving through a strongly coupled plasma into a string propagating in a higher dimensional space containing a black hole. Since the non-abelian theory in which the calculation is done is not QCD, but $\mathcal{N} = 4$ SYM, we take these results as an insight to describe energetic parton propagation in a model of jet quenching in heavy ion collisions. The different number of degrees of freedom of the two theories are expected to lead to differences in the stopping distance, which is the time that it takes to the endpoint of the string to cross the black hole horizon.

Even though we assume that the exchanges with the medium are soft enough to include non-perturbative effects, as described by gauge/gravity duality, the energetic partons that are produced in the collision generally have a high virtuality which they relax by successive splittings. The latter occur at length scales that are not resolvable by the medium, and they should proceed as in vacuum. This observation motivates us to adopt a hybrid description for the interplay between the multi scale jet and the QGP, using each description at the scale it is supposed to be valid. This phenomenological description has proven to be very successful in describing dijet and photon-jet data at different centralities. In addition, by the combination of the fragmentation functions of the leading and subleading jet in a dijet pair, we have found an observable highly sensitive to the specific energy loss mechanism (see Fig. 6-13), which is remarkable given the moderate dependence that other jet observables have. In view of the coming data sometime this year from run 2 at the LHC, we have computed predictions for the $\sqrt{s} = 5.02$ ATeV center of mass energy with special expectations on photon-jet measurements, for which the increase in statistics is presumed to be around a factor 10. This greatly improved precision will help us discriminate among the different models for energy loss given the sizeable separation their predictions present in observables such as photon-jet imbalance (see Fig. 6-8).

In the next part of the work we extend our hybrid model by the inclusion of two effects, broadening and medium response, which should help us improve the ability of our simu-

lations to describe the challenging physics of intra-jet observables such as jet shapes and fragmentation functions. The first effect, broadening, is due to the Brownian motion that probes experience in a thermal bath, and it will tend to broaden the distribution of particles within the jet. This represents a candidate mechanism capable of reproducing the observed behaviour in the modification of the transverse energy density of quenched jets, consisting in a depletion at mid r and an enhancement at larger r. As it turns out, the observable quantifying such modifications, the jet shapes, are rather insensitive to the inclusion of this effect due to the effectiveness of the strong quenching, which removes the softer fragments leaving a narrow structure that gets mildly tilted. However, by restricting the p_T range of the tracks entering this analysis, we have been able to produce a new observable which shows a remarkable dependence on the precise strength of the broadening mechanism (see Fig. 7-4). Measurements on this kind of observables could be then used to obtain a direct extraction of the actual in-medium broadening.

The second effect involves overall energy-momentum conservation. The rapidly thermalized energy deposited by the energetic partons modifies the plasma, inducing temperature and velocity fluctuations in the surrounding fluid cells. This perturbation propagates long distances in the form of a wake and eventually decays into soft hadrons, whose orientations keep a correlation with the jet direction and therefore produce a net effect even after background subtraction. We estimate the size of this effect by assuming that the perturbation is small, leading to important simplifications in its implementation. The observable consequences are best noticed in intra-jet measurements such as jet shapes and fragmentation functions, where it is clearly seen that the inclusion of such physics is in good agreement with the observed experimental trend, and it becomes simply unavoidable when comparisons against global measurements are performed (see Fig. 7-9). Despite this improvement, the tension present in the description of jet shapes points towards potential improvements of our model, such as the inclusion of coherence effects or a more rigorous analysis of medium back-reaction.

The hybrid approach has already provided us with a systematically improvable calculational framework within which we can test strongly coupled predictions for jet quenching by confronting them quantitatively with experimental measurements of jet observables. This demonstrates that this approach can now be used to explore and subsequently test new observables. Some of the physics effects left out so far, which could be implemented in our framework, include finite N_c, finite λ, and nonzero N_f/N_c corrections to (4.2), or how this energy loss rate changes in a strongly coupled theory that is not conformal. One could also consider the reduction in the phase space for the fragmentation of a parton in the PYTHIA shower as a consequence of the energy loss, or the possibility that multiple soft interactions with the medium induce additional splittings in the shower. A particularly interesting improvement involves coherence effects, which are related to the finite resolution power of the medium, a problem to which the last content of thesis is devoted.

The final part of this work consists in the computation of the inclusive two gluon stimulated emission within the context of perturbative QCD. By studying the full answer in different kinematical limits we arrive to the conclusion that jet propagation is perceived from the point of view of the plasma as a set of effective emitters depending on the resolution power, which for a thin plasma it is of the order of the Debye screening mass μ_D. As stated above, this physics is a missing piece of the Monte Carlo jet quenching model presented in this thesis and its inclusion is expected to have important consequences for the more differential observables, a task that will be undertaken in future work.

These are very exciting times for the physics of strong nuclear interactions. The strongly coupled nature of the QGP makes the study of this system extremely interesting, like other strongly coupled systems such as high temperature superconductors or cold atoms. We have seen how the very fundamental questions about the nature of the high temperature, strongly coupled phase of ordinary matter can be addressed by the study of jet quenching and its observable consequences. This thesis represents an effort in the confrontation of the seductive ideas of holography with experiments. The possibility that a rather familiar, although undeniably challenging theory such as QCD can indeed be described in terms of

strings which propagate in higher dimensions is not only convenient, but absolutely fascinating. Having the means to quantitatively confront new ideas, as we have done throughout the presented work, new observables, and new data is critical if we are eventually to understand the properties of the strongly coupled liquid quark-gluon plasma that Nature has served us.

Appendix A

Transverse Kicks Kinematics

We now study the broadening of the parton via a transverse kick of magnitude q in the rest frame of the fluid. The description of the random probability function will be done later. The kick is such that the energy of the quark (in the fluid frame) remains unchanged, and so does its virtuality.

The parton starts with a four momentum $P^\mu = E_F(1, \mathbf{w}_F)$, and ends with a momentum $P'^\mu = E_F(1, \mathbf{w}'_F)$ such that $\mathbf{w}'^2_F = \mathbf{w}^2_F$. In this frame, this condition is achieved by adding a longitudinal momentum transfer in addition to the transverse kick

$$\mathbf{w}'_F = \sqrt{1 - \frac{q^2}{E_F^2 \mathbf{w}_F^2}}\mathbf{w}_F + \frac{q}{E_F}\mathbf{e}_\perp \tag{A.1}$$

where $\mathbf{e}_\perp$ is a vector perpendicular to the parton velocity in the rest frame of the fluid . In terms of the lab frame quantities

$$E_F^2 w_F^2 = E_F - E(1 - w^2) \tag{A.2}$$

with $E_F = E\,\gamma_F\,(1 - \mathbf{wv})$, with γ_F the Lorentz factor of the fluid velocity $\mathbf{v}$. We would like to express now all vectors in terms of lab frame quantities. We define the four vector

$$W_T = \frac{1}{W_F^0}\,(W - (W \cdot u)u) \tag{A.3}$$

which is transverse to the fluid velocity $u \cdot W_T = 0$. In the fluid frame this four vector has components $W_T = (0, \mathbf{w}_F)$, and therefore

$$P'^{\mu} = P^{\mu} + \beta E_F W_T^{\mu} + q e_{\perp}^{\mu} \ , \qquad \beta = \sqrt{1 - \frac{q^2}{E_F^2 \mathbf{w}_F^2}} - 1 \tag{A.4}$$

and the four vector $e_{\perp}^{\mu}$ must satisfy the conditions

$$u \cdot e_{\perp} = 0 \, , \qquad W \cdot e_{\perp} = 0 \, , \qquad e_{\perp}^2 = -1 \tag{A.5}$$

To construct the general form of $e_{\perp}$ we ned to find a basis which fulfils those conditions. One such vector e_1^{μ} is easy to find. To construct the second one we start from the first

$$l_2^{\mu} = (0, \frac{\mathbf{w}}{|\mathbf{w}|} \times \frac{\mathbf{w} \times \mathbf{v}}{|\mathbf{w} \times \mathbf{v}|}) \, , \qquad e_1^{\mu} = (0, \frac{\mathbf{w} \times \mathbf{v}}{|\mathbf{w} \times \mathbf{v}|}) \tag{A.6}$$

and then l_2^{μ} satisfies two of the three conditions. We obtain the vector we want e_2^{μ} as

$$e_2^{\mu} = \frac{1}{\sqrt{N}} \left(l_2^{\mu} + \alpha \, W_{\perp}^{\mu} \right) \, , \qquad W_{\perp} = W - \frac{W^2}{u \cdot W} u \tag{A.7}$$

where we have introduced the transverse part of the parton velocity $W_{\perp}$. The parameters are found to be

$$\alpha = - \frac{(l_2 \cdot u) \, (u \cdot W)}{(u \cdot W)^2 - W^2} \, , \qquad N = \frac{(u \cdot W)^2 - W^2 (1 + (l_2 \cdot u)^2)}{(u \cdot W)^2 - W^2} \tag{A.8}$$

Note that the orthogonolaity relation $e_1 \cdot e_2 = 0$ is also satisfied. Having dealt with the kinematics, we can now streamline the procedure for determining the transverse kicks. At every time step interval in the lab frame, dt, the parton acquires a mean transversed momentum squared given by $\Delta Q^2 = \hat{q} \, dt_F$, where the relation between dt_F and dt is given by Eq. 4.21. We will model the jet transport parameter $\hat{q} = KT^3$ with T the local temperature. In this time interval, a random momentum of magnitude q is generated according to a gaussian probability distribution with width ΔQ^2.

Appendix B

Effective Feynman Rules in the Eikonal Limit

Here we will shortly review the relevant Feynman diagram technique applied in the light-cone gauge in the mixed representation, which is quite similar to the so-called time-ordered perturbation theory. Choosing the gauge vector to be purely "minus", $n \equiv (0, 1, \mathbf{0})$, leads to the gauge condition $n \cdot A = A^+ = 0$ for the gluon field. In particular, the gluon polarization vector becomes

$$\varepsilon_\lambda(k) = \left(0, \frac{\boldsymbol{k} \cdot \boldsymbol{\varepsilon}_\lambda(\boldsymbol{k})}{k^+}, \boldsymbol{\varepsilon}_\lambda(\boldsymbol{k})\right) . \tag{B.1}$$

B.1 Propagators

The scalar (Feynman) propagator for massless particles in vacuum reads

$$D(k) = \frac{i}{k^2 + i\epsilon} , \tag{B.2}$$

In terms of this, the quark and gluon propagators read

$$S(k) = \sum_s u^s(k)\bar{u}^s(k)\, D(k)\,, \tag{B.3}$$

$$G^{\mu\nu}(k) = \sum_\lambda \varepsilon_\lambda^{*\,\mu}(k)\varepsilon_\lambda^{\nu}(k)\, D(k)\,, \tag{B.4}$$

respectively, where

$$\sum_s u^s(k)\bar{u}^s(k) = \not{k}\,, \tag{B.5}$$

$$\sum_\lambda \varepsilon^{*\,\mu}(k)\varepsilon^{\nu}(k) = -g^{\mu\nu} + \frac{k^\mu n^\nu + k^\nu n^\mu}{k\cdot n} - k^2\frac{n^\mu n^\nu}{(k\cdot n)^2}\,. \tag{B.6}$$

The transverse part of the polarization vectors satisfy $\sum_\lambda \boldsymbol{\varepsilon}_\lambda^{*\,i}\boldsymbol{\varepsilon}_\lambda^{j} = \delta^{ij}$. Since all propagating partons are put on-shell, the latter term in Eq. (B.6) is irrelevant for our analysis. The gluon propagator is symmetric, and the only non-vanishing components read

$$G^{--}(k) = \frac{\boldsymbol{k}^2}{(k^+)^2}D(k)\,, \quad G^{-i}(k) = \frac{k^i}{k^+}D(k)\,, \quad G^{ij}(k) = \delta^{ij}D(k)\,, \tag{B.7}$$

where $i = (1,2)$. In the next subsection we will show that in the eikonal limit all the vertices become transverse and diagonal in spin and polarization, which allows them to absorb all the quark/gluon dependence (numerators). This leaves us with the momentum flow and pole structure which are encoded exlusively in the scalar part of the propagator.

We will work in the mixed representation, with (light-cone) time, energy and transverse momentum. For instance, energy-momentum conservation in a $q(l) \to q(p) + g(k)$ takes the following form

$$(2\pi)^4\delta^{(4)}(p+k-l) = (2\pi)^3\int \mathrm{d}x^+\, e^{i\left(p^- + k^- - l^-\right)x^+}\,\delta\left(p^+ + k^+ - l^+\right)\delta\left(\boldsymbol{p}+\boldsymbol{k}-\boldsymbol{l}\right) \tag{B.8}$$

and similarly for the four-gluon vertex. While external particles are naturally required to

be on-shell, the mixed representation also allows to put all internal propagators on-shell

$$D(x^+;k) \equiv D(x^+;\boldsymbol{k},k^+) = \int_{-\infty}^{\infty} \frac{\mathrm{d}k^-}{2\pi} e^{-ik^-x^+}\, D(k)\,, \tag{B.9}$$

$$= \frac{\Theta\left(x^+\right)}{2k^+} e^{-ik^-x^+ - \epsilon x^+}\,, \tag{B.10}$$

with $k^- = \boldsymbol{k}^2/(2k^+)$ in the last line. The ϵ-prescription regulates the behavior of the propagator at infinity. We note that we have to keep in mind that any integration of an *external* point involves the additional phases as in Eq. (B.8).

B.2 Leading Eikonal Vertices

Here we derive the relevant vertices and demonstrate their behavior in the eikonal approximation. This means that we only keep terms that are enhanced by a factor z^{-1}, where z is the fraction of a small energy over a large one. This automatically leads to the preservation of (quark) helicity and (gluon) polarization that floats through the vertices.

The triple gluon vertex reads

$$iV_{abc}^{\mu\nu\sigma}(K_1,K_2,K_3) = gf^{abc}\big[(K_1-K_2)^\sigma g^{\mu\nu} + (K_2-K_3)^\mu g^{\nu\sigma} + (K_3-K_1)^\nu g^{\mu\sigma}\big] \tag{B.11}$$

where all momenta are incoming and f^{abc} is the SU(3) structure constant. Enforcing energy-momentum conservation in the vertex, we will define the emission vertex describing $g(K_1+K_2) \to g(K_1) + g(K_2)$, where the momentum flow follows the time flow, as

$$\begin{aligned}\Gamma_{G}^{abc}(K_1,K_2) &= \varepsilon_\mu^*(K_1)\varepsilon_\sigma^*(K_2)\, iV_{abc}^{\mu\nu\sigma}(-K_1,K_1+K_2,-K_2)\,\varepsilon_\nu(K_1+K_2) \\ &= 2gf^{abc}\left[\frac{1}{z}\left(\boldsymbol{\kappa}\cdot\boldsymbol{\varepsilon}_2\right)\left(\boldsymbol{\varepsilon}_2\cdot\boldsymbol{\varepsilon}_{12}\right) + \left(\boldsymbol{\kappa}\cdot\boldsymbol{\varepsilon}_1\right)\left(\boldsymbol{\varepsilon}_2\cdot\boldsymbol{\varepsilon}_{12}\right) - \frac{1}{1+z}\left(\boldsymbol{\kappa}\cdot\boldsymbol{\varepsilon}_{12}\right)\left(\boldsymbol{\varepsilon}_1\cdot\boldsymbol{\varepsilon}_2\right)\right]\,,\end{aligned} \tag{B.12}$$

where $\boldsymbol{\kappa} \equiv \boldsymbol{k}_2 - z\boldsymbol{k}_1$, $z \equiv k_2^+/k_1^+$ and $\boldsymbol{\varepsilon}_i \equiv \boldsymbol{\varepsilon}(\boldsymbol{k}_i)$. In the eikonal approximation we only keep the leading z term in Eq. (B.12). We will however keep the apparently sub-

leading contribution to $\boldsymbol{\kappa}$ since $|\boldsymbol{\kappa}| \sim k^+(\theta_1+\theta_2)$ and we are interested in arbitrary angular ordering. The eikonal triple-gluon vertex becomes completely transverse and reads

$$\Gamma_{\scriptscriptstyle G}^{abc,k}(\boldsymbol{k}_1,k_1^+;\boldsymbol{k}_2,k_2^+) = 2gf^{abc}\,\frac{1}{z}\,\kappa^k\,, \tag{B.13}$$

where we have dropped a diagonal matrix for the propagation of the polarization. This ensures that the polarization of the hardest gluon is conserved in the vertex. On the other hand, including one gluon field from the medium in the triple gluon vertex leads to

$$\begin{aligned}\varepsilon_\mu^*(K_1)A_\sigma^c(K_2)\,iV_{abc}^{\mu\nu\sigma}(-K_1,K_1-K_2,K_2)\,\varepsilon_\nu(K_1-K_2)& \\ = 2gf^{abc}k_1^+A^{c-}(K_2)\,\boldsymbol{\varepsilon}_1\cdot\boldsymbol{\varepsilon}_{12}\,.&\end{aligned} \tag{B.14}$$

Using the decomposition in Eq. (2.24) for the medium potential and applying the transformation to the mixed representation allows us to define a triple-gluon interaction vertex

$$U_{\scriptscriptstyle G}^{ab}(x^+;k^+,\boldsymbol{q}) = 2g\,k^+\,f^{abc}\mathcal{A}^c(x^+,\boldsymbol{q})\,, \tag{B.15}$$

$$= u_{\scriptscriptstyle G}^{abc}(k^+)\,\mathcal{A}^c(x^+,\boldsymbol{q})\,, \tag{B.16}$$

where the transversality of the vertex is again suppressed.

Following the same approach as for the gluons, we will define properly contracted QCD vertices that absorb the numerators of the propagators. For the emission of a gluon, $q(K_1+K_2)\to q(K_1)+g(K_2)$, we define

$$V_{\scriptscriptstyle G}(K_1,K_2) = \bar{u}^t(K_1)\big(ig\gamma^\mu t^a\big)\varepsilon_\lambda^{*\,\mu}(K_2)\,u^s(K_1+K_2)\,, \tag{B.17}$$

where t^a is the SU(3) generator in the fundamental representation. In the eikonal limit, we take advantage of $\bar{u}^t(K_1)\gamma^\mu u^s(K_1+K_2) = 2K_1^\mu\delta^{ts}+\mathcal{O}(K_2/K_1)$, which conserves spin, to define

$$V_{\scriptscriptstyle G}^{a,i}(\boldsymbol{k}_1,k_1^+;\boldsymbol{k}_2,k_2^+) = 2ig\,t^a\,\frac{1}{z}\,\kappa^i\,, \tag{B.18}$$

where again $\boldsymbol{\kappa} \equiv \boldsymbol{k}_2 - z\boldsymbol{k}_1$ and $z \equiv k_2^+/k_2^+$ and we have suppressed a diagonal matrix for the spin components. For the interaction with the medium we simply replace the polarization vector $\varepsilon_\lambda^{*\mu}(K_2)$ in Eq. (B.17) by the medium field $A^\mu(Q)$, and find

$$U_{\scriptscriptstyle Q}(x^+; k^+, \boldsymbol{q}) = 2ig\, k^+\, t^a \mathcal{A}^a(x^+, \boldsymbol{q})\,, \tag{B.19}$$

$$= u_{\scriptscriptstyle Q}^a(k^+)\, \mathcal{A}^a(x^+, \boldsymbol{q})\,. \tag{B.20}$$

We note that the newly defined emission vertices, Eq. (B.13) and Eq. (B.18), allow us to absorb all spin and polarization information contained in the numerator of the quark and gluon propagators. We are therefore left with scalar propagators and the vertices for emission and interaction. The interaction vertices, Eq. (B.15) and Eq. (B.19), are scalars as well.

B.3 Effective Feynman Rules

As a summary, we provide a list of graphical rules that can be used in order to calculate any diagram in light-cone perturbation theory in the mixed representation.

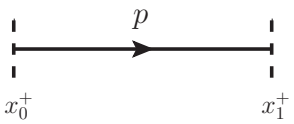

$$= D\left(x_1^+ - x_0^+; p^+, \boldsymbol{p}\right)\,, \tag{B.21}$$

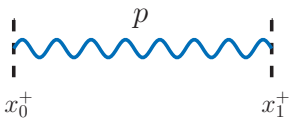

$$= D\left(x_1^+ - x_0^+; p^+, \boldsymbol{p}\right)\,, \tag{B.22}$$

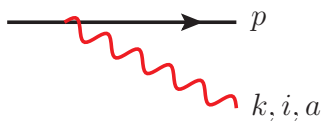

$$= V_G^{a,i}(\boldsymbol{\kappa}, z)\,, \tag{B.23}$$

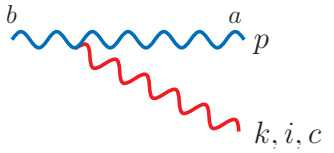

$$= \Gamma_G^{abc,i}(\boldsymbol{\kappa}, z)\,, \tag{B.24}$$

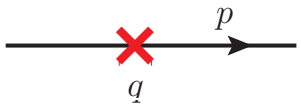

$$= U_Q(x^+; p^+, \boldsymbol{q})\,, \tag{B.25}$$

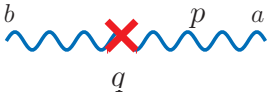

$$= U_G^{ab}(x^+; p^+, \boldsymbol{q})\,. \tag{B.26}$$

Finally, we will discuss the situation where the same parton line interacts twice with the medium. Due to the instantaneous nature of the interactions, see Eq. (2.25), the scalar propagator in between the two medium-insertions reduces to $\Theta(0)/(2k^+) = 1/(4k^+)$ and the double-interaction is denoted by a circle instead of two crosses. Since we can perform the integrations over the medium-momentum explicitly, we obtain the following two rules

$$= -\frac{1}{2}\alpha_s C_F \int \mathrm{d}x^+\, n(x^+)\,, \tag{B.27}$$

$$= \frac{1}{2}\alpha_s C_A \int \mathrm{d}x^+\, n(x^+)\,, \tag{B.28}$$

where, in order to obtain explicit expressions, we have assumed that $\mathcal{V}(\boldsymbol{q}) = (\boldsymbol{q}^2 + m_D^2)^{-2}$. However, in our Mathematica code we have calculated these diagrams using the automated procedure similarly to all the other diagrams.

Additionally, all newly produced final-state partons, i.e., partons that propagate from some vertex to the cut, have to be multiplied by the appropriate polarization vector, for gluons, or spinor, for fermions, and by the appropriate phase $e^{ip^-x^+}$, where p is the parton

momentum and x^+ the position of the last vertex. We summarise these rules below:

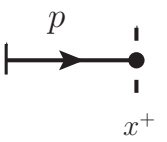

$$= e^{-ip^- x^+} u^s(p)\,, \tag{B.29}$$

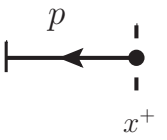

$$= e^{-ip^- x^+} \bar{u}^s(p)\,, \tag{B.30}$$

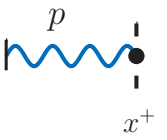

$$= e^{-ip^- x^+} \boldsymbol{\varepsilon}^i_\lambda(p)\,, \tag{B.31}$$

and similarly for final-state particles,

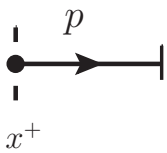

$$= e^{ip^- x^+} \bar{u}^s(p)\,, \tag{B.32}$$

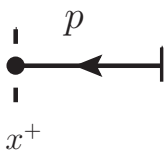

$$= e^{ip^- x^+} u^s(p)\,, \tag{B.33}$$

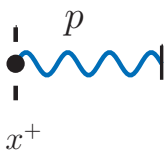

$$= e^{ip^- x^+} \boldsymbol{\varepsilon}^{*\,i}_\lambda(p)\,, \tag{B.34}$$

where the "cut" (corresponding to $x^+ = \pm\infty$) is represented by a small vertical line.

Appendix C

Short Derivation of the Antenna Spectrum in Medium

Since soft gluon radiation can be treated as a classical process, we can apply methods from classical Yang-Mills theory to obtain the amplitude for an emission off one of the legs of the antenna, which reads

$$\mathcal{M}^a_{\lambda,1} = 2ig \int_{\boldsymbol{q}} \int_0^\infty \mathrm{d}x^+ \left[T \cdot \mathcal{A}(x^+; \boldsymbol{q})\right]^{ab} \tilde{q}_1^b \times \left\{ \frac{\boldsymbol{\kappa}_1 - \boldsymbol{q}}{(\boldsymbol{\kappa}_1 - \boldsymbol{q})^2} - \left[\frac{\boldsymbol{\kappa}_1 - \boldsymbol{q}}{(\boldsymbol{\kappa}_1 - \boldsymbol{q})^2} - \frac{\boldsymbol{\kappa}_1}{\boldsymbol{\kappa}_1^2} \right] e^{i\frac{(\boldsymbol{\kappa}_1 - \boldsymbol{q})^2}{2k^+}x^+} \right\} \cdot \boldsymbol{\varepsilon}_\lambda(\boldsymbol{k}) \,, \tag{C.1}$$

where

$$\boldsymbol{\kappa}_1 = \boldsymbol{k} - \frac{k^+}{p_1^+}\boldsymbol{p}_1 \,, \tag{C.2}$$

is the transverse momentum of the gluon $\boldsymbol{k}$ with respect to the transverse momentum of one of the legs of the antenna and $[T \cdot \mathcal{A}]^{ab}\tilde{q}_1^b = if^{abc}\mathcal{A}^b\tilde{q}_1^c$. The full amplitude, corresponding to emissions off both legs reads simply $\mathcal{M}^a_{\lambda,1+2} = \mathcal{M}^a_{\lambda,1} + \mathcal{M}^a_{\lambda,2}$. The inclusive one-gluon cross section reads then

$$\frac{\mathrm{d}N}{\mathrm{d}^3k} = \frac{1}{(2\pi^3)2k^+} \sum_{\lambda,\lambda',a,a'} \langle \mathcal{M}^a_{\lambda,1+2} \mathcal{M}^{*,a'}_{\lambda',1+2} \rangle \,, \tag{C.3}$$

where the brackets $\langle \dots \rangle$ imply the medium average defined in Eq. (2.25). The medium-induced spectrum is obtained from this after redifining the potential as

$$\mathcal{V}(\boldsymbol{q}) \to \mathcal{V}(\boldsymbol{q}) - (2\pi)^2 \delta(\boldsymbol{q}) \int_{\boldsymbol{q}'} \mathcal{V}(\boldsymbol{q}') \,, \tag{C.4}$$

in order to account for virtual corrections in a completely analogous way to the medium-virtual diagrams considered in the Feynman diagram technique utilized in the main text.

A very similar situation to the one we are considering in the current work is the emission of a soft gluon off a colour dipole, or usually called an "antenna". We will label each of the emitters in this case simply by "1" and "2", and their kinematics is given by $p_i = (p_i^+, p_i^-, \boldsymbol{p}_i)$ while the momentum of the emitted gluon is $k = (k^+, k^-, \boldsymbol{k})$. Using the results in [194], we will here generalise their results for an antenna in a general colour configuration.

In vacuum, the square of the emission amplitude summed over colours and polarizations reads

$$\mathcal{P}^{(0)}_{\text{ant}}(k) \equiv \sum_{\lambda} \left| \mathcal{M}^{(0)}_{\lambda} \right|^2 = 4g^2 \left(\tilde{q}_1^2 \frac{1}{\boldsymbol{\kappa}_1^2} + \tilde{q}_2^2 \frac{1}{\boldsymbol{\kappa}_2^2} + 2\tilde{q}_1 \cdot \tilde{q}_2 \frac{\boldsymbol{\kappa}_1 \cdot \boldsymbol{\kappa}_2}{\boldsymbol{\kappa}_1^2 \boldsymbol{\kappa}_2^2} \right) , \tag{C.5}$$

where

$$\boldsymbol{\kappa}_i \equiv \boldsymbol{k} - z_i \boldsymbol{p}_i \,, \tag{C.6}$$

with $z_i \equiv k^+/p_i^+$ is the light-cone momentum fraction, is the transverse momentum of the emitted gluon with respect to the emitting antenna constituent.

In order to simplify the colour algebra, we have introduced the colour vectors $\mathcal{Q}_1^a$ and $\mathcal{Q}_2^a$ that obey the property $\mathcal{Q}_1^a + \mathcal{Q}_2^a = \mathcal{Q}_3^a$, where $\mathcal{Q}_3^2 \equiv \mathcal{Q}_3^a \cdot \mathcal{Q}_3^a$ is the total charge of the antenna. These vectors are defined such that for a quark $\mathcal{Q}_q^2 = C_F$, while for a gluon $\mathcal{Q}_g^2 = C_A$, where $C_F = (N_c^2 - 1)/(2N_c)$ and $C_A = N_c$. Finally, by squaring this relation we solve for the cross-term to find $\mathcal{Q}_1 \cdot \mathcal{Q}_2 = (\mathcal{Q}_3^2 - \mathcal{Q}_1^2 - \mathcal{Q}_2^2)/2$. The possible QCD $1 \to 2$

splittings give

$$\mathcal{Q}_1^2 = \mathcal{Q}_2^2 = C_F, \text{ and } \mathcal{Q}_3^2 = C_A \quad \text{for } g \to q + \bar{q}\,, \tag{C.7}$$

$$\mathcal{Q}_1^2 = \mathcal{Q}_2^2 = \mathcal{Q}_3^2 = C_A \quad \text{for } g \to g + g\,, \tag{C.8}$$

$$\mathcal{Q}_1^2 = \mathcal{Q}_3^2 = C_F, \text{ and } \mathcal{Q}_2^2 = C_A \quad \text{for } q \to q + g\,. \tag{C.9}$$

While the first two situations were analysed in references [124, 125, 193, 126, 194, 195], we are mostly interested in the latter process for the moment. Let us also introduce a compact notation that will prove very useful in the following sections. First, we define the building blocks

$$\boldsymbol{A}_1^a \equiv \mathcal{Q}_1^a \frac{\boldsymbol{\kappa}_1 - \boldsymbol{q}}{\left(\boldsymbol{\kappa}_1 - \boldsymbol{q}\right)^2}\,, \tag{C.10}$$

$$\boldsymbol{B}_1^a \equiv \mathcal{Q}_1^a \frac{\boldsymbol{\kappa}_1}{\boldsymbol{\kappa}_1^2}\,, \tag{C.11}$$

where the former will come in handy for the medium part. Note that $\boldsymbol{A}^a$ and $\boldsymbol{B}^a$ are both transverse vectors and vectors in colour space; dropping the superscript "a" simply defines the corresponding transverse vector. The same goes for any other similarly defined vector below.

For the colour configuration (C.9), the vacuum emission antenna spectrum takes the form

$$\mathcal{P}_{\text{ant}}^{(0)}(k) = 4g^2 \left[C_F \boldsymbol{B}_1^2 + C_A \left(\boldsymbol{B}_2^2 - \boldsymbol{B}_1 \cdot \boldsymbol{B}_2\right)\right]\,. \tag{C.12}$$

Due to the colour algebra, the antenna quark radiates as a free one. This comes about due to the combination of the radiation inside the cone off the antenna legs and the large-angle radiation outside the cone by the total charge. Additionally, the gluonic antenna leg can radiate inside the cone.

Proceeding now to the situation where one medium interaction is allowed, we define

the currents

$$\boldsymbol{L}_1^a \equiv \boldsymbol{A}_1^a - \boldsymbol{B}_1^a\,, \tag{C.13}$$

$$\boldsymbol{C}^a \equiv \boldsymbol{A}_1^a + \boldsymbol{A}_2^a\,, \tag{C.14}$$

where the former, Eq. (C.13), is often referred to as the "Lipatov vertex". Using this notation, it is possible to write the squared amplitude, after taking the medium average and summing over spins and colours, $\mathcal{P}_{\text{ant}}^{(1)}(k) \equiv \sum_\lambda \langle |\mathcal{M}_\lambda^{(1)}|^2 \rangle$, as

$$\mathcal{P}_{\text{ant}}^{(1)}(k) = 4g^4 C_A\, m_D^2 \int_{\boldsymbol{q}} \mathcal{V}^2(\boldsymbol{q}) \int_0^\infty \mathrm{d}x^+\, n\left(x^+\right) \tilde{w}_{\text{ant}}^{(1)}\left(x^+; k, \boldsymbol{q}\right)\,, \tag{C.15}$$

where

$$\begin{aligned}\tilde{w}_{\text{ant}}^{(1)}\left(x^+; k, \boldsymbol{q}\right) = {} & 2\left[1 - \cos\frac{x^+}{\tau_1}\right] \boldsymbol{L}_1^a \cdot \boldsymbol{C}^a + 2\left[1 - \cos\frac{x^+}{\tau_2}\right] \boldsymbol{L}_2^a \cdot \boldsymbol{C}^a \\ & - 2\left[1 - \cos\frac{x^+}{\tau_{12}}\right] \boldsymbol{L}_1^a \cdot \boldsymbol{L}_2^a\,,\end{aligned} \tag{C.16}$$

and $\tau_1 = 2k^+ \big/ \left(\boldsymbol{\kappa}_1 - \boldsymbol{q}\right)^2$, $\tau_2 = 2k^+ \big/ \left(\boldsymbol{\kappa}_2 - \boldsymbol{q}\right)^2$ and $\tau_{12} = \left(1/\tau_1 - 1/\tau_2\right)^{-1}$. While τ_1 and τ_2 are simply the formation times of a medium-induced gluon off either of the legs of the antenna, τ_{12} sets the time-scale for interference effects. Performing the colour decomposition, as given by Eq. (C.9), allows us to write

$$\begin{aligned}\tilde{w}_{\text{ant}}^{(1)}\left(x^+; k, \boldsymbol{q}\right) = {} & C_F\left[1 - \cos\frac{x^+}{\tau_1}\right]\left(\boldsymbol{L}_1^2 + \boldsymbol{A}_1^2 - \boldsymbol{B}_1^2\right) \\ & + C_A\Bigg\{\left[1 - \cos\frac{x^+}{\tau_2}\right]\left(\boldsymbol{L}_2^2 + \boldsymbol{A}_2^2 - \boldsymbol{B}_2^2 - \boldsymbol{A}_1 \cdot \boldsymbol{L}_2\right) \\ & - \left[1 - \cos\frac{x^+}{\tau_1}\right] \boldsymbol{A}_2 \cdot \boldsymbol{L}_1 + \left[1 - \cos\frac{x^+}{\tau_{12}}\right] \boldsymbol{L}_1 \cdot \boldsymbol{L}_2\Bigg\}\,.\end{aligned} \tag{C.17}$$

In order to make some sense out of this complicated expression, let us take the completely coherent scattering limit, i.e. $x^+ \to \infty$. In that case we can neglect all the cosines, and

Eq. (C.17) reduces to

$$\lim_{x^+\to\infty} \tilde{w}^{(1)}_{\text{ant}}\left(x^+;k,\boldsymbol{q}\right) = C_F\left[\boldsymbol{L}_1^2+\boldsymbol{A}_1^2-\boldsymbol{B}_1^2\right] + C_A\left[\boldsymbol{L}_2^2+\left(\boldsymbol{A}_2^2-\boldsymbol{A}_1\cdot\boldsymbol{A}_2\right)-\left(\boldsymbol{B}_2^2-\boldsymbol{B}_1\cdot\boldsymbol{B}_2\right)\right]. \tag{C.18}$$

Here we clearly see the expected features. In the medium, the Lipatov vertex gives rise to the Gunion-Bertsch spectrum, represented by $\boldsymbol{L}_i^2$. Secondly, the pure vacuum spectrum is affected by broadening, effectively replacing the vacuum spectrum with a broadened one with the appropriate weight. For the emission off the quark, since all interferences cancel, this is represented by $\boldsymbol{A}_1^2-\boldsymbol{B}_1^2$. For the emission off the gluon, due to the presence of the interference in the term proportional to C_A in Eq. (C.12), we replace the complete vacuum contribution completely analogously. A similar systematic was found for the $q\bar{q}$ antenna in [194].

The analysis of the antenna spectrum has thus provided us with crucial information. Whenever the medium scattering takes place long after the gluon formation and interference times, we simply see that $\mathcal{C}^{(1)}$ subtracts a piece of the vacuum radiation from $\mathcal{C}^{(0)}$ with a proper weight (see Eq. (C.15)) and replaces it with broadening. In addition to this, all colour charges radiate a Gunion-Bertsch spectrum. Naturally, in the general case, for finite scattering times we obtain a quite complicated interference pattern, Eq. (C.17). This can however be used to be compared to the two gluon (one hard, one soft) emission off a quark analysed in the main text, where the antenna picture has to appear naturally in the situation where the formation time of the hard gluon is exactly zero.

Appendix D

Description of the Background Subtraction Procedure

In the following we will describe the elements and logic steps taken to subtract the heavy ion background included in this work. The pion and proton background has been generated with a Monte Carlo distribution which is flat in the $\eta - \phi$ space and describes the measured p_T spectra and yield in [168] as a function of centrality. To subtract the background we have used the iterative noise/pedestal subtraction procedure. For the observables which involve jets with $p_T > 100$ GeV we have used a different version than for the observables that cover up to this p_T, according to the procedure adopted in the different experiments to which we confront our simulation. For the high p_T method, which covers most of the observables shown, the steps we take are the following:

(i) Discretize the $\eta - \phi$ space in cells of size 0.091×0.087. Sum the transverse energy E_T of all particles falling into the same cell.

(ii) Compute the average transverse energy and the deviation per rapidity strip, i.e. $\langle E_T(\eta) \rangle$ and $\sigma(\eta) = \sqrt{\langle E_T^2(\eta) \rangle - \langle E_T(\eta) \rangle^2}$.

(iii) Subtract from each cell the average plus a contribution proportional to the deviation, and set the value to zero if it becomes negative, i.e.

$$\hat{E}_T^i = \max\left(E_T^i - \left\langle E_T(\eta^i) \right\rangle - \beta\, \sigma(\eta),\, 0\right) \tag{D.1}$$

(iv) Run anti-k_T clustering algorithm using all calorimetric cells different from zero. The cells are introduced as null 4-vectors with transverse momentum E_T (the total transverse energy of the cell), with a ϕ and η corresponding to the geometric center of the cell.

(v) Repeat step (ii) excluding all cells belonging to a jet with transverse energy above $E_T^{\rm cut}$.

(vi) Repeat steps (iii) and (iv) using the values obtained in previous step.

This procedure involves fixing two parameters, namely β and $E_T^{\rm cut}$, which in general depend on the jet radius and the p_T range under study. The factor β controls the effect of background fluctuations. For an idealistic homogeneous background there would be no need for a β different from zero. For an increasingly from cell to cell fluctuating background one needs to increase this factor accordingly, at the expense of potentially overkilling the signal of interest. The value of $E_T^{\rm cut}$ decides whether a group of cells should correspond to signal and be therefore excluded from the background estimation.

These two should be chosen under the guidance that the p_T of a jet embedded into a background which is after subtracted is, in average, as close as possible to the original one (below 2% for jets with $p_T \sim 100\,\mathrm{GeV}$), which would mean that one has a good jet energy scale (JES). This test is done with Monte Carlo simulations using PYTHIA jets.

For the low p_T region, the adopted procedure uses the same space discretization and follows as:

(i) Reconstruct jets through anti-k_t with all radius using the uncorrected E_T of all the calorimetric cells introducing them as null vectors.

(ii) Select a set of seed jets with R=0.2 which have at least a constituent cell with $E_T > 3$ GeV and whose cell with maximum transverse energy has to satisfy $E_T^{\rm max} / \langle E_T \rangle > 4$, where $\langle E_T \rangle$ is the average transverse energy of the cells within the jet.

(iii) Compute the average transverse energy and the deviation per rapidity strip, i.e. $\langle E_T(\eta)\rangle$ excluding those cells that belong to the seed jets.

(iv) Subtract from each cell the average transverse energy for that rapidity strip, $\hat{E}_T^i = E_T^i - \langle E_T(\eta^i)\rangle$

(v) The second subtraction uses a combination of the seed jets with $R = 0.2$ of previous step with updated kinematics satisfying $p_T^{\text{jet}} > 25$ GeV and a set of seed track jets with $p_T^{\text{jet}} > 10$ GeV. Track jets are built using only tracks with $p_T^{\text{track}} > 4$ GeV and with reconstruction radius $R = 0.4$.

(vi) Recompute the average transverse energy $\langle E'_T(\eta)\rangle$ excluding those cells that lie within $\Delta R = 0.4$ from the seed jet axis, where ΔR is the distance in $\eta - \phi$ space.

(vii) Subtract the new average energy from all cells and update all the kinematics for jets of all radii. Only the jets with $E_T > 20$ GeV will go into further analysis.

$(viii)$ In order to suppress the contribution of combinatorial jets, we impose that the reconstructed jets have to lie within $\Delta R = 0.2$ of a track jet (defined above) with $p_T > 7$ GeV.

For the specific purposes of this work, and depending on the precise observable we want to compare to, we will need to apply corrections on the jets extracted in PbPb events. For all observables we will apply the JES correction, which takes into account the remaining average disagreement between generator level jets and embedded jets. Then, for data that is not unfolded the jet energy resolution (JER) effects are included. This amounts to smearing the jet energies with a gaussian whose width corresponds to $\sigma_{extra} = \sqrt{\sigma^2_{\text{LHC}} - \sigma^2_{we}}$, where we take into account that the JER from the real background measured at CMS is different from the one of our simplified background. This a jet p_T dependent function that is calculated with Monte Carlo simulations by fitting the energy reconstruction efficiency (reconstructed jet energy over generator level jet energy as a function of generator level jet energy) for each jet p_T bin with a gaussian and extracting the corresponding σ.

To compare to unfolded data we will perform the simplest version of the so called bin-by-bin unfolding. This affects basically the jet spectrum measurements, and the correction applied consists in multiplying the measured quenched distribution by the ratio of two other spectrums, the generator level PYTHIA jet spectrum over the reconstructed PYTHIA jet spectrum.

Bibliography

[1] A. Chodos, R. L. Jaffe, K. Johnson, C. B. Thorn and V. F. Weisskopf, Phys. Rev. D **9** (1974) 3471. doi:10.1103/PhysRevD.9.3471

[2] F. Karsch and E. Laermann, In *Hwa, R.C. (ed.) et al.: Quark gluon plasma* 1-59 [hep-lat/0305025].

[3] A. Bazavov *et al.* [HotQCD Collaboration], Phys. Rev. D **90** (2014) 094503 doi:10.1103/PhysRevD.90.094503 [arXiv:1407.6387 [hep-lat]].

[4] K. Rajagopal, Acta Phys. Polon. B **31**, 3021 (2000) [Comments Nucl. Part. Phys. A **2**, 120 (2002)] [AIP Conf. Proc. **549**, 95 (2000)] doi:10.1063/1.1345236 [hep-ph/0009058].

[5] L. D. McLerran and R. Venugopalan, Phys. Rev. D **49**, 2233 (1994) doi:10.1103/PhysRevD.49.2233 [hep-ph/9309289].

[6] H.-J. Drescher and Y. Nara, Phys. Rev. C **75**, 034905 (2007) doi:10.1103/PhysRevC.75.034905 [nucl-th/0611017].

[7] D. A. Teaney, arXiv:0905.2433 [nucl-th].

[8] M. L. Miller, K. Reygers, S. J. Sanders and P. Steinberg, Ann. Rev. Nucl. Part. Sci. **57** (2007) 205 doi:10.1146/annurev.nucl.57.090506.123020 [nucl-ex/0701025].

[9] S. Chatrchyan *et al.* [CMS Collaboration], Phys. Lett. B **724**, 213 (2013) doi:10.1016/j.physletb.2013.06.028 [arXiv:1305.0609 [nucl-ex]].

[10] S. Chatrchyan *et al.* [CMS Collaboration], Phys. Rev. C **89**, no. 4, 044906 (2014) doi:10.1103/PhysRevC.89.044906 [arXiv:1310.8651 [nucl-ex]].

[11] A. Kurkela and Y. Zhu, Phys. Rev. Lett. **115** (2015) no.18, 182301 doi:10.1103/PhysRevLett.115.182301 [arXiv:1506.06647 [hep-ph]].

[12] P. M. Chesler and L. G. Yaffe, Phys. Rev. Lett. **102** (2009) 211601 doi:10.1103/PhysRevLett.102.211601 [arXiv:0812.2053 [hep-th]].

[13] P. M. Chesler and L. G. Yaffe, Phys. Rev. D **82** (2010) 026006 doi:10.1103/PhysRevD.82.026006 [arXiv:0906.4426 [hep-th]].

[14] J. Casalderrey-Solana, M. P. Heller, D. Mateos and W. van der Schee, Phys. Rev. Lett. **111** (2013) 181601 doi:10.1103/PhysRevLett.111.181601 [arXiv:1305.4919 [hep-th]].

[15] P. M. Chesler, JHEP **1603** (2016) 146 doi:10.1007/JHEP03(2016)146 [arXiv:1601.01583 [hep-th]].

[16] U. W. Heinz and J. Liu, arXiv:1512.08276 [nucl-th].

[17] P. Kovtun, D. T. Son and A. O. Starinets, Phys. Rev. Lett. **94**, 111601 (2005) doi:10.1103/PhysRevLett.94.111601 [hep-th/0405231].

[18] N. Armesto and E. Scomparin, *Heavy-ion collisions at the Large Hadron Collider: a review of the results from Run 1*, arXiv:1511.0215.

[19] J. D. Bjorken, *Energy Loss of Energetic Partons in Quark - Gluon Plasma: Possible Extinction of High p(t) Jets in Hadron - Hadron Collisions*, .

[20] **Atlas Collaboration** Collaboration, G. Aad et al., *Observation of a Centrality-Dependent Dijet Asymmetry in Lead-Lead Collisions at* $\sqrt{s_{NN}} = 2.77$ *TeV with the ATLAS Detector at the LHC*, *Phys.Rev.Lett.* **105** (2010) 252303, [arXiv:1011.6182].

[21] **CMS** Collaboration, S. Chatrchyan et al., *Observation and studies of jet quenching in PbPb collisions at nucleon-nucleon center-of-mass energy = 2.76 TeV*, *Phys. Rev.* **C84** (2011) 024906, [arXiv:1102.1957].

[22] **CMS** Collaboration, S. Chatrchyan et al., *Jet momentum dependence of jet quenching in PbPb collisions at* $\sqrt{s_{NN}} = 2.76$ *TeV*, *Phys. Lett.* **B712** (2012) 176–197, [arXiv:1202.5022].

[23] **CMS** Collaboration, S. Chatrchyan et al., *Studies of jet quenching using isolated-photon+jet correlations in PbPb and pp collisions at* $\sqrt{s_{NN}} = 2.76$ *TeV*, *Phys. Lett.* **B718** (2013) 773–794, [arXiv:1205.0206].

[24] **CMS** Collaboration, S. Chatrchyan et al., *Measurement of jet fragmentation into charged particles in pp and PbPb collisions at* $\sqrt{s_{NN}} = 2.76$ *TeV*, *JHEP* **10** (2012) 087, [arXiv:1205.5872].

[25] **ATLAS** Collaboration, G. Aad et al., *Measurement of the jet radius and transverse momentum dependence of inclusive jet suppression in lead-lead collisions at* $\sqrt{s_{NN}}$*= 2.76 TeV with the ATLAS detector*, *Phys. Lett.* **B719** (2013) 220–241, [arXiv:1208.1967].

[26] **ATLAS** Collaboration, G. Aad et al., *Measurement of the Azimuthal Angle Dependence of Inclusive Jet Yields in Pb+Pb Collisions at* $\sqrt{s_{NN}} = 2.76$ *TeV with the ATLAS detector*, *Phys. Rev. Lett.* **111** (2013), no. 15 152301, [arXiv:1306.6469].

[27] **CMS** Collaboration, S. Chatrchyan et al., *Modification of jet shapes in PbPb collisions at* $\sqrt{s_{NN}} = 2.76$ *TeV*, *Phys. Lett.* **B730** (2014) 243–263, [arXiv:1310.0878].

[28] **ALICE** Collaboration, B. Abelev et al., *Measurement of charged jet suppression in Pb-Pb collisions at* $\sqrt{s_{NN}}$ *= 2.76 TeV*, *JHEP* **03** (2014) 013, [arXiv:1311.0633].

[29] **CMS** Collaboration, S. Chatrchyan et al., *Evidence of b-Jet Quenching in PbPb Collisions at* $\sqrt{s_{NN}} = 2.76$*??TeV*, *Phys. Rev. Lett.* **113** (2014), no. 13 132301, [arXiv:1312.4198]. [Erratum: Phys. Rev. Lett.115,no.2,029903(2015)].

[30] **CMS** Collaboration, S. Chatrchyan et al., *Measurement of jet fragmentation in PbPb and pp collisions at $\sqrt{s_{NN}} = 2.76$ TeV*, *Phys. Rev.* **C90** (2014), no. 2 024908, [arXiv:1406.0932].

[31] **ATLAS** Collaboration, G. Aad et al., *Measurement of inclusive jet charged-particle fragmentation functions in Pb+Pb collisions at $\sqrt{s_{NN}} = 2.76$ TeV with the ATLAS detector*, *Phys. Lett.* **B739** (2014) 320–342, [arXiv:1406.2979].

[32] **ATLAS** Collaboration, G. Aad et al., *Measurements of the Nuclear Modification Factor for Jets in Pb+Pb Collisions at $\sqrt{s_{\rm NN}} = 2.76$ TeV with the ATLAS Detector*, *Phys. Rev. Lett.* **114** (2015), no. 7 072302, [arXiv:1411.2357].

[33] **ALICE** Collaboration, J. Adam et al., *Measurement of jet suppression in central Pb-Pb collisions at $\sqrt{s_{\rm NN}}$ = 2.76 TeV*, *Phys. Lett.* **B746** (2015) 1–14, [arXiv:1502.0168].

[34] **CMS** Collaboration, *Nuclear modification factor of high transverse momentum jets in PbPb collisions at $\sqrt{s_{\rm NN}}$ = 2.76 TeV*, *CMS Physics Analysis Summary.* **CMS PAS HIN-12-004**.

[35] **ALICE** Collaboration, J. Adam et al., *Measurement of jet quenching with semi-inclusive hadron-jet distributions in central Pb-Pb collisions at $\sqrt{s_{\rm NN}} = 2.76$ TeV*, *JHEP* **09** (2015) 170, [arXiv:1506.0398].

[36] **PHENIX** Collaboration, S. S. Adler et al., *Suppressed π^0 production at large transverse momentum in central Au+ Au collisions at S(NN)**1/2 = 200 GeV*, *Phys. Rev. Lett.* **91** (2003) 072301, [nucl-ex/0304022].

[37] **STAR** Collaboration, J. Adams et al., *Transverse momentum and collision energy dependence of high p(T) hadron suppression in Au+Au collisions at ultrarelativistic energies*, *Phys. Rev. Lett.* **91** (2003) 172302, [nucl-ex/0305015].

[38] R. Baier, Y. L. Dokshitzer, A. H. Mueller, S. Peigne, and D. Schiff, *Radiative energy loss of high-energy quarks and gluons in a finite volume quark - gluon plasma*, *Nucl.Phys.* **B483** (1997) 291–320.

[39] B. Zakharov, *Fully quantum treatment of the Landau-Pomeranchuk-Migdal effect in QED and QCD*, *JETP Lett.* **63** (1996) 952–957.

[40] R. Baier, Y. L. Dokshitzer, A. H. Mueller, and D. Schiff, *Medium induced radiative energy loss: Equivalence between the BDMPS and Zakharov formalisms*, *Nucl. Phys.* **B531** (1998) 403–425, [hep-ph/9804212].

[41] U. A. Wiedemann, *Gluon radiation off hard quarks in a nuclear environment: Opacity expansion*, *Nucl.Phys.* **B588** (2000) 303–344.

[42] M. Gyulassy, P. Levai, and I. Vitev, *NonAbelian energy loss at finite opacity*, *Phys.Rev.Lett.* **85** (2000) 5535–5538, [nucl-th/0005032].

[43] M. Gyulassy, P. Levai, and I. Vitev, *Reaction operator approach to nonAbelian energy loss*, *Nucl.Phys.* **B594** (2001) 371–419, [nucl-th/0006010].

[44] X.-N. Wang and X.-f. Guo, *Multiple parton scattering in nuclei: Parton energy loss*, *Nucl.Phys.* **A696** (2001) 788–832, [hep-ph/0102230].

[45] P. B. Arnold, G. D. Moore, and L. G. Yaffe, *Photon and gluon emission in relativistic plasmas*, *JHEP* **0206** (2002) 030, [hep-ph/0204343].

[46] S. Jeon and G. D. Moore, *Energy loss of leading partons in a thermal QCD medium*, *Phys.Rev.* **C71** (2005) 034901, [hep-ph/0309332].

[47] S. Wicks, W. Horowitz, M. Djordjevic, and M. Gyulassy, *Elastic, inelastic, and path length fluctuations in jet tomography*, *Nucl. Phys.* **A784** (2007) 426–442, [nucl-th/0512076].

[48] G.-Y. Qin, J. Ruppert, C. Gale, S. Jeon, G. D. Moore, and M. G. Mustafa, *Radiative and collisional jet energy loss in the quark-gluon plasma at RHIC*, *Phys. Rev. Lett.* **100** (2008) 072301, [arXiv:0710.0605].

[49] J. Casalderrey-Solana and C. A. Salgado, *Introductory lectures on jet quenching in heavy ion collisions*, *Acta Phys. Polon.* **B38** (2007) 3731–3794, [arXiv:0712.3443].

[50] A. Majumder and M. Van Leeuwen, *The Theory and Phenomenology of Perturbative QCD Based Jet Quenching*, *Prog. Part. Nucl. Phys.* **A66** (2011) 41–92, [arXiv:1002.2206].

[51] G. Ovanesyan and I. Vitev, *An effective theory for jet propagation in dense QCD matter: jet broadening and medium-induced bremsstrahlung*, *JHEP* **1106** (2011) 080, [arXiv:1103.1074].

[52] Y. Mehtar-Tani, J. G. Milhano, and K. Tywoniuk, *Jet physics in heavy-ion collisions*, *Int. J. Mod. Phys.* **A28** (2013) 1340013, [arXiv:1302.2579].

[53] G. Y. Qin and X. N. Wang, Int. J. Mod. Phys. E **24** (2015) no.11, 1530014 doi:10.1142/S0218301315300143 [arXiv:1511.00790 [hep-ph]].

[54] I. P. Lokhtin, L. V. Malinina, S. V. Petrushanko, A. M. Snigirev, I. Arsene and K. Tywoniuk, Comput. Phys. Commun. **180**, 779 (2009) [arXiv:0809.2708 [hep-ph]].

[55] T. Renk, "Parton shower evolution in a 3-d hydrodynamical medium," Phys. Rev. C **78**, 034908 (2008) [arXiv:0806.0305 [hep-ph]].

[56] N. Armesto, L. Cunqueiro and C. A. Salgado, "Q-PYTHIA: A Medium-modified implementation of final state radiation," Eur. Phys. J. C **63**, 679 (2009) [arXiv:0907.1014 [hep-ph]].

[57] B. Schenke, C. Gale, and S. Jeon, *MARTINI: An Event generator for relativistic heavy-ion collisions*, *Phys.Rev.* **C80** (2009) 054913, [arXiv:0909.2037].

[58] K. C. Zapp, J. Stachel, and U. A. Wiedemann, *A local Monte Carlo framework for coherent QCD parton energy loss*, *JHEP* **1107** (2011) 118, [arXiv:1103.6252].

[59] R. K. Ellis, W. J. Stirling, and B. R. Webber, *QCD and collider physics*, *Camb. Monogr. Part. Phys. Nucl. Phys. Cosmol.* **8** (1996) 1–435.

[60] J. C. Collins, D. E. Soper and G. F. Sterman, Adv. Ser. Direct. High Energy Phys. **5** (1989) 1 [hep-ph/0409313].

[61] K. J. Eskola, V. J. Kolhinen and C. A. Salgado, Eur. Phys. J. C **9** (1999) 61 doi:10.1007/s100520050513 [hep-ph/9807297].

[62] S. Chatrchyan *et al.* [CMS Collaboration], "Studies of dijet pseudorapidity distributions and transverse momentum balance in pPb collisions at $\sqrt{s_{NN}}$=5.02 TeV," arXiv:1401.4433 [nucl-ex].

[63] M. Gyulassy, I. Vitev, X. N. Wang and B. W. Zhang, In *Hwa, R.C. (ed.) et al.: Quark gluon plasma* 123-191 [nucl-th/0302077].

[64] S. S. Gubser, I. R. Klebanov and A. W. Peet, Phys. Rev. D **54** (1996) 3915 doi:10.1103/PhysRevD.54.3915 [hep-th/9602135].

[65] S. C. Huot, S. Jeon and G. D. Moore, Phys. Rev. Lett. **98** (2007) 172303 doi:10.1103/PhysRevLett.98.172303 [hep-ph/0608062].

[66] G. Policastro, D. T. Son and A. O. Starinets, Phys. Rev. Lett. **87** (2001) 081601 doi:10.1103/PhysRevLett.87.081601 [hep-th/0104066].

[67] J. Casalderrey-Solana, H. Liu, D. Mateos, K. Rajagopal and U. A. Wiedemann, "Gauge/String Duality, Hot QCD and Heavy Ion Collisions," arXiv:1101.0618 [hep-th].

[68] J. M. Maldacena, Int. J. Theor. Phys. **38** (1999) 1113 [Adv. Theor. Math. Phys. **2** (1998) 231] doi:10.1023/A:1026654312961 [hep-th/9711200].

[69] S. Weinberg and E. Witten, Phys. Lett. B **96** (1980) 59. doi:10.1016/0370-2693(80)90212-9

[70] G. 't Hooft, Nucl. Phys. B **72** (1974) 461. doi:10.1016/0550-3213(74)90154-0

[71] J. Polchinski, Phys. Rev. Lett. **75** (1995) 4724 doi:10.1103/PhysRevLett.75.4724 [hep-th/9510017].

[72] O. Aharony, S. S. Gubser, J. M. Maldacena, H. Ooguri and Y. Oz, Phys. Rept. **323** (2000) 183 doi:10.1016/S0370-1573(99)00083-6 [hep-th/9905111].

[73] C. P. Herzog, A. Karch, P. Kovtun, C. Kozcaz and L. G. Yaffe, JHEP **0607** (2006) 013 doi:10.1088/1126-6708/2006/07/013 [hep-th/0605158].

[74] J. M. Maldacena, Phys. Rev. Lett. **80** (1998) 4859 doi:10.1103/PhysRevLett.80.4859 [hep-th/9803002].

[75] S. S. Gubser, D. R. Gulotta, S. S. Pufu and F. D. Rocha, "Gluon energy loss in the gauge-string duality," JHEP **0810**, 052 (2008) [arXiv:0803.1470 [hep-th]].

[76] Y. Hatta, E. Iancu and A. H. Mueller, "Jet evolution in the $\mathcal{N} = 4$ SYM plasma at strong coupling," JHEP **0805**, 037 (2008) [arXiv:0803.2481 [hep-th]].

[77] P. M. Chesler, K. Jensen and A. Karch, "Jets in strongly-coupled $\mathcal{N} = 4$ super Yang-Mills theory," Phys. Rev. D **79**, 025021 (2009) [arXiv:0804.3110 [hep-th]].

[78] P. M. Chesler, K. Jensen, A. Karch and L. G. Yaffe, "Light quark energy loss in strongly-coupled $\mathcal{N} = 4$ supersymmetric Yang-Mills plasma," Phys. Rev. D **79**, 125015 (2009) [arXiv:0810.1985 [hep-th]].

[79] P. Arnold and D. Vaman, "Jet quenching in hot strongly coupled gauge theories revisited: 3-point correlators with gauge-gravity duality," JHEP **1010**, 099 (2010) [arXiv:1008.4023 [hep-th]].

[80] P. Arnold and D. Vaman, "Jet quenching in hot strongly coupled gauge theories simplified," JHEP **1104**, 027 (2011) [arXiv:1101.2689 [hep-th]].

[81] P. Arnold and D. Vaman, "Some new results for 'jet' stopping in AdS/CFT: long version," J. Phys. G **38**, 124175 (2011) [arXiv:1106.1680 [hep-th]].

[82] A. Ficnar, "AdS/CFT Energy Loss in Time-Dependent String Configurations," Phys. Rev. D **86**, 046010 (2012) [arXiv:1201.1780 [hep-th]].

[83] P. Arnold, P. Szepietowski and D. Vaman, "Coupling dependence of jet quenching in hot strongly-coupled gauge theories," JHEP **1207**, 024 (2012) [arXiv:1203.6658 [hep-th]].

[84] P. Arnold, P. Szepietowski, D. Vaman and G. Wong, "Tidal stretching of gravitons into classical strings: application to jet quenching with AdS/CFT," JHEP **1302**, 130 (2013) [arXiv:1212.3321 [hep-th]].

[85] A. Ficnar and S. S. Gubser, "Finite momentum at string endpoints," Phys. Rev. D **89**, 026002 (2014) [arXiv:1306.6648 [hep-th]].

[86] A. Ficnar, S. S. Gubser and M. Gyulassy, "Shooting String Holography of Jet Quenching at RHIC and LHC," arXiv:1311.6160 [hep-ph].

[87] P. M. Chesler and K. Rajagopal, "Jet quenching in strongly coupled plasma," arXiv:1402.6756 [hep-th].

[88] A. Karch and E. Katz, "Adding flavor to AdS / CFT," JHEP **0206**, 043 (2002) doi:10.1088/1126-6708/2002/06/043 [hep-th/0205236].

[89] P. M. Chesler and K. Rajagopal, arXiv:1511.07567 [hep-th].

[90] P. M. Chesler and L. G. Yaffe, Phys. Rev. Lett. **99** (2007) 152001 doi:10.1103/PhysRevLett.99.152001 [arXiv:0706.0368 [hep-th]].

[91] K. Adcox *et al.* [PHENIX Collaboration], "Suppression of hadrons with large transverse momentum in central Au+Au collisions at $\sqrt{s_{NN}}$ = 130-GeV," Phys. Rev. Lett. **88**, 022301 (2002) [nucl-ex/0109003].

[92] C. Adler *et al.* [STAR Collaboration], "Centrality dependence of high p_T hadron suppression in Au+Au collisions at $\sqrt{s}_{NN}$ = 130-GeV," Phys. Rev. Lett. **89**, 202301 (2002) [nucl-ex/0206011].

[93] U. Heinz and R. Snellings, "Collective flow and viscosity in relativistic heavy-ion collisions," Ann. Rev. Nucl. Part. Sci. **63**, 123 (2013) [arXiv:1301.2826 [nucl-th]].

[94] J. Casalderrey-Solana, C. A. Salgado, "Introductory lectures on jet quenching in heavy ion collisions," Acta Phys. Polon. **B38**, 3731-3794 (2007). [arXiv:0712.3443 [hep-ph]].

[95] P. Jacobs and X.-N. Wang, "Matter in extremis: Ultrarelativistic nuclear collisions at RHIC," Prog. Part. Nucl. Phys. **54**, 443 (2005) [arXiv:hep-ph/0405125].

[96] J. Casalderrey-Solana and D. Teaney, "Heavy quark diffusion in strongly coupled $\mathcal{N} = 4$ Yang-Mills," Phys. Rev. D **74**, 085012 (2006) [hep-ph/0605199].

[97] S. S. Gubser, "Drag force in AdS/CFT," Phys. Rev. D **74**, 126005 (2006) [hep-th/0605182].

[98] H. Liu, K. Rajagopal and U. A. Wiedemann, "An AdS/CFT Calculation of Screening in a Hot Wind," Phys. Rev. Lett. **98**, 182301 (2007) [hep-ph/0607062].

[99] P. M. Chesler, Y.-Y. Ho and K. Rajagopal, "Shining a Gluon Beam Through Quark-Gluon Plasma," Phys. Rev. D **85**, 126006 (2012) [arXiv:1111.1691 [hep-th]].

[100] M. Chernicoff, J. A. Garcia, A. Guijosa and J. F. Pedraza, J. Phys. G **39**, 054002 (2012) [arXiv:1111.0872 [hep-th]].

[101] C. Marquet and T. Renk, "Jet quenching in the strongly-interacting quark-gluon plasma," Phys. Lett. B **685**, 270 (2010) [arXiv:0908.0880 [hep-ph]].

[102] B. Betz, M. Gyulassy and G. Torrieri, "Sensitivity of Azimuthal Jet Tomography to Early Time Energy-Loss at RHIC and LHC," J. Phys. G **38**, 124153 (2011) [arXiv:1106.4564 [nucl-th]].

[103] A. Ficnar, J. Noronha and M. Gyulassy, "Falling Strings and Light Quark Jet Quenching at LHC," Nucl. Phys. A **910-911**, 252 (2013) [arXiv:1208.0305 [hep-ph]].

[104] B. Betz and M. Gyulassy, "Constraints on the Path-Length Dependence of Jet Quenching in Nuclear Collisions at RHIC and LHC," arXiv:1404.6378 [hep-ph].

[105] J. Casalderrey-Solana, J. G. Milhano and P. Q. Arias, "Out of Medium Fragmentation from Long-Lived Jet Showers," Phys. Lett. B **710**, 175 (2012) [arXiv:1111.0310 [hep-ph]].

[106] J. Casalderrey-Solana, J. G. Milhano and U. A. Wiedemann, "Jet Quenching via Jet Collimation," J. Phys. G **38**, 035006 (2011) [arXiv:1012.0745 [hep-ph]].

[107] J.-P. Blaizot, E. Iancu and Y. Mehtar-Tani, "Medium-induced QCD cascade: democratic branching and wave turbulence," Phys. Rev. Lett. **111**, 052001 (2013) [arXiv:1301.6102 [hep-ph]].

[108] P. M. Chesler, M. Lekaveckas and K. Rajagopal, "Heavy quark energy loss far from equilibrium in a strongly coupled collision," JHEP **1310**, 013 (2013) [arXiv:1306.0564 [hep-ph]].

[109] P. K. Kovtun and A. O. Starinets, "Quasinormal modes and holography," Phys. Rev. D **72**, 086009 (2005) [hep-th/0506184].

[110] J. Casalderrey-Solana, E. V. Shuryak and D. Teaney, "Conical flow induced by quenched QCD jets," J. Phys. Conf. Ser. **27**, 22 (2005) [Nucl. Phys. A **774**, 577 (2006)] [hep-ph/0411315].

[111] W. A. Horowitz and M. Gyulassy, "Testing AdS/CFT Drag and pQCD Heavy Quark Energy Loss," J. Phys. G **35**, 104152 (2008) [arXiv:0804.4330 [hep-ph]].

[112] W. A. Horowitz and M. Gyulassy, "The Surprising Transparency of the sQGP at LHC," Nucl. Phys. A **872**, 265 (2011) [arXiv:1104.4958 [hep-ph]].

[113] W. A. Horowitz and M. Gyulassy, "Quenching and Tomography from RHIC to LHC," J. Phys. G **38**, 124114 (2011) [arXiv:1107.2136 [hep-ph]].

[114] F. Dominguez, C. Marquet, A. H. Mueller, B. Wu and B.-W. Xiao, "Comparing energy loss and p-perpendicular – broadening in perturbative QCD with strong coupling $\mathcal{N} = 4$ SYM theory," Nucl. Phys. A **811**, 197 (2008) [arXiv:0803.3234 [nucl-th]].

[115] K. M. Burke, A. Buzzatti, N. Chang, C. Gale, M. Gyulassy, U. Heinz, S. Jeon and A. Majumder *et al.*, "Extracting jet transport coefficient from jet quenching at RHIC and LHC," arXiv:1312.5003 [nucl-th].

[116] J. Casalderrey-Solana and X.-N. Wang, "Energy dependence of jet transport parameter and parton saturation in quark-gluon plasma," Phys. Rev. C **77**, 024902 (2008) [arXiv:0705.1352 [hep-ph]].

[117] E. Iancu, "The non-linear evolution of jet quenching," arXiv:1403.1996 [hep-ph].

[118] J.-P. Blaizot and Y. Mehtar-Tani, "Renormalization of the jet-quenching parameter," arXiv:1403.2323 [hep-ph].

[119] I. P. Lokhtin, A. V. Belyaev and A. M. Snigirev, "Jet quenching pattern at LHC in PYQUEN model," Eur. Phys. J. C **71**, 1650 (2011) [arXiv:1103.1853 [hep-ph]].

[120] K. C. Zapp, "JEWEL 2.0.0: directions for use," Eur. Phys. J. C **74**, 2762 (2014) [arXiv:1311.0048 [hep-ph]].

[121] T. Sjostrand, S. Mrenna and P. Z. Skands, "A Brief Introduction to PYTHIA 8.1," Comput. Phys. Commun. **178**, 852 (2008) [arXiv:0710.3820 [hep-ph]].

[122] K. J. Eskola, H. Paukkunen and C. A. Salgado, "EPS09: A New Generation of NLO and LO Nuclear Parton Distribution Functions," JHEP **0904**, 065 (2009) [arXiv:0902.4154 [hep-ph]].

[123] S. Chatrchyan *et al.* [CMS Collaboration], Eur. Phys. J. C **74** (2014) no.7, 2951 doi:10.1140/epjc/s10052-014-2951-y [arXiv:1401.4433 [nucl-ex]].

[124] Y. Mehtar-Tani, C. A. Salgado and K. Tywoniuk, "Anti-angular ordering of gluon radiation in QCD media," Phys. Rev. Lett. **106**, 122002 (2011) [arXiv:1009.2965 [hep-ph]].

[125] Y. Mehtar-Tani, C. A. Salgado and K. Tywoniuk, "Jets in QCD Media: From Color Coherence to Decoherence," Phys. Lett. B **707**, 156 (2012) [arXiv:1102.4317 [hep-ph]].

[126] J. Casalderrey-Solana and E. Iancu, "Interference effects in medium-induced gluon radiation," JHEP **1108**, 015 (2011) [arXiv:1105.1760 [hep-ph]].

[127] A. Beraudo, J. G. Milhano and U. A. Wiedemann, "Medium-induced color flow softens hadronization," Phys. Rev. C **85**, 031901 (2012) [arXiv:1109.5025 [hep-ph]].

[128] A. Beraudo, J. G. Milhano and U. A. Wiedemann, "The Contribution of Medium-Modified Color Flow to Jet Quenching," JHEP **1207** (2012) 144 [arXiv:1204.4342 [hep-ph]].

[129] P. Aurenche and B. G. Zakharov, "Jet color chemistry and anomalous baryon production in AA-collisions," Eur. Phys. J. C **71** (2011) 1829 [arXiv:1109.6819 [hep-ph]].

[130] G. Soyez, "A Simple description of jet cross-section ratios," Phys. Lett. B **698**, 59 (2011) [arXiv:1101.2665 [hep-ph]].

[131] C. Shen, Z. Qiu, H. Song, J. Bernhard, S. Bass and U. Heinz, Comput. Phys. Commun. **199** (2016) 61 doi:10.1016/j.cpc.2015.08.039 [arXiv:1409.8164 [nucl-th]].

[132] C. Shen, J. F. Paquet, U. Heinz and C. Gale, Phys. Rev. C **91** (2015) no.1, 014908 doi:10.1103/PhysRevC.91.014908 [arXiv:1410.3404 [nucl-th]].

[133] P. Huovinen and P. Petreczky, Nucl. Phys. A **837** (2010) 26 doi:10.1016/j.nuclphysa.2010.02.015 [arXiv:0912.2541 [hep-ph]].

[134] Y. Aoki, S. Borsanyi, S. Durr, Z. Fodor, S. D. Katz, S. Krieg and K. K. Szabo, JHEP **0906** (2009) 088 doi:10.1088/1126-6708/2009/06/088 [arXiv:0903.4155 [hep-lat]].

[135] A. Bialas, M. Bleszynski and W. Czyz, "Multiplicity Distributions in Nucleus-Nucleus Collisions at High-Energies," Nucl. Phys. B **111**, 461 (1976).

[136] B. Abelev *et al.* [ALICE Collaboration], Phys. Rev. C **88** (2013) no.4, 044909 doi:10.1103/PhysRevC.88.044909 [arXiv:1301.4361 [nucl-ex]].

[137] M. Cacciari, G. P. Salam and G. Soyez, "FastJet User Manual," Eur. Phys. J. C **72** (2012) 1896 [arXiv:1111.6097 [hep-ph]].

[138] M. Cacciari, G. P. Salam and G. Soyez, "The Anti-k_t jet clustering algorithm," JHEP **0804**, 063 (2008) [arXiv:0802.1189 [hep-ph]].

[139] CMS Collaboration, "Nuclear modification factor of high transverse momentum jets in PbPb collisions at $\sqrt{s_{NN}} = 2.76$ TeV", CMS PAS HIN-12-004.

[140] J. Rusnak for the STAR Collaboration, "Inclusive Spectrum of Fully Reconstructed Charged Jets in Central Au+Au Collisions at $\sqrt{s_{NN}} = 200$ GeV by the STAR Collaboration", talk at the conference "Hard Probes 2013, Cape Town, South Africa, November 2013.

[141] Y. Yilmaz, "Jet quenching in heavy-ion collisions at LHC with CMS detector", PhD thesis, http://web.mit.edu/mithig/theses/Yetkin-Yilmaz-thesis.pdf

[142] The ATLAS Collaboration, "Measurement of inclusive jet charged particle fragmentation functions in Pb+Pb collisions at $\sqrt{s_{NN}} = 2.76$ TeV with the ATLAS detector", ATLAS-CONF-2012-115.

[143] CMS Collaboration, "Jet shapes and fragmentation functions", CMS-HIN-12-013.

[144] T. Renk, arXiv:1406.6784 [hep-ph].

[145] CMS Collaboration [CMS Collaboration], CMS-PAS-HIN-13-006.

[146] A. Milov [ATLAS Collaboration], Nucl. Phys. A **910-911** (2013) 131 doi:10.1016/j.nuclphysa.2012.12.062 [arXiv:1209.0088 [nucl-ex]].

[147] ATLAS Collaboration, "Measurement of jet fragmentation in 5.02 TeV proton-lead and 2.76 TeV proton-proton collisions with the ATLAS detector", ATLAS-CONF-2015-022.

[148] D. d'Enterria, K. J. Eskola, I. Helenius and H. Paukkunen, "Confronting current NLO parton fragmentation functions with inclusive charged-particle spectra at hadron colliders," Nucl. Phys. B **883**, 615 (2014) [arXiv:1311.1415 [hep-ph]].

[149] X. N. Wang and Y. Zhu, "Medium Modification of γ-jets in High-energy Heavy-ion Collisions," Phys. Rev. Lett. **111**, no. 6, 062301 (2013) [arXiv:1302.5874 [hep-ph]].

[150] Y. Tachibana and T. Hirano, "Momentum transport away from a jet in an expanding nuclear medium," Phys. Rev. C **90**, no. 2, 021902 (2014) [arXiv:1402.6469 [nucl-th]].

[151] Y. He, T. Luo, X. N. Wang and Y. Zhu, "Linear Boltzmann Transport for Jet Propagation in the Quark-Gluon Plasma: Elastic Processes and Medium Recoil," Phys. Rev. C **91**, 054908 (2015) [arXiv:1503.03313 [nucl-th]].

[152] E. Iancu and B. Wu, "Thermalization of mini-jets in a quark-gluon plasma," arXiv:1506.07871 [hep-ph].

[153] CMS Collaboration, "Measurement of transverse momentum flow relative to the dijet system in PbPb and pp collisions at sqrt(sNN) = 2.76 TeV," CMS PAS HIN-14-010.

[154] F. D'Eramo, M. Lekaveckas, H. Liu and K. Rajagopal, "Momentum Broadening in Weakly Coupled Quark-Gluon Plasma (with a view to finding the quasiparticles within liquid quark-gluon plasma)," JHEP **1305**, 031 (2013) [arXiv:1211.1922 [hep-ph]].

[155] J. Casalderrey-Solana, Y. Mehtar-Tani, C. A. Salgado and K. Tywoniuk, "New picture of jet quenching dictated by color coherence," Phys. Lett. B **725**, 357 (2013) [arXiv:1210.7765 [hep-ph]].

[156] J. Casalderrey-Solana and A. Ficnar, arXiv:1512.00371 [hep-th].

[157] H. Liu, K. Rajagopal and U. A. Wiedemann, Phys. Rev. Lett. **97** (2006) 182301 doi:10.1103/PhysRevLett.97.182301 [hep-ph/0605178].

[158] J. Casalderrey-Solana and D. Teaney, JHEP **0704** (2007) 039 doi:10.1088/1126-6708/2007/04/039 [hep-th/0701123].

[159] K. Rajagopal, A. V. Sadofyev and W. van der Schee, arXiv:1602.04187 [nucl-th].

[160] H. Stoecker, Nucl. Phys. A **750**, 121 (2005) doi:10.1016/j.nuclphysa.2004.12.074 [nucl-th/0406018].

[161] L. M. Satarov, H. Stoecker and I. N. Mishustin, Phys. Lett. B **627**, 64 (2005) doi:10.1016/j.physletb.2005.08.102 [hep-ph/0505245].

[162] J. Casalderrey-Solana, E. V. Shuryak and D. Teaney, hep-ph/0602183.

[163] J. P. Blaizot, Y. Mehtar-Tani and M. A. C. Torres, Phys. Rev. Lett. **114**, no. 22, 222002 (2015) doi:10.1103/PhysRevLett.114.222002 [arXiv:1407.0326 [hep-ph]].

[164] L. Fister and E. Iancu, JHEP **1503**, 082 (2015) doi:10.1007/JHEP03(2015)082 [arXiv:1409.2010 [hep-ph]].

[165] B. Betz, M. Gyulassy, D. H. Rischke, H. Stocker and G. Torrieri, J. Phys. G **35**, 104106 (2008) doi:10.1088/0954-3899/35/10/104106 [arXiv:0804.4408 [hep-ph]].

[166] B. Betz, J. Noronha, G. Torrieri, M. Gyulassy, I. Mishustin and D. H. Rischke, Phys. Rev. C **79**, 034902 (2009) doi:10.1103/PhysRevC.79.034902 [arXiv:0812.4401 [nucl-th]].

[167] Y. Tachibana and T. Hirano, arXiv:1510.06966 [nucl-th].

[168] B. Abelev *et al.* [ALICE Collaboration], Phys. Rev. C **88**, 044910 (2013) doi:10.1103/PhysRevC.88.044910 [arXiv:1303.0737 [hep-ex]].

[169] M. Cacciari and G. P. Salam, Phys. Lett. B **659**, 119 (2008) doi:10.1016/j.physletb.2007.09.077 [arXiv:0707.1378 [hep-ph]].

[170] M. Cacciari, G. P. Salam and G. Soyez, JHEP **0804**, 005 (2008) doi:10.1088/1126-6708/2008/04/005 [arXiv:0802.1188 [hep-ph]].

[171] M. Cacciari, J. Rojo, G. P. Salam and G. Soyez, Eur. Phys. J. C **71**, 1539 (2011) doi:10.1140/epjc/s10052-011-1539-z [arXiv:1010.1759 [hep-ph]].

[172] O. Kodolova, I. Vardanian, A. Nikitenko and A. Oulianov, Eur. Phys. J. C **50**, 117 (2007). doi:10.1140/epjc/s10052-007-0223-9

[173] J. Casalderrey-Solana, D. C. Gulhan, J. G. Milhano, D. Pablos and K. Rajagopal, JHEP **1410**, 19 (2014) Erratum: [JHEP **1509**, 175 (2015)] doi:10.1007/JHEP09(2015)175, 10.1007/JHEP10(2014)019 [arXiv:1405.3864 [hep-ph]].

[174] J. Casalderrey-Solana, D. C. Gulhan, J. G. Milhano, D. Pablos and K. Rajagopal, JHEP **1603**, 053 (2016) doi:10.1007/JHEP03(2016)053 [arXiv:1508.00815 [hep-ph]].

[175] M. Dasgupta, F. A. Dreyer, G. P. Salam and G. Soyez, arXiv:1602.01110 [hep-ph].

[176] K. C. Zapp, F. Krauss and U. A. Wiedemann, JHEP **1303**, 080 (2013) doi:10.1007/JHEP03(2013)080 [arXiv:1212.1599 [hep-ph]].

[177] K. Zapp, J. Stachel and U. A. Wiedemann, Phys. Rev. Lett. **103**, 152302 (2009) doi:10.1103/PhysRevLett.103.152302 [arXiv:0812.3888 [hep-ph]].

[178] K. Zapp, G. Ingelman, J. Rathsman, J. Stachel and U. A. Wiedemann, Eur. Phys. J. C **60**, 617 (2009) doi:10.1140/epjc/s10052-009-0941-2 [arXiv:0804.3568 [hep-ph]].

[179] V. Khachatryan *et al.* [CMS Collaboration], JHEP **1601**, 006 (2016) doi:10.1007/JHEP01(2016)006 [arXiv:1509.09029 [nucl-ex]].

[180] Y. Mehtar-Tani and K. Tywoniuk, Phys. Lett. B **744**, 284 (2015) doi:10.1016/j.physletb.2015.03.041 [arXiv:1401.8293 [hep-ph]].

[181] Y. T. Chien and I. Vitev, arXiv:1509.07257 [hep-ph].

[182] J. P. Blaizot, F. Dominguez, E. Iancu and Y. Mehtar-Tani, JHEP **1301** (2013) 143 doi:10.1007/JHEP01(2013)143 [arXiv:1209.4585 [hep-ph]].

[183] L. ApolinÃąrio, N. Armesto, J. G. Milhano and C. A. Salgado, JHEP **1502** (2015) 119 doi:10.1007/JHEP02(2015)119 [arXiv:1407.0599 [hep-ph]].

[184] A. Kurkela and U. A. Wiedemann, Phys. Lett. B **740** (2015) 172 doi:10.1016/j.physletb.2014.11.054 [arXiv:1407.0293 [hep-ph]].

[185] R. Baier, A. H. Mueller, D. Schiff and D. T. Son, Phys. Lett. B **502** (2001) 51 doi:10.1016/S0370-2693(01)00191-5 [hep-ph/0009237].

[186] P. B. Arnold, G. D. Moore and L. G. Yaffe, JHEP **0301** (2003) 030 doi:10.1088/1126-6708/2003/01/030 [hep-ph/0209353].

[187] T. Liou, A. H. Mueller and B. Wu, Nucl. Phys. A **916** (2013) 102 doi:10.1016/j.nuclphysa.2013.08.005 [arXiv:1304.7677 [hep-ph]].

[188] B. Wu, JHEP **1412** (2014) 081 doi:10.1007/JHEP12(2014)081 [arXiv:1408.5459 [hep-ph]].

[189] J. Ghiglieri and D. Teaney, Int. J. Mod. Phys. E **24** (2015) no.11, 1530013 doi:10.1142/S0218301315300131 [arXiv:1502.03730 [hep-ph]].

[190] J. Ghiglieri, G. D. Moore and D. Teaney, JHEP **1603** (2016) 095 doi:10.1007/JHEP03(2016)095 [arXiv:1509.07773 [hep-ph]].

[191] P. Arnold and S. Iqbal, JHEP **1504** (2015) 070 doi:10.1007/JHEP04(2015)070 [arXiv:1501.04964 [hep-ph]].

[192] M. Fickinger, G. Ovanesyan and I. Vitev, JHEP **1307** (2013) 059 doi:10.1007/JHEP07(2013)059 [arXiv:1304.3497 [hep-ph]].

[193] N. Armesto, H. Ma, Y. Mehtar-Tani, C. A. Salgado and K. Tywoniuk, JHEP **1201** (2012) 109 doi:10.1007/JHEP01(2012)109 [arXiv:1110.4343 [hep-ph]].

[194] Y. Mehtar-Tani, C. A. Salgado and K. Tywoniuk, JHEP **1204** (2012) 064 doi:10.1007/JHEP04(2012)064 [arXiv:1112.5031 [hep-ph]].

[195] Y. Mehtar-Tani, C. A. Salgado and K. Tywoniuk, JHEP **1210** (2012) 197 doi:10.1007/JHEP10(2012)197 [arXiv:1205.5739 [hep-ph]].

[196] M. SjÃűdahl, Eur. Phys. J. C **73** (2013) no.2, 2310 doi:10.1140/epjc/s10052-013-2310-4 [arXiv:1211.2099 [hep-ph]].

[197] J. F. Gunion and G. Bertsch, Phys. Rev. D **25** (1982) 746. doi:10.1103/PhysRevD.25.746